WELD DEVELOPMENT FOR INCOLOY ALLOY 908, A LOW THERMAL EXPANSION SUPERALLOY

by

Chang Heui Jang

B.S., Nuclear Engineering
Seoul National University (1986)
and
M.S., Nuclear Engineering
Korea Advanced Institute of Science and Technology (1988)

Submitted to the Department of Nuclear Engineering
in partial fulfillment of the requirements for the degree of

DOCTOR OF PHILOSOPHY

at the

MASSACHUSETTS INSTITUTE OF TECHNOLOGY

January 1995

Signature of Author _____

Department of Nuclear Engineering
January 13, 1995

Certified by _____

Dr. Ronald G. Ballinger
Professor, Nuclear Engineering and Materials Science and Engineering
Thesis Supervisor

Certified by _____

Dr. Joseph Minervini
Plasma Fusion Center
Thesis Reader

Accepted by _____

Dr. Allan F. Henry
Chairman, Departmental Committee on Graduate Studies

WELD DEVELOPMENT FOR INCOLOY ALLOY 908,
A LOW THERMAL EXPANSION SUPERALLOY

by

CHANG HEUI JANG

Submitted to the Department of Nuclear Engineering
on January 13, 1995 in partial fulfillment of the
requirements for the Degree of Doctor of Philosophy in
Nuclear Engineering

ABSTRACT

In this thesis, an systematic approach was taken to: (1) understand the fundamental processes operative in welding alloy 908 and (2) development of appropriate filler wire compositions based on (1).

Improvement of fracture toughness was achieved in two ways:

- By reducing the concentration of niobium in weld filler wire,
- By homogenizing the weld prior to aging heat treatment.

Both methods reduced or eliminated Laves phase and/or the size of surrounding brittle area.

Solidification characteristics of alloy 908 welds is that:

- During the weld solidification, niobium segregates into interdendritic zone and precipitated in the formation of cubic MC carbides and hexagonal Laves phases.
- The area surrounding these secondary phases is enriched with niobium and become brittle after aging heat treatment.

Fractography analysis of welds revealed that:

- Fracture occurs by a typical ductile dimple rupture mechanism, voids initiating at MC carbides and Laves phases.
- Voids grows, first by the failure of surrounding brittle area, then by plastic deformation of ductile matrix.

Thus, the segregation of niobium was identified as a primary cause of weld degradation.

Thesis Supervisor: Dr. Ronald G. Ballinger
Associate Professor of Nuclear Engineering
and Materials Science and Engineering

Dedication

To my wife, Seunghee, my son, Kevin and
my mother and father.

Table of Contents

List of Figures

List of Tables

Nomenclature

GTAW	: Weld joined by manual multi-pass gas tungsten arc welding using filler wire.
EBW	: Weld joined by electron beam welding without filler.
LBW	: Weld joined by laser beam welding without filler.
FW	: Weld joined by flash welding method.
UTS	: Ultimate tensile strength.
MA	: Mill annealed condition. After heat treated for 1 hour at 980 °C followed by slow cooling. The condition of as recieved plates.
SA	: Solution anneal. Heat treatment for 1 hour at 980 °C followed by water quenching.
HT	: Homogenization. Heat treatment for 1 hour at 1050 °C followed by water quenching.
Aging	: Precipitation hardening heat treatment for 200 hours at 650 °C in vacuum.
ITER	: International thermonuclear experimental reactor.
VHN	: Vickers microhardness number, kg/mm^2.
σ_y	: Yield strength, MPa.
K_Q	: Plane strain fracture toughness, $MPa\sqrt{m}$.
XXX-GTAW	: Weld joined by manual multi-pass gas tungsten arc welding using filler wire designated as XXX.
AW	: As welded condition.
F	: Top half of the weld sliced from 7-mm thick GTAW.
R	: Bottom half of the weld sliced from 7-mm thick GTAW.
T	: Top quater of the weld sliced from 13 mm-thick GTAW.
TB	: Second quater of the weld sliced from 13 mm-thick GTAW.
BT	: Third quater of the weld sliced from 13 mm-thick GTAW.
B	: Bottom quater of the weld sliced from 13 mm-thick GTAW.

I. Introduction

Incoloy alloy 908 (afterward, alloy 908) is a nickel-iron base superalloy with a low coefficient of thermal expansion and mechanical properties optimized for use as a structural material in Nb3Sn superconducting magnets such as those proposed for use in the International Thermonuclear Experimental Reactor (ITER).[1] Strengthening is achieved by precipitation of γ' [$Ni_3(Al,Ti,Nb)$] during the superconductor reaction heat treatment. Alloy 908 exhibits superior mechanical and thermal properties for its application as a conduit for ITER magnet.[2]

The manufacturing of Cable-In-Conduit Conductor (CICC) type superconducting cable for ITER requires joining multiple of extruded conduit segment. A schematic of the process steps for the conduit is shown in Figure 1.[3] The extruded conduit design, shown in Figure 2, consists of a rectangular shape with circular hole at the center. Individual conduit sections can be about 10 meters in length. The total conduit length will be approximately 1000 meters. This will require that approximately 100 welds will be made for each coil. Considering the number of weld joints in the finished cable assembly, it is crucial to have a physically sound and mechanically strong and tough weld joint. However, preliminary studies indicated that there was considerable mechanical property degradation in alloy 908 welds.[2]

In many of precipitation hardening superalloys, such as Inconel 718 and alloy 908, segregation of some of the alloying elements with subsequent precipitation of brittle intermetallic phases during solidification has been considered to be the primary reason of weld properties degradation.[5,6] The presence of brittle secondary phases within the interdendritic area of the weld introduces microscopic inhomogeneity. These secondary phases provide void initiation sites during fracture, and contribute to low fracture toughness of the weld. To improve the fracture toughness of welds in alloy 908, the solidification characteristics and fracture mechanism must be understood.

Currently there exits no approved filler wire material for use in welding alloy 908. Based on the above discussion it was anticipated that special filler wire compositions would have to be designed if property degradation was to be minimized. In this thesis, an systematic

approach was taken to: (1) understand the fundamental processes operative in welding alloy 908 and (2) development of appropriate filler wire compositions based on (1).

Several approaches were taken to understand the relationships between solidification characteristics and weld mechanical properties of alloy 908 welds. First, the weld microstructure was defined as a function of welding technique. Welding methods used included electron beam welding and laser beam welding, as well as gas tungsten arc welding. Additionally, flash welding, a solid state welding technique was evaluated. Second, post weld heat treatments were used to modify the microstructure of welds. Based on the results of these investigations, new weld filler metal compositions were developed and the effects of alloying element content on solidification and mechanical properties at room temperature were evaluated. Based on this analysis, two weld filler compositions were chosen, and used in the evaluation of the effects of cold work and test temperature on the mechanical properties. Finally, weld mechanical properties in combination with anticipated fabrication processes for superconducting magnets were evaluated and a final optimum filler wire composition was chosen.

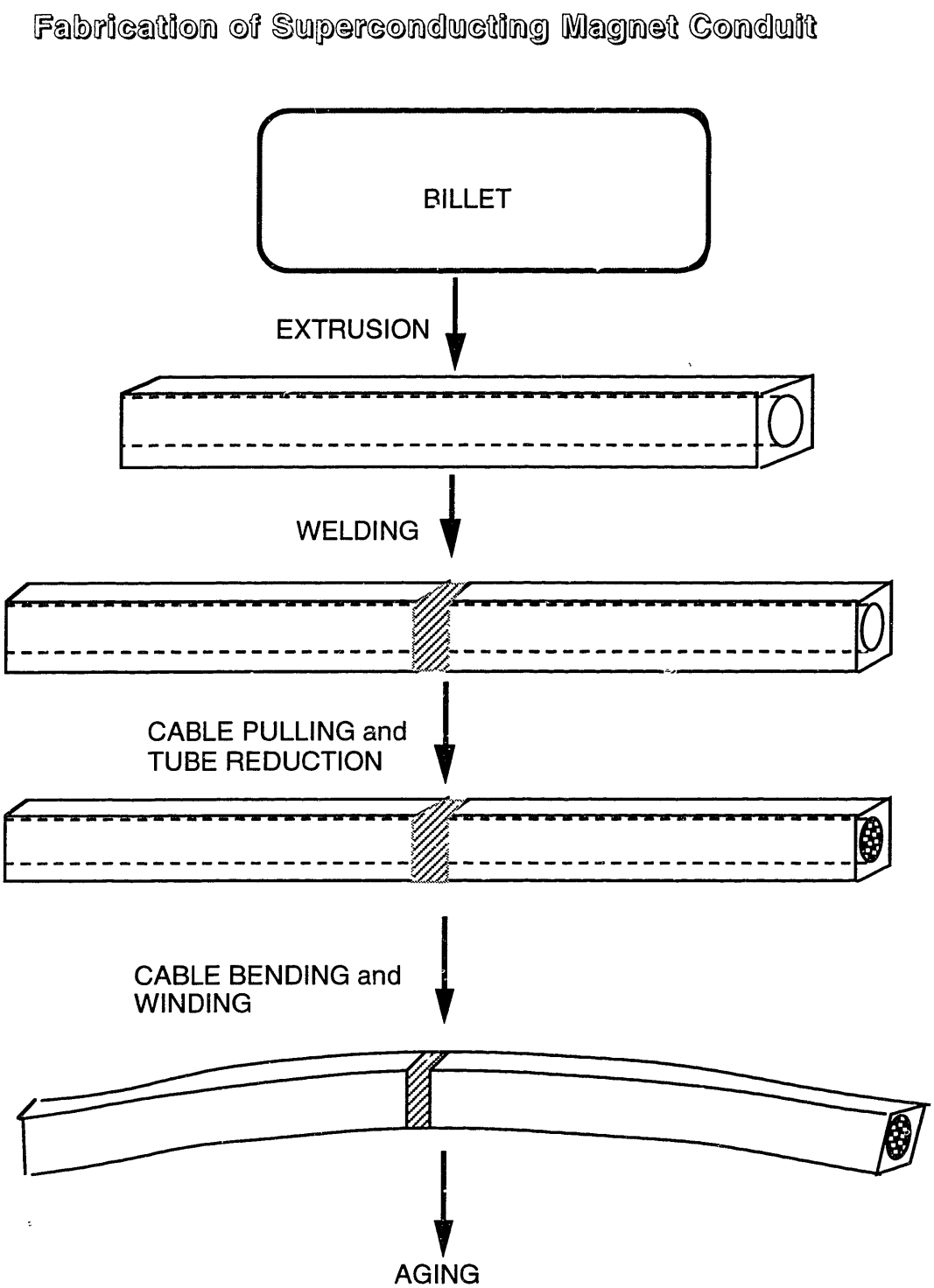

Figure 1. A schematic of fabrication processes of superconducting magnet assembly using Nb_3Sn superconducting wires and alloy 908 conduits.

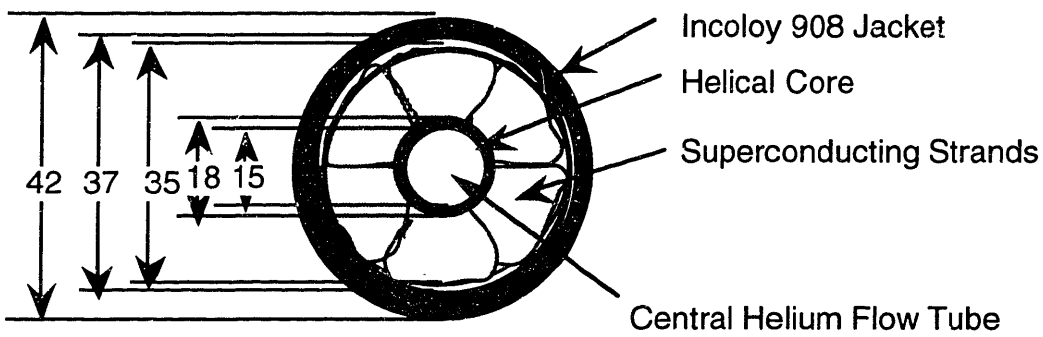

a) Toroidal Field Coil 2

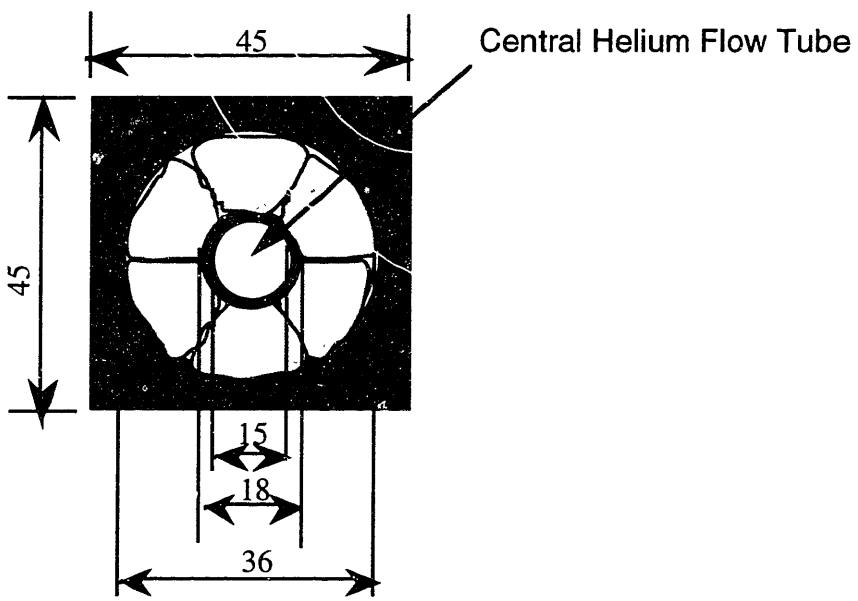

b) Central Solenoid Coil 2

Figure 2. Cable in conduit conductors for ITER magnet. [4]

II. Literature Review

II.1 Development of Alloy 908 for Fusion Application

II.1.1. Description of CICC Superconductor

The replacement of normal conducting materials by superconductors can result in considerable improvement in performance of large scale electromagnetic devices. This is especially true where high power and/or high magnetic fields are required. Applications include high energy particle accelerators, controlled thermonuclear fusion reactors, and superconducting magnet energy storage systems.[7] High current density and very small heat loss can considerably reduce the size and weight compared to that of conventional magnets. The most widely used superconductor materials for large scale applications are NbTi and Nb_3Sn. Both of these are classified as type II superconductors. The characteristics of type II superconductors are; 1) relatively high critical temperature, T_c, 2) high upper critical field (Hc_2) with high critical current density, J_c, and 3) gradual reversion to normal state between Hc_1 and Hc_2. A schematic relationship among the three parameters is shown in Figure 3. The critical current density represents the upper limit of the current carrying capacity of a superconducting material and is a strong function of both the applied field and temperature. The upper critical field vs. temperature and magnetic field for various superconductors are shown in figures 4 and 5. The properties of the two most widely used superconductors are compared in Table 1. NbTi represents the dominant usage for magnetic fields up to 10 Tesla. It is an excellent engineering material; strong, flexible and easily processed. For magnetic field above 10 Tesla, Nb_3Sn alloys dominate. Nb_3Sn is brittle, its properties are strain sensitive, and the material is difficult to fabricate. These properties make the design of a high filed magnet using Nb_3Sn a difficult engineering challenge.[11]

In most practical conductors, the superconducting material is in the form of very fine filaments within a matrix of normal conductor (usually high quality copper) to stabilize the system against magnetic and mechanical and thermaldisturbance. In the so-called "Cable-In-Conduit-Conductor", or CICC design, the magnets are fabricated using superconducting cables that are enclosed in metallic conduit.[12] The conduit serves as a distributed

structural component that bears a large fraction of the high electromagnetic force. Two of the CICC superconductor designs to be used in the magnet of International Thermonuclear Experimental Reactor (ITER) are shown in Figure 2. In this design cooling is provided by the forced flow of liquid helium through the central tube.

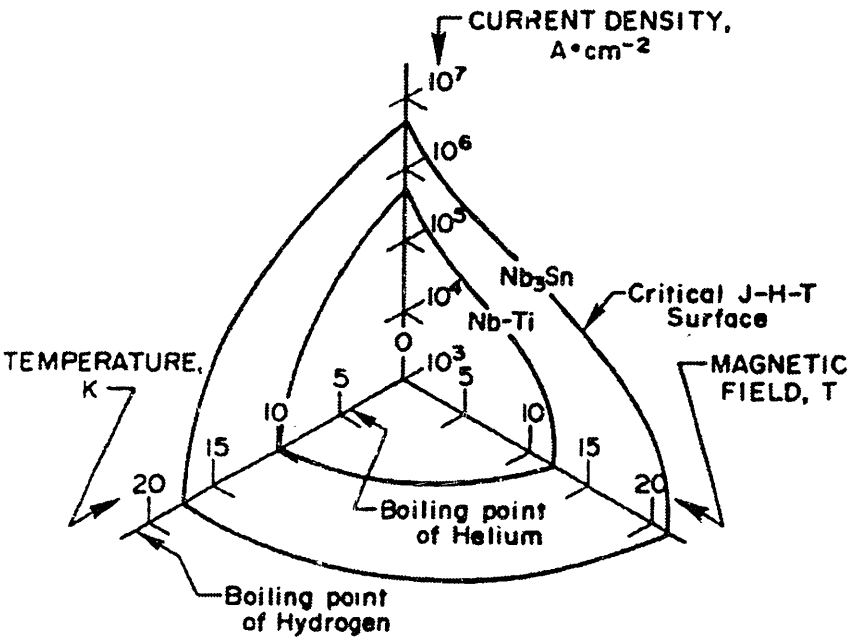

Figure 3. Schematic relation of critical parameters for type II superconductors. [8]

Table 1. Comparison of the properties of type II superconductors [10]

Superconductor	Tc, K	H_{c2}, Tesla at 4.2K	J_c, GA/m^2 at 4.2K (10T)	crystal structure
NbTi	9.8	12	0.2	metallic-BCC
Nb3Sn	18	26.9	4.3	brittle-A15

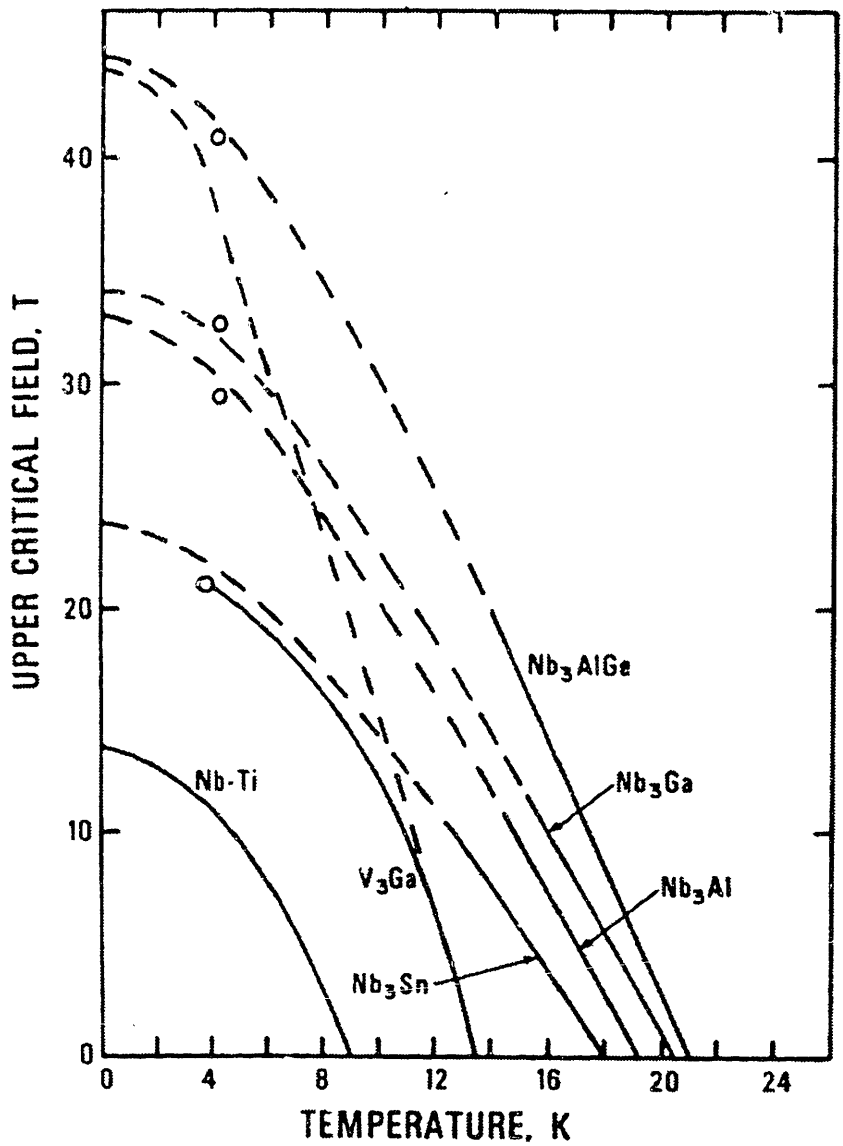

Figure 4. Temperature dependence of upper critical field (Hc_2) of superconductors. [8]

The manufacturing of a multifilamentary superconductor involves several complex processing steps.[12] For a ductile superconductor such as NbTi, the process starts with hot extrusion of NbTi rods from a large ingot with intermediate anneals at 800 °C. Each rod is inserted into a copper tube having a hexagonal outer shape. A number of these are then nested in a large copper can, the can is evacuated, and a lid welded on the end. The entire assembly is then reduced, initially by hot extrusion, followed by conventional wire drawing with intermediate annealing. During the final drawing, the wire receives an additional reduction in cross-sectional area, which introduces sufficient cold-work for

adequate flux pinning. After drawing, the wire is given an additional low temperature (~400 °C) anneal to form a strong-pinning dislocation cell structure and to enhance the critical current.[8]

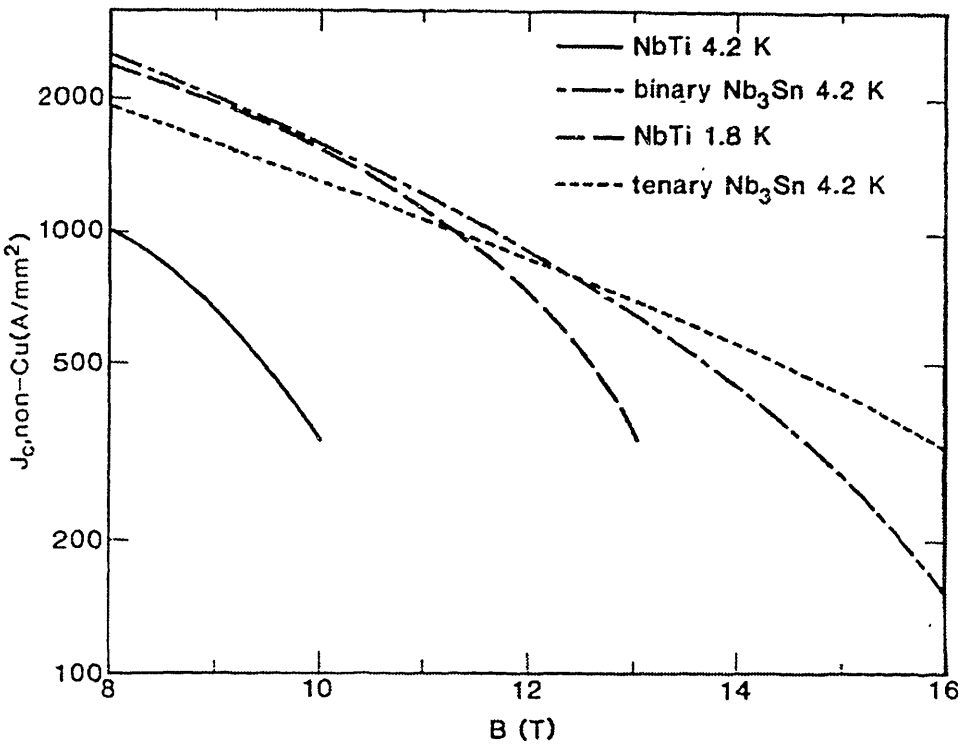

Figure 5. Critical current densities attainable in the non-copper fraction of composite superconductors vs. magnetic field in the conductors. [9]

When it is desirable to fabricate even higher field magnets, such as that for ITER which requires a magnetic field of about 13 Tesla,[9] superconducting materials of higher Hc_2, for example A15 compounds such as Nb_3Sn (Tc = 18K) and Nb_3Al (Tc = 19K) have to be considered. However these compounds are brittle and cannot be drawn directly into filaments by the process described above. One solution is the so-called "bronze" process.[12] In this process, the multifilamentary conductor is prepared by the same as process as that described for NbTi, except that the filaments are pure niobium and the matrix is a Cu-Sn alloy or bronze. The billet is processed into wire, exactly as for NbTi multifilamentary conductor. Another process, the "internal-tin" process starts with the incorporation of pure Nb, in rod or mesh form, into a copper billet that is the partially

drawn. Rods of pure Sn are then inserted into the billet at locations adjacent to the Nb and finally the billet is drawn into wire form. After drawing, certain heat treatments steps have to be taken to form the superconductor. The final annealing treatment, at a temperature ranging from 650 °C to 800 °C, causes tin to diffuse into the niobium forming Nb_3Sn filaments in a dilute alloy matrix. For these two processes, the superconductor assembly has to be formed into final shape before being subjected to the heat treatment. This process is also sometimes termed as "wind-then-react".

Strain can have a severe effect on the properties of a high field superconductor including critical current density, J_c, critical temperature, T_c and critical magnetic field, H_{c2}. The strain dependence of the critical current density for Nb_3Sn superconductor is shown in Figure 6. The reduction in J_c with strain, termed as strain degradation, can be significant.[13,14,15] Similarly, strain can also effect T_c and H_{c2}.[13]

The sources of strain can be many and include: (1) fabrication where the superconductor is subjected to winding tension and bending, (2) the difference in thermal expansion coefficient between the conductor itself and the magnet structure, (3) within the magnet itself during cool-down from Nb_3Sn heat treatment temperature to operating temperature and, (4) the elastic strain caused by Lorentz force when the magnet is energized. Fabrication strain and operating strain can be eliminated or reduced by proper selection of fabrication process and design. Thermally induced strain can be controlled by selecting proper structural material to match the coefficient of thermal expansion with superconductor. In the wind-then-react fabrication process, by which Nb_3Sn superconductor is fabricated, fabrication strain is not present because superconductor forms by heat treatment after fabrication.[13]

The hoop stress caused by Lorentz force is proportional to the size of the magnet and can be as high as the ultimate tensile strength of the superconductor. The magnetic stress will have a significant degrading effect on the superconductor unless there is adequate structural support provided by the conduit. Accordingly, the conduit has to be designed to minimize the effect of the magnetic stress on the superconductor.[11, 16,17]

Provided that the fabrication process is adequate, and the mechanical properties of the conduit are adequate to provide structural support needed to contain the magnetic forces developed when the magnet is energized, the most significant effects on superconductor performance result from thermally induced strain. The mismatch in thermal expansion coefficient of the components imposes significant strain on the superconductor during cool-

down from Nb_3Sn formation temperature to operating temperature. There are two significant sources of strain. First, the thermal expansion coefficient mismatch between bronze matrix and Nb_3Sn induces a compressive prestrain of up to 0.5%.[13] Second, a conduit alloy with a coefficient of thermal expansion (COTE) much greater than that of Nb_3Sn increases the initial compressive prestrain on Nb_3Sn.[14, 15] Ideally, the contribution by conduit materials can be eliminated by using a material that exhibits a mean COTE less than or close to that of Nb_3Sn. In actual magnet design, a small amount of compressive prestrain is preferred to provide a buffer against any additional tensile strain induced by magnetic field.[14]

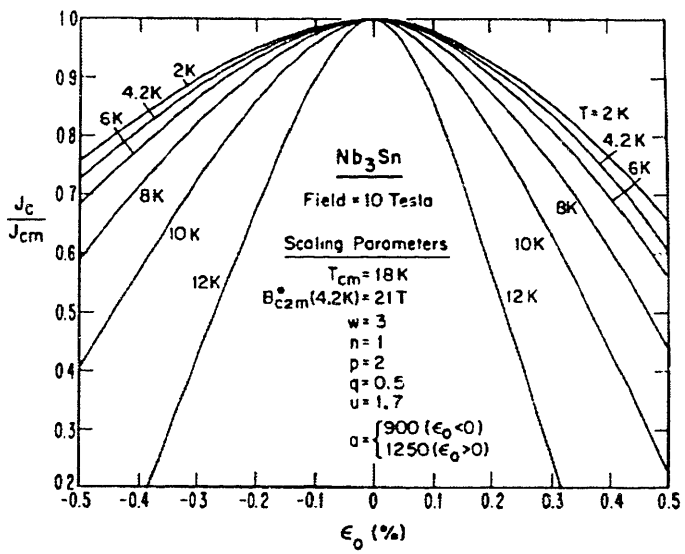

Figure 6. Strain dependence of critical current density of Nb3Sn superconductor.[13]

Steeves et al. investigated the effect of thermally induced strain on J_C using various materials with a wide range of COTEs over the temperature range of 1000K to 4.2K.[15] The results are shown in Figure 7. They found that the use of stainless steel caused significant degradation in the J_C of the conductor. On the other hand, a low COTE Ni-Fe base superalloy (alloy 903) did not contribute to the degradation of J_C. The result of this study was to stimulate interest in low COTE superalloys as a candidate for CICC conduit materials.

II.1.2 Development of Alloy 908

The most important advantage of using a low thermal expansion alloy as a conduit material is that there is little degradation of the performance of Nb_3Sn superconductor by the conduit itself. To be used as a conduit material, besides having a low coefficient of thermal expansion, adequate mechanical properties are required. The conduit must withstand the stresses at 4K from the magnetic field, differential thermal contraction, and internal helium pressure.[16,17] Consequently, the stresses on conduit are high both during steady state operation as well as during accident conditions. During operation, cyclic stresses are imposed as a result of the pulsating magnetic field, internal pressure, and cool-down. Accident conditions are represented by a "quench" where a magnetic or mechanical disturbance can locally heat a small portion of the superconductor so that it becomes resistive. The heat generated in that region can in turn raise the temperature of superconductor and revert the whole superconductor to the normal satate through a thermal runaway process. Because of the high current densities carried by the superconductor, the reversion to the normal state can generate a large amount of heat, enough to vaporize the coolant. The conduit must be able to withstand the pressure rise due to vaporization of coolant.

To meet the static and cyclic operational conditions of high field magnets which use Nb_3Sn superconductors, rigorous mechanical properties goals have been proposed. The selection of the materials for the magnet become further complicated by the fact that the reaction heat treatment, used to form the Nb_3Sn superconductor, must be applied after the magnets are assembled. Thus the heat treatment for the superconductors and the conduit material must be the same. This puts severe restrictions on heat treatments for the conduit and has required the development of a special alloy, alloy 908, for use in this application. Some of the proposed mechanical properties reqirements of structural materials for fusion applications are shown in Figure 8. The 4K yield strength-fracture toughness specification after heat treatment varies from 1000 MPa - 200 MPa$\sqrt{m}$ [17] to 1200 MPa - 200 MPa$\sqrt{m}$.[16] The requirement for the weld was set at 1000 MPa - 150 MPa$\sqrt{m}$ at 4K.[17] Both the base and weld metal must have enough ductility to survive the drawing and winding process following welding of the conduit sections. The fatigue properties of the conduit material must be comparable to that of stainless steel. The mechanical properties laid out by the Superconducting Magnet Development Group at the MIT Plasma Fusion Center for both the base and weld metal at 4K, were: Young's modulus greater than 138

MPa, yield strength greater than 1000 MPa, total tensile elongation greater than 15 %, and a fracture toughness greater than 100 MPa$\sqrt{m}$.[1]

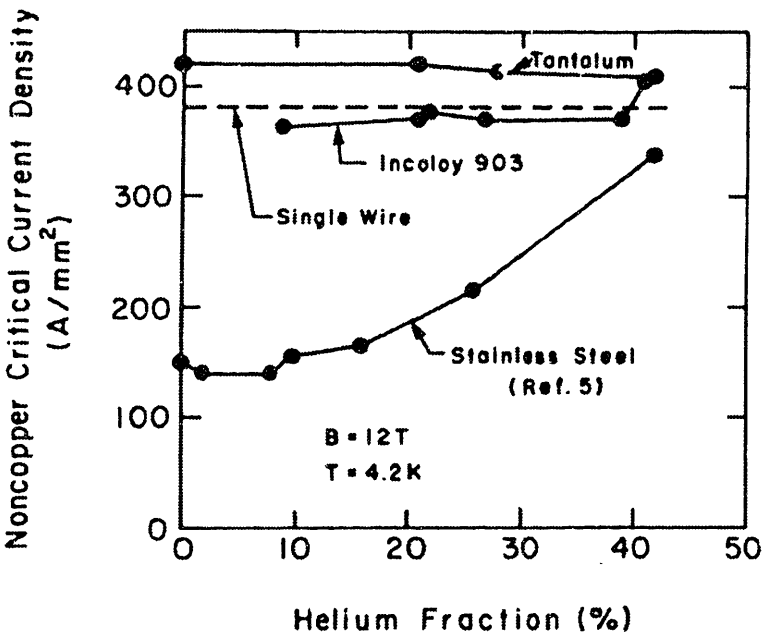

Figure 7. Comparison of the performance of Nb3Sn superconductor assembly with various sheath materials.[15]

There are number of heat treatment schedules used to form Nb_3Sn.[18] In general, however, those conditions represent an overaging condition for many Fe-Ni based superalloys. Overaging usually results in coarsening of strengthening precipitates. This leads to a reduction in strength as well as ductility and toughness. Overaging can also result in the transformation of metastable strengthening phases to less effective stable phases which also degrade ductility and toughness.[19] Thus, proper microstructural stability is needed to retain strength and ductility. The alloy should also be resistant to environmentally assisted cracking or embrittlement and be able to withstand heat treatment in a variety of furnace atmospheres.

Considering above requirements alloy 908 was developed at MIT in coorperation with Inco. Alloys International.[1,20] The chemical composition of the alloy is shown in Table 2 along with that of other related alloys. Alloy 908 is strengthened by γ' precipitation. The Al, Ti and Nb content of the alloy are controlled to insure sluggish γ' formation and

increased γ' stability. The sluggish γ' formation contributes to the improved weldability of the alloy as well as allowing for compatibility with the normally longer (for a superalloy) thermal cycle necessary for Nb_3Sn formation. The amount of chromium was optimized to retain a low thermal expansion coefficient while providing some protection against embrittlement by oxygen. The thermal expansion properties are shown in Figure 9 with that of other alloys. By substituting alloy 908 for stainless steel, the prestrain imposed on the cable is reduced to an optimum value.[14]

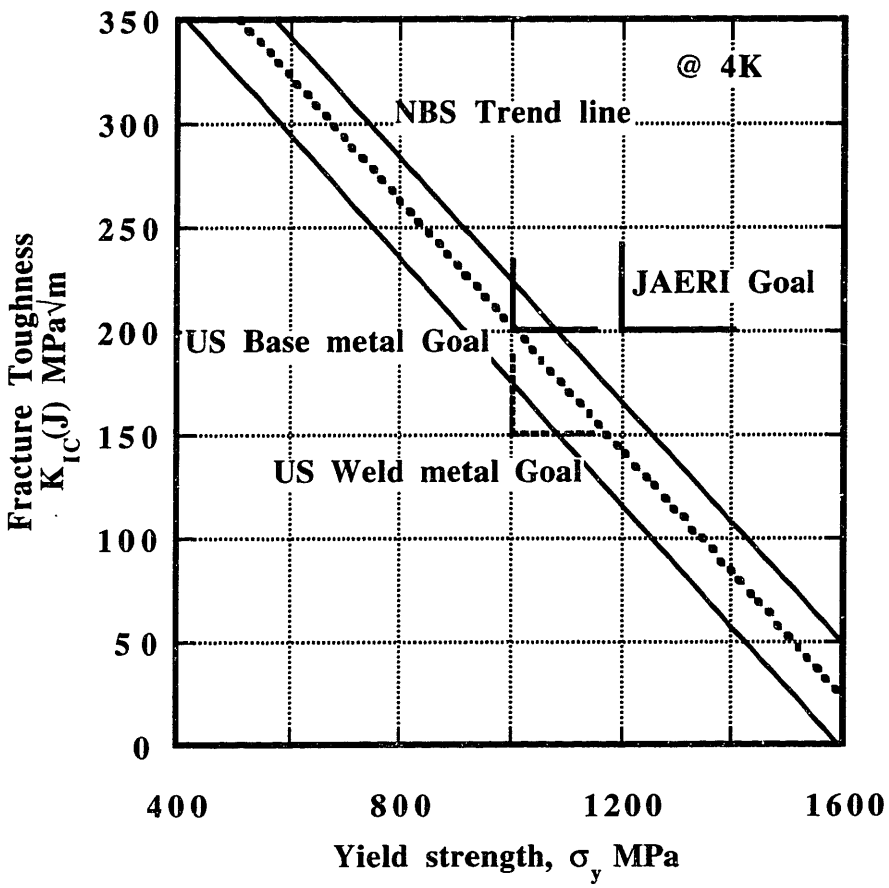

Figure 8. Strength-Toughness requirements for structural materials for high field superconductor for fusion application. [17]

The mechanical properties of alloy 908 are shown in Table 3. Both base and weld metal show sufficient strength at both room temperature and 4K.[2] The fatigue crack growth rate of both base and weld metal is comparable to that of stainless steel. However, initial tests conducted at MIT showed a marked decrease in ductility and fracture toughness of welds while maintaining considerable strength.[2, 21] Considering that these data were collected on the as welded + aged condition, the possibility of further reduction in both ductility and fracture toughness after cold work, which would be imposed during magnet fabrication, raised some concern over the integrity of the conduit during operation.

Table 2. Chemical composition of alloy 908 and other superalloys

	Ni	Fe	Co	Cr	Nb	Ti	Al	Mo	Si	C
alloy 908	48.7	40.8		4.1	3.0	1.5	1.1		0.2	0.01
alloy 903	38.0	41.0	15.0		3.0	1.4	0.7		0.1	0.05
Inconel 718	52.5	18.5		19.0	5.1	0.9	0.5	3.0	0.2	0.04
A286	26.0	54.0		15.0		2.0	0.2	1.3	0.5	0.05

Table 3.Mechanical properties of alloy 908 at various temperature.
(After heat treatment, 200 hrs @ 650 °C)[2]

	298K			4K		
MATERIAL	σ_y (MPa)	K_{IC} (MPa$\sqrt{m}$)	CVN (J)	σ_y (MPa)	K_{IC} (MPa$\sqrt{m}$)	CVN (J)
Base	1075±41	196±5	73±1	1227±14	235±5	71±1
Filler GTAW	1061±14	106±8		1278±45	105±1	

Note: σ_y : Yield strength, MPa
K_{IC} : Fracture toughness, MPa$\sqrt{m}$
CVN : Charpy impact energy, J

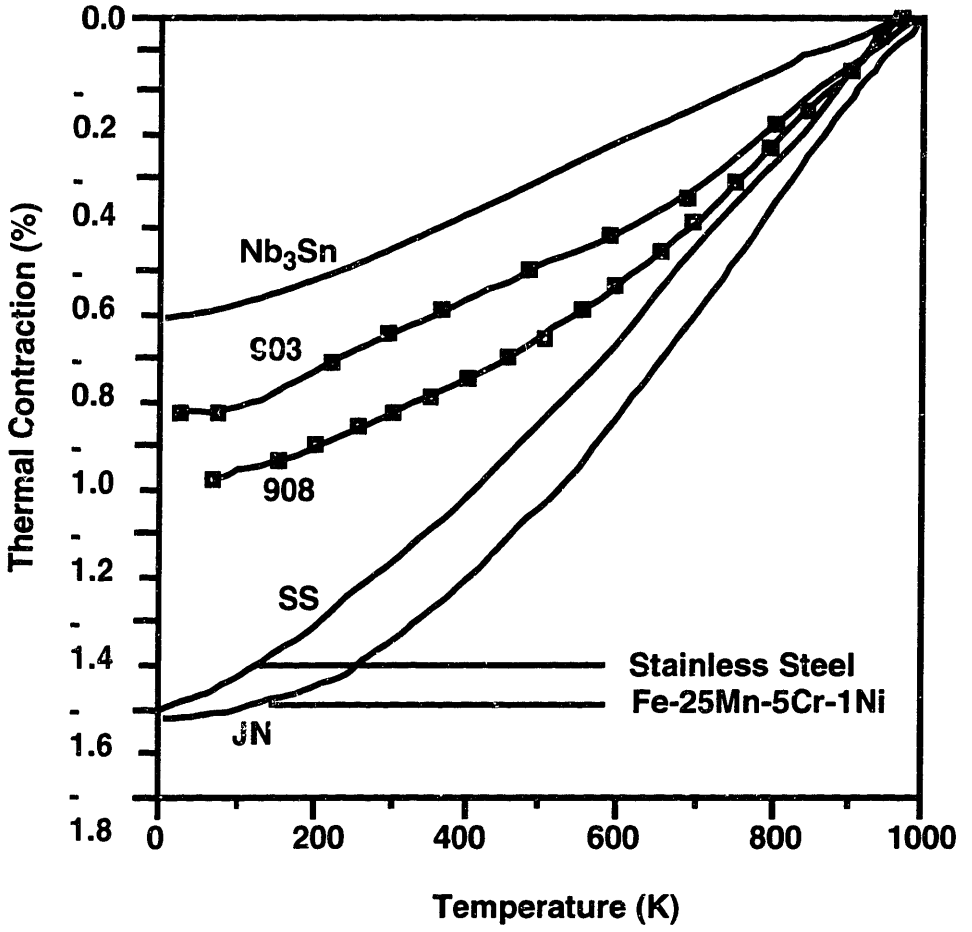

Figure 9. Thermal contraction of Nb_3Sn and various structural materials from 1000K to 4K.[1]

II.2 Physical metallurgy of welding

II.2.1 Weld solidification and microstructure

Solidification and the resulting microstructure of a weld can be thought of as a small scale casting under specialized conditions; a moving heat source, turbulent liquid pool, high temperature gradient, high dendrite growth rate, and mixing with the base metal. An explanation of typical weld microstructures has been summarized by David and Vitek,[22] Brody, [23] and Easterling.[24] In fusion welding, weld solidification is essentially a dynamic process in which the solidification behavior depends on the welding speed and heat input. Because of large temperature gradients within the melt, together with the

characteristic properties of the arc, the melt can be extremely turbulent. Turbulence can have a positive effect, providing extremely good mixing in the melt.

During all practical fusion welding, a certain degree of dilution, or melting back, of the base metal occurs. The net effect of dilution is a change in weld composition. In multi-pass welding, the degree of dilution is a function of location. Clearly, the root pass will undergo far more dilution than subsequent passes. Dilution significantly affects the weld microstructure, influencing such parameters as the dendrite arm spacing and degree of segregation.

At the onset of solidification of the weld pool, each base metal grain on the fusion line serves as a growth site for a fusion zone grain. Therefore, the crystallographic orientation of each fusion zone grain will be the same as that of the base metal grain on which it grows epitaxially. Also, the resulting columnar grain sizes are effectively determined by the base metal grain size at the fusion boundary. As the grains grow, there is competition between neighbors. The grains with favorable crystallographic orientation (with the direction of strongest heat flow direction) will survive and continue to grow. In cubic alloys, the preferred growth direction are the cube axis directions <100>.[25]

If the velocity of the heat source has a vector **u** and the speed of crystal growth has a vector **V**, then the geometric condition is met such that

$$\mathbf{V} = \mathbf{u}\cos\theta \qquad \text{Eq. 1}$$

where θ is the angle between **u** and **V**. Since **u** is constant, **V** will vary considerably depending on position. This is illustrated in Figure 10. Equation 1 implies that initially crystal growth is relatively slow but increases toward the centerline. If the weld speed is low, crystal growth is able to keep up with the moving heat source by gradually changing direction. If weld speed is increased, the shape of solidification structure is modified toward that shown in Figure 10-b. In this case, growing crystals have to make sudden changes in direction at the weld centerline which can have detrimental effects on the resulting mechanical properties.

During equilibrium solidification, the growth mode is planar, in which solid forms with the composition of bulk material during solidification except during the initial stage of solidification, as shown in Figure 11. A simple binary phase diagram is shown in Figure 12. During equilibrium solidification, liquid with solute composition of C_O is solidifies over the temperature range of T_L to T_S to form a homogeneous solid with solute

composition of C_O. Therefore, the solute composition in resulting material is uniform throughout the solid. However, during typical fusion welding, equilibrium solidification is generally not observed.

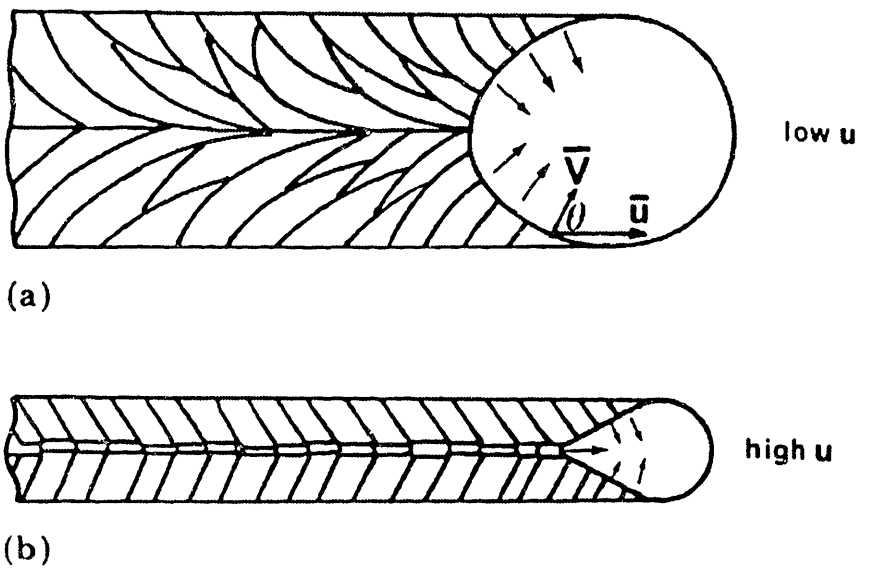

Figure 10. Diagram showing variation of thermal gradient and growth rate along solidification front for differently shaped weld pool. a) elliptical, b) tear drop shaped. [24]

The actual temperature gradient of the melt will have a profound impact on the resulting weld microstructure. Within the columnar grains, solute build-up at the liquid/solid interface promotes interface instability due to constitutional undercooling, as shown in Figure 13, and promotes a cellular-dendritic structure. As the solute content at the liquid/solid interface increases, the equilbrium liquidus temperature corresponding to the solute content at the interface becomes lower than that of bulk material. Thus, the thermodynamic temperature profile , designated as "Liquidus" in Figure 13, is developed. This phenomenon is termed "constitutional undercooling". Cellular-dendritic growth occurs when the gradient of this thermodynamic temperature profile is greater than the actual temperature gradient in the liquid. Mathmatically, this condition is expressed as follows;

$$\frac{dT_L}{dx} < -\frac{m_L C_O (1-k)}{D_L / V} = \frac{\Delta T_O}{D_L / V} \qquad \text{Eq. 2}$$

where V is the solidification front velocity and equal to the welding speed at the trailing edge of weld pool, and dT_L/dx is the temperature gradient in the melt (= G_L). ΔT_O is the equilibrium solidification temperature interval and equal to the diffrence between liquidus and solidus temperature (= $T_L - T_S$). m_L is the slope of liquidus line (line 2 in Figure 12). D_L is diffusion coefficient of solute elements in the liquid. The equilibrium partition ratio, k is defined as follows;

$$k = \frac{C_S^*}{C_L^*}$$

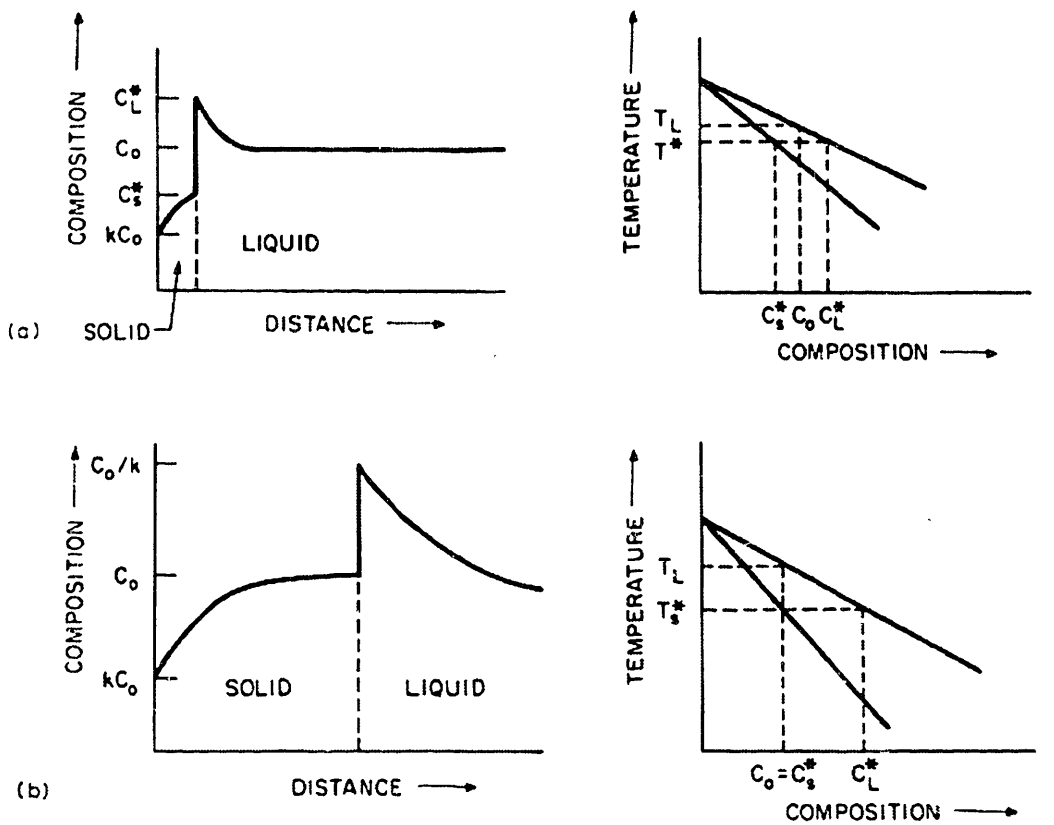

Figure 11. Solute redistribution during plane front growth. a) initial stage of solidification, b) steady state solidification stage.[24]

where C_S^* and C_L^* are the solute composition of solid and liquid, respectively, at the interface. For typical fusion welding conditions, shown in Table 4, equation 2 can be easily met. Thus, it is likely that almost entire weld zone solidifies as a cellular-dendritic

structure except the very first solid. Therefore in the practical sense, the entire weld zone structure can be treated as cellular-dendritic microstructure. From this simple treatment, it is also shown that higher welding speed and shallow temperature gradient promote the formation of a cellular-dendritic microstructure.

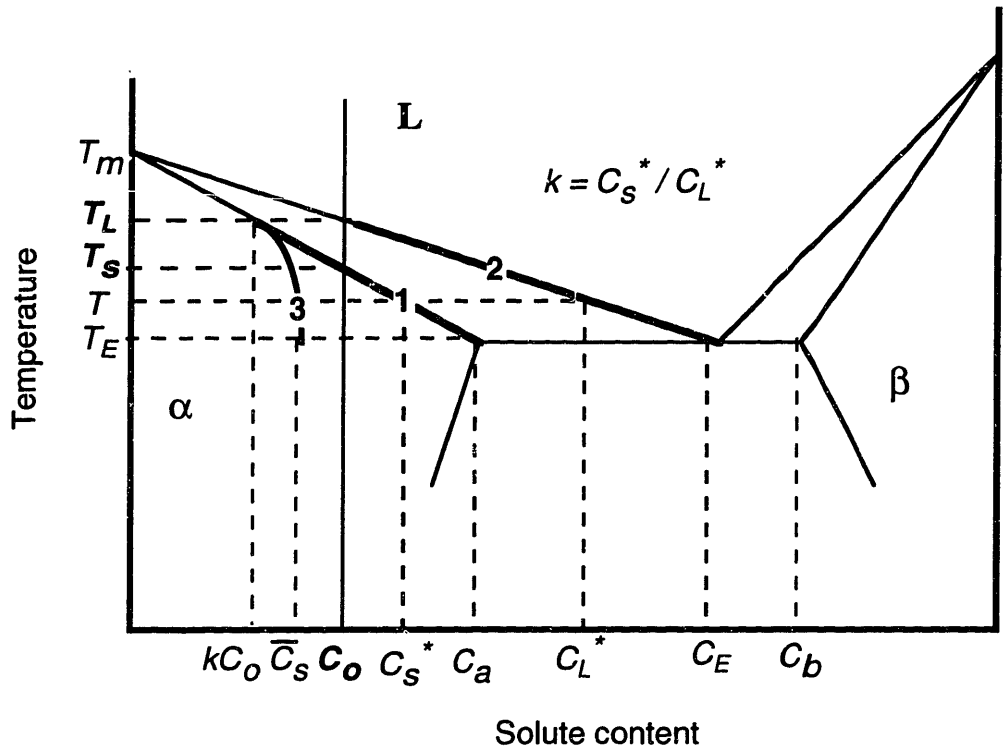

Figure 12. Average solute composition in solid during solidification, shown with binary phase diagram.

During cellular-dendritic solidification, numerous primary dendrite arms form within a single dendrite. The primary arms within a columnar grain are parallel to the preferred crystallographic growth direction most closely aligned with the predominant heat flow direction. Numerous secondary arms branch from each primary arm. The secondary arm spacing, d_2 depends on local solidification time t_S (which is related to the inverse of the cooling rate).[26] For various alloy systems, the following general correlation has been reported;[23]

$$d_2 = C \cdot t_s^n \qquad 0.3 < n < 0.5 \qquad \text{Eq. 3}$$

where C is a constant and n is an exponent for fitting. The secondary arms effectively divide the liquid into isolated pools. Within the trapped liquid, the solute concentration increases as the growing solid rejects certain alloying elements into the liquid.

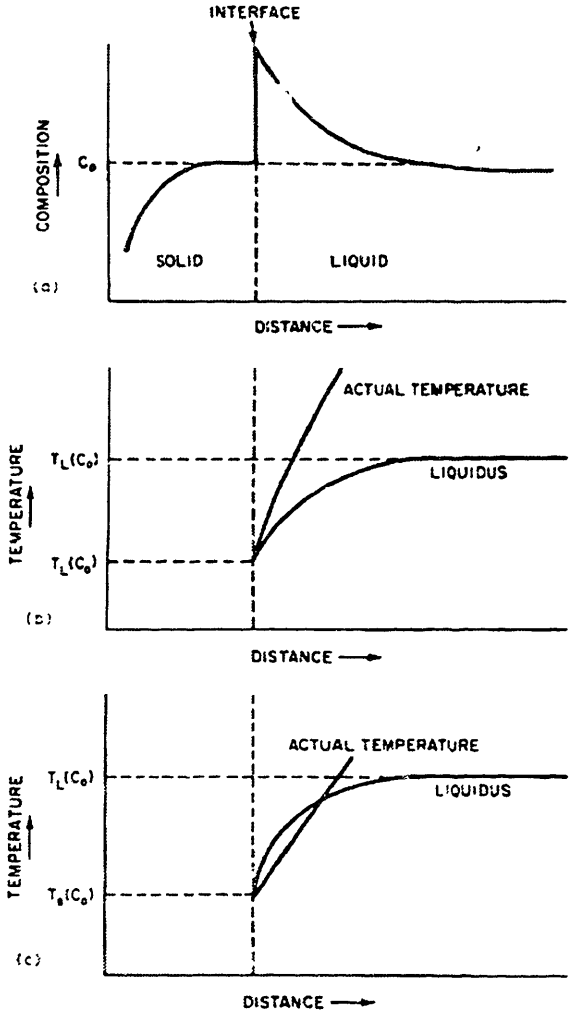

Figure 13. Development of constitutional supercooling during plane front alloy solidification. a) solute build up ahead of solidification front, b) condition for plane front stability, and c) condition for constitutional supercooling. [22]

Table 4. Test of equation 2 to check the occurrence of cellular-dendritic growth condition in typical fusion welding processes.

Welding method		G_L	$\Delta T_o V/D_L$
Arc Welding	V ~ 0.2 cm/sec ΔT_o ~ 50 °C D_L ~ 3 x 10^{-5} cm^2/sec	~ 500 °C/cm	3.3 x 10^5 °C/cm
EBW & LBW	V ~ 2 cm/sec ΔT_o ~ 50 °C D_L ~ 3 x 10^{-5} cm^2/sec	~ 1500 °C/cm	3.3 x 10^6 °C/cm

II.2.2. Microsegregation in weld

Microsegregation in alloys during and as a result of solidification has long been recognized as a consequence of the partitioning of solute between solid and liquid. During equilibrium solidification conditions where diffusion in the solid and liquid is complete, the composition of both liquid and solid adjusts during cooling in accordance with the phase diagram so that the final composition of solid is equal to the composition of original melt. Therefore, for ideal conditions, no microsegregation will develop within the solidified structure. On the other hand, at very high solidification rates, solidification can be completed without microsegregation due to the trapping of solute by the rapidly moving interface, causing the partition ratio to be unity.[26] However, under practical conditions, where achieving a high enough solidification rate is not likely and diffusion within the solid is restricted, the resulting solidified structure is inhomogeneous in composition. In alloys which are single phase at equilibrium, microsegregation can promote the precipitation of secondary phases from the solute enriched liquid. A coarse, non-coherent secondary phase, and an inhomogeneous microstructure arising from microsegregation will result in poor weldability and/or poor mechanical properties, especially low fracture toughness and ductility.

The solidification process is schematically represented by the binary phase diagram shown in Figure 12. During solidification of the weld pool, local thermodynamic equilibrium is maintained at the liquid/solid interface. The solute composition of the newly formed solid at a particular time will be governed by the equilibrium partition ratio k. Because initially the liquid is at the bulk composition, C_o, the first drop of solid will be formed with a solute composition of kC_o. If convection within the liquid is rapid and diffusion in the solid is

slow enough to be neglected during the solidification time interval, liquid will be enriched with solute ejected at the interface. The solute concentration in the liquid will rise as solidification proceeds and follow line 2 in Figure 12. Also, at any given time, newly forming solid with solute composition of $C_S^* = kC_L^*$ following line 1 is added to the dendrite. Because the diffusion of solute in the solid is negligible, the compositional difference remains unattenuated. The average composition of bulk solid will follow line 3. In the liquid, the overall concentration of solute will increase until it reaches the eutectic composition. From the final liquid with eutectic composition, the primary phase with C_a and secondary-phase with C_b form simultaneously by eutectic decomposition as follows:

$$L \Rightarrow \alpha + \beta$$

When solidification is completed, the solute concentration within the primary phase is $\overline{C}_S$ which is less than the overall composition of alloy, C_o. The secondary phases, formed by eutectic reaction, are aften stable to very high temperatures and remain undissolved after most heat treatment conditions, and thus have detrimental effects on mechanical properties, particularly ductility.

A simple quantitative description of microsegregation is illustrated by the Scheil model.[27] The schematic of solute segregation by the Scheil model is shown in Figure 14. The composition of the solid at the liquid-solid interface C_S^* can be expressed as a function of solid fraction f_S

$$C_S^* = kC_O(1 - f_S)^{(k-1)} \qquad \text{Eq. 4}$$

or in terms of liquid composition C_L and liquid fraction f_L

$$C_L = C_O f_L^{(k-1)} \qquad \text{Eq. 5}$$

Elements with k less than unity will be rejected from the growing solid into the liquid phase. For values of k greater than unity, the liquid is depleted in solute. Thus, the amount of liquid which participates in the eutectic reaction is

$$f_E = \left(\frac{C_E}{C_O}\right)^{1/(k-1)} \qquad \text{Eq. 6}$$

The above equation can be used to quantify the degree of segregation in terms of the final eutectic liquid fraction, f_E. The degree of segregation is large when k is small and C_o is

large. The above equations are derived under the assumptions of no solid diffusion and uniform liquid composition. The Scheil model predicts that some eutectic will form no matter what the initial composition is. The model also predicts no effects of solidification rate on microsegregation, as measured by maximum composition, minimum composition, or amount of interdendritic eutectic.

If diffusion in the solid plays a role during dendritic solidification, the more complicated Brody-Flemings' model [28] can be used to take into account of the decrease in microsegregation. Equation 4 can be modified to consider the effect of diffusion.

$$C_S^* = k\, C_O \left(1 - \frac{f_S}{1+\alpha k}\right)^{k-1} \qquad \text{Eq. 7}$$

where

$$\alpha = \frac{4 D_S t_S}{{d_2}^2}$$

D_S is solute diffusion coefficient in solid, t_S is local solidification time and d_2 is the secondary dendrite spacing. The dimensionless parameter αk determines the extent of diffusion in the solid phase. For $\alpha k \ll 1$, microsegregation approaches the maximum predicted by the Scheil model. For $\alpha k \gg 1$, the composition of the primary solid phase approaches uniformity.

The size and shape of the fusion zone is closely related to the welding heat input rate and welding power density. The corresponding temperature field determines the overall solidification and transformation behavior in the weld.[29] The temperature profile around the weld can be determined analytically. If the heat input of a given welding process is q and the heat source moves with a speed of u, the heat flux per unit length of weld is given as q/u. At a given point in the heat affected zone (HAZ) the temperature T(r,t) can be approximated as follows;[24]

$$T(r,t) = T_0 + \frac{q/u}{2\pi\lambda t}\exp\left(-\frac{r^2}{4at}\right) \qquad \text{Eq. 8}$$

where

$$a = \frac{\lambda}{\rho C_p}$$

T_0 is the preheat temperature, λ is thermal conductivity of the base metal, a is the thermal diffusivity and r defines the distance of the reference point to the weld center line. ρ is

density and C_p is specific heat. Though Equation 8 can not be used to find the temperature distribution within the weld, it gives a fairly useful indication of the size and shape of the melt region. The resulting temperature profiles are illustrated in Figure 15. The figure shows that, as the heat source moves across the workpiece, large temperature gradients occur in the vicinity of the melt and then drop off rapidly as the heat source moves away. It can be concluded that a higher weld velocity and/or a higher thermal conductivity will tend to produce a narrower and more elongated melt region. Also, the cooling rate along the centerline of weld (where r = 0) can be calculated as follows;

$$\frac{dT}{dt} = \frac{2\pi\lambda}{q/u}(T - T_o)^2 \qquad \text{Eq. 9}$$

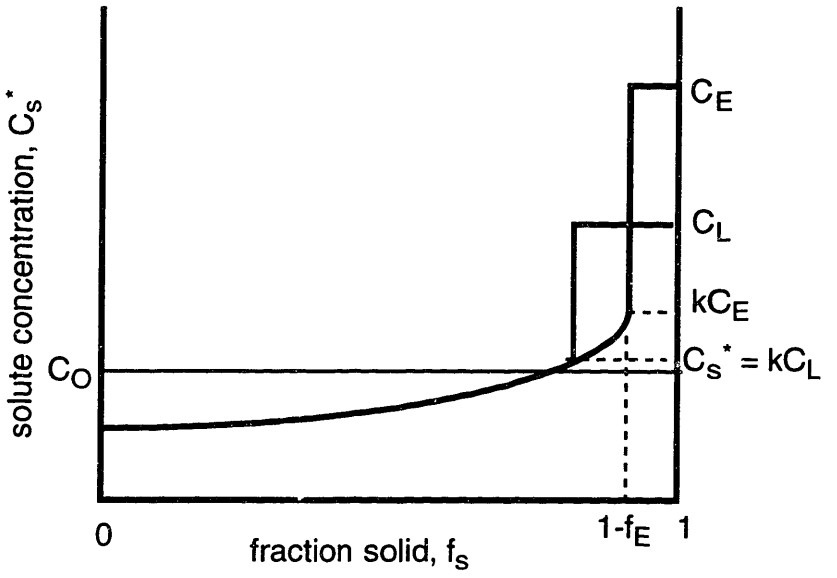

Figure 14. Schematics of solute segregation by Scheil equation.

Using this equation, a rough estimation of weld cooling rate can be evaluated for various welding methods. As a special case, the cooling rate at the liquid/solid boundary along the trailing edge of the weld pool can be approximated as follow;[30]

$$\frac{dT}{dt} = \frac{2\pi\lambda}{q/u}T_m^2 \qquad \text{Eq. 10}$$

where T_m is melting temperature of the material. The temperature gradient at the liquid/solid interface can be estimated.

$$\frac{dT}{dx} = \frac{dT}{dt}\frac{dt}{dx} = \frac{dT}{dt} \bullet \frac{1}{u} = \frac{2\pi\lambda}{q} T_m^{\,2} \qquad \text{Eq.11}$$

The above equation implies that for a given material, the temperature profile within the heat affected zone is determined by the heat input rate per unit length. From this temperature profile, the size of heat affected zone and the size of fusion zone can be determined approximately.

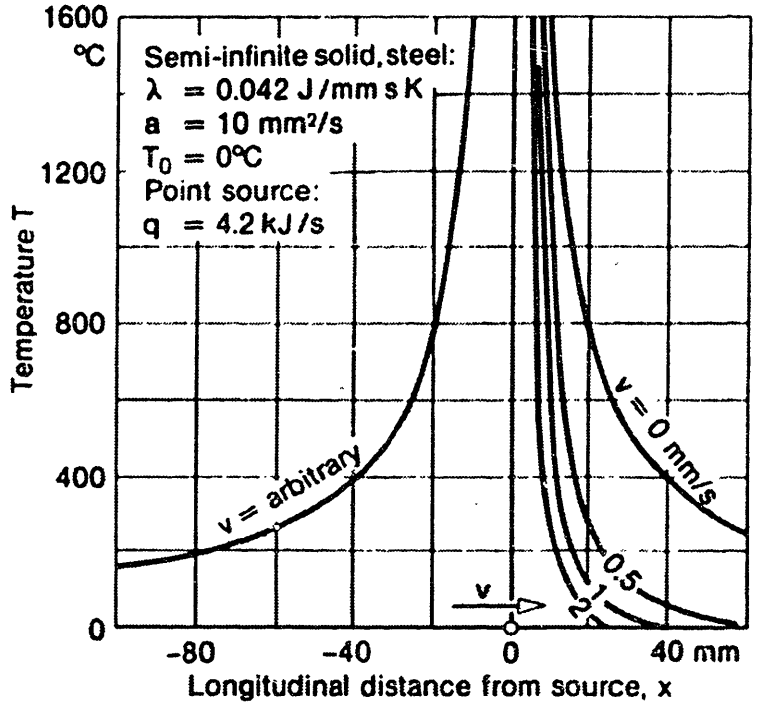

Figure 15. Temperature profiles along the weld center line for moving point source on semi-infinite solid.[29]

Conventional fusion welding processes, such as gas tungsten arc welding (GTAW), gas metal arc welding (GMAW), and submerged arc welding (SMAW) are chracterized by low energy density and low speed which results in a rather large weld fusion zone. With a

larger heat input rate per unit length, the cooling rate is slower than other methods with a shallow temperature gradient in HAZ. Advanced welding techniques such as electron beam welding (EBW) and laser beam welding (LBW) use high energy densities, about three orders of magnitude higher than arc welding[30] and high welding speed. This results in a narrow weld fusion zone. Because the amount of material being fused during welding is small, and the welding speed is high, the heat input rate per unit length is smaller in EBW and LBW processes. With a lower heat input rate per unit length, the cooling rate is much greater than that of other fusion welding methods. The cooling rate in welds using modern high energy beam process such as EBW and LBW is about 10^2 to 10^3 times as high as that of conventional processes such as arc welding.[22] The resulting dendritic spacing is smaller and microsegregation is reduced with much smaller HAZ as well.

II.3 Welding Metallurgy of Superalloys

II.3.1 Segregation of Alloying Elements.

In nickel-base or nickel-iron-base superalloys, which are highly alloyed to promote precipitation of hardening phases [γ' ($Ni_3(Al,Ti)$), γ'' (Ni_3Nb)], extensive precipitation of carbides and intermetallic compounds during solidification have been reported.[31,32] Most of the γ' or γ'' forming elements have a very low equilibrium partition ratio, k, in the austenitic matrix and are likely to be ejected from growing dendrites and enriched within the interdendritic liquid. The results can be the formation of various intermetallic compounds with parent elements or other alloying elements either by solid state diffusion or by segregation during solidification. Donachie and Kriege [33] have performed an extensive study to tabulate intermetallic compounds in superalloys, formed by high temperature solid state diffusion.

During solidification, local thermodynamic equilibrium at the solid/liquid interface determines the redistribution of solute, and eventually precipitation of intermetallic compounds in the solidified structure. For simplicity, often times, the equilibrium partition coefficient, k is treated as a constant over the freezing temperature range. In reality, the value of k varies somewhat significantly with temperature.[34] Also, k for a specific element differs in different alloy system and composition.[34,35,36] The equilibrium partition ratios of some elements from various researchers are summarized in Table 5.

The most severe segregation behavior is expected for niobium. Its partition ratio varies from 0.16 to 0.58 depending on the alloy system and temperature. In controlled low expansion superalloys, its partition ratio is from 0.42 to 0.58. The partition ratio of Ti is slightly greater than that of Nb. Lecomte-Beckers studied the solidification behavior of IN100 which contains large amounts of Al and Ti and utilizes a high percentage of the strengthening phase γ' [$Ni_3(Ai,Ti)$].[35] The partition ratio of Ti varied from 0.32 to 0.65 depending on the composition of the alloys. On the other hand, Al and Cr showed a partition ratio of near unity which meant that the composition of these elements in the dendrites is almost the same as that in the liquid. Knorovsky et al. reported segregation of Nb, Mo and Si in the fusion zone of Inconel 718.[36]

Table 5. Equilibrium partition ratio of selected alloying elements

	Nb	Ti	Al	Mo	Cr	ref.
Inconel 718	0.25	0.39 - 0.51		0.80		34
	0.5					36
X-750	0.16 - 0.34	0.40 - 0.44				34
Alloy 625	0.25 - 0.34	0.44 - 0.50		0.86 - 0.90		34
IN100		0.32 - 0.65	0.75 - 1.23	0.73 - 0.90	0.75 - 1.11	35
		0.57 - 0.73	0.92 - 1.33	0.65 - 0.83	0.79 - 0.99	37
Alloy 903	0.58	0.76	0.95			38
	0.47	0.43				39
Alloy 909	0.42 - 0.51	0.40 - 0.72				39

II.3.2 Precipitation of secondary phases

During solidification, secondary phases form in the solute enriched liquid by eutectic reaction. Vincent performed an extensive investigation of the weld microconstituents in Inconel 718 and found that Laves phases and MC carbonitride comprises most of the secondary phases present in the fusion and heat affected zones.[31] It is also reported that while only large (2 - 10 μm) and irregular carbides are present in the base metal, small (~

0.5 μm) carbides are also present in the fusion and heat affected zone associated with Laves phases. The composition of the carbide in the base metal can be either Nb-rich (85 a/o Nb - 15a/o Ti, major phase) or Ti-rich (85 a/o Ti - 15a/o Nb, minor phase). However, the composition of carbides in the fusion zone and HAZ are always Nb-rich (80 a/o Nb and 10 a/o Ti) but may also contain other elements (Mo, Cr, Fe, and Ni). The major intermetallic phase found in the fusion zone and at HAZ boundary is the hexagonal Laves phase. Within the HAZ, the Laves phase morphology ranges from one of isolated particles to continous sheet to a massive dendritic wall.[31] The most unusual feature of Laves phase is that many of the larger Laves sheets are decorated with small (20 - 50 nm) MC carbide particles. This is thought to be due to the rejection of carbon by Laves phase.[31]

Knorovsky et al. constructed a solidification diagram for Inconel 718 studying the weldability of Ni-base superalloys.[36] Using Scanning Electron Microscopy (SEM), Energy Dispersive Sepctrometry (EDS) and Transmission Electron Microscopy (TEM) microprobe examination, the composition of the dendritic core, eutectic constituent, eutectic γ, and Laves phase were determined. Also liquidus, solidus, γ/NbC, and γ/Laves eutectic temperatures were determined by differential thermal analysis (DTA). They found that the bulk of the eutectic solidification product was the γ/Laves constituent. The Laves phase constituent was the predominant phase and the carbide and Laves microconstituents were not intermixed.[36] Laves phase (22.4 w/o Nb) and eutectic γ (9.3 w/o Nb) forms from the eutectic liquid (19.1 w/o Nb) at 1196 °C following the γ/MC eutectic reaction at 1250 °C. The equilibrium partition ratio calculated was 0.5 for Nb and found to be constant over the solidification process.

The crystal structure of Laves phase is $MgZn_2$-type topologically close-packed hexagonal with a nominal formula of MN_2. Vincent suggested that if Nb, Mo, and Ti represent the large M atom and Ni, Fe, and Cr to be a small N atom, the overall composition is close to MN_2.[31] He also found a small (~1a/o) but persistent Si content. The dimensionless parameter α in the Brody-Flemings equation for Nb in Inconel 718 was calculated as 5 x 10^{-3} for given welding conditions with a dendrite size of 10 to 20 μm. This implies that solid state diffusion is negligible during the solidification process.[36]

Thompson et al. [40] reported a 70 % increase in NbC volume fraction but no significant change in the amount of Laves phase present when the carbon content in cast Inconel 718 was increased from 0.02 to 0.06 %. The increased NbC content was accompanied by an increased susceptibility to liquation cracking. It is well documented that HAZ liquation cracking susceptibility is related to the constitutional liquation of NbC well below the

solidus temperature of wrought Inconel 718.[41] The source of HAZ cracking frequently cited is the liquation of Laves phases[32, 40, 42] in the cast alloy and MC carbides[41] in the wrought alloy. The reduction of Laves phases resulted in better weldability of Rene 220C which does not contain Fe.[42]

In a study of casting of alloy 625, Sawai et al. [43] observed interdendritic precipitation of (Nb,Ti)C and $(Ni,Cr)_2(Nb,Mo)$ due to microsegregation of solute elements. Due to the relatively slow cooling in casting (3 - 30 °C/min compared to 300 °C/sec which is typical of gas tungsten arc welding) [44], there is enough time for solid state diffusion of Nb to alleviate the degree of segregation. The amount of Laves phase in the solidified structure has been found to be less in slow cooled (3 °C/min) than in fast cooled specimens (30 °C/min). On the other hand, the diffusivity of carbon is much greater than Nb and Ti and the cooling rate has little influence on carbon microsegregation and precipitation of carbide. In a separate study of the welding of alloy 625, Cieslak found high hot cracking susceptibility of Nb-bearing alloys.[32] Within the group of alloys containing about 3.5% Nb, the predominant microconstituent in low carbon alloys (0.009 %) was Laves phase, whereas it is the MC carbide in high carbon alloys (0.035 %). Silicon containing alloys show increasing Laves phase content with high Si content. The composition of MC carbide is 60 - 73 % Nb and 7 -18 % Mo with 10 % of Ni, Fe, Cr. The composition of Laves phase is about 18% Nb, 18.5% Mo with 60 % of (Ni+Cr). In summary, the evolution of solidification microstructure in alloy 625 fusion welds is dominated by the segregation of Nb.

The competition of carbide and Laves phase during solidification was studied by Nakao et al. using IN-519 with various C and Nb contents.[45] When the atomic ratio Nb/C is close to 1, the predominant phase is NbC. When the Nb/C atomic ratio is larger than 1, Laves phase becomes the dominant phase and contributes to an increase in hot cracking susceptibility. When the Nb/C atomic ratio is less than 1, $Cr_{23}C_6$ carbide which has a lower eutectic temperature than NbC begins to precipitate and hot cracking susceptibility increases again.

II.3.3 Segregation in 900-series Superalloys

The 900-series alloys are Cr-free low thermal expansion Fe-Ni-Co alloys which derive high strength from precipitation of γ', $Ni_3(Al,Ti,Nb)$. The welding metallurgy of 900-series superalloys are closely related to that of Inconel 718 and other Nb containing Fe-Ni

alloys. Alloy 903, representative of this family of alloys, was introduced as the first commercial low COTE superalloy in the mid-70's and today remains the most widely used and most extensively studied alloy in this family.

In an earlier study on the weldability of alloy 903, Baeslack III et al. [46] and Ernst et al. [39] have reported the formation of γ/Laves phase eutectic as the major secondary solidification component in the gas tungsten arc weld fusion zone. They observed that the liquation cracking susceptibility of the weld metal was significantly greater than that of solution annealed base metal and concluded that the constitutional liquation of Laves phase was primarily responsible for the increased susceptibility. SEM/EDS analysis on the fusion zone and HAZ [39,47] revealed Laves phase rich in Nb, Ti and Si. The occurrence of a second eutectic reaction in the fusion zone involving fine carbide as well as γ/Laves reaction was suggested but not extensively studied.[43] Nakkalil et al. [38,48] studied the microstructure of electron beam welded alloy 903 and argued that the low silicon content (0.07 %) and high carbon content (0.028 %) of the alloy made the γ/MC eutectic constituent far predominant over the γ/Laves constituent in the solidification microstructure of the fusion zone. This discrepancy may have originated from the difference in the composition of Incoloy 903 used by the two groups of researchers. They also reported the presence of Si in the Laves phase. They observed relatively small partitioning of Ti into the Laves phase. Cieslak also observed predominantly γ/MC eutectic phases in high C (0.038 %) - low Si (0.03 %) alloy 625 weld zone.[42] Nakkalil also suggested that liquation cracking in the HAZ of electron beam welded thermomechanically treated alloy 903 originated from the constitutional liquation of the large and fine carbide as well as the Nb-rich phosphides present on the grain boundary.

In other 900-series superalloys with higher Nb (5% compared to 3% in 903), there was an increase in fusion zone hot cracking susceptibility with the amount of alloying elements.[39] The weld solidification cracking susceptibility originated from the partitioning of Nb, Ti and Si to grain and solidification substructure boundaries during solidification and the formation of a low melting point terminal γ/Laves eutectic. The amount of γ/Laves eutectic increased with the amount of Nb, Ti and Si. Also an increased Si content along with lower carbon in Incoloy 909 resulted in an increase in the amount of TCP (topologically close-packed phase) including Laves and silicide.[39] In high carbon alloys, fine carbides were also observed in proximity to the dendritic cores, suggesting that they were formed at higher temperature than the γ/Laves eutectic.

The solidification characteristics and weld microstructure of alloy 908 have been subjected to a very limited number of investigations due to the relatively recent introduction of the alloy. Preliminary research done by Jang [49] indicated Laves phase as the dominant secondary constituent in the weld. SEM/EDS analysis on the precipitates within the gas tungsten arc weld of alloy 908 revealed that there is no clear morphological difference between the Laves phase and MC carbide.

II.4 Mechanical Properties of Weld

II.4.1 Role of Secondary Phases

The degradation of fracture toughness and/or ductility in the welds of precipitation hardening superalloys, especially Nb-containing superalloys, have been reported by various researchers. The mechanical properties of some superalloy welds are summarized in Table 6. Extensive room temperature tensile tests of Inconel 718 weld have been conducted at Inco Alloys International.[50] The ductility of Inconel 718 weld after direct aging was reduced to about 30 % of that of base metal with comparable heat treatment. Mayor [51] also observed a substantial decrease in ductility of welds in Inconel 718 and 706. Weld fracture toughness has been reported as about 50 % of the base metal (55 MPa$\sqrt{m}$ compared to 110 MPa$\sqrt{m}$).[51] Logsdon [52] also reported about a 30 % decrease in the weld fracture toughness. He reported an even bigger drop in the fracture toughness of Inconel 706, which has lower Nb+Ta content, after welded using 718 filler metal. The low fracture toughness of welds in Inconel 718 have been attributed to the existence of Laves phase and orthorhombic δ phase in the interdendritic region of weld.

The fracture surface of the Inconel 718 weld indicated that microvoid initiation occurs at Laves phase.[51] James [53] also considered Laves phase responsible for the low toughness. The role of brittle secondary phases and inclusions on the ductility and fracture toughness of structural alloys have been well recognized. A direct relationship between inclusion density in austenitic stainless steel welds and the fracture surface dimple density has been reported.[54] Logsdon also studied the mechanical properties of JBK-75 and A-286, precipitation hardening Fe-base superalloys, and observed considerable loss of fracture toughness in autogenous welds.[55] However, for Inconel X750, the fracture toughness of welds were greater than that of base metal at 4K.[56] Unfortunately, no extensive investigation to identify the solidification constituents within the weld were conducted except for the observance of a Nb, Ti rich carbide. Considering the composition

of X750, low Fe (6.5 %) and Nb+Ta (1 %), it is unlikely that any significant amount of topologically close packed phases would have formed in the weld except possibly fine carbide.

There are limited published data on the mechanical properties of 900-series superalloys. Fracture toughness testing using about 1.6 mm thick sheet resulted in mixed behavior within the alloys.[57] For alloy 903 and 905, fracture toughness either increased or decreased depending on orientation at 4K. However, the thickness of the specimen was not sufficient for valid fracture toughness testing for some of the tests. The test results on Incoloy 909, whose thickness requirement were met, showed substantial reduction of toughness after welding. For newly developed alloy 908, loss of ductility and fracture toughness of welds has been reported.[2, 21] The fracture toughness of gas tungsten arc welds decreased to about 50 % of that if the base metal. About the same decrease in Charpy impact energy was observed at all three temperature tested, RT, 77K and 4K.

Table 6. Mechanical properties of selected superalloys

Materials	Temp	Base		Weld		ref.
		s_y, MPa	K_{IC}, MPa$\sqrt{m}$	s_y, MPa	K_{IC}, MPa$\sqrt{m}$	
Inconel 718	4K	1408	112	1373	52	51
JBK-75	4K	1238		1415	133	55
Alloy 909	4K	1236	70	1084	39	57
X-750	4K	867	76	958	134	56
Alloy 908	RT	1075	196	1061	106	2
	4K	1227	235	1279	105	2

II.4.2 Effect of Post Weld Heat Treatment

Various post-weld heat treatments (PWHT) have been used to improve ductility and/or fracture toughness of superalloy welds. For Inconel 718, a high temperature solution treatment (1066 °C) has proved effective in improving ductility.[50] It has also been

reported [52] that a 1066°C solution treatment in forged Inconel 718 before the aging heat treatment improved both ductility and fracture toughness at 4K by removing the fine (Nb,Ti)C carbide network. However, a 980 °C solution anneal was not effective in modifying the microstructure, and resulted in low fracture toughness. Mills compared two annealing temperatures used after welding, and concluded that the benefit of higher temperature (1093 °C) over lower temperature (955 °C) is a substantial improvement of fracture toughness by removing/reducing Laves phase within the weld.[58] He reported an increased toughness of welds after high temperature annealing as a method for the removal or reduction of Laves phase in the weld. Lower annealing temperatures (955 °C) were not effective in improving weld ductility of Inconel 718 and 706.[51] A homogenization treatment of 1050°C/1hr after welding recovered ductility and fracture toughness of alloy 908 by removing Laves phase from the interdendritic area.[21]

The time-temperature-transformation (TTT) curve for Inconel 718 [19] and Incoloy 909 [59] are shown in figures 16 and 17. Laves phase remains stable until the temperature reaches around 1040 °C. The behavior of alloy 908 which has about 4.5 % of Nb + Ti is thought to be very similar to that of Inconel 718 and Incoloy 903. A previous study of gas tungsten arc welded alloy 908 demonstrated the effectiveness of 1050 °C annealing in the removal of Laves phases in the weld and recovered ductility and Charpy impact energy.[6, 21]

II.4.3 Effects of Welding Methods

There are not enough reported data to allow an analysis of the effect of welding method on mechanical properties. Differences in dendritic spacing, and solidification microstructure will strongly effect the resulting mechanical properties. Nevertheless, the degree of microsegregation remains fairly constant over wide ranges of cooling rate attainable by various welding methods.

The use of multi-pass gas tungsten arc welding results in the modification of the microstructure of the underbead by the following welding passes. Depending on the location, in-situ solution annealing or precipitation hardening is possible. For thick section welding, the difference in mechanical properties within the weld require extra consideration when choosing design values.[60] Various welding techniques, such as gas tungsten arc welding, electron beam welding, laser beam welding and flash welding, have been applied to weld alloy 908.[6, 61] Preliminary tensile properties measurements showed minimal

effects of welding methods even though about a two-fold decrease in dendritic spacing have been achieved in electron beam and laser beam welding.

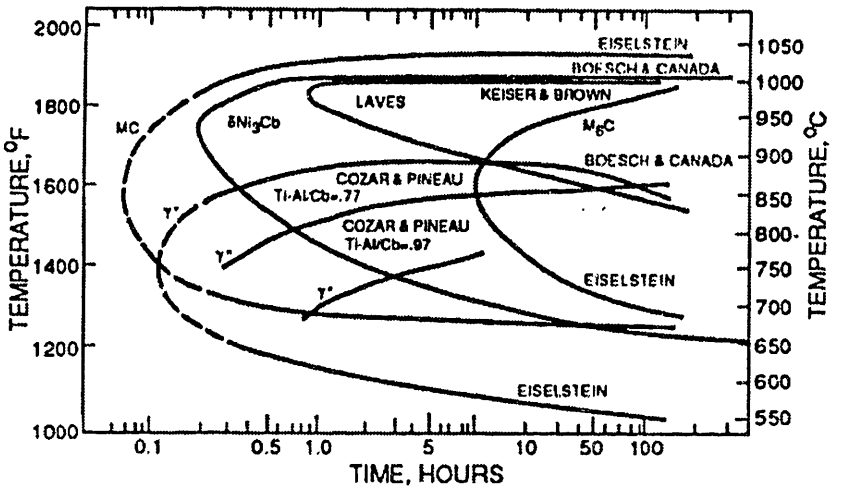

Figure 16. Time-Temperature-Transformation (TTT) curve of Inconel 718.[19]

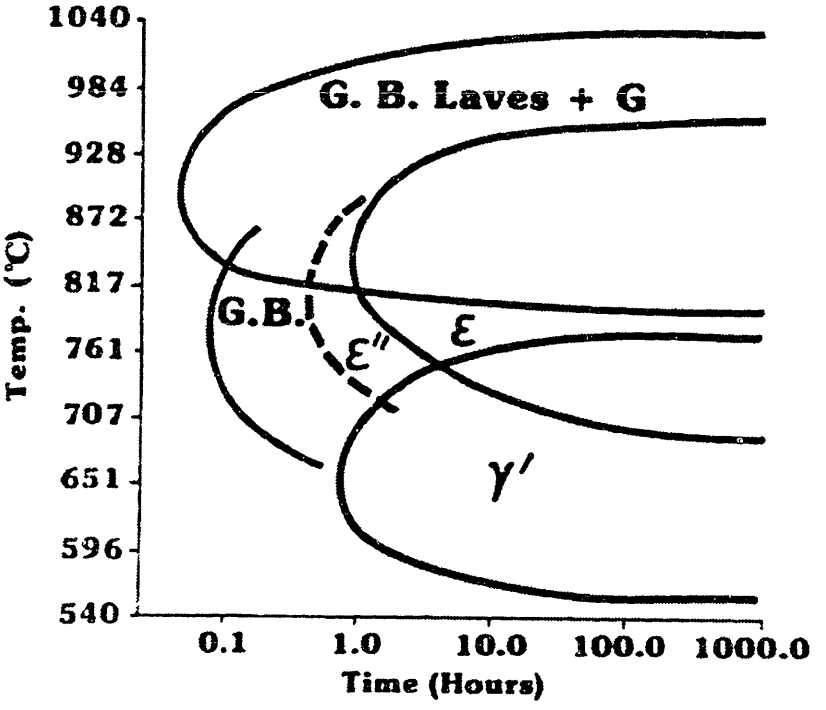

Figure 17. Time-Temperature-Transformation (TTT) curve of Incoloy 909.[59]

II.5 Scope of Research

The similarity of chemical composition of alloy 908 to other Ni-Fe base superalloys suggests that the solidification characteristics and weld microstructure of alloy 908 should be close to those of Ni-Fe base superalloys. However, there exists no reported data on the weld solidification of alloy 908 except limited results from work done at MIT. There are contradicting reports on whether the dominant phase in the solidified weld fusion zone is Laves phase or MC carbide. Also, some differences in composition, such as the absence of Co and more Si and less C in alloy 908, can effect the solidification characteristics and weld microstructure including precipitation of secondary phases. Thus, the solidification behavior and microstructure of alloy 908 weld needs to be chracterized.

Because the 900-series superalloys were developed for primarily high temperature applications while minimizing welding of components, there are not many reported data on mechanical properties, such as tensile properties and fracture toughness of welds at room temperature and lower temperature. The mechanical properties including, tensile, fatigue and fracture toughness of alloy 908 weld need to be evaluated. Also the fracture mechanism of welds need to be understood in association with microstructure.

The purpose of this thesis is to improve mechanical properties, especially, fracture toughness of alloy 908 weld based on an understanding of the welding and solidification metallurgy, in conjunction with the relevant mechanical properties evolution. To achieve this goal, following research scope was set:

1. Characterize solidification behavior of alloy 908 weld such as, microsegreagtion of alloying elements and precipitation of secondary phases by examining
   - The effects of welding methods on the solidification behavior and mechanical properties.
   - The effects of post weld heat treatment on the weld microstructure and mechanical properties.

2. Understand the relationship between microstructure and mechanical properties.

3. Based on the proceeding understanding, develop new filler metal compositions. Evaluate mechanical properties, such as tensile, fatigue and fracture toughness of weld.

4. Understand fracture mechanism of weld in association with microstructure.

5. Evaluate weld mechanical properties at various stages of fabrication process, including welding, tube reduction and winding.

6. Evaluate the mcehanical properties of simulated production welding.

The overall steps of research are shown as a flow chart in Figure 18. First, by examining the effect of various welding techniques, the characteristics of elemental segregation and precipitation and their contribution to the mechanical properties of weld will be studied. Second, the effect of high temperature solution annealing heat treatment on the microstructure and precipitation of secondary phases will be examined. Then, by controlling the amount of alloying elements in weld filler metals, the optimum composition which would give reasonable strength-fracture toughness values suitable for use in engineering applications for ITER magnets will be determined.

Additionally, the weld properties at various stages of fabrication process, including welding, tube reduction and winding, have to be characterized to ensure the integrity of weld. Finally, automated welding process will be used to simulate the probable orbital welding process which will be used in the actual fabrication of conduit.

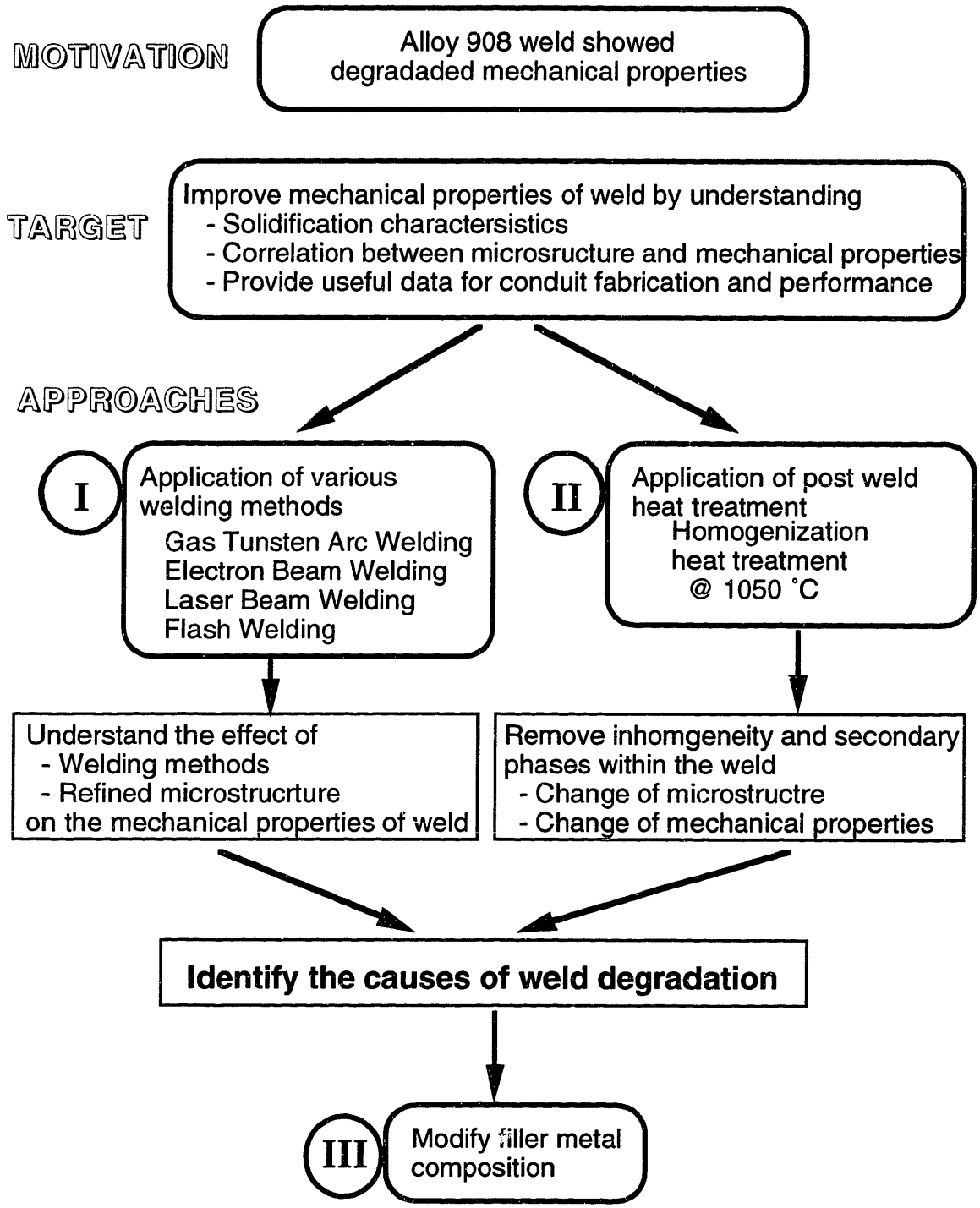

Figure 18. Flow chart of research plan for alloy 908 weld development.

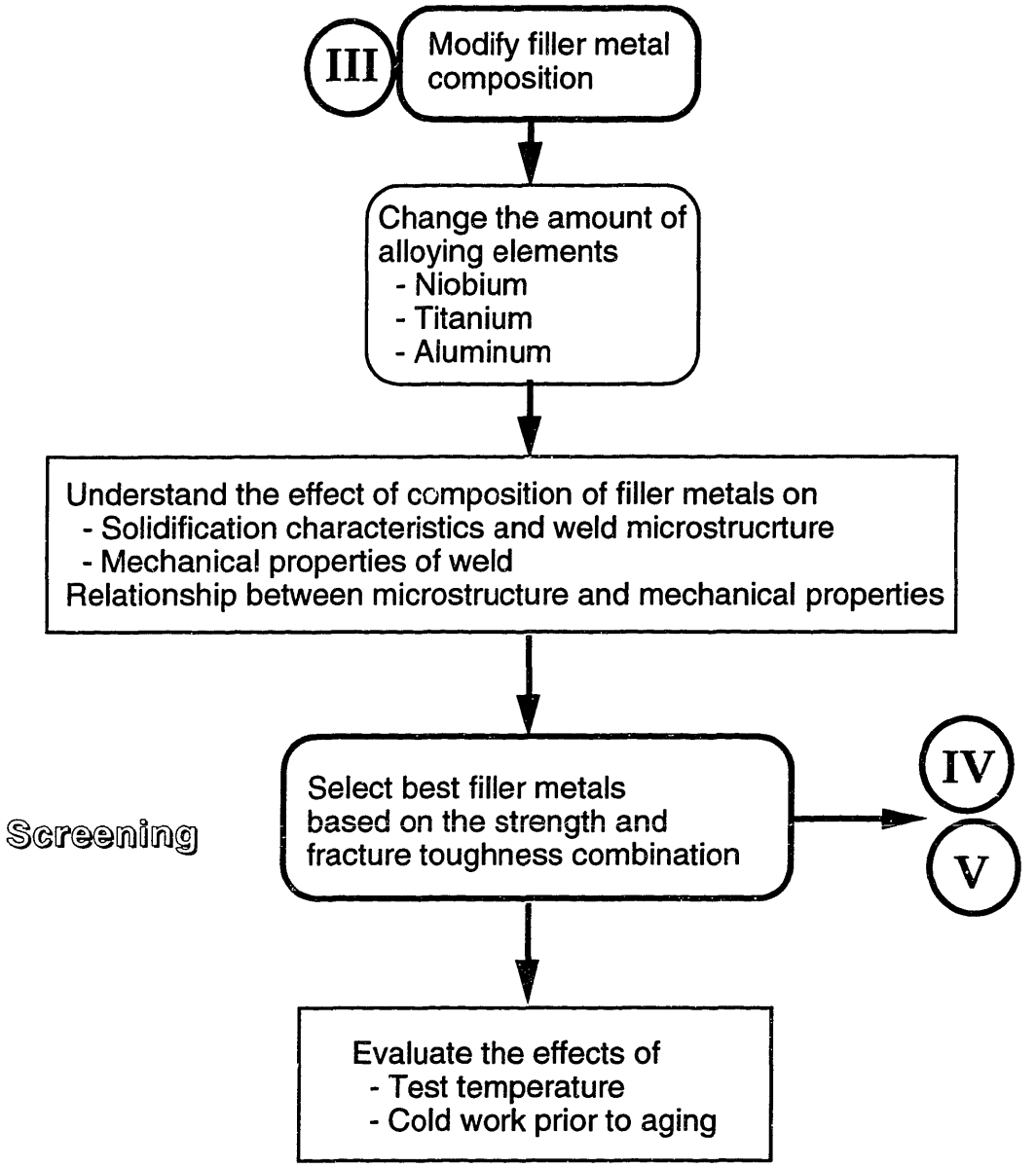

Figure 18. Continue.

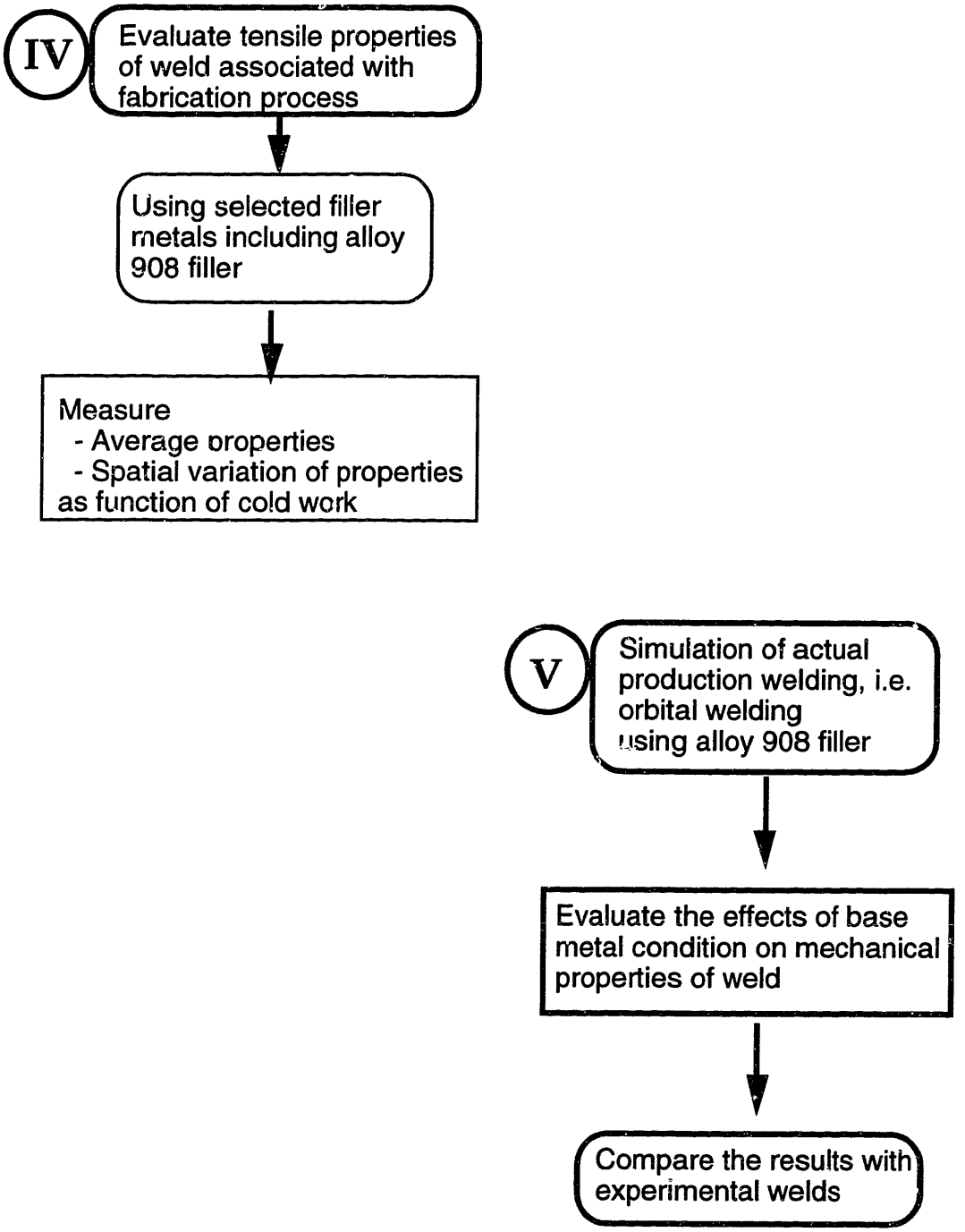

Figure 18. Continue.

III. Materials and Procedures

III.1. Materials

The nominal composition of alloy 908 is shown in Table 7. Base metal alloy 908 for this research was produced by vacuum induction melting (VIM) followed by electroslag remelting (ESR) at the Inco Alloys International, Huntington, West Virginia. Ingots were homogenized at 1191 °C for 16 hours and fast cooled. A series of forging and reheating steps reduced the ingots to 7 mm -thick plates which were finally mill-annealed at 980 °C for 1 hour followed by slow cooling. The general microstructure of alloy 908 consists of a single phase austenitic structure. γ' precipitation occurs during heat treatment. In the rolling direction, some of the carbides are found along the flow lines.

Table 7. Nominal composition of alloy 908.

Element	Fe	Ni	Cr	Nb	Al	Ti	Si	C
weight %	40.8	48.7	4.1	3.0	1.1	1.5	0.2	0.01

III.2. Welding Methods

III.2.1. Gas Tungsten Arc Welding

A. Manual Multi-Pass Gas Tungsten Arc Welding

Manual gas tungsten arc welding was used for most of the weld development studies. The design for edge preparation is shown in Figure 19. Base plates were taken from 7 mm-thick plates supplied in the mill annealed condition (MA). Plates for welding were prepared as 300 mm-long 50 mm-wide plates with a 90° single V-groove design. The adjacent surfaces of the weld groove (at least 12 mm on both sides) were skimmed to remove

surface contamination. Plates were sand blasted to remove surface contamination after weld edge preparation. Before welding, plates and filler wires were further cleaned with acetone to remove grease or oil contamination.

A special welding fixture, shown in Figure 20, was used to provide proper shielding and constraint for the workpiece during welding. A continuous flow of argon shielding gas was provided through the electrode cup, the holes in the clamping plates, and the holes in a groove on the backing plate. Welding was done manually with 12 - 15 V and 140 - 180 A with a travel speed of about 2 mm/sec. For the first pass, during which both the root of the base plates and filler wire have to be fused together, the highest power was needed. For subsequent passes, less power was needed. For 7 mm-thick plates, about 5 to 6 passes were needed to complete the weld. A more detailed description of the welding steps is summarized in Table 8.

B. Automatic Multi-Pass Pulsed-GTAW

Automatic multi-pass pulsed-gas tungsten arc welding was used to closely simulate the orbital welding of actual magnet conduit.[62] Two base plate conditions were used: (1) the mill-annealed condition (MA) which is the same as the as-received condition (AR) used in manual-GTAW and other welding methods which will be mentioned later, and (2) a homogenized condition (HT) for plates subjected to the homogenization heat treatment of 1050 °C/ 1 hr followed by water quenching before edge preparation. Care was taken to maintain flatness of plates during heat treatment and quenching. The design for edge preparation is shown in Figure 21. Plates for welding were prepared as 380 mm-long 75 mm-wide plates. A single U-groove with mixed angle design was used to reduce lateral contraction during welding. The adjacent surfaces of the weld groove (at least 12 mm on both sides) were skimmed to remove oxide and reduce the chance of contamination during welding. Welding was done without back reinforcement except for one plate of the HT condition.

III.2.2 Electron Beam Welding and Laser Beam Welding

Electron beam welding (EBW) uses energy from a focused electron beam to heat and fuse metals to be joined. The focused electron beam can provide high energy density and deep

penetration. As the electron beam moves along the joint, surface tension draws molten metal from the leading edge of the hole to the trailing edge where weld metal solidifies in less than a second.[63] Welds can be made in deep, narrow space with an extremely narrow weld zone at very high speed. Electron beam welding is done in vacuum.

Laser beam welding (LBW) uses a high energy laser source, usually a CO_2 laser to heat and fuse closely fit workpieces. Welding is done in the same manner as electron beam welding and produces an equally deep, narrow fusion zone. Laser beam welding is done in an inert shielding gas, usually argon. With both of the high energy density welding methods, the molten metal solidifies quickly in a deep narrow fusion zone. The weld is formed with less distortion and a smaller heat affected zone.

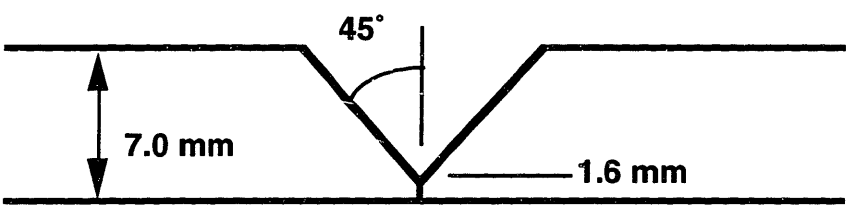

Figure 19. A Schematic of groove design for multi-pass manual gas tungsten arc welding.

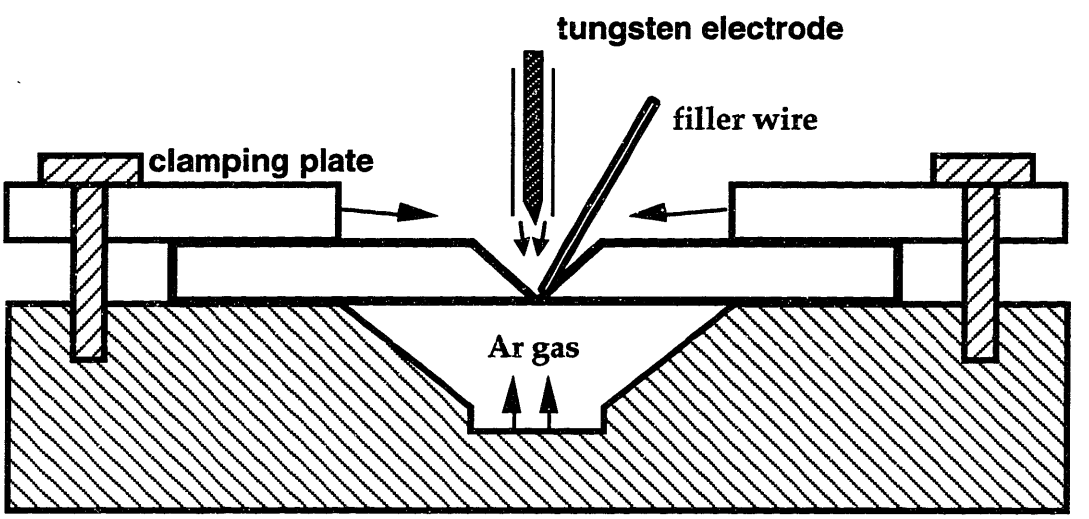

Figure 20. A schematic of the welding fixture. Flow of argon shielding gas was shown as arrows

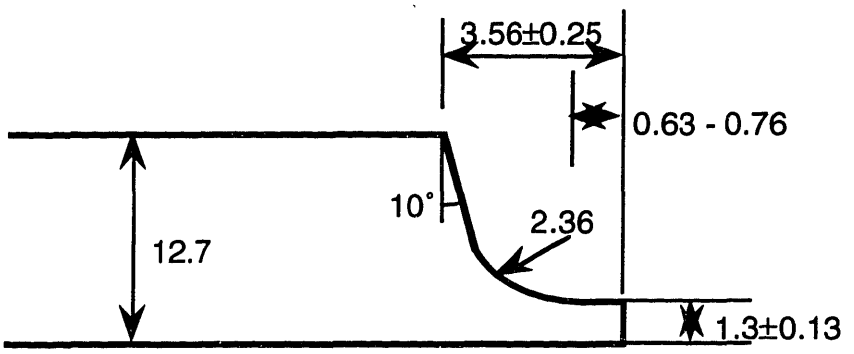

Figure 21. Single U-groove with mixed angle design used for automatic pulsed-gas tungsten arc welding. (in mm)

Table 8. Welding condition of multi-pass manual gas tungsten arc welding.

Power supply	Direct current, straight polarity
Electrode	2.4 mm dia. 2 % thoriated-tungsten electrode (EWTh-2)
Cup size	≥ 10
Shielding gas	Argon, Welding grade (99.99 % pure)
Gas flow rate at electrode cup	10 L/min with backing pressure of 0.1 MPa
Backing pressure at workpiece	0.17 MPa
Electrode to workpiece distance	1.3 mm with 60° inclined angle
Voltage	12 -15 V
Current	140 - 180 A
Travel speed	2 mm/sec
Welding wire	1.6 mm dia. bare wire

Because the beam is focused in a narrow spot, the workpieces have to be fit very tightly. Plates for EBW and LBW were prepared with a square-butt joint design. EB welding was done in vacuum at a speed of 25 mm/sec with a power of 3.6 KW. LB welding was done in an argon environment at a speed of 17 mm/sec with a power of 5 KW. A single pass completed welding. A more detailed description of the welding condition is summarized elsewhere.[61]

III.2.3 Flash welding

Flash welding (FW) is a resistance welding process that produces coalescence at the facing surfaces of a butt joint by electric heating from flashing action (intermittent arcs) followed by the application of pressure at the end of the flashing action. The flashing action is caused by the very high current densities at small contact points between the workpieces. When the surfaces are sufficiently heated, they are brought together under axial pressure by the process known as 'upsetting'. This pressure expels the molten metal and oxide present at the interface, and welds underlying clean metal surfaces. This upset process usually introduces heavy deformation, as high as 50 % [30], and produces outward flow of heated metal forming hyperbolic shaped flow lines.

Plates for flsh welding were prepared as 7 mm-thick 25 mm-wide and 100 mm-long pieces. The pieces were welded at both in air and argon gas environments. The plates, initially separated by 55 mm, were flashed over 20 mm at an acceleration of 0.05 mm/sec^2, and then were welded by upsetting over a 8 mm distance in 0.25 sec using 50 kN force. Because welded pieces were not large enough to make test specimens, they were electron beam welded to blocks of alloy 908 basc metal to obtain sufficient material, as shown in Figure 22. Care was taken to align the joint along the anticipated crack front.

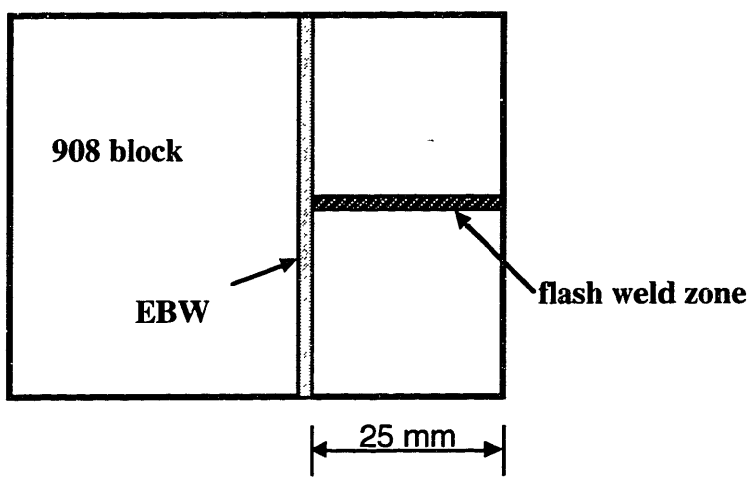

Figure 22. Flash weld joined to alloy 908 block by electron beam welding.

III.3 Weld Filler Metal Compositions

Based on the nominal composition of alloy 908, the composition of new filler metals were selected by controlling the amount of minor alloying elements. The compositions of newly developed filler metals are shown in Table 9. The chromium composition of filler metals was maintained at 4 % which has been optimized for improved oxidation resistance and low thermal expansion coefficient for fusion applications.[1] The amount of the three major precipitation hardening elements (Nb, Ti, Al) was modified slightly.

Niobium is primarily a γ'' former in many alloy systems. However, due to the relative abundance of Al and Ti, it partitioned into γ' and was the most effective element in achieving precipitation hardening by increasing lattice mismatch between γ-matrix and γ' while maintaining coherency.[1] Niobium also suppresses the coarsening of γ' by heavily partitioning into γ'. This is due to the slow diffusing properties of the element. It is also known that the low diffusion coefficient of Nb reduced premature hardening during welding and consequently the likelihood of strain aging cracking. Despite all these advantages, the chances of hot cracking in both HAZ and underbead weld increases with Nb content.[39] Most of all, the Laves phase formed within interdendritic region of weld is known to provide void initiation sites during fracture and is thought to be responsible for low fracture toughness. Therefore, the amount of niobium was reduced in the design of potential filler metal compositions.

Titanium is a γ' former along with Al in superalloys. Even though it can also form Laves phase with Fe, its larger equilibrium partition ratio and higher solubility in both Fe and Ni make this less likely than with Nb. Two Ti composition, 1.85 % and 2.3 % were used.

Aluminum is primarily a γ' former and stabilizes γ' or γ'' against premature transformation to η or δ phases during aging. The equilibrium partition coefficient of Al is almost unity in most superalloys and the Al composition is homogeneous in solidified structures. The composition of aluminum was controlled to from 0.5 % to 1.5 %.

The sum of Al and Ti composition effect the weldability of superalloys. To achieve good weldability the atomic percent of Al + Ti should be lower than 6 %.[64] All the weld filler metal meet this criteria.

Molybdenum is used in superalloys to promote strong solid solution hardening. Also, Mo has a higher equilibrium partition ratio than Nb and Ti. About 2 % of Mo was added to the selected filler metals with low precipitation hardening elements content.

Table 9.Chemical composition of new filler metals. (in weight percent)

filler	Fe	Ni	Cr	Nb	Al	Ti	Mo
9FA	40.14	50.11	4.01	3.04	1.08	1.83	
9GA	41.35	50.23	4.02	1.51	1.12	1.85	
9GB	40.98	50.25	4.03	1.50	1.07	2.32	
9GC	40.88	50.32	4.03	1.52	1.54	1.84	
9GD	40.45	50.28	4.00	1.48	1.59	2.31	
9FC	41.72	50.15	4.03	0.99	1.00	1.84	
9HA	41.67	51.15	4.07	0.52	1.09	1.85	
9HB	44.64	49.72	4.03	0.50	0.55	0.57	
9HC	40.65	49.95	4.01	0.51	1.05	1.84	1.95
9HD	42.86	49.40	3.99	0.50	0.57	0.58	1.97

* Final products of filler metals prepared by Inco. Alloys International Inc.

Silicon is added to 900-series superalloys to improve notch-rupture strength.[59] Silicon enhances the formation of iron-silicide along the grain boundary and inhibits grain growth. Silicon, however, was found in Laves phases in various alloy systems and is believed to enhance the formation of Laves phases. There is no benefit of inhibiting grain growth in the weld where the grains are already elongated and much larger than that in the base metal. Therefore the amount of silicon was limited to below 0.001 %. The carbon content of the welds were limited to below 0.001 %. However, as will be discussed later, these strict requirements can not be easily achieved in industrial practice. Thus, it is thought that Si and C content in filler metals are about the same as those in alloy 908 base metal.

Weld filler metals were produced by vacuum induction melting (VIM) at Inco Alloys International, Huntington, West Virginia. Ingots were homogenized at 1190 °C for 16 hours and fast cooled. Weld filler metals were prepared as 300 mm long x 16 mm diameter rods. The rods were cold drawn into 1.6 mm diameter wires with intermediate anneal at 1040 °C after every 3 reductions. Wires were annealed at 1040 °C after the final drawing step. Test welding with new filler wires were done by the manual multi-pass GTA welding procedure described in Table 8.

III.4 Post Welding Thermomechanical Treatment

III.4.1 Post Weld High Temperature Heat Treatment

Some of the welded plates were subjected to high temperature heat treatment before machining. Two post weld heat treatment conditions were used. The first was a solution annealing heat treatment (SA) for 1 hr at 980 °C in air followed by water quenching. The other is homogenization heat treatment (HT) for 1 hr at 1050 °C in air followed by water quenching.

III.4.2 Cold Work

Some of the weld plates were reduced in thickness before machining by cold rolling to examine the effect of cold work on the mechanical properties of welds. To provide uniform cold work, both the face and root of the weld were machined off to make flat surfaces before cold rolling was applied. The rolling direction was transverse to the welding direction. The amount of thickness reduction (CW) was in the range of 5 % to 13 %.

III.5 Specimen Machining

Various weld mechanical properties, such as tensile, fatigue and fracture toughness, were measured. Specimens for mechanical testing were machined from welded plates keeping the welds in the middle as shown in Figure 23. The tensile specimen design is shown in Figure 24. The design illustrated in Figure 23 was used for the measurement of weld averaged tensile properties of 7 mm-thick welded plates, and used when comparing the properties of different welds. Smaller specimens, shown in Figure 25, were used to evaluated spatial variation of tensile properties within the weld. Small tensile specimens were sliced from 7-mm thick welds and 13-mm thick alloy 908 weld used in a previous study[2] as shown in Figure 26. The specimen taken from the face and the root of a 7 mm-thick welds was designated as F and R, respectively. For a 13 mm-thick weld, specimens were designated as T (top), TB, BT, and B (bottom) from the face to the root of weld.

Compact tension specimens were used to measure both fatigue crack growth rate and fracture toughness. Two compact tension fracture toughness test specimen designs were

used. A larger arger specimen, shown in Figure 27, was used in most cases. A smaller specimen design, shown in Figure 28, was used when material was limited.

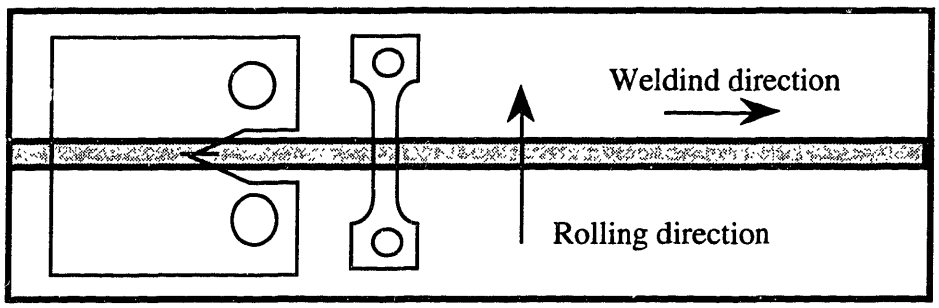

Figure 23. Specimen orientation with respect to the welding and rolling direction.

III.6 Mechanical Testing

Specimens were heat treated after being machined. Specimens were aged for 200 hours at 650°C in vacuum less than 1.0 x 10^{-5} torr. Temperature was maintained within ± 5 °C of set point. Before testing specimens were polished down to 600 grit and etched to reveal and check the location of the weld zone. When measuring mechanical properties in the unaged condition, specimens were tested without heat treatment.

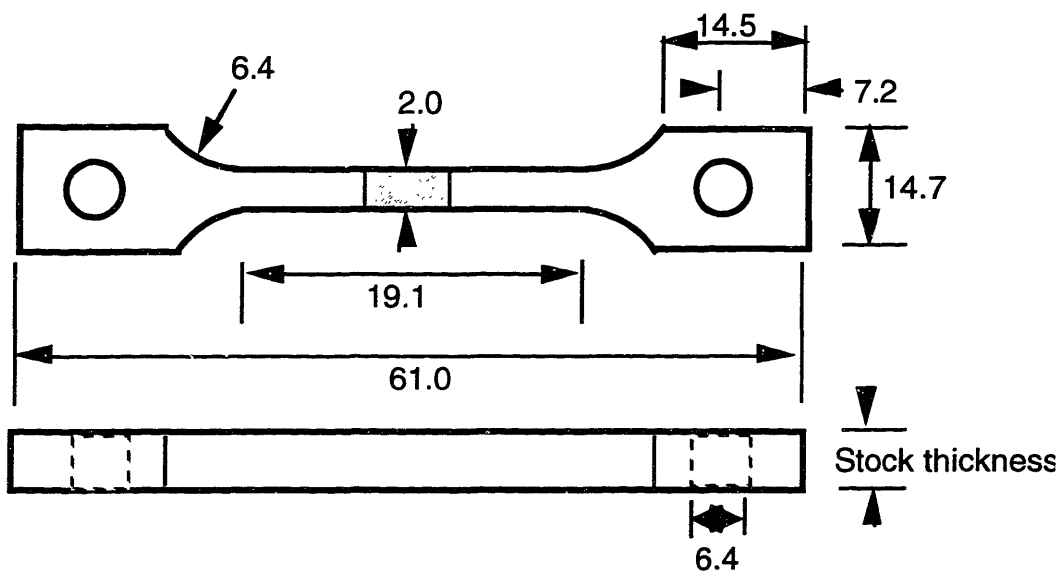

Figure 24. Standard size tensile specimen (dimensions are in millimeter).

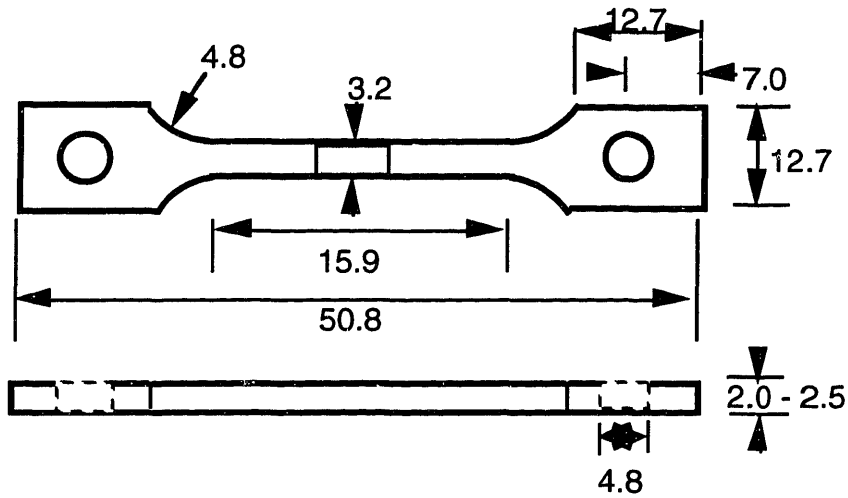

Figure 25. Sub-size tensile specimen design. Dimensions are in millimeter.

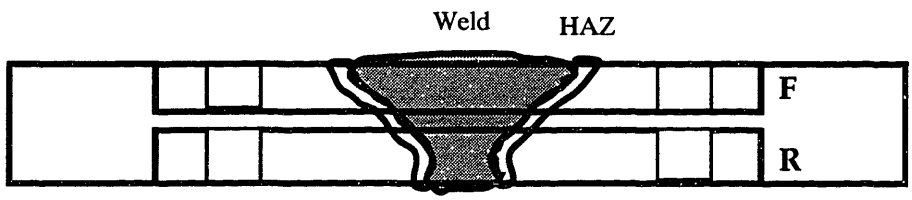

a) specimen ID from 7 mm-thick weld

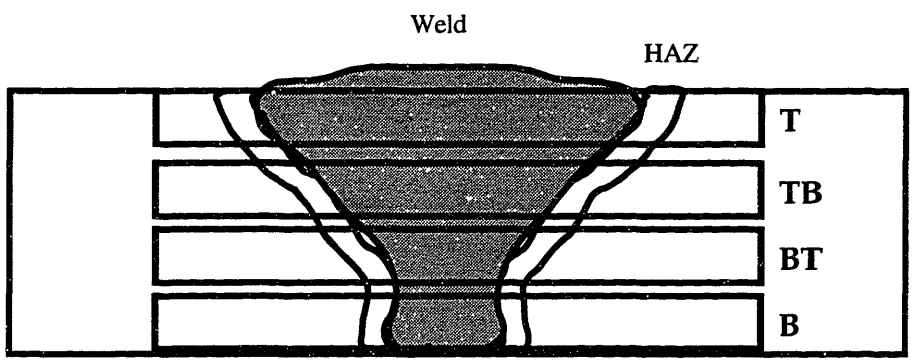

b) specimen ID from 13 mm-thick weld

Figure 26. Specimen identification sliced from welded plates

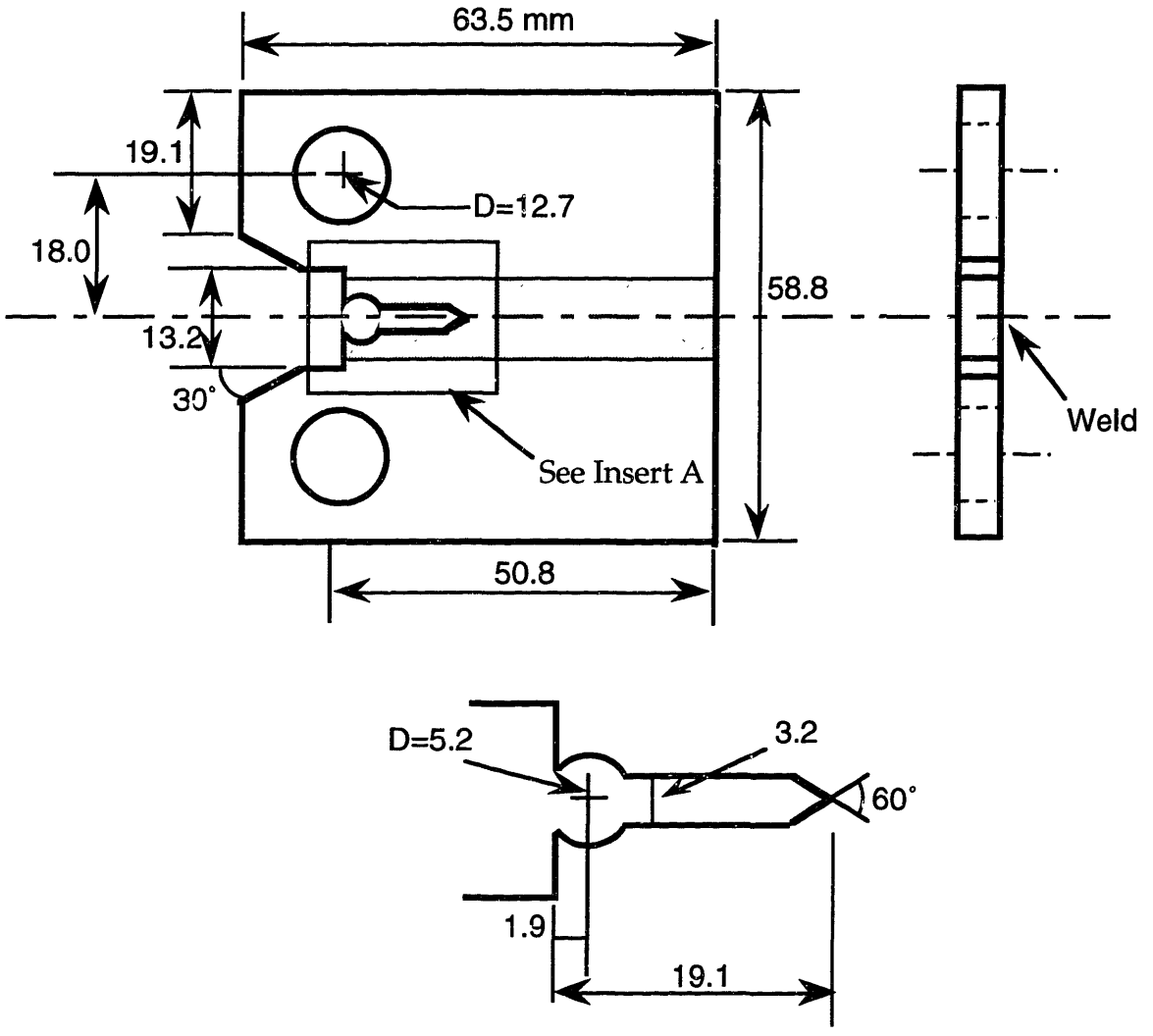

Figure 27. A 2" wide compact tension specimen for fatigue and fracture toughness testing.

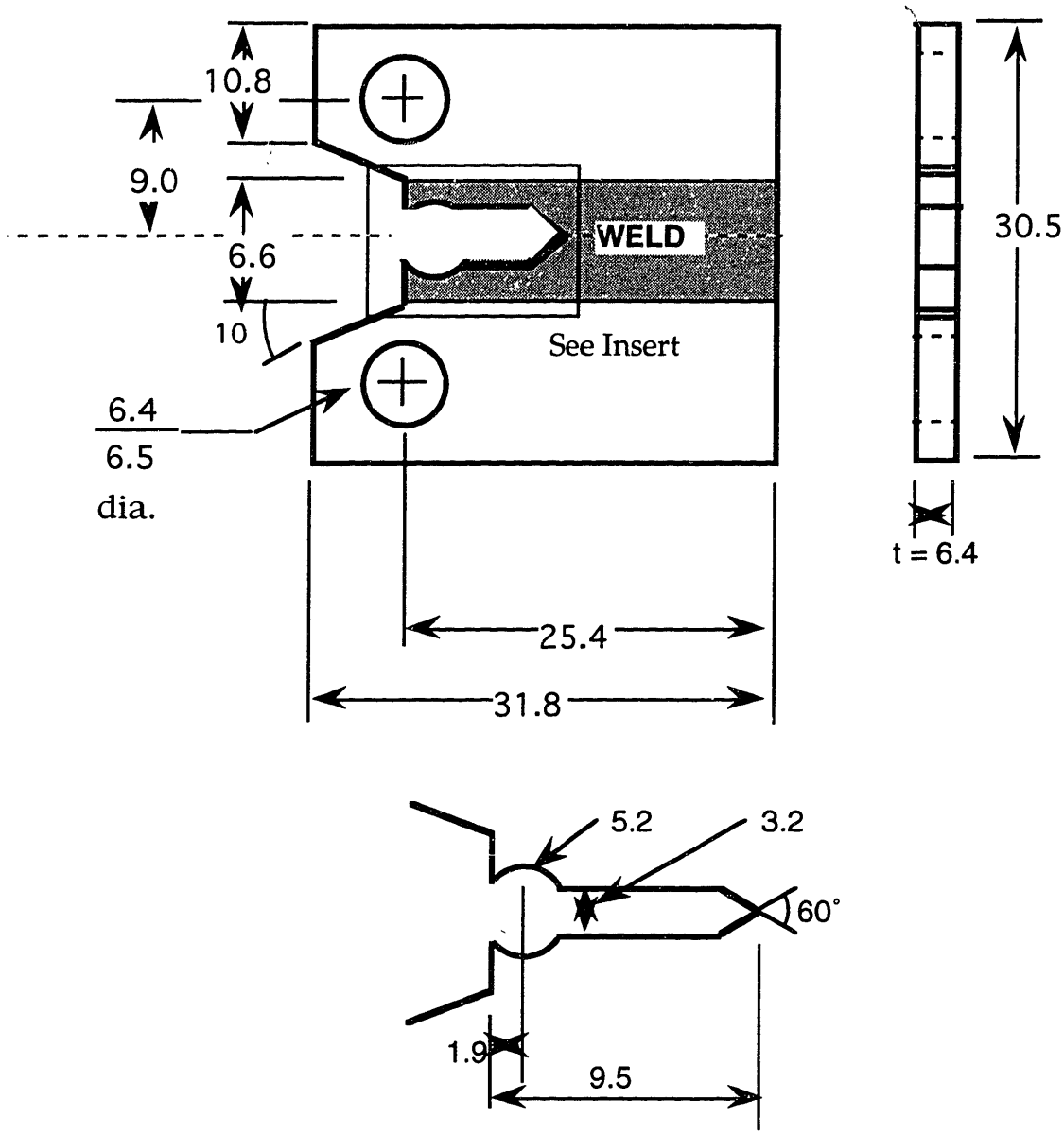

Insert: Magnified Tip Area

Figure 28. A 1" wide compact tension specimen for fatigue and fracture toughness testing.

Mechanical tests were done using a cryogenic test facility . The test facility consists of a computer controlled MTS servohydraulic fatigue machine equipped with a specially designed load frame. The loading system is designed to operate at temperature as low as 4K, using a stainless steel dewar filled with liquid nitrogen or liquid helium.

Tensile test were performed in accordance to ASTM standard E-8 at a strain rate of 2×10^{-4} mm/mm-sec. Specimen strain was measured using a Shepic model extensometer designed to be used down to 4K.

Fatigue crack growth rate measurements were made in accordance to ASTM E-647 using compact tension specimens. A ΔK range of from 17.5 to 60 MPa$\sqrt{m}$ with a loading ratio, $R = 0.1$ was used. Crack length was measured either directly using a traveling microscope equipped with stroboscope or indirectly by an unloading compliance.

The fatigue crack growth threshold value was also determined using the reducing ΔK method with fixed K_{max}.[65] Fatigue crack growth rates were measured by increasing ΔK until the reaches 33 MPa$\sqrt{m}$. Then, fixing K_{max}, K_{min} was gradually increased, thus decreasing ΔK. Even though ΔK is decreasing, K_{eff} increased gradually thus minimizing crack closure effects. Crack growth rates were measured until $da/dN \leq 1.0 \times 10^{-7}$ mm/cycle at which point, corresponding ΔK were determined as a ΔKth.

J-integral fracture toughness testing was done in accordance to ASTM E-813 and E-1157. The initial a/W for fracture toughness testing was in the range of 0.59 to 0.61. Crack length during fracture toughness testing was measured by unloading compliance. Tests were stopped after a crack growth increment of more than 2 mm which was enough to calculate J_{IC} using power fitting. The plane strain fracture toughness (K_{IC}) was then calculated as follows;

$$K_{IC} = \sqrt{\frac{J_{IC}E}{1-\nu^2}}$$

where E = Young's modulus

ν = poisson's ratio

Because the specimen was relatively thin, a uniform crack front was generally not maintained during tests, even for specimens with side-grooves. Thus fracture toughness values were presented as a tentative fracture toughness, J_Q or K_Q, instead of J_{IC} or K_{IC}. For each condition at least 2 tensile and 3 fracture toughness tests were performed unless mentioned otherwise.

For some of the welds, Vickers microhardness (VHN) was measured to study the variation of strength across weld and aging response.

III.7 Microstructural Analysis

Specimens for microstructural analysis were mounted and polished to 0.05 μm using alumina powder and etched using 10 % HCl + 90 % Methanol + 2 g/100 ml $CuCl_2$ solution. When electrolyte etching was needed a 10 % HCl + 90 % Methanol solution with appropriate voltage-ampere combination was used. Precipitate chemistries were examined using extraction replicas. Fracture surfaces were analyzed under Scanning Eletron Microscopy (SEM) equipped with Energy Dispersive Spectrometry (EDS). The chemistry of the particles sitting in the voids on fracture surfaces were also analyzed, in situ.

Particles were extracted electrolytically using a 10 % HCl + 90 % Methanol solution with the current density of 20 mA/cm^2 and collected on Millipore 0.2 μm polymer filter paper. Due to the samll size of the γ', only Laves phase and carbides were thought to be collected by filtering. X-ray diffraction analysis was done on the extracted precipitates using a Rigaku RU-300 diffractometer.

Thermal properties of filler wires are examined by differential thermal analysis (DTA) on a small amount of material (about 150 mg). Specimens were heated from 1000 °C to about 1450 °C at the rate of 10 °C/min while measuring the temperature difference between the sample and a reference material. The same condition was used during the cool-down. From the resulting temperature difference vs. reference temperature curve, equilibrium temperatures of a material, such as liquidus, solidus and transformation temperature, were determined.

IV. Results and Discussion

IV.1. Welds with Various Welding Methods

IV.1.1 Microstructure of Fusion Welds

Typical microstructures of gas tungsten arc weld (GTAW), electron beam weld (EBW), and laser beam weld (LBW) are shown in Figure 29. All of the welds showed a typical cellular-dendritic microstructure with precipitates present within the interdendritic zone. The most significant difference among the welds is the secondary dendritic arm spacing which can be estimated as the average distance between the interdendritic precipitates. The dendritic spacing measured is about 10 μm for GTA welds, 4 μm for EB weld, and 5.6 μm for LB weld. Macroscopically, compared to the rather irregular weld microstructure of multi-pass GTA weld, high energy density welding methods, such as EB weld and LB weld form deep narrow welds with a center symmetric dendritic structure.

Scanning electron micrographs of the three weld microstructures are shown in Figure 30. In all of the welds, precipitates are spaced about the same interval as secondary dendritic specings. In the immediate vicinity of precipitates, lightly colored deep etched zones are visible in both optical and SEM micrographs. These regions are though to be the Nb enriched γ matrix formed by eutectic reaction. The precipitates are enriched in Nb. The microstructure of welds will be discussed later in section IV.2.

At higher magnification, shown in Figure 30-d), it is clear that precipitates are totally isolated from the surrounding γ matrix forming a so-called divorced eutectic. This is unusual considering that large lamellar-γ/Laves eutectic (about 5 μm) has been reported for GTA welded Inconel 718 [36], and other 900-series superalloys.[39] As shown in microstructure of the LB weld, several precipitates are closely located within the lightly etched matrix. This suggest that these precipitates were formed within same interdendritic liquid.

IV.1.2 Microstructure of Flash Weld

In flash welding (FW), which is a kind of solid state welding method, a very narrow (≈ 0.5 mm) weld zone is formed as shown in Figure 31. Within the weld zone, a fine grain structure is visible. The grain size within the weld zone is actually smaller than that of the surrounding base metal. The upset pressure applied to form the joint introduces heavy plastic deformation on the joint surface. This heavy deformation initiates recrystallization in the joint. Surrounding the weld, hyperbolic shaped flow lines decorated with primary carbides are clearly visible. Such flow lines indicate the direction in which molten metal was expelled during upsetting. Within the weld zone, which is formed under high uniaxial compressive pressure, flow lines are aligned perpendicularly to the upset direction. Apparently, no secondary precipitate has formed during welding with this technigue.

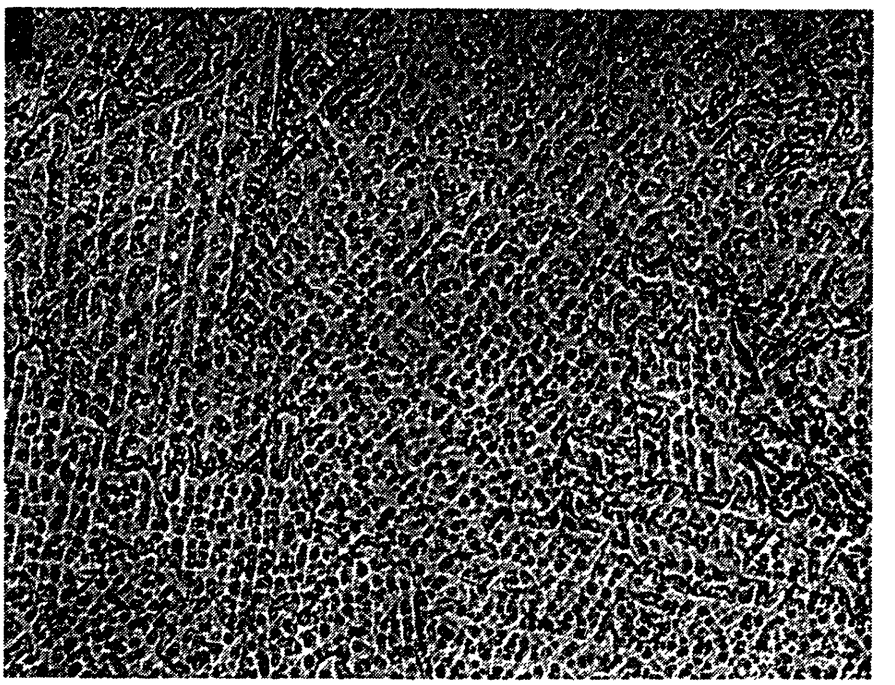

a) GTA weld, 200X

Figure 29. Optical micrographs of various fusion welds.

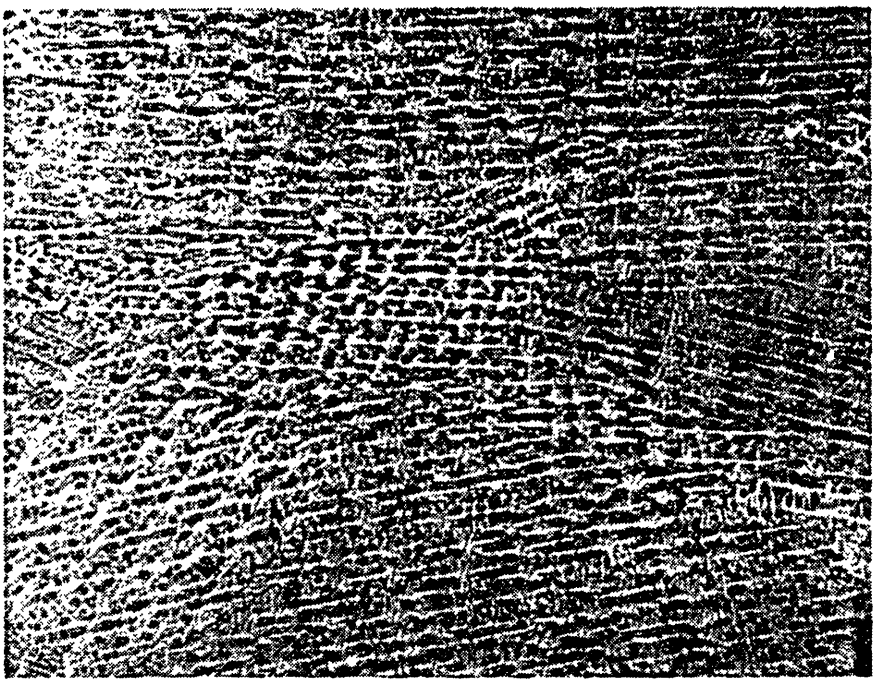

b) EB weld, 500X

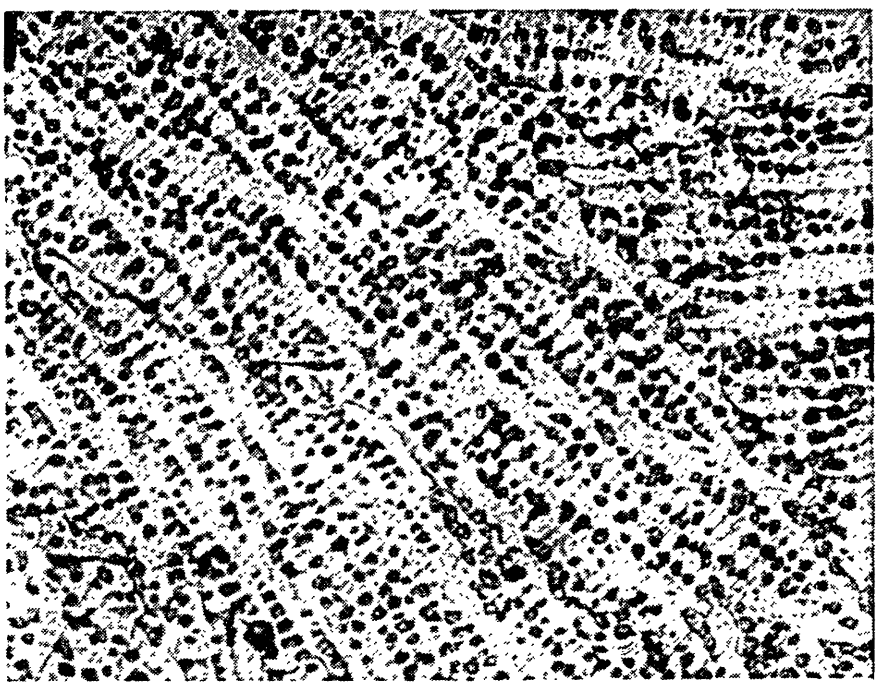

c) LB weld, 500X

Figure 29. Continue.

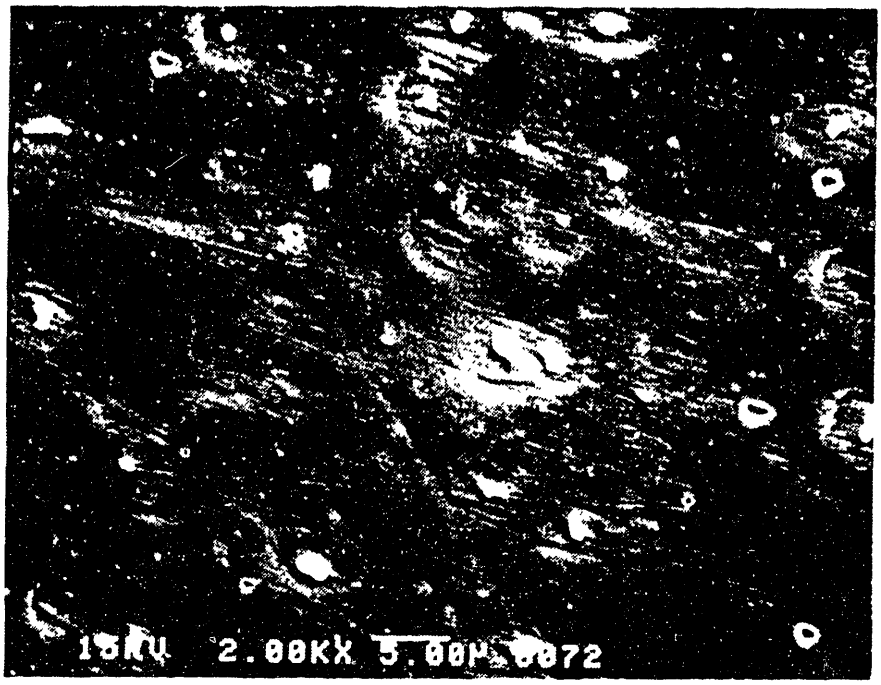

a) GTA weld, 2000X

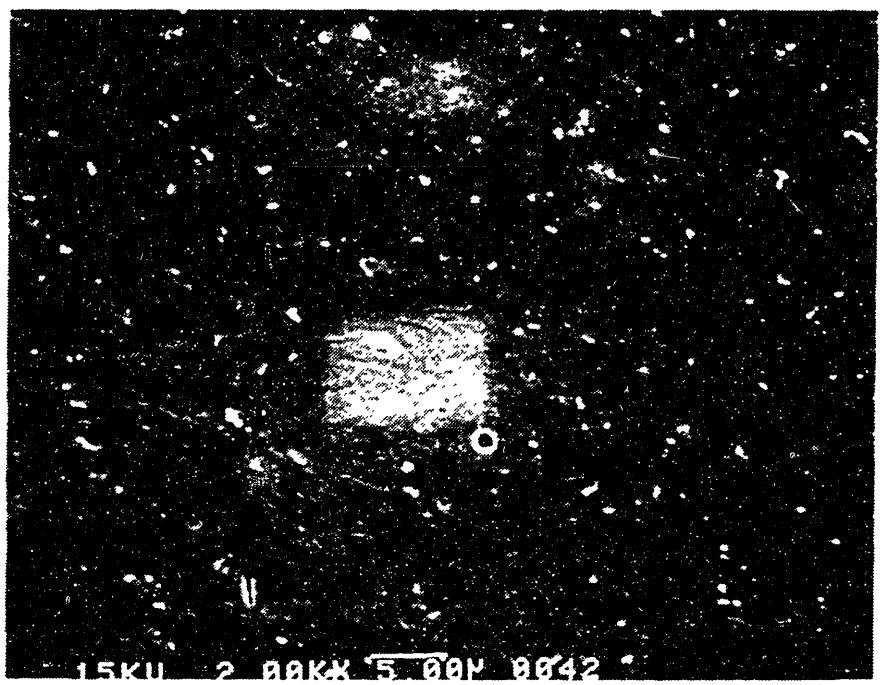

b) EB weld, 2000X

Figure 30. SEM micrographs of various fusion welds

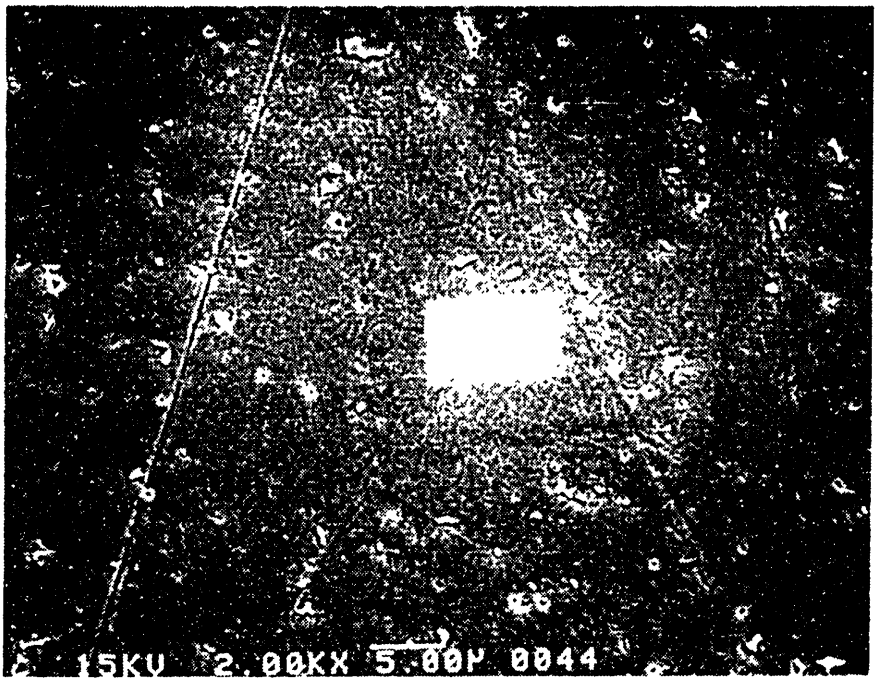

c) LB weld, 2000X

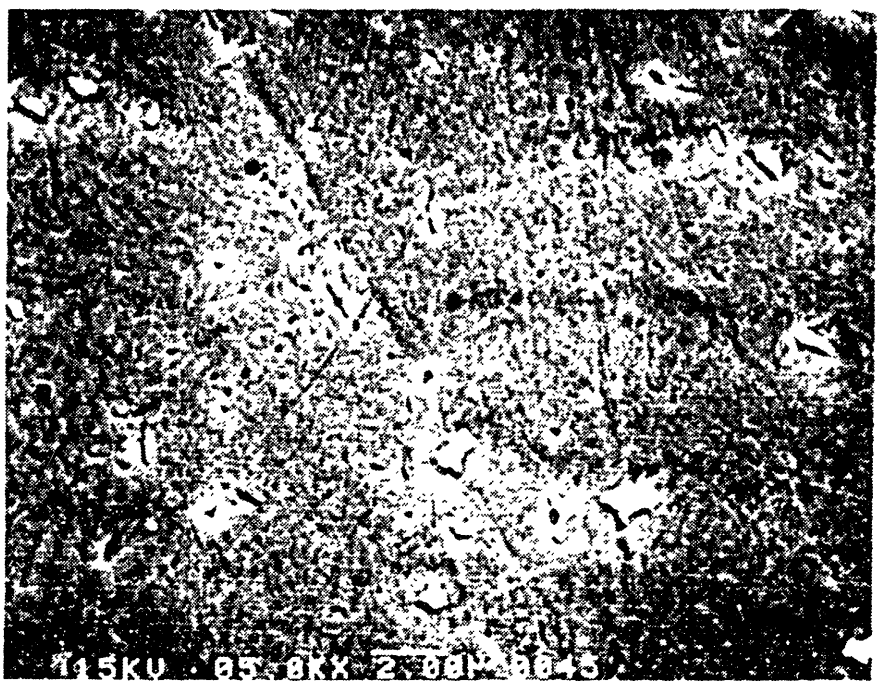

d) LB weld, 5000X

Figure 30. Continue.

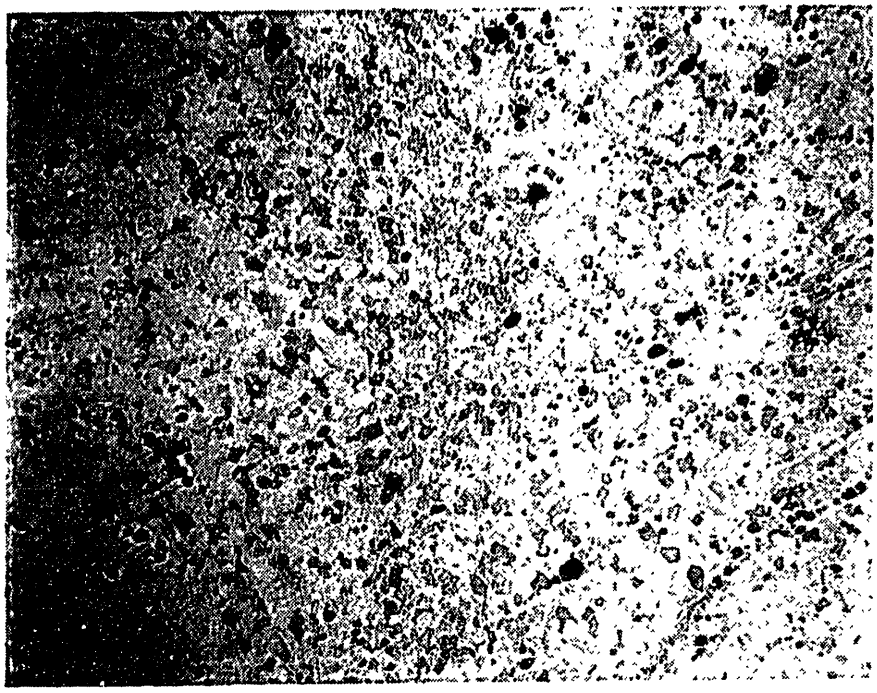

a) Optical micrograph of flash weld, 50X

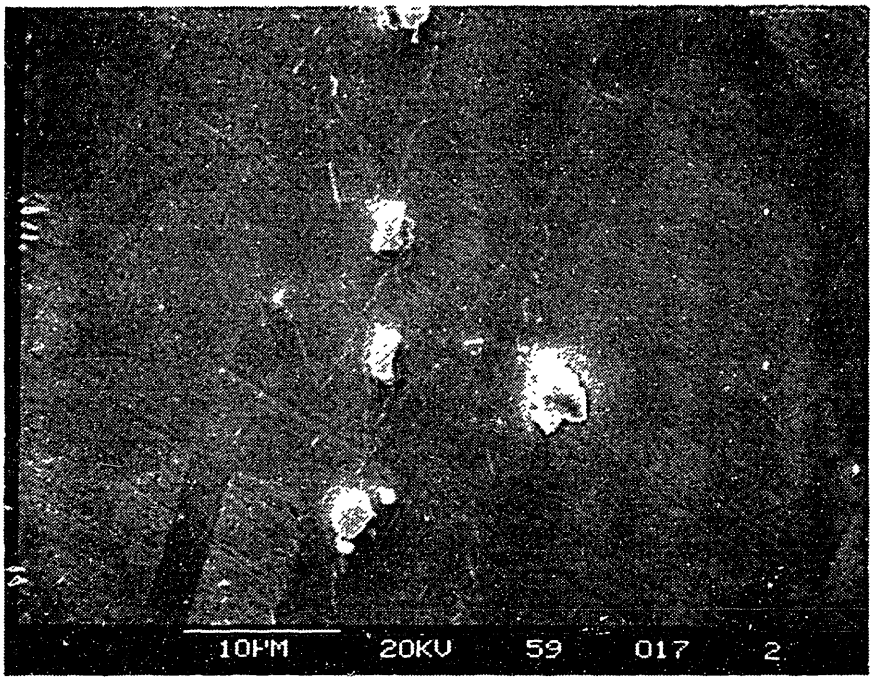

b) SEM micrograph of flash weld, 2000X

Figure 31. Optical and SEM micrographs of flash weld.

IV.1.3 Mechanical Properties of welds

A. Tensile Properties

The room temperature tensile test results are summarized in Table 10. The effect of different welding methods is relatively small in yield strength (σ_y), but significant in ultimate tensile strength (UTS). Compared to GTA welding, EB welding and LB welding results in a a slightly higher yield strength. The UTS of an EB weld is much larger than that of GTA and about the same as that of the base metal. Of the three fusion welds, EB welding shows the largest ductility.

Both of the flash weld conditions give similar tensile properties, having yield strength slightly higher than that of GTA weld and, UTS slightly less than that of base metal. The ductility of flash weld is about 10 %, similar to that of the EB weld.

B. Fatigue Crack Growth Rate and Fracture Toughness of Welds

The results of fatigue crack growth rate tests and fracture toughness tests are summarized in Table 11. The fatigue crack growth rate in EB welds, LB welds, and flash welds are much greater than that in GTA welds.

Fracture toughness of GTA welds, EB welds and LB welds show very similar values. Both of the flash welds showed very low fracture toughness, even lower than GTA weld. As in fatigue crack growth, the crack path in the fracture toughness tests propagated straight along the center of weld without forming any sizable plastic zone along the way. The existence of oxygen in the welding atmosphere does not seem to have any effects on the properties of flash welds. The similarity of properties ruled out the possible detrimental effect of fine oxide along the weld centerline.

IV.1.4 Fractography Analysis

Fracture surfaces of fusion welds are shown in Figure 32. Fracture occurs by a predominantly dimple rupture mechanism. The average dimple diameter on the GTA weld fracture surface is about 10 μm. The average size of the dimples on the surface corresponds to the dendrite arm and precipitate spacing. Within the dimples, a debris-like

fractured structure is visible along with the wavy deformation marks which have formed by slip on favorable planes during dimple growth.[66] The fracture surface of the EB weld is almost identical to that of GTA weld except for the diameter of the dimples which are about 4 μm.

Table 10. Room temperature tensile properties of various welds.

	Aging	σ_y, MPa	UTS, MPa	elongation, %
Base[a)]	650°C/200hr	1075 ± 41	1433 ± 0	16.5 ± 0.8
GTAW	650°C/200hr	1034	1306	6.9
EBW	650°C/200hr	1041 ± 1	1429 ± 4	11.3 ± 0.5
LBW	650°C/200hr	1051 ± 3	1358 ± 6	4.5 ± 0.1
FW in air	650°C/200hr	1060 ± 2	1402 ± 1	10.1 ± 0.5
FW in argon	650°C/200hr	1073 ± 22	1413 ± 16	11.3 ± 0.5

a) Data from [2]

b) Data without error are the results of one test

Table 11. Fatigue crack growth rate and fracture toughness of welds with various welding methods.

	PWHT	da/dN, mm/cy @$\Delta K = 25$ MPa$\sqrt{m}$	J_Q, KJ/m^2	K_Q (J_Q), MPa$\sqrt{m}$
GTAW	650°C/200hr	2.7×10^{-5}	72.2 ± 17.1	120 ± 14
EBW	650°C/200hr	10.5×10^{-5}	78.9 ± 20.0	125 ± 16
LBW	650°C/200hr	7.0×10^{-5}	78.8 ± 14.2	125 ± 11
FW in air	650°C/200hr	13.7×10^{-5}	37.6	87
FW in argon	650°C/200hr	-	30.2	78

* For EBW, average of 4 tests

For LBW, average of 5 tests

Only 1 test result for both of FW

The fracture surface of LB weld is different in character than that for the GTA weld and EB weld. In addition to the 5 μm diameter dimples which correspond to the precipitate spacing, numerous smaller dimples are present. Most of the tiny dimples are featureless and sometimes are part of large dimples. The relative cleanness at the dimple base indicates that the origin of these dimples is something other than precipitates within the interdendritic area. SEM micrograph of LB weld, shown in Figure 30, reveals that numerous sub-micron size defects are present along with precipitates. It is quite possible that microvoids are initiated at these defects as well as at the precipitates. Another distinctive feature of the LB weld is the existence of voids as large as 1 mm. It is likely that these voids are due to the presence of trapped argon gas from welding process. As shown in Figure 33, such voids are visible on the fracture surface even with the naked eye.

The fracture surface of a typical flash weld is shown in Figure 34 and shows rather large featureless dimples at the base. No sizable particles were found in the base of the dimples. Macroscopically, the fracture surface of the flash weld is smooth. The crack plane is well defined. On the surface of the compact tension specimen, the crack looks nearly perfectly straight without any sizable plastic zone around it, suggesting crack growth occurred with little resistance.

IV.1.5 Summary and Discussion

Various welding techniques were used to evaluate mechanical properties of alloy 908 welds. With high speed, high power density welding processes, such as EB welding and LB welding, much finer weld microstructures have been achieved. Within the dendritic structure, precipitates, mostly cubic MC carbide and hexagonal Laves phase are formed in the interdendritic region. Macroscopically, compared to the rather irregular weld microstructure of multi-pass GTA welds, high energy density welding methods, such as EB weld and LB weld form deep narrow welds with a center symmetric dendritic structure. The LB weld microstructure shows a similar dendritic spacing to that of EB weld. However, the mechanical properties are much degraded with much lower UTS and ductility. The LB weld contains large pores containing argon gas. There are also a number of unidentifiable micro-defects within the fusion zone. These defects cause premature failure during tensile testing and resulted in poor ductility.

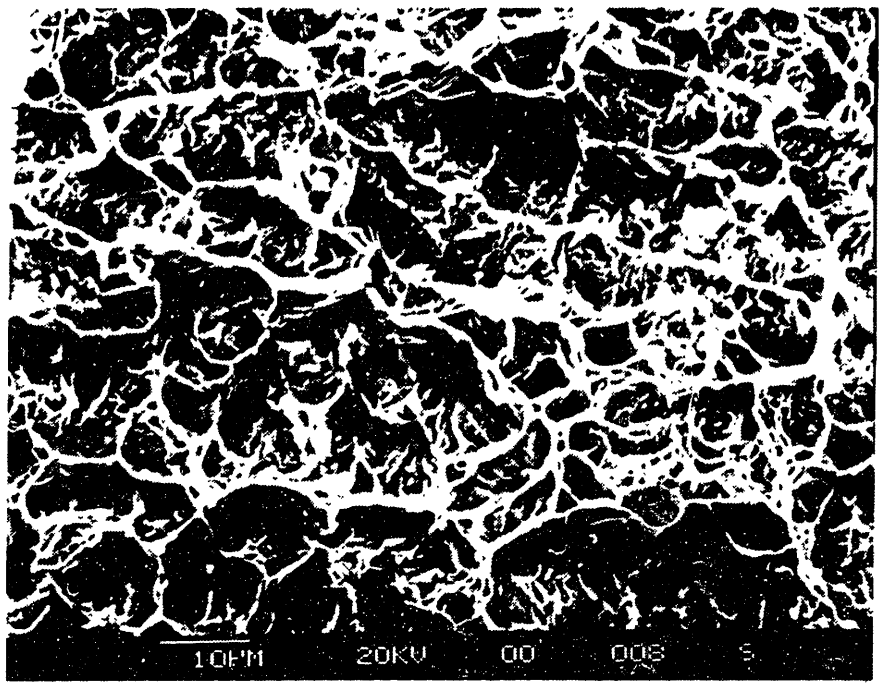

a) GTA weld, at 1000X

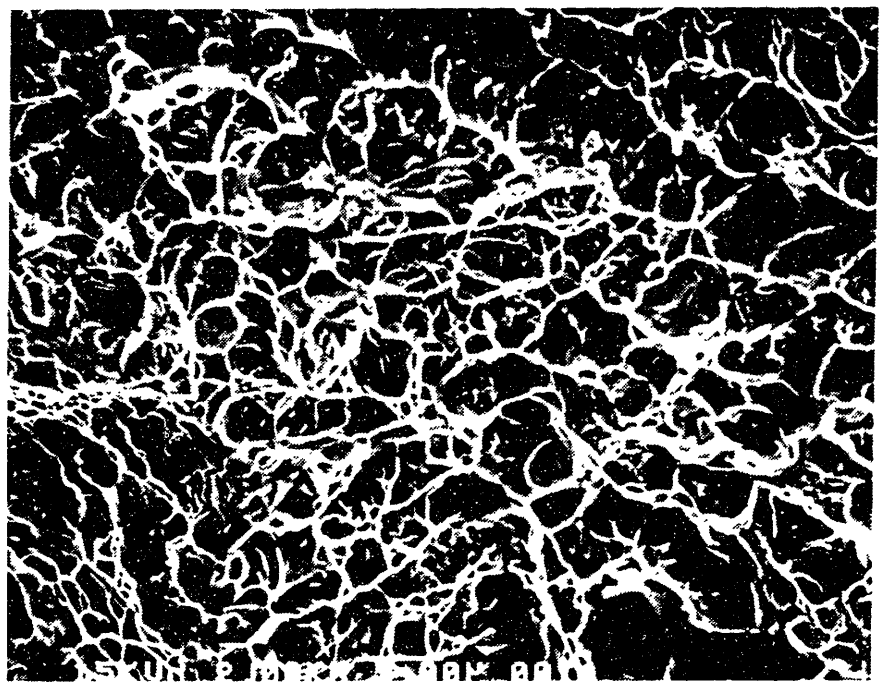

b) EB weld, at 2000X

Figure 32. Fracture surfaces of various fusion welds.

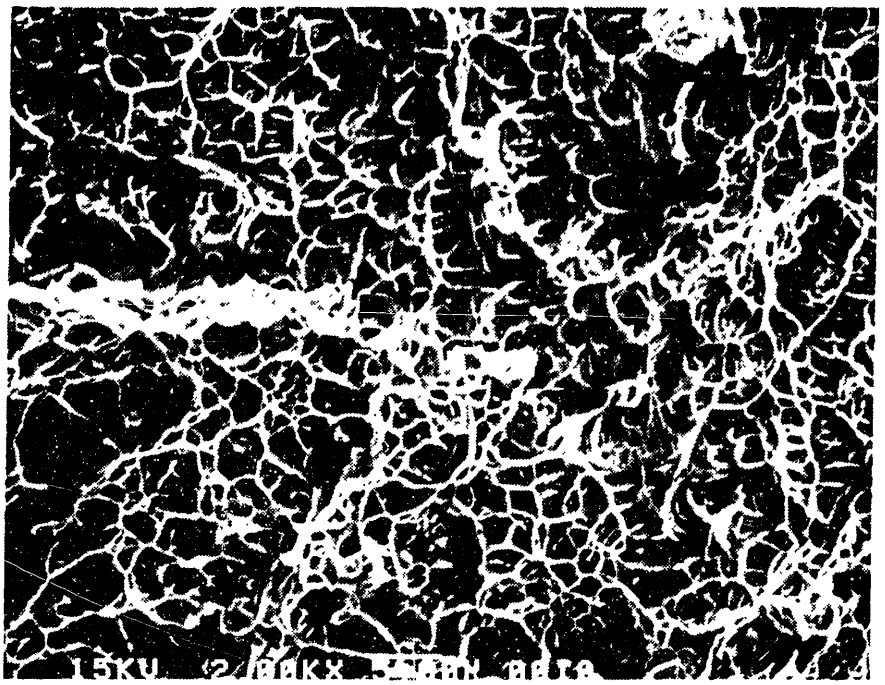

c) LB weld, at 2000X

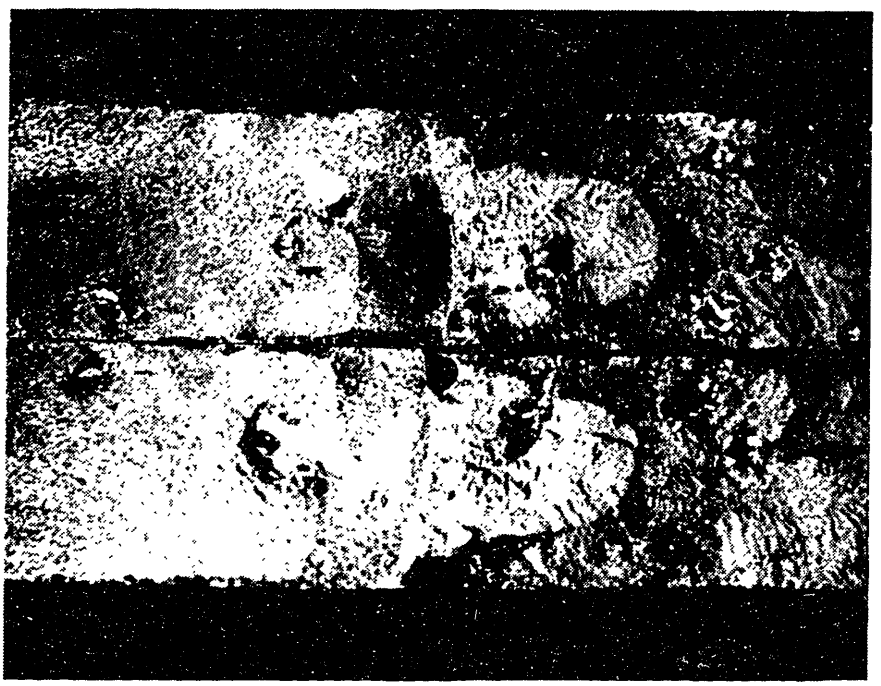

Figure 33. Fracture surface of LB weld at 5X, showing pores on the surface.

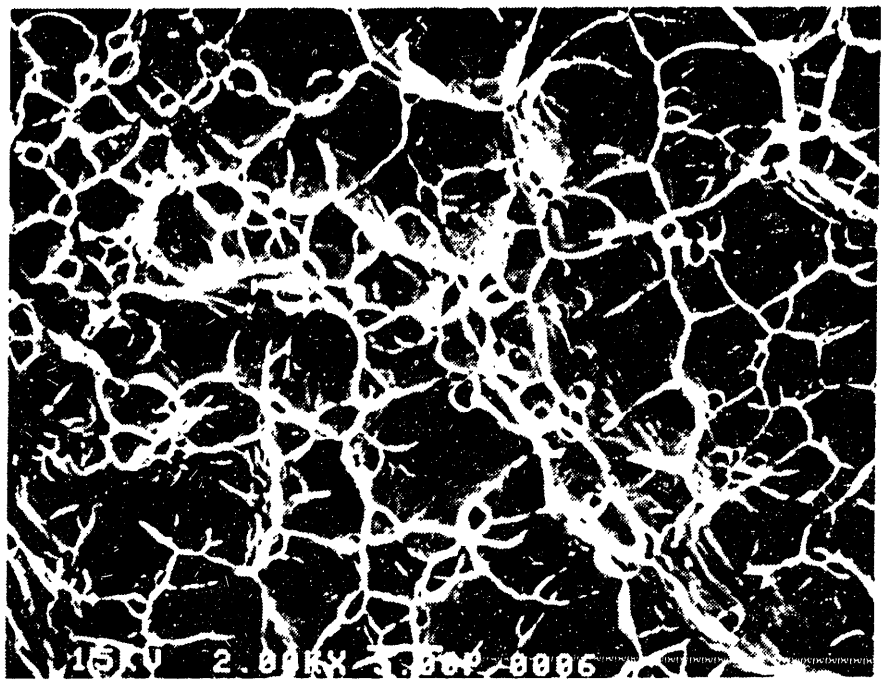

Figure 34. Fracture surface of flash weld.

The high crack growth rate in EB welds and LB welds can be attributed to the symmetric dendritic microstructure. In manual-GTA welding, the subsequent weld beads are not exactly deposited on the same position as the previous weld bead. The dendrite orientation in each weld beads thus tend to be different from that of the previous one. The resulting dendritic microstructure is rather irregular in orientation. In EB welding and LB welding, the dendritic orientation becomes symmetric along the weld centerline leaving a well defined boundary. This boundary stretches from the root to the face of weld. Thus, a crack can propagate without any crack front adjustment which is needed in multi-pass GTA weld where the weakest plane changes in adjacent grains. The absence of microscopic crack deviation resulted in a larger crack growth rate in the EB and LB welds.

The fracture toughness of LB welds is about the same as that of EB welds. However, the existence of macroscopic pores caused intermittent pop-in during the J-integral test. The fracture surface of LB welds shows much finer dimple distribution than that of a EB weld. Unlike EB welding, most of the dimples seem to have originated at the micro-defects rather than at the precipitates.

The fracture surface of flash welds shows a dimple rupture fracture mechanism. The origin of microvoids, however, can not be identified. During welding, the external upset pressure results in the formation of characteristic flow lines around weld along which some of the carbides are aligned. The number density of carbides is not high enough to explain the smoothness of the fracture surface. A more plausible explanation could be the preferential crack growth along the already weakened plane perpendicular to the upset direction. When the crack tip is aligned to one of these planes, it would propagate quickly without resistance, resulting in low fracture toughness. The high fatigue crack growth rate observed can be explained by the same mechanism. The fatigue crack growth rate of flash welded alloy 908 has been reported by Nyilas et al.[67] He reported much lower fatigue crack growth rate than in the present study. It is unclear why there is such a discrepancy. The presence of oxygen in environment has no appreciable effects on the overall mechanical properties of the flash weld.

The strength, fracture toughness and elongation of welds are plotted in the same graph in Figure 35. All of the welds show at least 1030 MPa yield strength and 1300 MPa ultimate tensile strength. Apparently, there is no difference in fracture toughness for the different fusion welding methods. Flash weld showed improved strength and ductility but resulted in far worse fatigue and fracture properties.

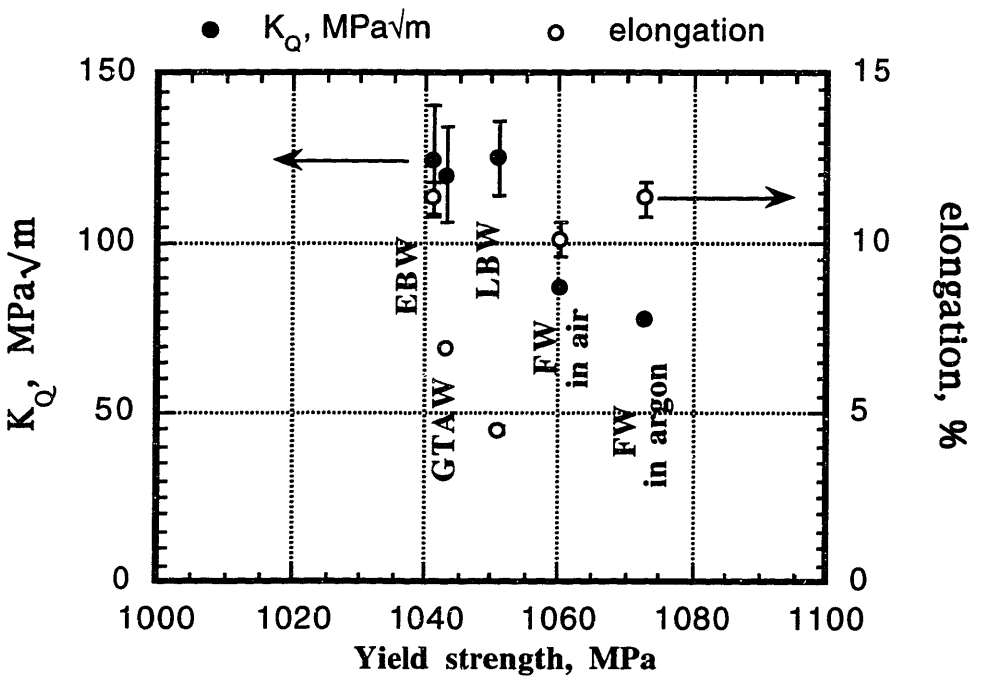

Figure 35. Strength-toughness-ductility plot of various welds.

IV.2 Post Weld Heat Treatment

IV.2.1 Microstructure of homogenized welds

The optical microstructure of as welded GTA welds and homogenized at 1050 °C for various times are shown in Figure 36. In the as welded condition, the dendritic microstructure dominates the weld fusion zone. At the homogenization temperature, 1050 °C, the dendritic structure starts to disappear at as early as 5 minutes. In some interdendritic zones, precipitates also start to disappear. After 10 minutes, the dendritic structure is weakened further, and twinned grains are visible. After 30 minutes, the dendritic structure is barely visible and a regular grain structure is clearly visible in the fusion zone. After 1 hour, the dendritic structure has completely disappeared, leaving behind sparsely distributed precipitates and a well defined grain structure. There is a lot of variation in the grain size with extensive annealing twins. Thus, after a homogenization heat treatment for 1 hr, the dendritic microstructure has been replaced with a recrystallized structure.

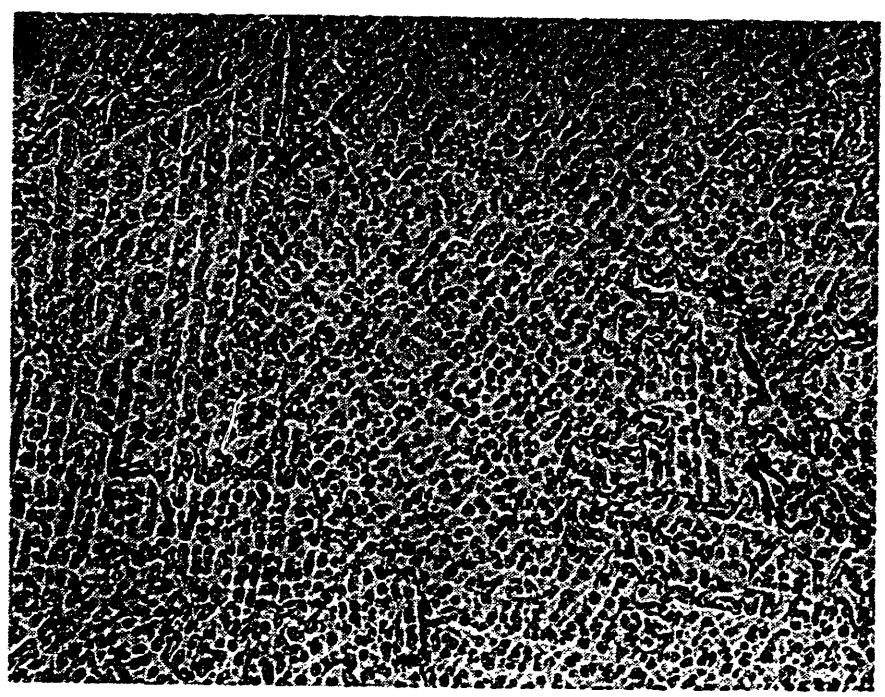

a) As welded, 200X

Figure 36. Evolution of microstructure of GTA weld using 908 filler during homogenization heat treatment at 1050°C.

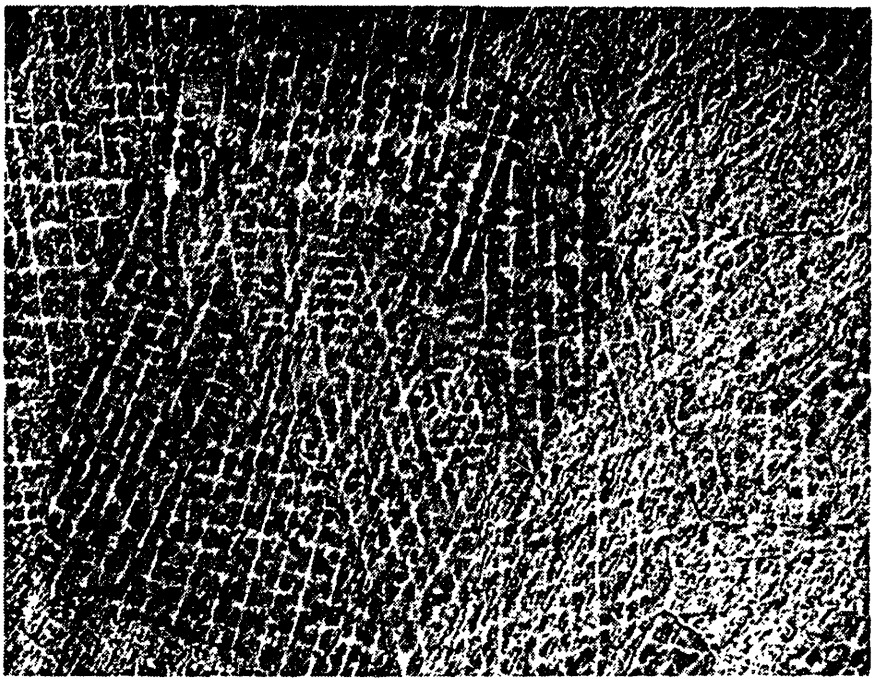

b) After 5 minutes at 1050°C, 200X

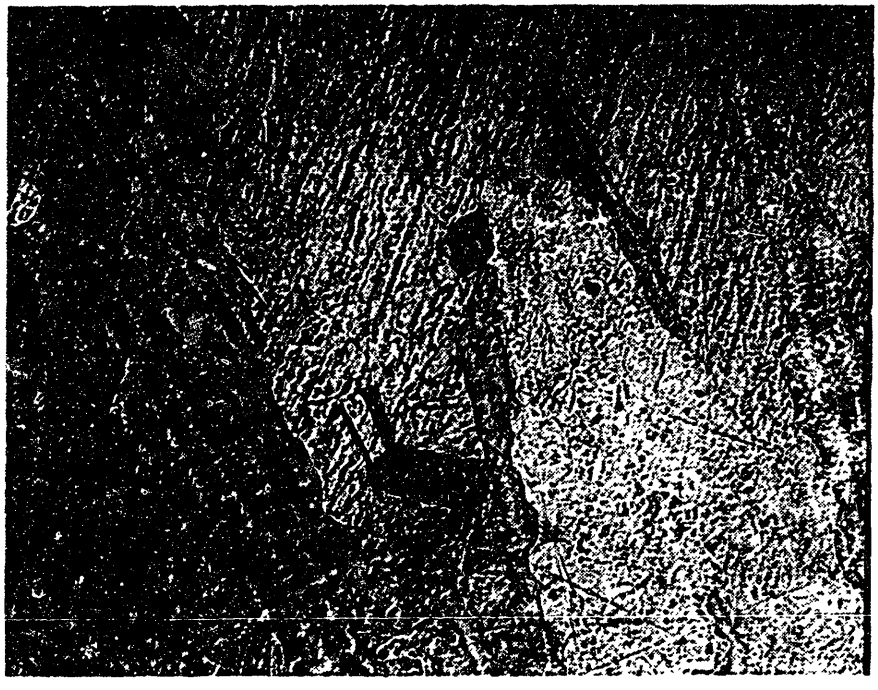

c) After 10 minutes at 1050°C, 200X

Figure 36. Continue.

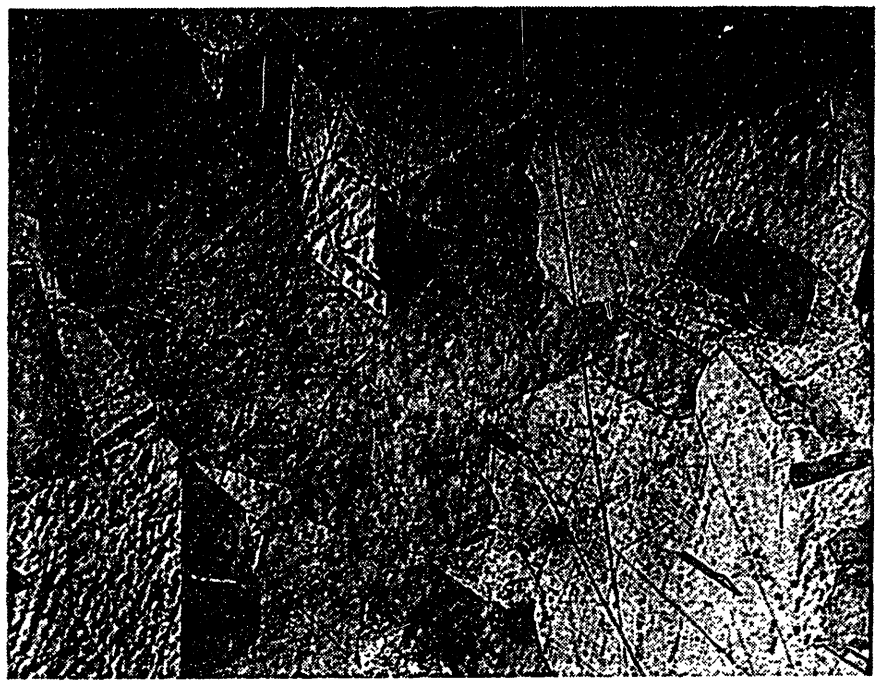

d) After 30 minutes at 1050°C, 200X

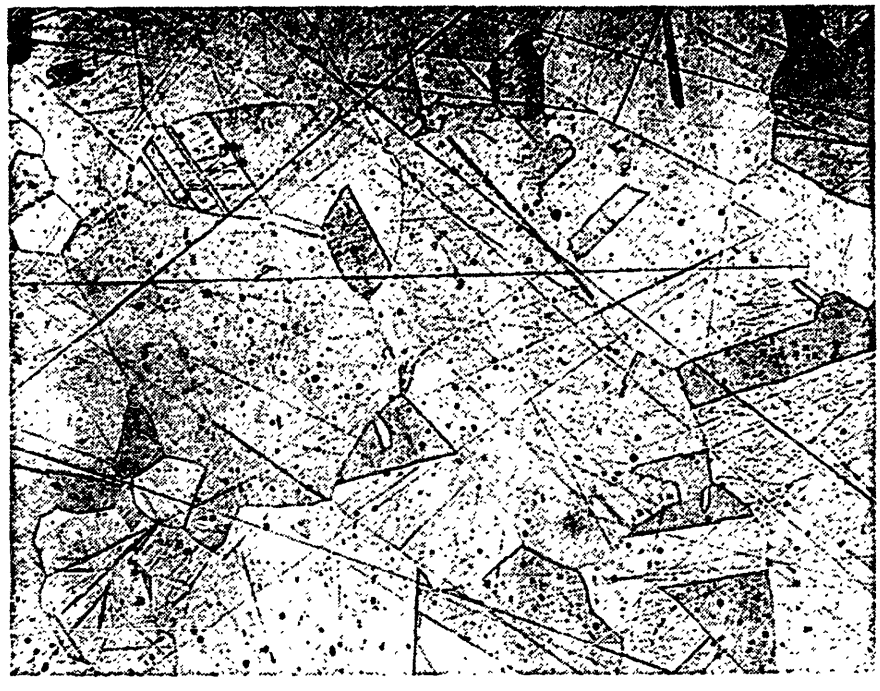

e) After 1 hour at 1050°C, 200X

Figure 36. Continue.

SEM micrographs of as welded GTA weld are shown in Figure 37. (for comparison purpose, Figure 30-a) is again used as Figure 37-a)) Precipitates with various shapes are present in the interdendritic zones which are deeply etched. The chemical composition of the precipitates are mostly one of the two Nb-rich phases commonly found in Nb-containing superalloys. The results of EDS analysis of extracted particles are summarized in Table 12. One class of the precipitates has about 35 % Nb, 37 % Ni, 22 % Fe with 2 % Si and is thought to be hexagonal Laves phase. The other has about 86 % Nb and 13 % Ti with trace amounts of other elements. The most clear difference in the chemical composition of Laves and MC carbide is the existence of Si in Laves phase and its virtual absence in MC carbide. The partition of Si into Laves phases is well documented in various alloy systems and the results of this study are consistent with results on other 900-series alloys.[39, 47] Also shown are the results of chemical composition analysis around precipitates, and in the interdendritic area free of precipitates. The chemical composition of these areas represent the composition of eutectic γ which separated from the precipitates during the final stages of solidification.

There is no clear morphological difference between Laves and MC carbide formed in the weld fusion zone. However, occasionally, MC carbides with clearly cubical shape are observed as shown in Figure 37-b). On the same micrograph, the identity of precipitates are shown. The L and MC represent Laves phase and MC carbide, respectively. In some of the interdendritic zones, more than one type of precipitates are present, as shown in Figure 38, which is the magnified micrograph of the Figure 37-a). Laves and MC carbides precipitate side-by-side without a clear boundary between them.

After a homogenization heat treatment for 1 hour, Laves phases have disappeared and only MC carbides were detected in the extraction. This is illustrated in the SEM micrograph of the weld, shown in Figure 39. The amount of precipitate has decreased substantially. EDS analysis of all of the precipitates confirmed their identity as MC carbides. Again there are no distinctive morphological characteristics between the carbides.

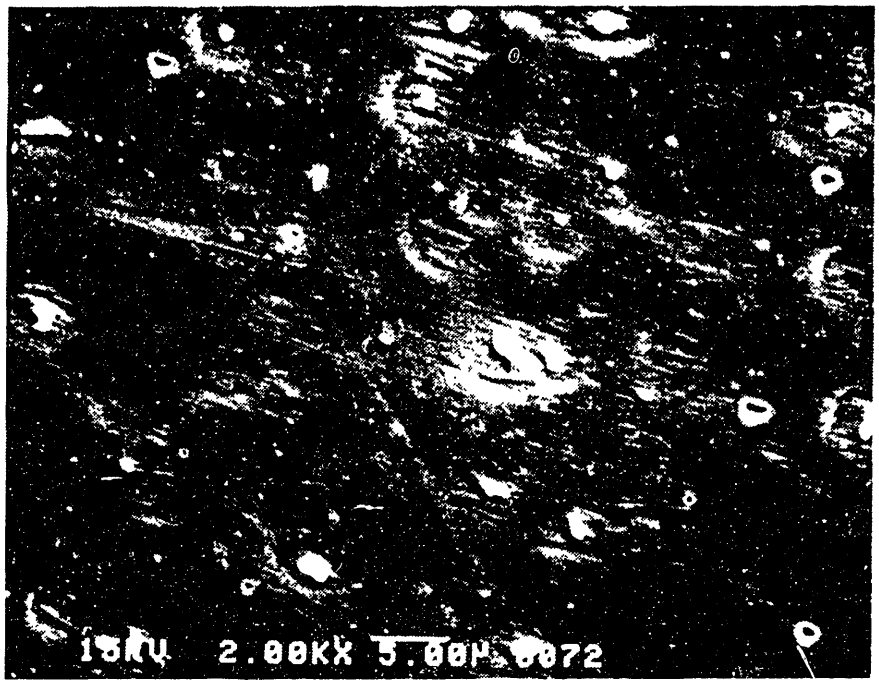

a) As welded, 2000X

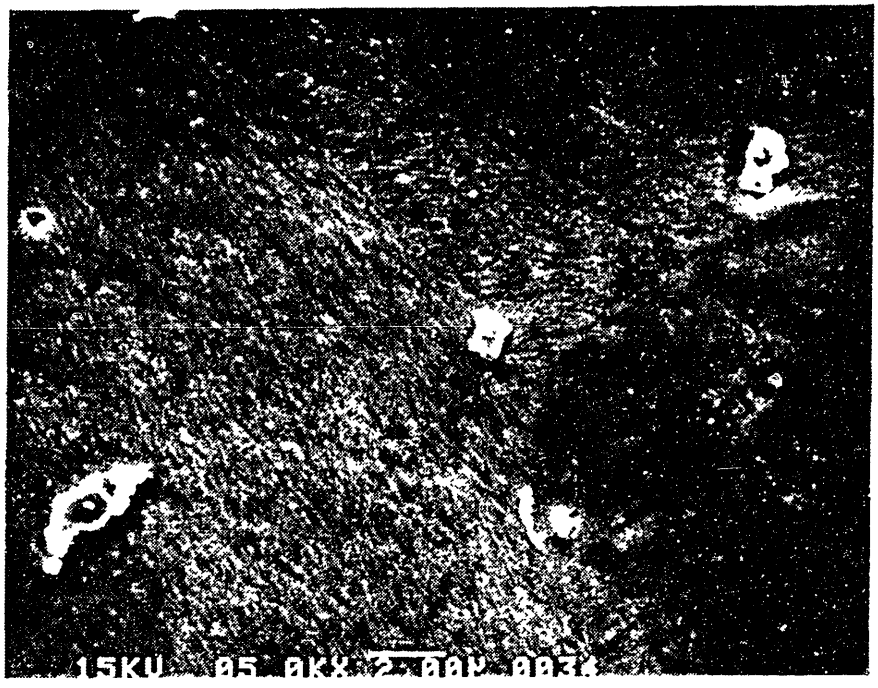

b) As welded, 5000X

Figure 37. Precipitates in the as welded GTA weld using 908 filler weld. Both Laves (L) and MC carbides (MC) are shown.

Table 12. Chemical composition of precipitates found in GTA weld using 908 filler, in as-welded condition and after homogenization heat treatment. (in weight percent)

		Fe	Ni	Cr	Nb	Al	Ti	Si
908-GTAW AW	Laves	21.5	37.3	.3	35.5	0.1	2.5	1.9
	eutectic γ	33.7	48.2		10.0	1.3	2.7	0.4
	dendrite core	43.8	47.0	4.9	1.6	1.4	0.9	0.3
	NbC	0.1	1.2	0.0	85.8	0.1	12.7	0.1
	(Nb,Ti)C		2.2		67.2		30.6	
908-GTAW AW + HT	NbC	0.8	0.9	0.5	83.5	0.3	14.0	0.0

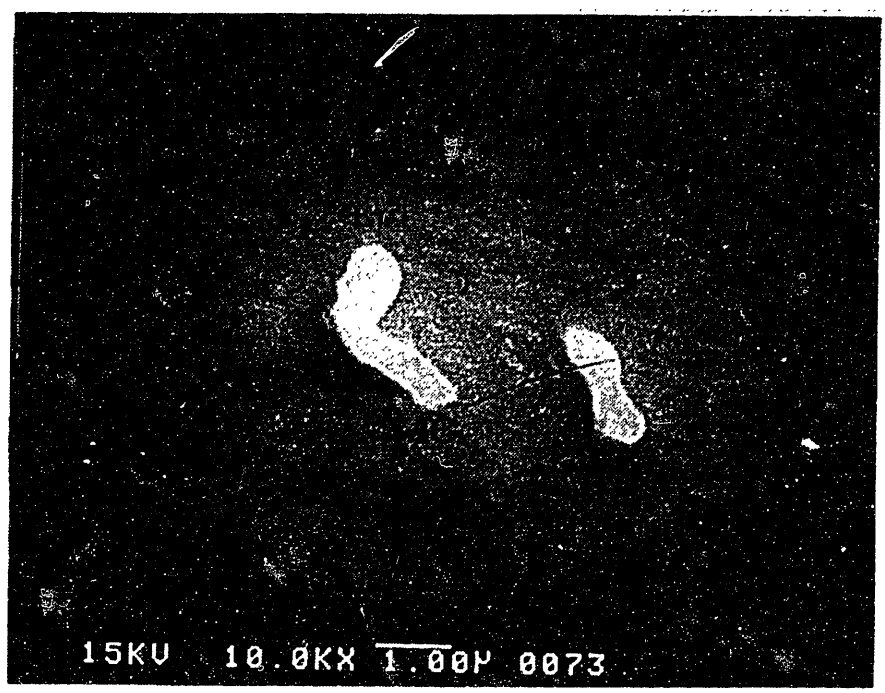

Figure 38. Precipitates in as welded GTA weld using 908 filler, showing side-by-side precipitation of Laves and MC carbide.

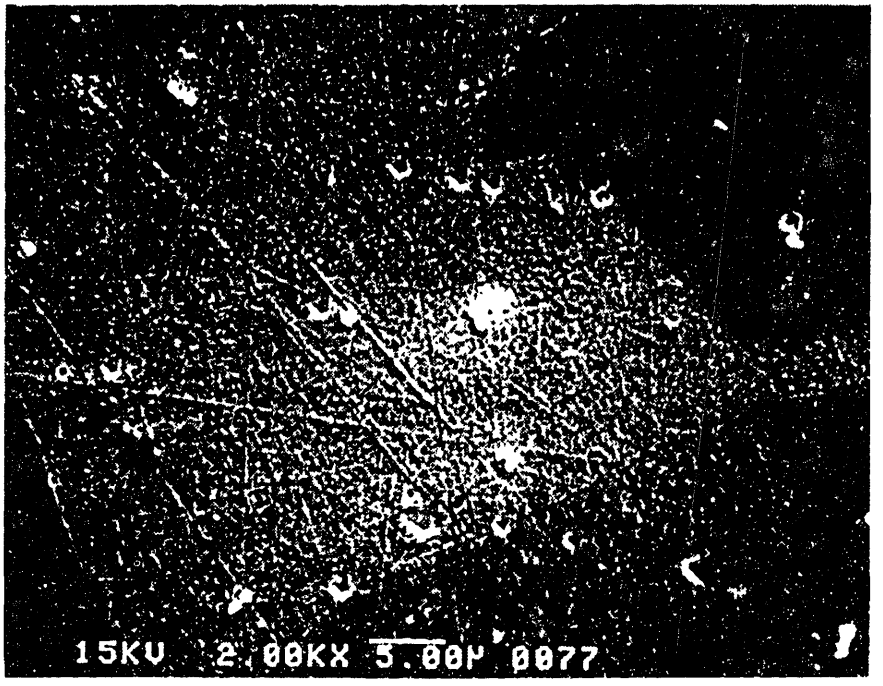

a) At 2000X

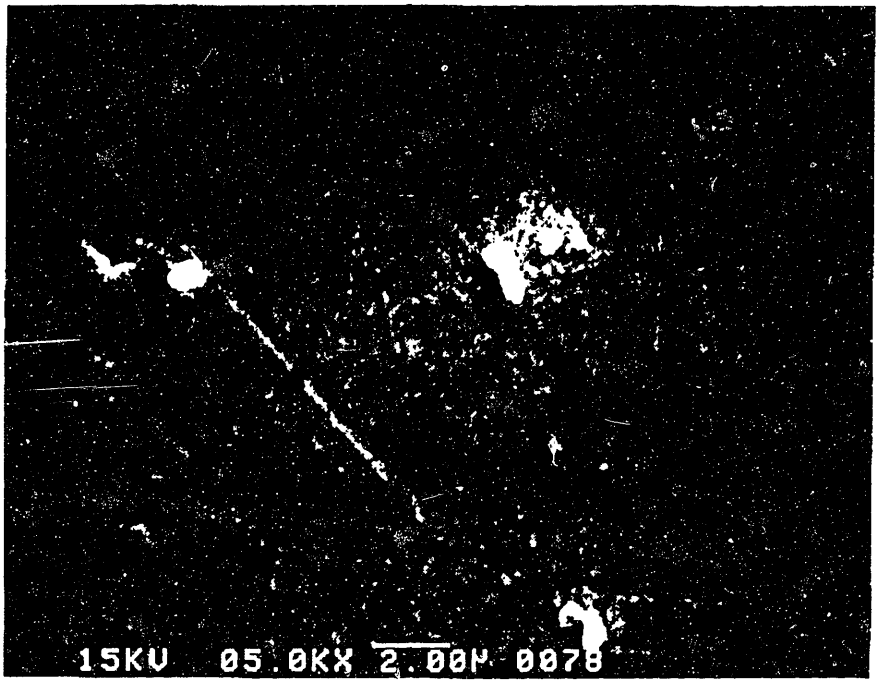

b) At 5000X

Figure 39. SEM micrographs of homogenized GTA weld using 908 filler. All precipitates are MC carbides.

IV.2.2 X-ray Diffraction Analysis of Precipitated Phases

X-ray diffraction patterns of the particles extracted from the as welded GTA weld using 908 filler, and after homogenization heat treatment (1050°C/1hr) are shown in Figure 40. The diffraction planes and corresponding d-spacings are summarized in Table 13. Some strong peaks representing $(Fe,Ni)Fe_2O_4$ are observed when the amount of the extracted particles are small. Oxide could have been formed during the extraction process by electrochemical oxidation of the Ni-Fe matrix exposed to the solution. Crystal structure and lattice parameters of phases were determined by using standard phase identification methods.[68] The results are summarized in Table 14. Two distinctive phases were identified in the as welded condition. One of them is a hexagonal phase with lattice parameter of a = 4.77 Å and c = 7.76 Å. It is thought to be $MgZn_2$-type Laves phase considering chemical composition. The other is a cubic (Nb,Ti)C carbide with lattice parameter of 4.43 Å and 4.41 Å. MC with larger lattice parameter is thought to be Nb-rich carbide, whereas MC with smaller lattice parameter is Ti-rich MC carbide whose chemical compositions are shown before in Table 12. After a homogenization heat treatment, the peaks representing Laves phase have disappeared and only the peaks representing MC carbides are left behind. The lattice parameters of these phases are closely related to those of the phases formed by solid state diffusion during aging even though the stoichiometry of the solidification precipitates are different.[33]

IV.2.3 Hardness Measurement of Welds

The results of Vickers microhardness measurements on GTA welds are shown in Figure 41 as function of post weld heat treatment. In the as-welded condition, hardness is about 250 VHN for GTA welds. When heat treated, the reduction of hardness are the same at both 980 °C and 1050 °C until 5 minutes. As the time increases, the hardness of weld decreases at 1050 °C, but does not change at 980 °C. At 1050 °C, the hardness barely changes after 30 minutes. After 1 hour heat treatment, the hardness is 220 VHN for 980 °C solution annealing treatment, and 175 VHN for 1050 °C homogenization treatment.

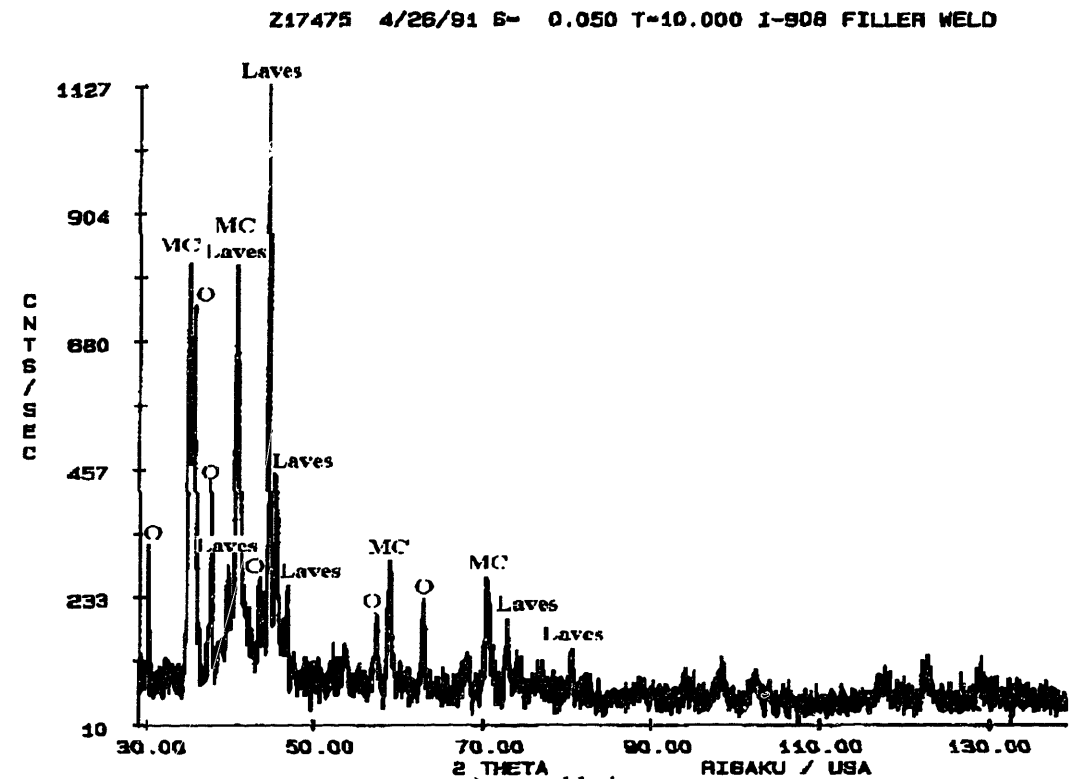

a) as welded

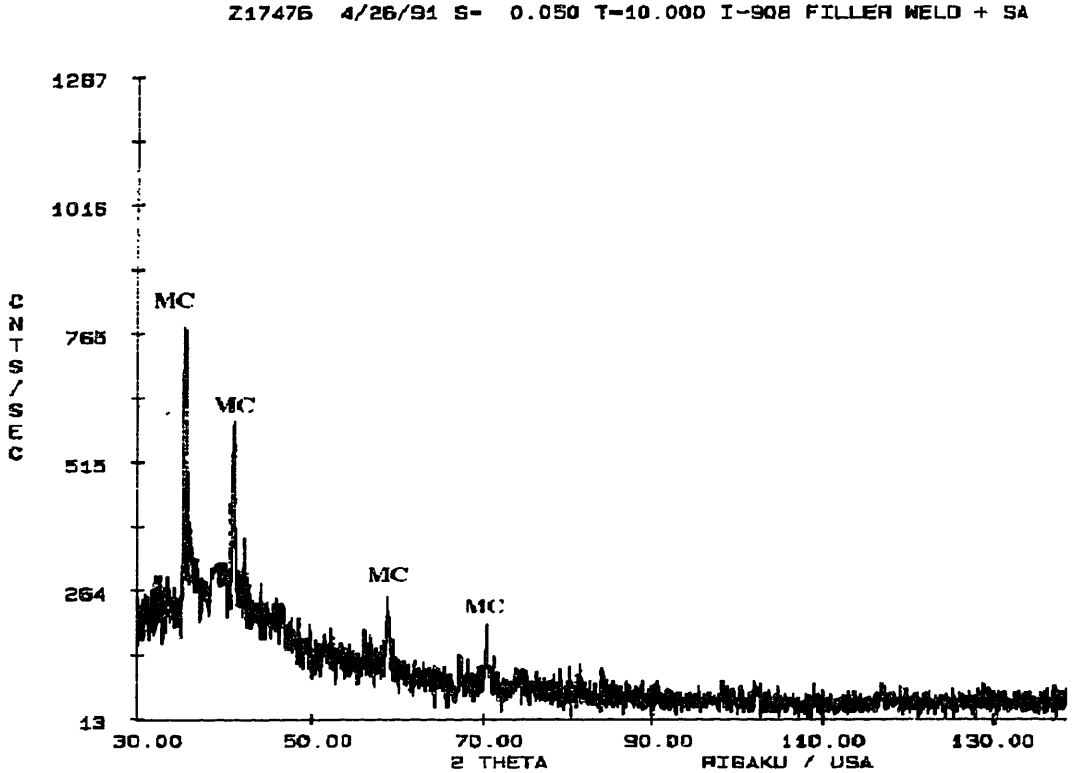

b) after homogenization

Figure 40. X-ray diffraction patterns of extracted particles from the GTA weld using 908 filler.

Table 13. Peaks found in XRD on extracted particles within weld

908-GTAW				908-GTAW			
As weld				Homogenized 1050°C/1hr			
d-spacing, Å	I/Io	phase	hkl	d-spacing, Å	I/Io	phase	hkl
2.5566	52	NbC	111	2.5524	100	NbC	111
2.5475	72	TiC	111	2.5405	62	TiC	111
2.3811	38	Laves	110				
2.2150	69	NbC	200	2.2176	74	NbC	200
2.2072	72	TiC	200	2.2062	77	TiC	200
2.1995	53	Laves	103				
2.1944	46	Laves	103				
2.0269	100	Laves	112				
2.0002	38	Laves	112				
1.9927	38	Laves	201				
1.9395	22	Laves	004				
1.5643	26	NbC+TiC	220	1.5643	29	NbC+TiC	220
1.3363	23	NbC+TiC	311	1.3346	25	NbC+TiC	311
1.2965	18	Laves	302				
1.1922	12	Laves	220				

Table 14. Lattice parameters of precipitates found in GTA weld using 908 filler.

Precipitates	Carbides	Laves
Structure	FCC	$MgZn_2$ type
lattice parameters, (A)	**a** = 4.43 (NbC) **a** = 4.41 (TiC)	**a** = 4.77, **c** = 7.76

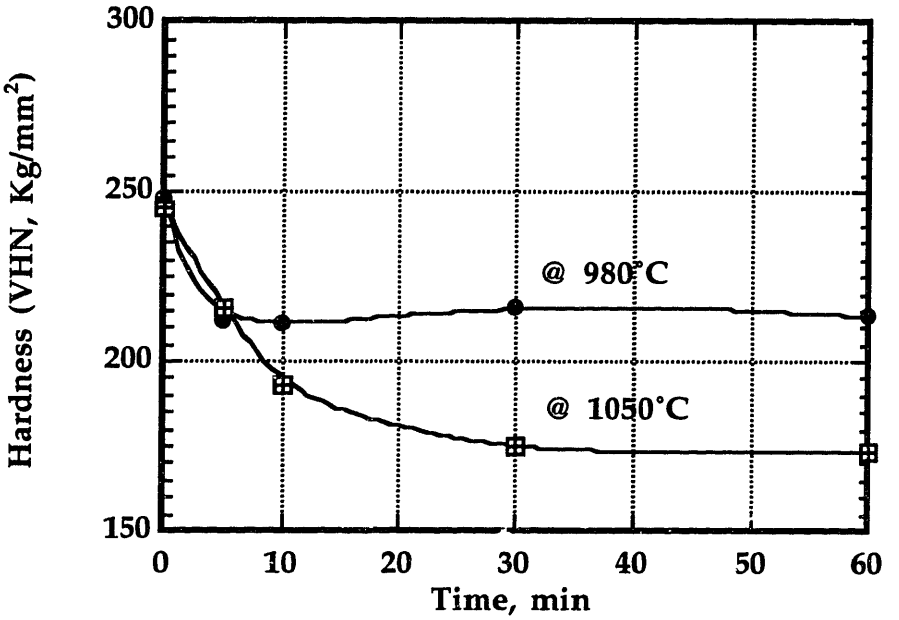

Figure 41. Microhardness of post weld heat treated GTA weld using 908 filler

VI.2.4. Mechanical Properties

A. Tensile Properties

The results of room temperature tensile tests for aged welds are summarized in Table 15. With the standard aging condition of 650°C/200hr in vacuum, the homogenized EB weld exhibits lower strength and ductility than the solution annealed EB weld. For the same homogenization heat treated EB weld, the 700°C/100hr aging heat treatment showed much higher strength than the materials aged at 650°C/200hr without losing ductility. Both the yield strength and ultimate tensile strength are about 140 MPa higher when aged for 100 hour at 700°C. This suggests that the 650 °C/200 hrs aging condition is not the optimum heat treatment for strengthening of a solution annealed or homogenized weld.

One of the GTA welds with new filler, GTA weld using 9FA filler (9FA-GTAW), was also homogenized and aged. It showed slightly higher strength and much improved ductility than that for a homogenized EB weld.

Table 15. Room temperature tensile properties of various welds. (Average of two tests)

	PWHT	Aging	σ_Y, MPa	UTS, MPa	elongation, %
EBW	980°C/1hr	650°C/200hrs	906±4	1291±3	15.3±0.5
	1050°C/1hr	650°C/200hrs	839±7	1175±29	11.8±1.7
	1050°C/1hr	700°C/100hrs	981±17	1321±18	11.8±1.3
9FA-GTAW	1050°C/1hr	650°C/200hrs	860	1210	15.6

B. Fatigue Crack Growth Rate and Fracture Toughness of Welds

The results of fatigue crack growth tests (with R = 0.1) are shown in Figure 42. Generally, the fatigue crack growth rates in homogenized welds are less than those of non-homogenized welds. The power law exponents in Paris' equation are about 4 in both cases.

The results of the fracture toughness tests are summarized in Table 16. In the table, the minimum thickness required for valid plane strain fracture toughness (thickness » $25J_Q/\sigma_Y$) measurements are shown. For both the solution annealed and homogenized EB weld, the fracture toughnesses are so high that the thickness requirement for a valid J-integral test was not satisfied. The thickness of the specimens were within the range of from 5 to 7 mm, which is far less than needed for plane strain fracture toughness testing of homogenized EB weld and solution annealed EB weld. Still, based on the thickness of the specimen to satisfy thickness requirement (about 5mm of thickness corresponds to 200 MPa$\sqrt{m}$), it can be conservatively estimated that the fracture toughness of the welds are at least 200 MPa$\sqrt{m}$. Homogenized GTA welds using 9FA filler showed fracture toughness of about 195 MPa$\sqrt{m}$.

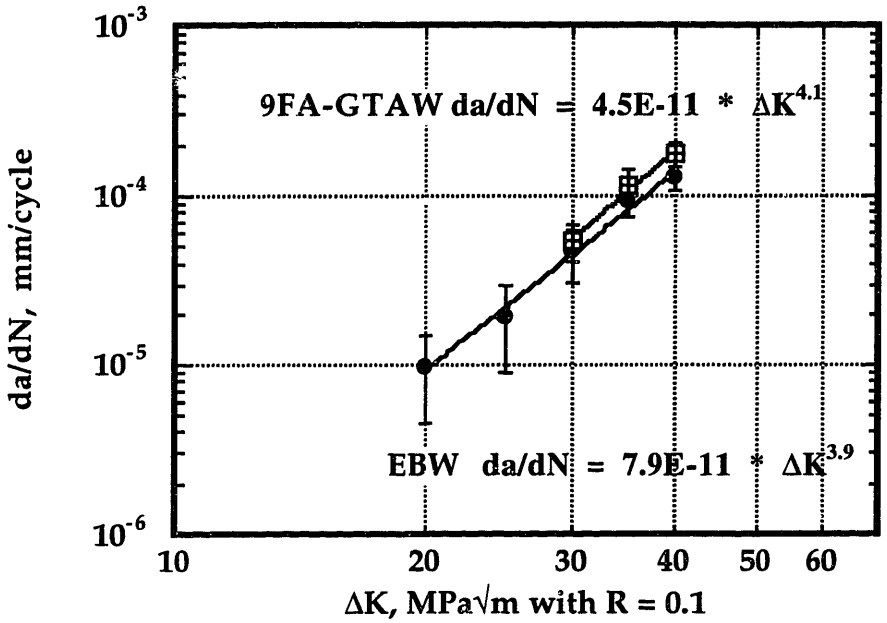

Figure 42. Fatigue crack growth rate welds after homogenization heat treatment.

Table 16. Room temperature fracture properties of the post weld heat treated welds.

	PWHT	Aging	J_Q, KJ/m^2	$25J_Q/\sigma_Y$, mm	K_Q, MPa√m
EBW	980/1hr	650°C/200hrs	337±28	>7.7	259±11
	1050°C/1hr	650°C/200hrs	585±3	>14.5	342±1
9FA-GTAW	1050°C/1hr	650°C/200hrs	193±58	>4.7	194±30

IV.2.5 Fractography of homogenized welds

The fracture surface of a homogenization heat treated GTA weld using 9FA filler is shown in Figure 43. The fracture surface is typical of a ductile dimple rupture mechanism. At the base of the dimples, sub-micron size particles from which microvoids were initiated, are

visible. These particles are rich in either Nb or Ti as confirmed by EDS analysis. Due to the geometric complexity, and small size of the particle, the exact composition could not be determined. Based on analysis of particles from the homogenized GTA welds using 908 filler, which has an almost identical chemical composition, the particles are thought to be cubic MC carbide rich in either Nb or Ti left behind after the homogenization heat treatment. The presence of extensive deformation marks within the dimple also implies, qualitatively, high toughness.

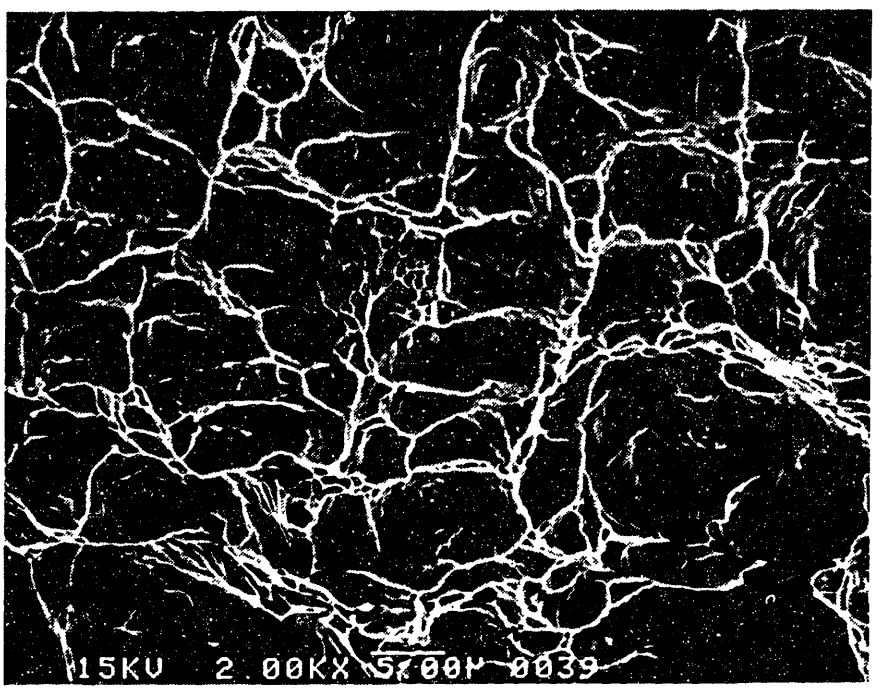

Figure 43. Fracture surface of J-integral tested GTA weld using 9FA filler + 1050°C/1hr + Aged (650°C/200hrs) material.

IV.2.6 Summary and Discussion

Various options of post weld heat treatment have been investigated. If the weld is heat treated directly after welding, both solution annealing and homogenization heat treatments decreases hardness significantly within 5 minutes. The hardness continues to decrease during the homogenization heat treatment.

Microscopically, the dendritic structure of weld almost disappears after the 1050°C/1hr heat treatment. Recrystallization is completed at the same time. The homogenization process

also eliminates hexagonal Laves phase from the weld, leaving only cubic MC carbides. This is confirmed by both EDS and X-ray diffraction analysis.

The effects of post weld heat treatment are generally, to increase fracture toughness and ductility with lower strength compared to directly aged welds. After an aging treatment at 650 °C/ 200hrs, a solution annealed weld shows higher strength and ductility than a homogenization heat treated weld. For a homogenization treated weld, 700 °C/100hrs aging resulted in higher strength than 650 °C/ 200hrs aging. Fracture toughness of post weld heat treated welds are at least 200 MPa$\sqrt{m}$ at room temperature.

IV.3 New Weld Filler Metals

IV.3.1 Microstructure of New Welds

The microstructure of the GTA welds using new filler metals are shown in Figure 44. The region shown is the center of the weld fusion zone in each case. Cellular-dendritic microstructure with interdendritic segregation and precipitation is apparent in all GTA welds. The amount of precipitates in the interdendritic zone decreases gradually as the Nb content of the filler changes from 3 % (9FA filler) to 0.5 % (9HA filler). Qualitatively, both the number density and size of the precipitates decreases simultaneously. Between the primary dendrites, numerous regions of segregation, formed from liquid trapped by the secondary dendrite arm, emanated from the primary dendrite. The spacing between the secondary dendrite is about 10 μm in all of the GTA welds. The dendritic spacing is known to be governed by the thermal properties rather than small differences in the chemical composition.[23] None-the-less, small changes in thermal properties, such as the liquidus and solidus temperature, can be expected due to the compositional differences. Thermal conductivity which determines the cooling rate of the weld is not effected by compositional variation.

At higher magnification, shown in Figure 45, the differences between the high-Nb and the low-Nb welds becomes clear. The precipitates in high-Nb welds are larger and located in the larger interdendritic zone. Randomly shaped precipitates are mostly formed as isolated eutectic rather than the lamellar eutectic structure. In some areas, several isolated precipitates are formed from the same final eutectic liquid. Two general chemical composition were detected by EDS analysis. One of them is close to the Laves phase composition, the other is close to MC carbide composition. In the low-Nb weld, the precipitates are more sparsely distributed and smaller in size. The interdendritic areas are also small and not connected to each other. All of the precipitates in the low-Nb weld exhibit the MC carbide composition.

Chemical composition of precipitates were determined by EDS analysis using an extraction replica taken from the weld area. The results are summarized in Table 17. For GTA welds with 9FA filler (9FA-GTAW), which has approximately the same chemical composition except slightly higher titanium, most of the phases are either Laves or Nb-rich MC carbide with some smaller amount of Ti-rich MC carbide. The overall precipitation behavior of GTA welds with 9FA filler (9FA-GTAW) is nearly identical to that of GTA welds with 908 filler (908-GTAW). In GTA welds with 9GA filler (9GA-GTAW), the precipitates are not

appreciably different from those in GTA welds with 9FA filler. As with the gas tungsten arc weld with 9FA filler, Laves phase and Nb-rich carbide are the major precipitates. In GTA welds with 9FC filler (9FC-GTAW), which has 1 % Nb, only carbides were detected. The titanium content in the carbide is increased to 17 % compared to about 13 % in GTA welds with 9GA filler. Most of the precipitates in GTA welds with 9HA filler are though to be MC carbide, but with higher Ti content. The titanium content in Nb-rich MC carbide increases to about 20%. Also, a substantial amount of Al (5 %) is present in the Nb-rich MC carbide in GTA welds with 9HA filler. Another carbide, (Nb,Ti)C is present as a major precipitation phase in GTA welds with 9HA filler. In this carbide, the amount of Nb and Ti are about equal in atomic fraction. It should be mentioned that even though the weld filler wire has a very low concentration of carbon, sufficient carbon for carbide formation could be supplied into weld from the base metal by dilution and, considering the high diffusivity of carbon in austenite,[69] by direct diffusion.

Several unidentified precipitates with chemical composition, not characteristic of either Laves or MC carbides were detected in trace amounts in all of the GTA welds. They are all enriched in Nb and can be categorized in two separate phases based on chemical composition. One of them had a composition range of 1 - 2 % Si, 15 - 20 % Ni, 4 - 14 % Fe with less than 2 % of Al. A prominent phosphorous peak was detected as well. The titanium content of this phase increases as the Nb content in the filler wire decreases. The composition of this phase is somewhat similar to phosphide phase found in the heat affected zone of electron beam welded Inconel 718 [31] and forged alloy 903.[70] The other phase was only found in the GTA welds with 9HA filler, contained more Si and Al with trace amounts of Ni and Fe. These phases were only observed in trace amounts and would not have significant effects on the mechanical behavior of the GTA welds.

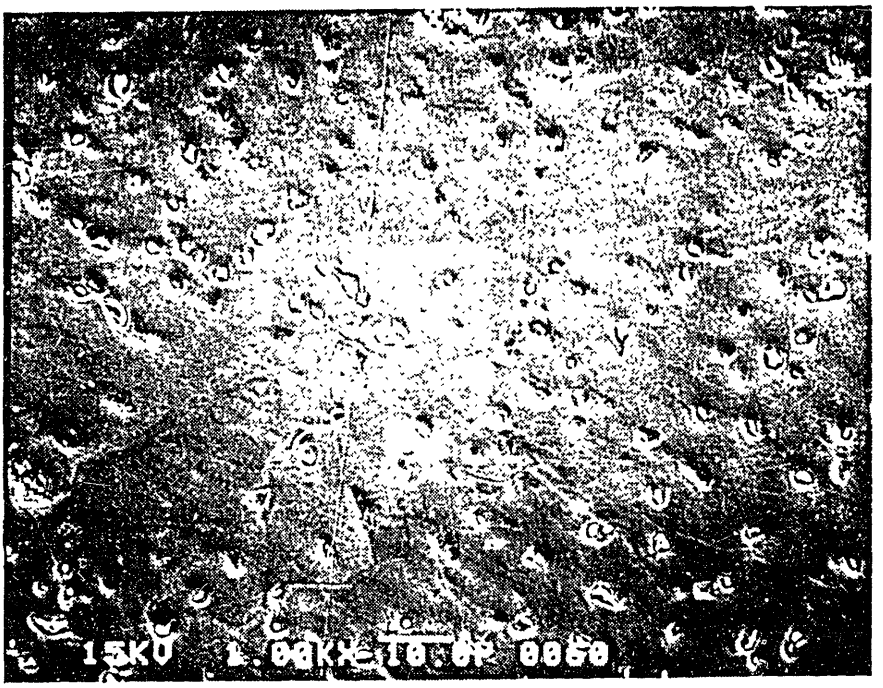

a) GTA weld with 3% Nb filler (9FA filler)

b) GTA weld with 1.5% Nb filler (9GA filler)

Figure 44. SEM microsgraphs of fusion zone of GTA welds with various filler, at 2000X

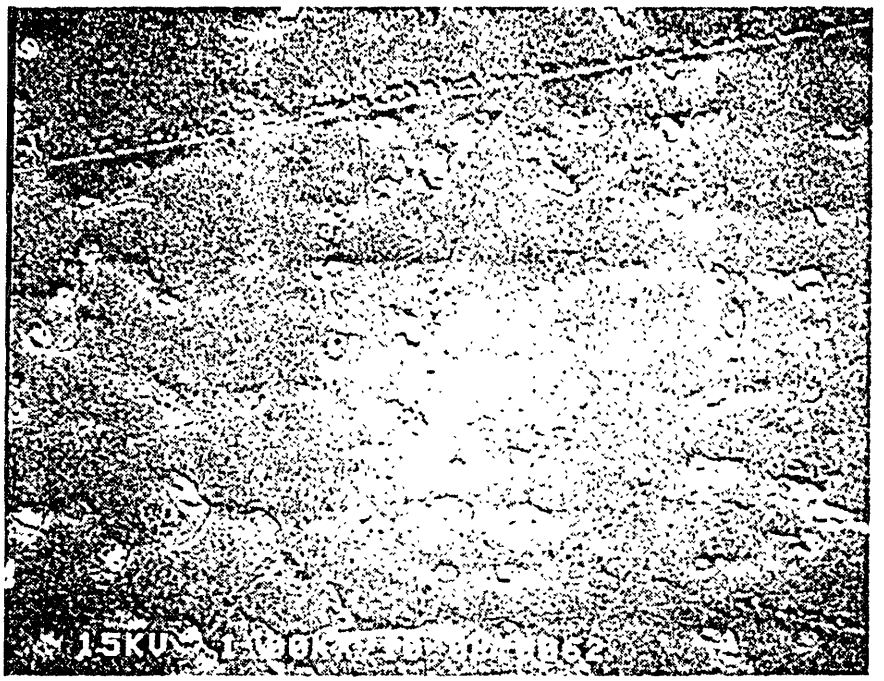

c) GTA weld with 1.0% Nb filler (9FC filler)

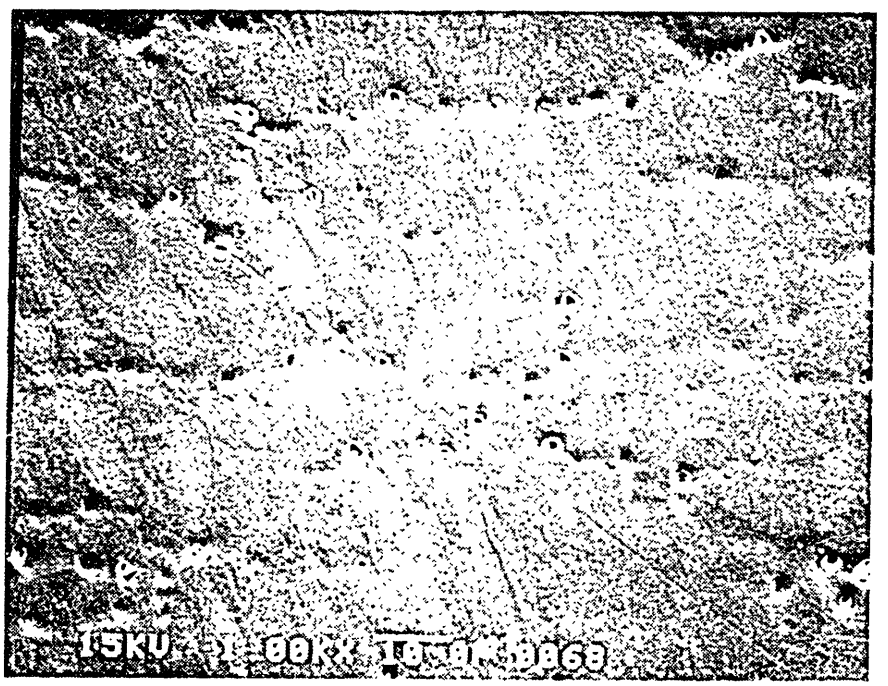

d) GTA weld with 0.5% Nb filler (9HA filler)

Figure 44. Continue.

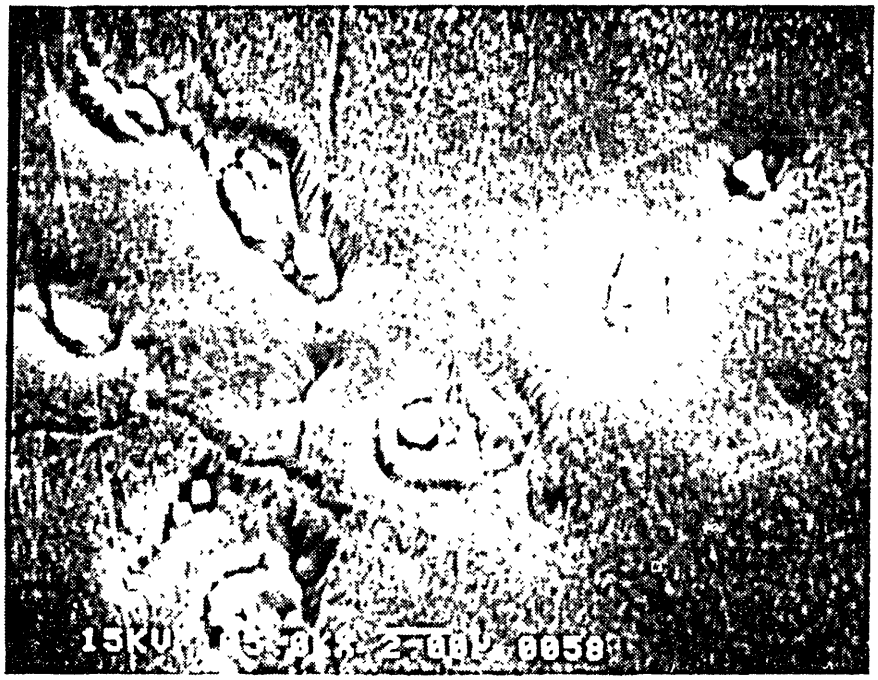

a) GTA weld with 3% Nb filler (9FA filler)

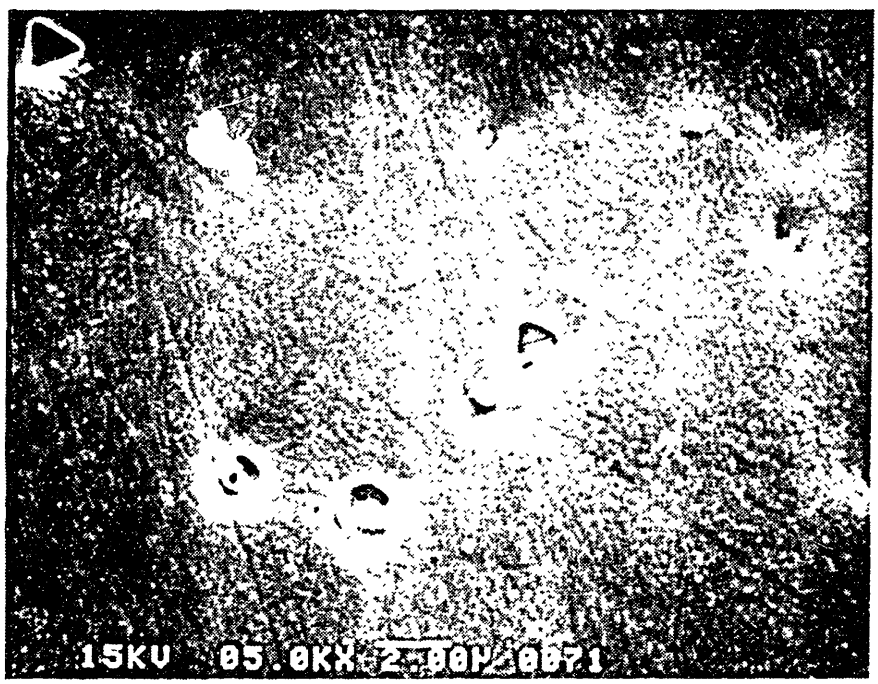

b) GTA weld with 0.5% Nb filler (9HA filler)

Figure 45. SEM micrographs of GTA welds with various filler, at 5000X

Table 17. Chemical composition of precipitates found in GTA welds with new fillers. (EDS on extraction replica, in weight percent).

Filler	Phase		Fe	Ni	Cr	Nb	Al	Ti	Si
9FA	Laves	M	25.2	34.2	2.2	32.5	1.5	3.3	1.1
	NbC	M	3.6	5.0	0.3	78.1	1.2	11.8	0.1
	TiC	m	0	0	0	32.1	2.4	63.7	0.8
	??	m	9.7	14.8	0.8	64.2	2.1	7.3	1.2
9GA	Laves	M	27.1	32.6	1.7	33.5	0.4	3.2	1.6
	NbC	M	0.7	1.5	0.4	83.3	0.5	13.4	0
	??	m	13.8	18.3	1.6	54.2	1.8	8.8	1.5
9FC	NbC	M	0.4	0.7	0	79.8	1.1	17.1	0.7
	(Nb,Ti)C	m	0	0.8	0	67.6	1.2	29.8	0.7
9HA	NbC	M	0.5	2.3	0.5	71.4	5.1	20.1	0.2
	(Nb,Ti)C	M	1.4	3.5	0.3	61.5	0.9	32.0	0.4
	??	m	1.3	0	3.2	50.4	3.6	36.3	5.2
	??	m	4.3	17.7	1.6	50.8	0.7	23.1	2.0

Note: Precipitates present in major phases are designated as M
Precipitates present in minor or trace amount are designated as m.

IV.3.2 Results of Differential Thermal Analysis (DTA)

Figure 46 shows a set of differential thermal analysis (DTA) results for 908 filler wire. These results were typical of all of the filler wires developed. The purpose of the thermal analysis was to determine the precipitation and dissolution temperature of Laves and MC carbides, corresponding eutectic temperatures, as well as the solidus and liquidus temperatures. However, it was very difficult to determine any other temperature except the solidus and liquidus temperature. The peak in the cooling curve (around 1235 - 1250 °C) is for carbide precipitation. No peaks were observed representing Laves phase formation during cool-down. Part of the problem was the choice of the sample. Because the samples are taken from the filler wire, which is virtually in single phase except for a few primary carbides, no distinguishable peak representing precipitate dissolution should have been

observed. During cooling, solute enrichment in the liquid, needed for the eutectic reaction, can not be achieved due to the extensive diffusion.

The liquidus and solidus temperatures are determined as the temperature at the onset of melting and at the completion of melting, and summarized in Table 18. The solidus and liquidus temperature decreases as the Nb content decreases. The solidification temperature range (ΔT_m), which is the difference between liquidus and solidus temperature decreases gradually at the same time. As the Nb content in filler wire decreases, both solidus and liquidus temperature increases. Meanwhile, the equilibrium melting temperature range (Tm) which will affect the hot cracking of Nb bearing alloys [32], decreases as the Nb content decreases.

Table 18. Solidus and liquidus temperature of filler metals found by DTA.

Filler metal	Nb, wt.-%	T_S, °C	T_L, °C	ΔT_m, °C
908	3.0	1320	1394	74
9FA	3.04	1323	1389	66
9GA	1.51	1355	1406	51
9FC	0.99	1364	1412	48
9HA	0.52	1375	1412	37

IV.3.3 Mechanical Properties of Welds with New Filler Materials

A. Room Temperature Tensile Properties

The results of room temperature tensile tests of GTA welds with new filler metals are summarized in Table 19. Specimen orientation is transverse to the welding direction. This orientation results in both base and weld metal being located within the gauge section. Welds with 9FA and 9G-series filler showed at least 990 MPa yield stress with 1260 MPa ultimate tensile stress. Welds with 9H-series filler showed considerably lower strength than the others. Despite considerable differences in strength, the ductility of weld does not change with composition of the filler wire.

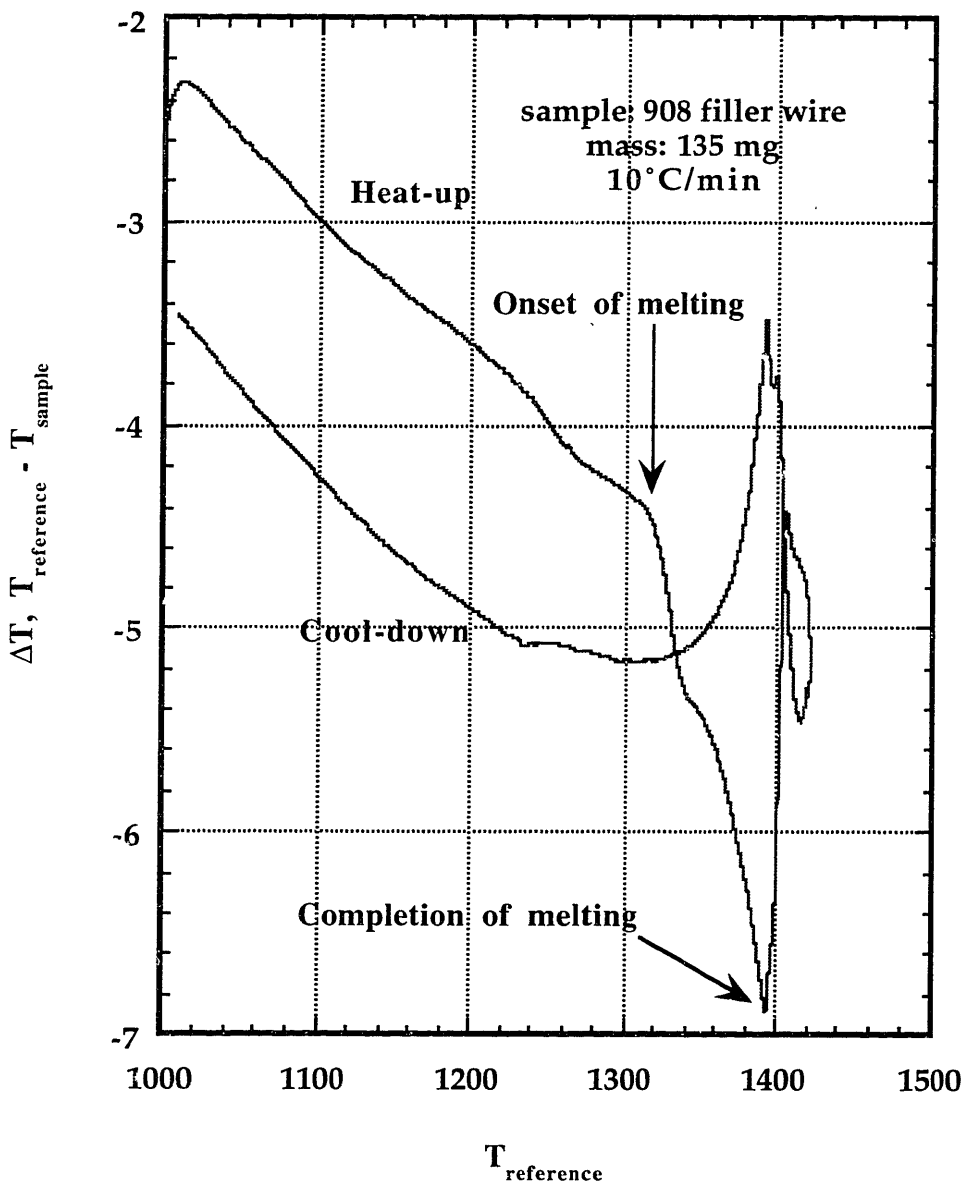

Figure 46. Result of differential thermal analysis (DTA) of 908 filler wire.

Table 19. Room temperature tensile properties of weld with new filler metals.

	Aging	σ_y, MPa	UTS, MPa	elongation, %
9FA-GTAW	650°C/200hr	1053±14	1317±15	8.2±0.7
9FC-GTAW	650°C/200hr	971±22	1240±12	8.6±0.8
9GA-GTAW	650°C/200hr	990±8	1266±21	9.1±0.7
9GB-GTAW	650°C/200hr	1021±3	1290±15	7.9±0.3
9GC-GTAW	650°C/200hr	1025	1291	9.3
9GD-GTAW	650°C/200hr	1044±22	1316±18	8.3±0.4
9HA-GTAW	650°C/200hr	970±13	1223±10	7.8±1.8
9HB-GTAW	650°C/200hr	833±1	1097±27	7.7±1.9
9HC-GTAW	650°C/200hr	978±11	1258±12	9.0±2.5
9HD-GTAW	650°C/200hr	785±29	1116±1	9.8±2.3

Weld strength vs. Nb content of the weld filler is plotted in Figure 47. As the Nb content decreases from 3 % to 1 %, both the yield strength and UTS decrease by about 80 MPa. The rate of decrease in yield strength with Nb content is about 40 MPa / % Nb. For UTS, the rate of decrease is 37 MPa / % Nb. The changes in tensile properties become less significant as the Nb content approaches 0.5 %. The yield strength of GTA welds with 9FC filler (1.0 % Nb) and GTA welds with 9HA filler (0.5 % Nb) is about the same. During weld solidification, some of Nb and Ti are tied up in carbide. Also, segregation of Nb and Ti and subsequent precipitation of Laves phase reduces the amount of these elements in solid solution. Thus, the amount of Nb and Ti available for precipitation of γ' is less than that in filler metals used. When the Nb content increases from 0.5 % to 1 %, the additional Nb in the filler metal is consumed to form carbides rather than remaining in solid solution and contribute to γ' precipitation. Thus, there is no gain in the strength of the weld. This explains the proximity of the strength of GTA welds with 9FC filler and 9HA filler. The ductility of GTA welds varies from 6 % to 10 % and shows no significant dependece on the Nb content in filler wire.

The effect of Ti content of the weld filler is shown in Figure 48. The variation of strength as a function of Ti content is illustrated by comparing the properties of the GTA welds with 9G-series fillers. The rate of change in yield strength with Ti content is about 52 MPa / %

Ti. For UTS, the rate of decrease is 51 MPa / % Ti. Ductility of GTA welds varies from 7.5 % to 10 %. As the Ti content of the filler metals increases, the ductility of GTA welds decreases slightly.

The effect of Al content of the weld filler is shown in Figure 49. The variation of strength as a function of Al content is illustrated by comparing the properties of the GTA welds with 9G-series fillers. The rate of change in yield strength with Ti content is about 60 MPa / % Al. For UTS, the rate of decrease is 54 MPa / % Al. Ductility of GTA welds varies from 7.5 % to 10 %.

The change of strength as function of the content of the strengthening elements are summarized in Table 20. The strengthening effect is the greatest for aluminum and the smallest for niobium.

The two Mo-added filler, 9HC and 9HD-GTAW show very little change in strength compared to their counterpart without Mo addition. There is a little improvement in ductility, however.

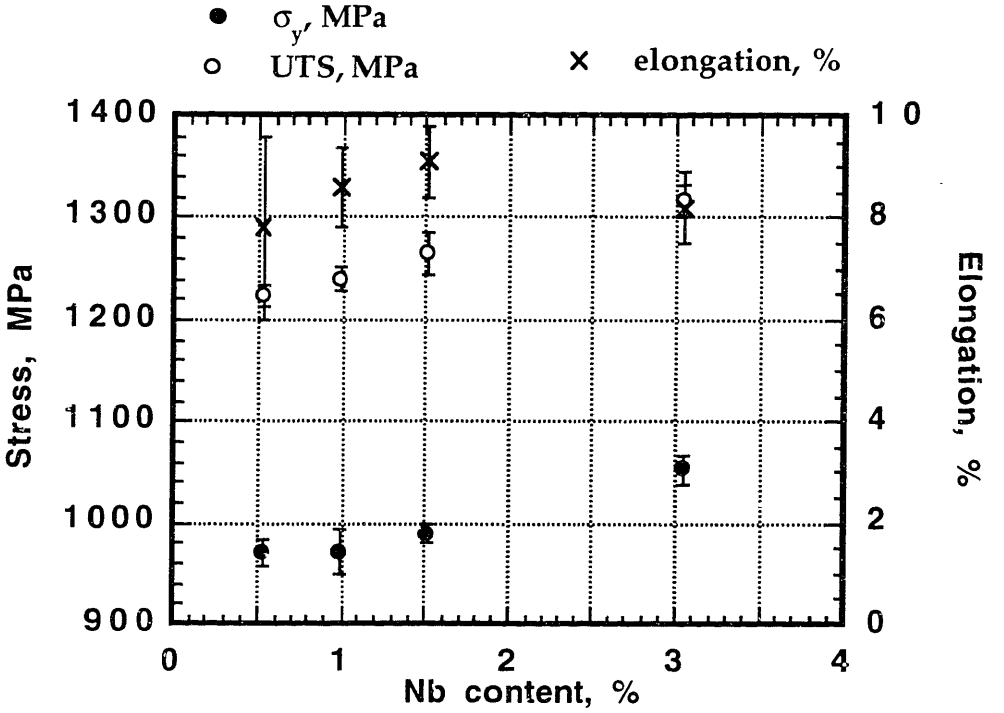

Figure 47. Effects of Nb content in the weld filler on the tensile properties of GTA welds. (after aged at 650°C/200hrs in vacuum)

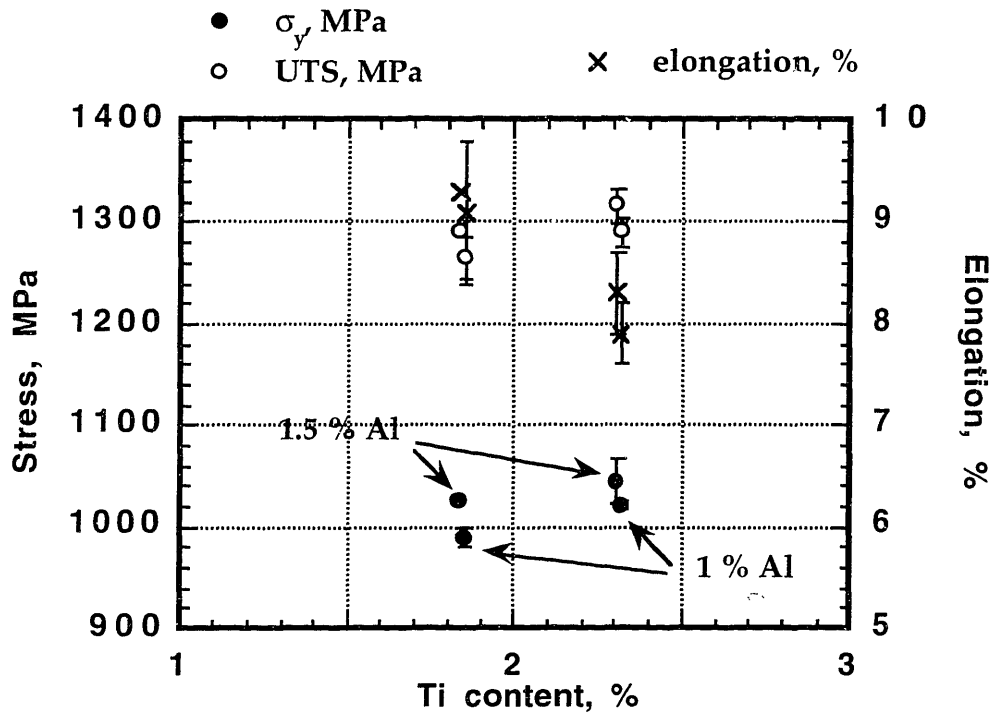

Figure 48. Effects of Ti content in the weld filler on the tensile properties of GTA welds. GTA welds with 9G-series fillers are compared. (after aged at 650°C/200hrs in vacuum)

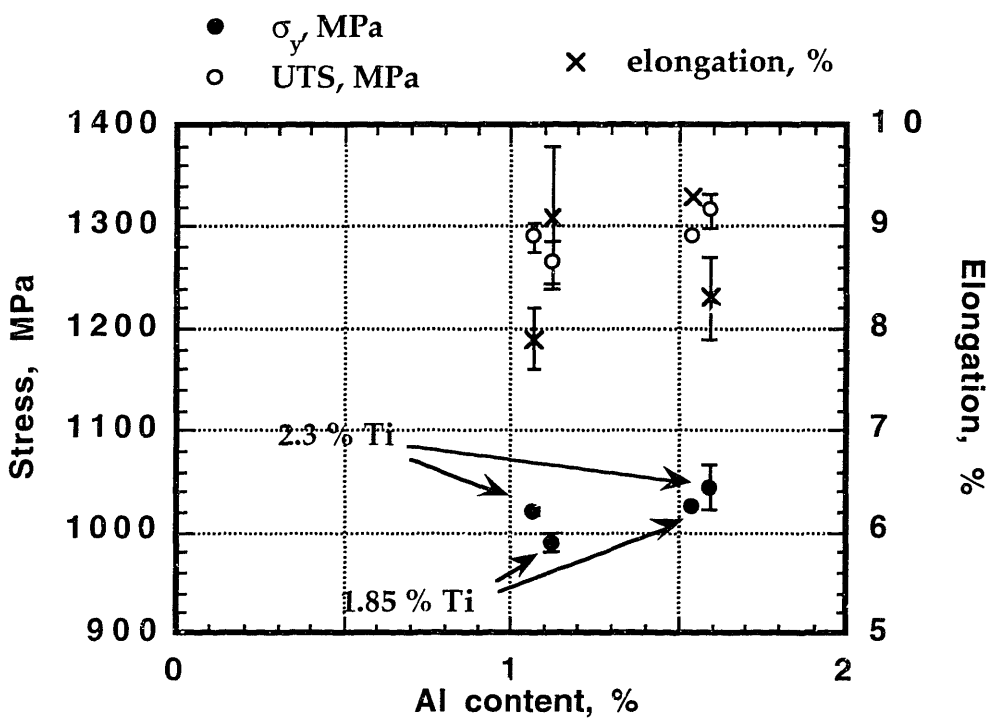

Figure 49. Effects of Al content in the weld filler on the tensile properties of GTA welds. GTA welds with 9G-series fillers are compared. (after aged at 650°C/200hrs in vacuum)

Table 20. The effect of alloying elements on the strength of GTA welds. Change of strength of welds when the amount of strengthening elements changes by 1 % are shown.

	Elements	$\Delta \sigma_y$, MPa	ΔUTS, MPa
weight %	Nb	40.3	36.6
	Ti	52.3	50.8
	Al	59.7	53.6

B. Room Temperature Fatigue and Fracture Properties

Fatigue crack growth rates and fracture toughness of GTA welds in the as-welded + aged condition are summarized in Table 21. The ΔK range used for the Paris' law regression, shown below:

$$\frac{da}{dN} = C \cdot (\Delta K)^m$$

was from 17.5 MPa$\sqrt{m}$ to 60 MPa$\sqrt{m}$ for GTA welds with 908, 9FA, 9FC, 9GA, and 9HA fillers. The Paris' law parameters are also shown in the table for these welds. Paris' law constants are about 2 - 5 x 10^{-11} mm/cycle and exponents in the range of 4.1 - 4.3. There is little effect of filler wire composition on fatigue crack growth rate. Fatigue crack growth rates for GTA welds with different Nb contents are shown in Figure 50, along with those for 908 welds.

Fracture toughness as function of the Nb content is plotted in Figure 51. As the Nb content decreases from 3 % to 0.5 %, the fracture toughness increases by about 50 %. The most significant change in fracture toughness occurs when the Nb content decreases from 1 % to 0.5 %. The GTA welds with 9H-series filler metals (low Nb content, 0.5 %) exhibit a much higher fracture toughness than GTA welds with the other fillers. The GTA welds with molybdenum added filler metals, 9HC and 9HD, show lower fracture toughness than their counterparts without Mo.

C. Selection of Improved Welds for Further Test

Figure 52 shows the data for strength vs. toughness plotted for each filler metal. Two new filler metals, 9HA and 9HB fillers located in the upper right corner (high strength and high toughness), were selected for further testing. The effects of a moderate amount of cold work, which is expected in the actual conductor manufacturing process was evaluated. The effects of cold work on the tensile properties of GTA welds with 908 filler were evaluated, also. The actual magnet operating temperature is at 4K. Therefore, the properties at 4K were also focused on.

Table 21. Fatigue crack growth rate and fracture toughness of various GTA welds at room temperature. (after aged for 200 hours at 650°C in vacuum)

Weld	Paris' law C	Paris law m	R	K_Q (J_Q), MPa$\sqrt{m}$
908-GTAW	4.1×10^{-11}	4.2	0.997	120±14
9FA-GTAW	5.0×10^{-11}	4.1	0.956	119±16
9FC-GTAW	2.2×10^{-11}	4.3	0.941	133±18
9GA-GTAW	2.1×10^{-11}	4.3	0.982	127±12
9GB-GTAW				121±13
9GC-GTAW				125±15
9GD-GTAW				101±12
9HA-GTAW	2.1×10^{-11}	4.3	0.982	165±9
9HB-GTAW				183±15
9HC-GTAW				144±17
9HD-GTAW				155±20

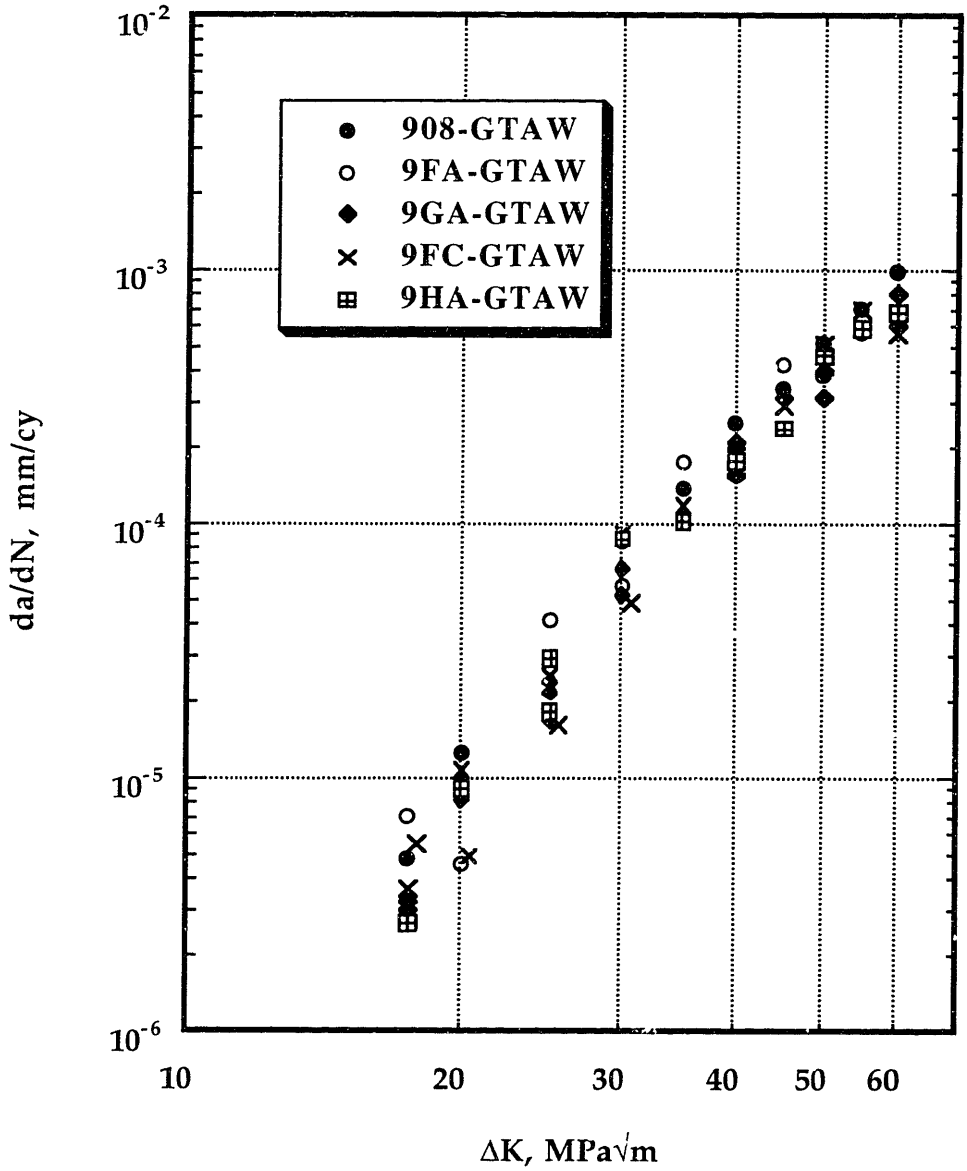

Figure 50. Fatigue crack growth rate of GTA welds with varying Nb contents

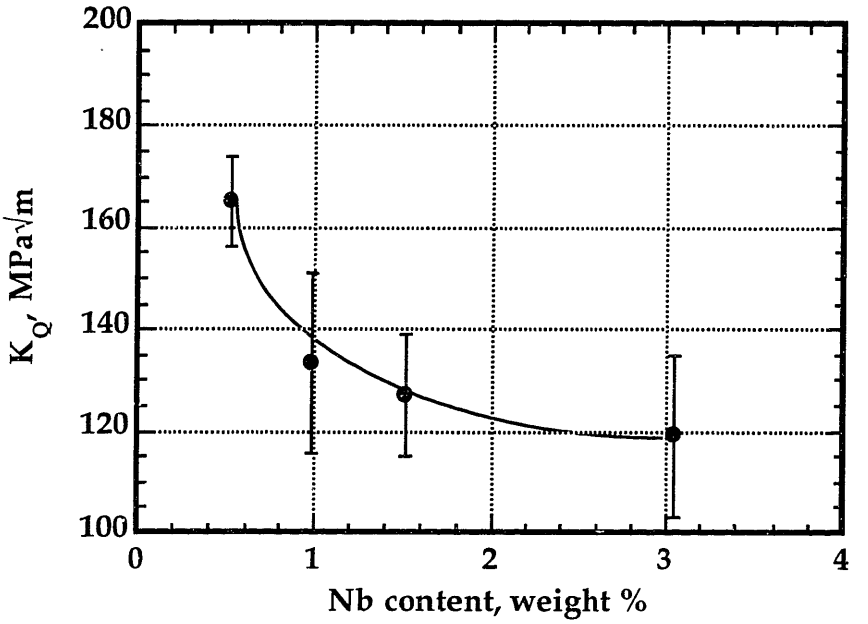

Figure 51. Fracture toughness of GTA welds as function of the Nb content in filler.

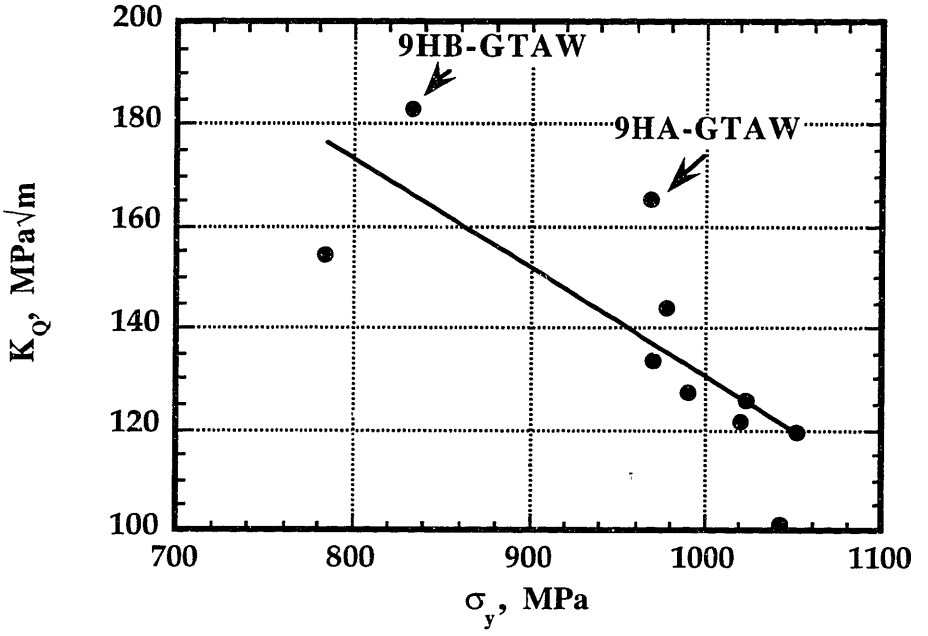

Figure 52. Strength-toughness plot of GTA welds with new filler metals. Two GTA welds, selected for further test are identified in the plot.

D. Effect of Cold Work and Temperature on Tensile properties

The effect of cold work prior to aging on room temperature tensile properties is shown in Table 22. The change in tensile properties with cold work are plotted in Figure 53. Cold work resulted in increased strength and ductility in GTA welds with 908 filler. For GTA welds with 9HA filler, changes in strength were small. Ductility of GTA welds increased slightly. For GTA welds with 9HB filler, strength increased but ductility decreased.

The results of tensile tests performed at 4K are shown in Table 23. The effect of cold work prior to aging on the tensile properties of GTA welds at 4K are plotted in Figure 54. The effect of cold work is greater for GTA welds with 9HA filler than GTA welds with 9HB filler. Ductility decreases after cold work.

Table 22. Room temperature tensile properties of cold-worked GTA welds. (after aged for 200 hours at 650°C in vacuum)

	CW, %	σ_y, MPa	UTS, MPa	elongation, %
908-GTAW	9	1104±30	1298±23	8.4±1.0
9HA-GTAW	9	991±35	1210±33	8.8±0.6
9HB-GTAW	9	949±18	1157±18	6.1±0.8

Table 23. Tensile properties of weld specimens at 4K. (after aged for 200 hours at 650°C in vacuum)

	CW, %	σ_y, MPa	UTS, MPa	elongation, %
908-GTAW+SA	9	1250	1696	11.3
9HA-GTAW	-	1074	1538	14.7
9HA-GTAW	9	1251	1690	13.2
9HB-GTAW	-	1001	1522	9.4
9HB-GTAW	9	1067	1505	8.5

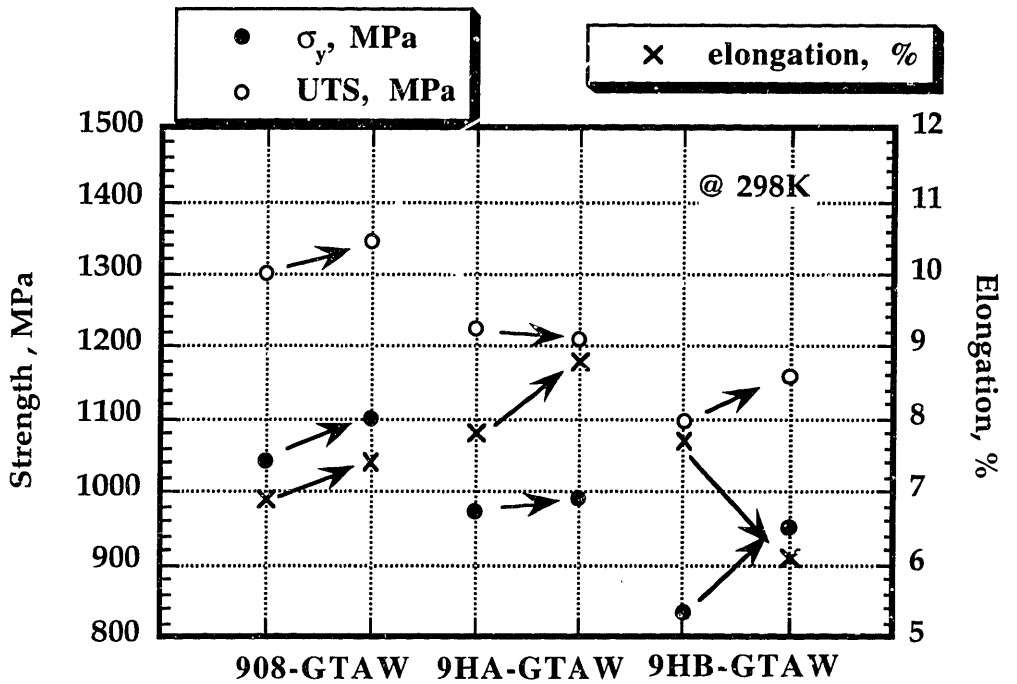

Figure 53. Effect of cold work on the tensile properties of GTA welds at room temperature.

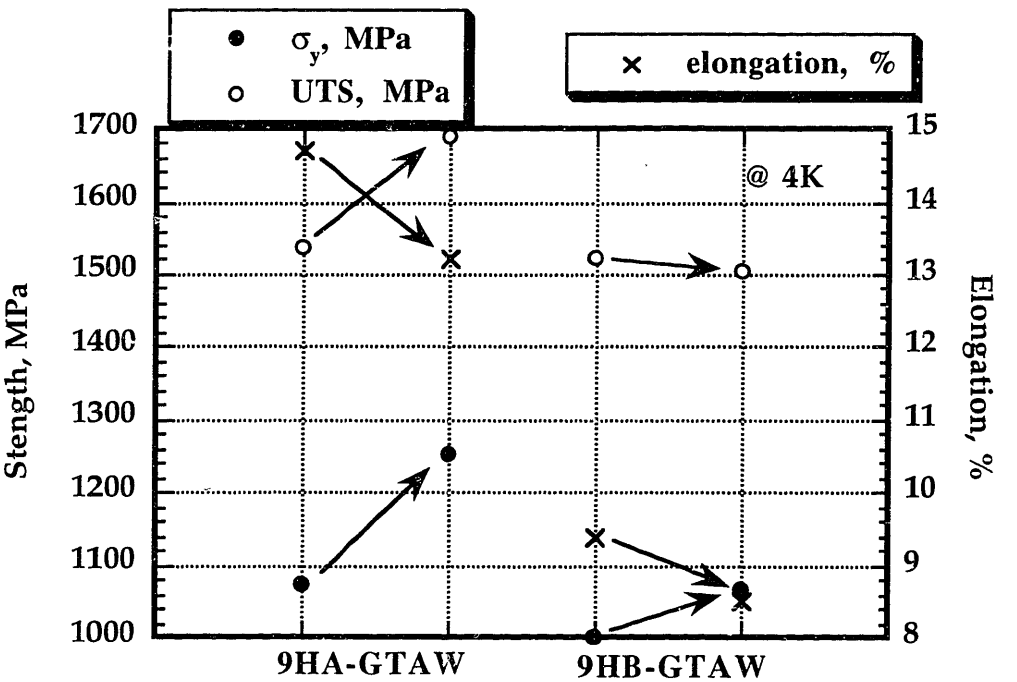

Figure 54. Effect of cold work on the tensile properties of GTA welds at 4K.

The effect of test temperature on the tensile properties of GTA welds are shown in Figure 55. As the temperature decreases from room temperature to 4K, both strength and ductility increase. The increase in UTS is far greater than that of yield strength. The UTS increased more than 300 MPa. For GTA welds with 9HA filler, elongation at 4K is 5% more than that at 298K.

The effect of test temperature on the tensile properties of cold worked GTA welds are shown in Figure 56. As the temperature decreases from room temperature to 4K, both the strength and ductility increase. The increase in UTS is far greater than that of yield strength. The UTS increased more than 300 MPa. The cold worked GTA welds with 9HA filler showed yield strength over 1250 MPa, with a UTS about 1700 MPa and, elongation over 13 % at 4K. The cold worked GTA welds with 9HB filler showed a yield strength over 1150 MPa, with a UTS about 1500 MPa and, elongation about 8.5 % at 4K.

Overall, the temperature effect is much more significant and consistent than the cold work effect.

Figure 57 shows the evolution of tensile properties from as-welded + aged condition tested at room temperature to as-welded + cold worked + aged condition tested at 4K. Generally, overall tensile properties at the actual operating condition are better than room temperature properties with aged GTA weld.

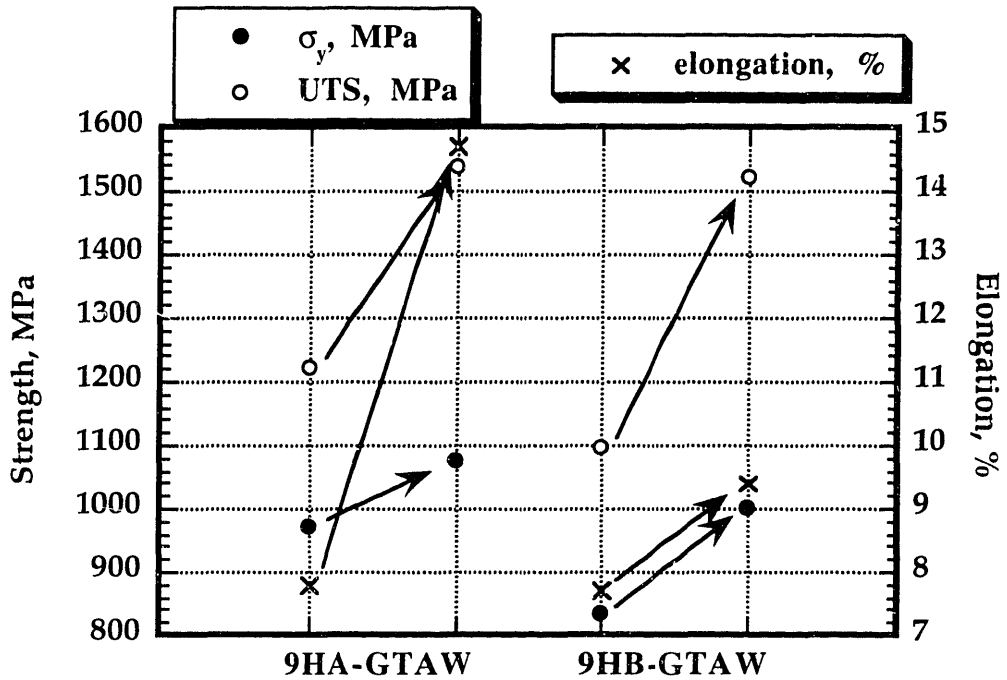

Figure 55. Effect of temperature on the tensile properties of as-weld + aged condition. Direction of arrows are from room temperature to 4K.

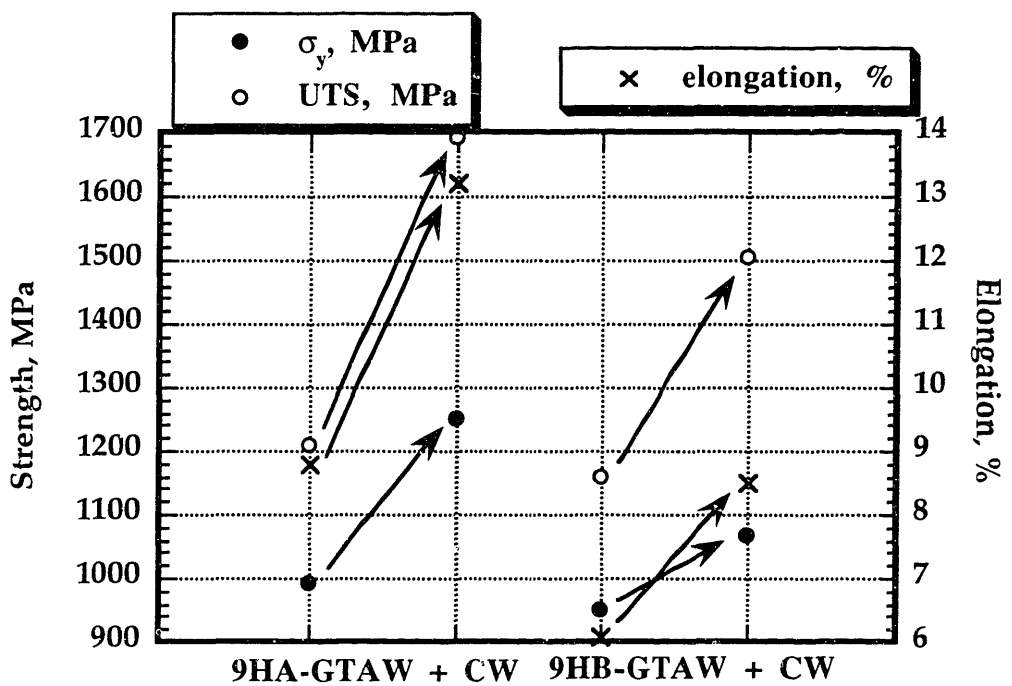

Figure 56. Effect of temperature on the tensile properties of as-welded + cold worked + aged GTA weld. Direction of arrows are from room temperature to 4K.

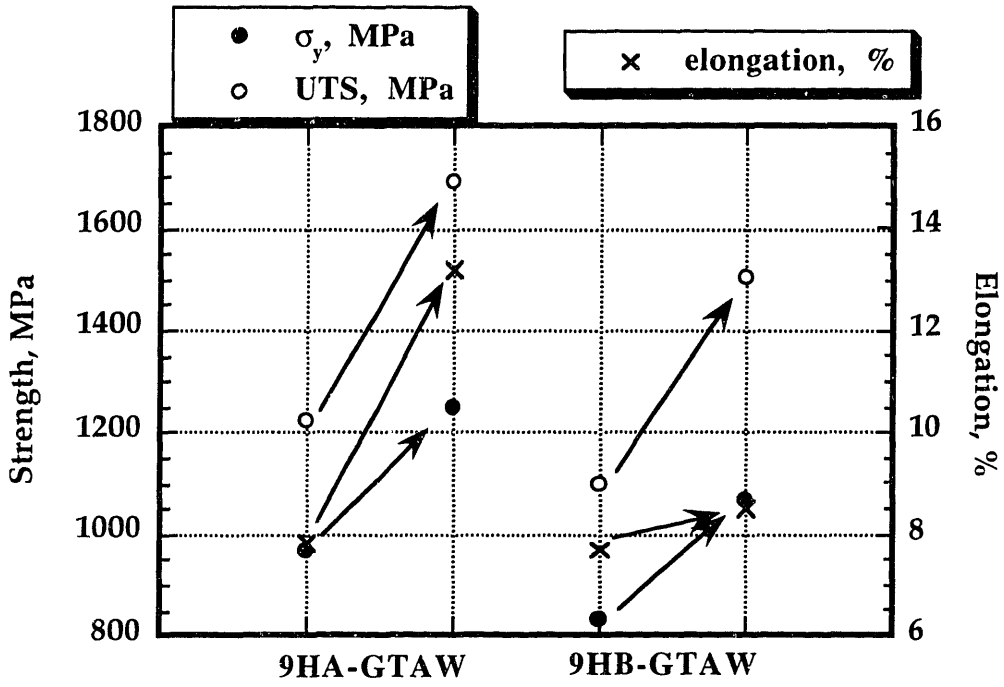

Figure 57. Effect of cold work and temperature on the tensile properties of GTA welds. Direction of arrows are from as-welded + aged condition tested at room temperature to as-welded + cold worked + aged condition tested at 4K.

E. Effect of Cold Work and Temperature on Fracture Toughness

The results of fracture toughness testing at 4K are summarized in Table 24. Also shown are the results for cold worked GTA welds tested at room temperature. Figure 58 shows the effect of cold work on fracture toughness at room temperature. While the fracture toughness of GTA welds using 9HA filler increased slightly with cold work, that for GTA welds with 9HB filler showed the opposite behavior. Figure 59 shows the effect of cold work on fracture toughness at 4K. At 4K, fracture toughness decreased with cold work prior to aging.

The effect of test temperature on fracture toughness of as-welded + aged GTA welds are shown in Figure 60. Decreasing the test temperature from room temperature to 4K decreased fracture toughness of GTA welds with 9HA filler, but increased that of GTA welds with 9HB filler.

The effect of test temperature on fracture toughness of as-welded + cold worked + aged GTA welds are shown in Figure 61. Decreasing the test temperature from room temperature to 4K decreased the fracture toughness of both GTA welds.

Figure 62 shows the evolution of fracture toughness from as-welded + aged condition tested at room temperature to as-welded + cold worked + aged condition tested at 4K. AW+9%CW+Aged at 4K. The latter showed 10 - 30 % lower fracture toughness than the former.

A strength vs. toughness plot for GTA welds with 9HA filler and 9HB filler is showun in Figure 63. The cold worked GTA welds with 9HA filler showed yield strength - fracture toughness combination of 1250 MPa - 120 MPa$\sqrt{m}$ at 4K. The cold worked GTA welds with 9HB filler showed yield strength - fracture toughness combination of 1160 MPa - 160 MPa$\sqrt{m}$ at 4K.

Table 24. Fracture toughness of various GTA welds at room temperature. (after aged for 200 hours at 650°C in vacuum)

Weld	Cold Work	Test T, °C	K_Q (J_Q), MPa$\sqrt{m}$
9HA-GTAW	-	4K	150
	9 %	RT	170
	9 %	4K	121 ± 1
9HB-GTAW	-	4K	214
	9 %	RT	173 ±8
	9 %	4K	161

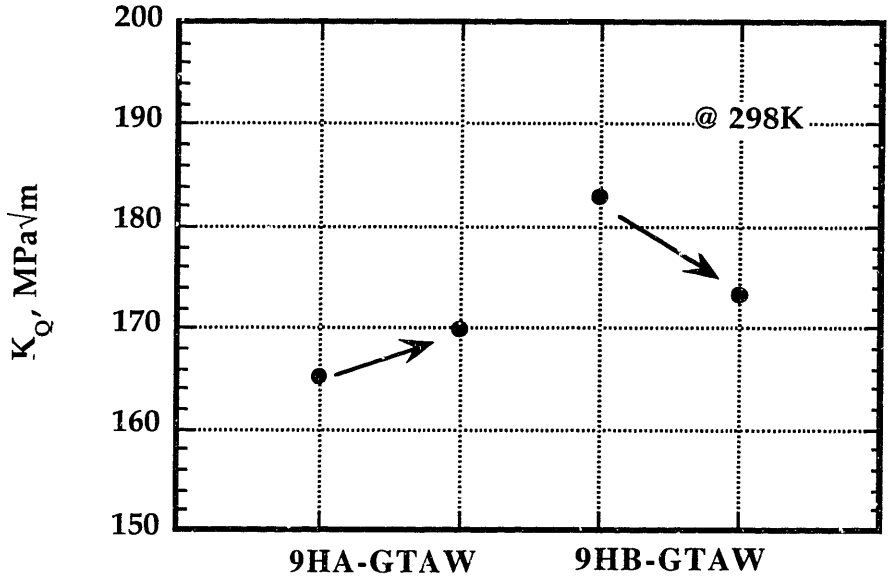

Figure 58. Effect of cold work prior to aging on fracture toughness of GTA welds at room temperature. Arrows indicate the direction of cold work.

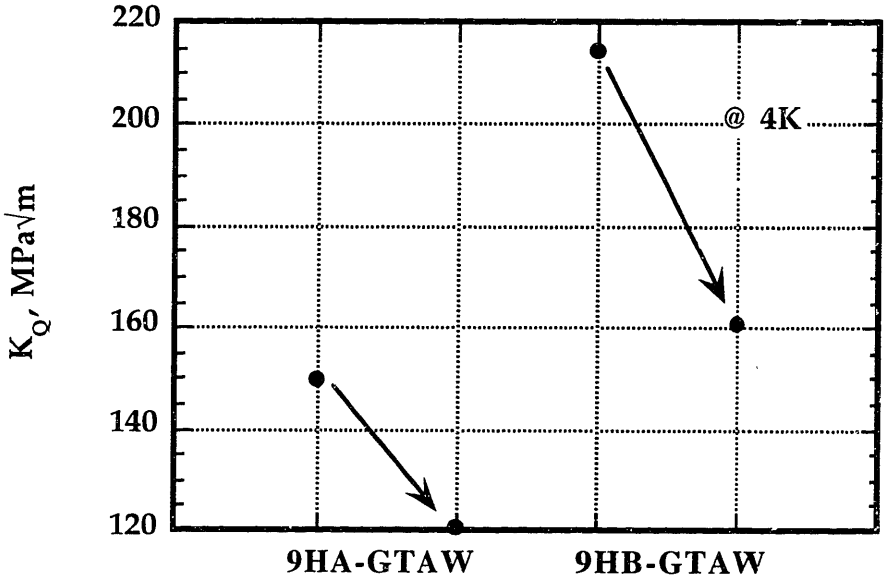

Figure 59. Effects of cold work prior to aging on fracture toughness of GTA welds at 4K. Arrows indicate the direction of cold work.

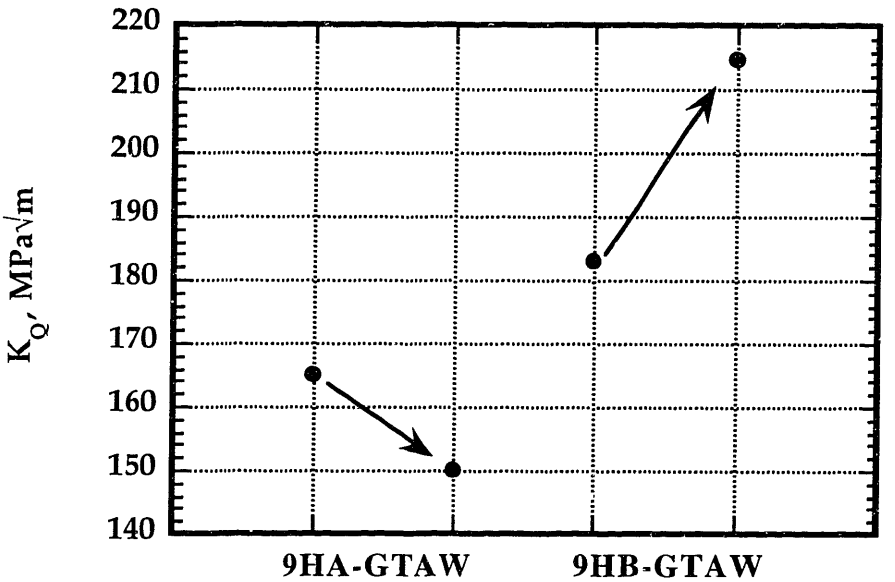

Figure 60. Effects of test temperature on fracture toughness of as-welded + aged GTA welds. Direction of arrows are from room temperature to 4K.

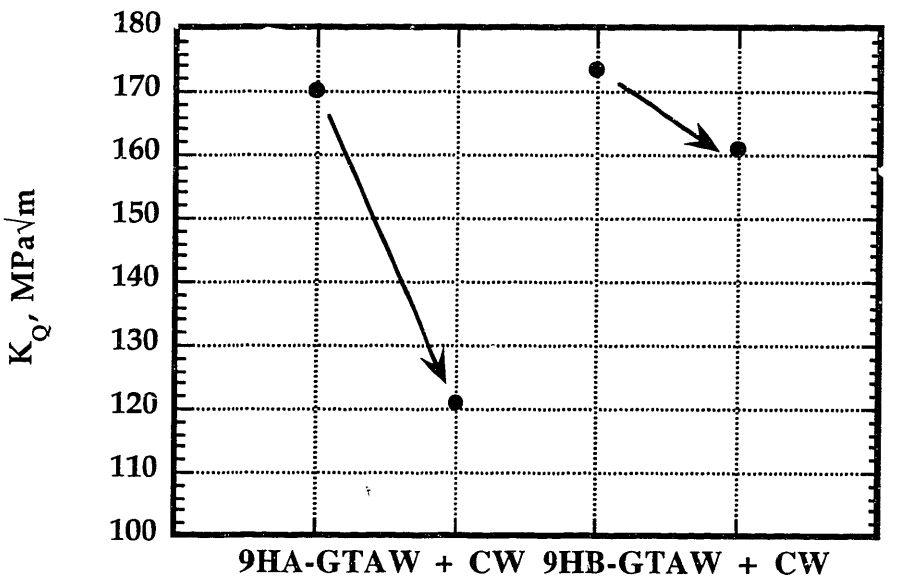

Figure 61. Effect of test temperature on fracture toughness of as-welded + cold worked + aged GTA welds. Direction of arrows are from room temperature to 4K.

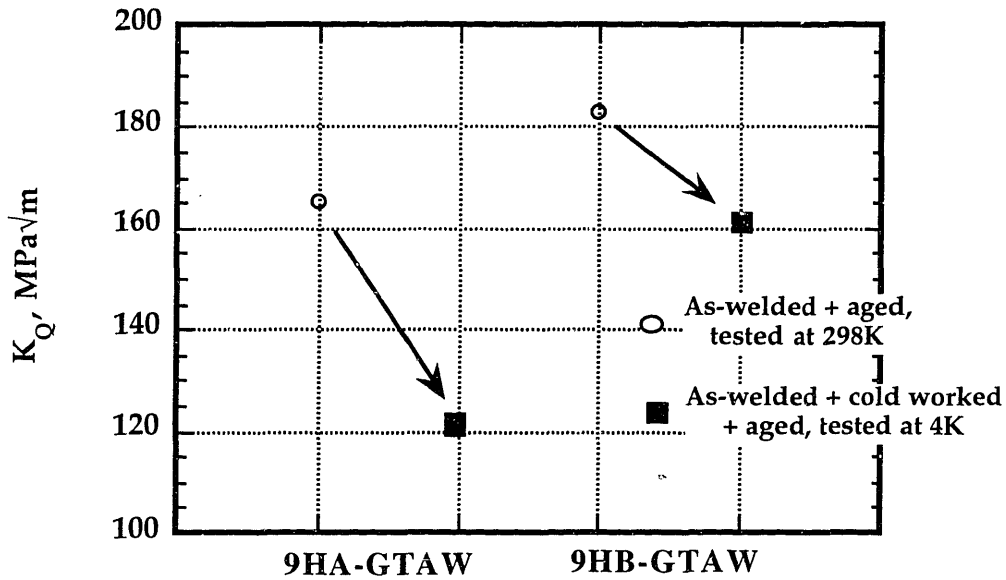

Figure 62. Effect of cold work and temperature on fracture toughness of GTA welds. Direction of arrows are from as-welded + aged condition tested at room temperature to as-welded + cold worked + aged condition tested at 4K.

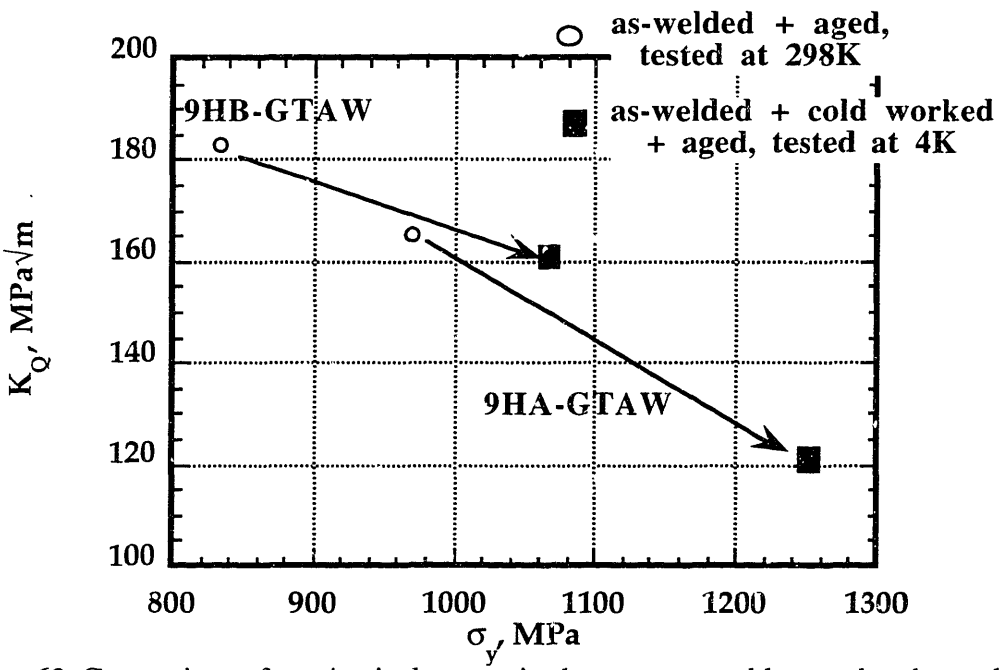

Figure 63. Comparison of mechanical properties between as-weld + aged and tested at 298K, and as-weld + 9% cold work + aged and tested at 4K.

IV.3.4 Fractography Analysis of Welds

The fracture surfaces of the various GTA welds are shown in Figure 64. All of the fracture surfaces show a typical ductile dimple rupture failure. On the fracture surfaces of GTA welds with 9FA filler and 9GA filler, the dimples contained particles sitting at their base, surrounded by a debris-like broken structure and wavy deformation marks on the wall of the dimple. On the fracture surface of GTA welds with 9FC filler, the structure on the base of dimple is finer and less in amount. For GTA welds with 9HA filler, the debris-like structure is hardly present at the base of the dimples, wavy deformation marks being dominant. At lower magnification, illustrated in Figure 65, the relation between the dimples and dendritic structure can be seen. The continous array of dimples coincides with the general features of the dendritic structure.

The composition of the particles at the base of the dimples on the surfaces of GTA welds with 9FA filler and 9HA filler were examined by EDS and shown in Figure 66. Because the particles are small and sitting at the base of the dimples, the compositions shown in Figure 66 are mixture of the composition of particles as well as that of the surrounding matrix. Still, particles can be identified qualitatively. Particle A in Figure 66-a) is thought to be an MC carbide, considering high Nb and Ti contents. Particles B and C are thought to be Laves phases, considering high Si content as well as high Nb content. Thus, both Laves and MC carbides are detected at the dimple base on the fracture surface of GTA welds with 9FA filler. However, the particles at the base of dimples were too small to be used for EDS analysis.

As with the fracture surface, the surface of fatigue cracks, shown in Figure 67, show markedly different features depending on filler wire composition. The fatigue surface of GTA welds with 9FA filler is consisted of the repetition of the area filled with debris-like broken structure and smooth featureless areas. The fatigue surface of GTA welds with 9HA filler shows a much cleaner structure, having needle-like structure aligned with the dendritic structure. The size of the broken structure is much smaller in GTA welds with 9HA filler. In both GTA welds, the spacing between the broken structure is about 10 - 20 μm, which corresponds to the primary dendritic spacing.

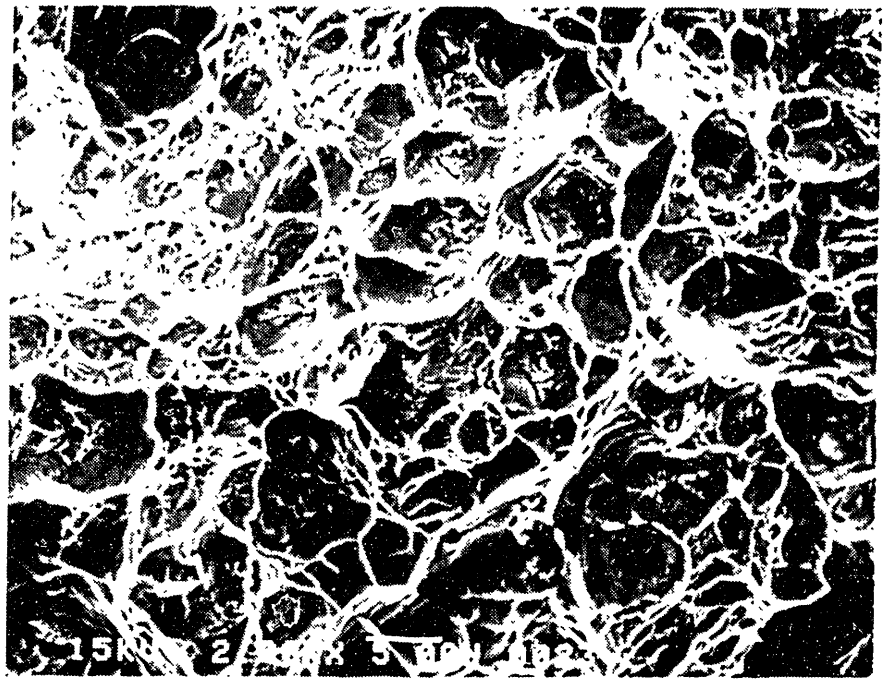

a) GTA weld with 9FA filler, 2000X

b) GTA weld with 9GA filler, 2000X

Figure 64. Fracture surfaces of GTA welds with various filler wires.

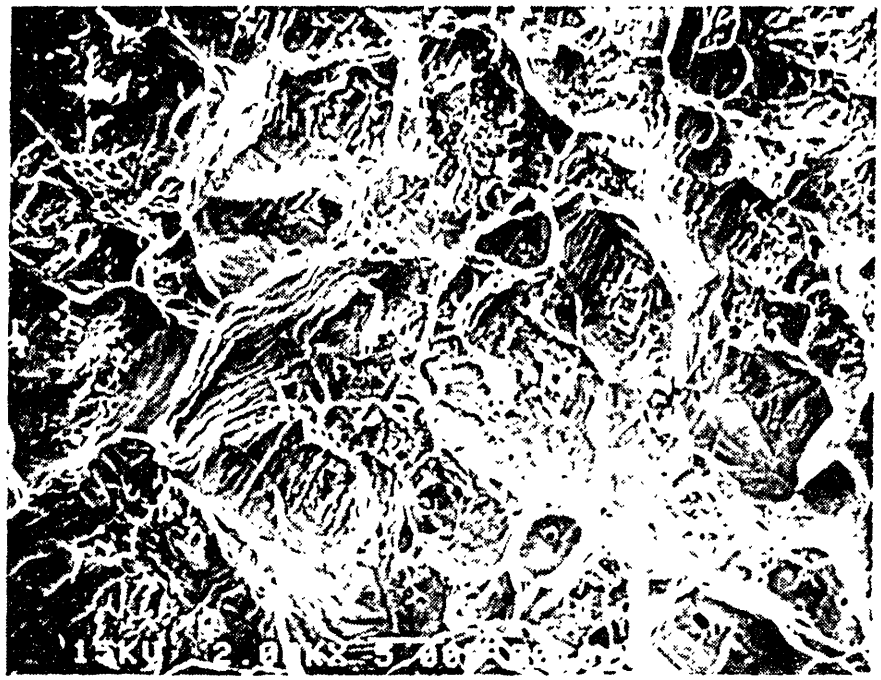

c) GTA weld with 9FC filler, 2000X

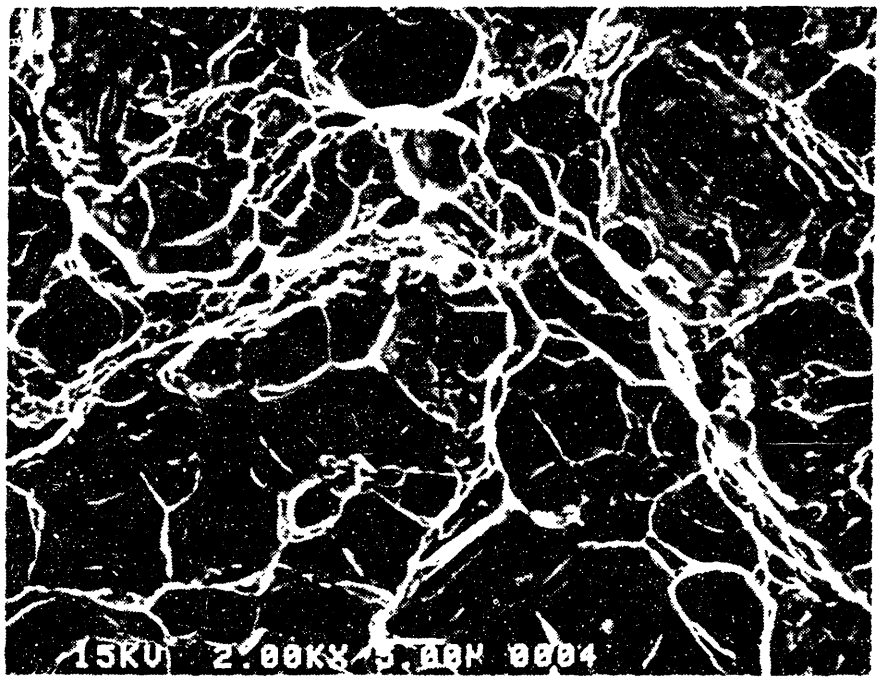

d) GTA weld with 9HA filler, 2000X

Figure 64. Continue.

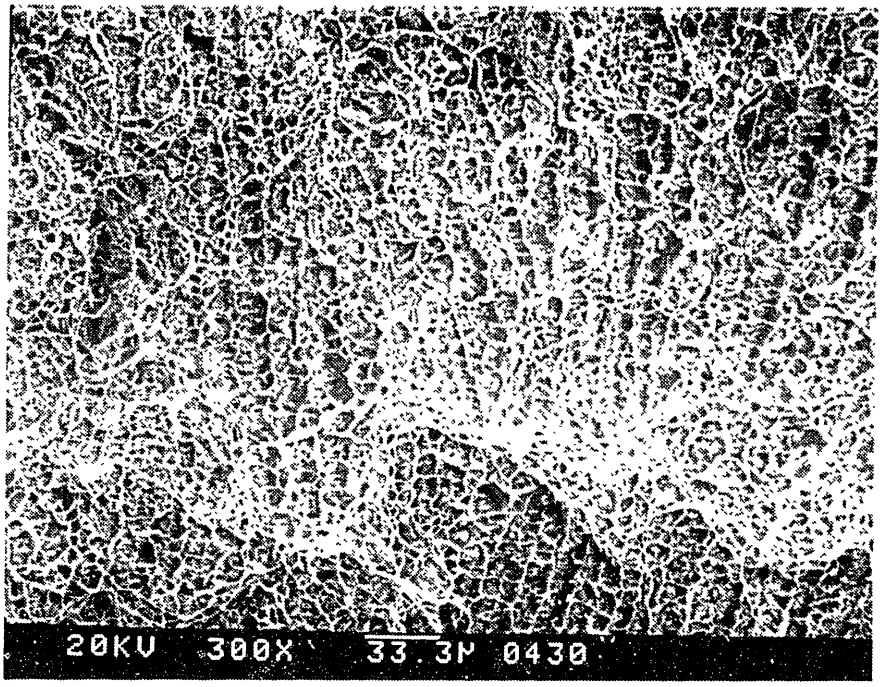

a) GTA weld with 9FA filler, 300X

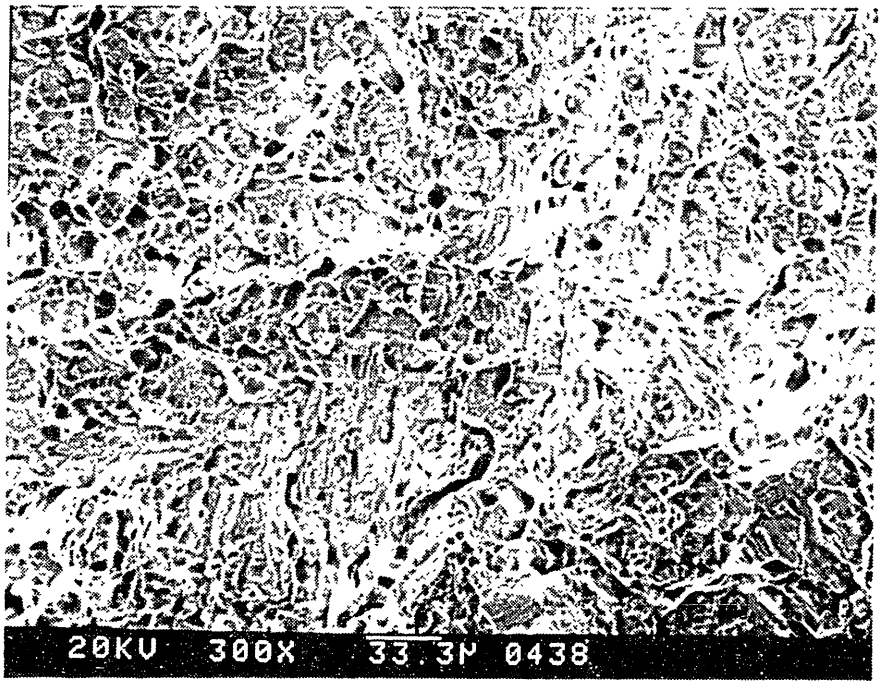

b) GTA weld with 9HA filler, 300X

Figure 65. Fracture surfaces of GTA welds at lower magnification, showing continuous arrays of dimples along the dendritic structure.

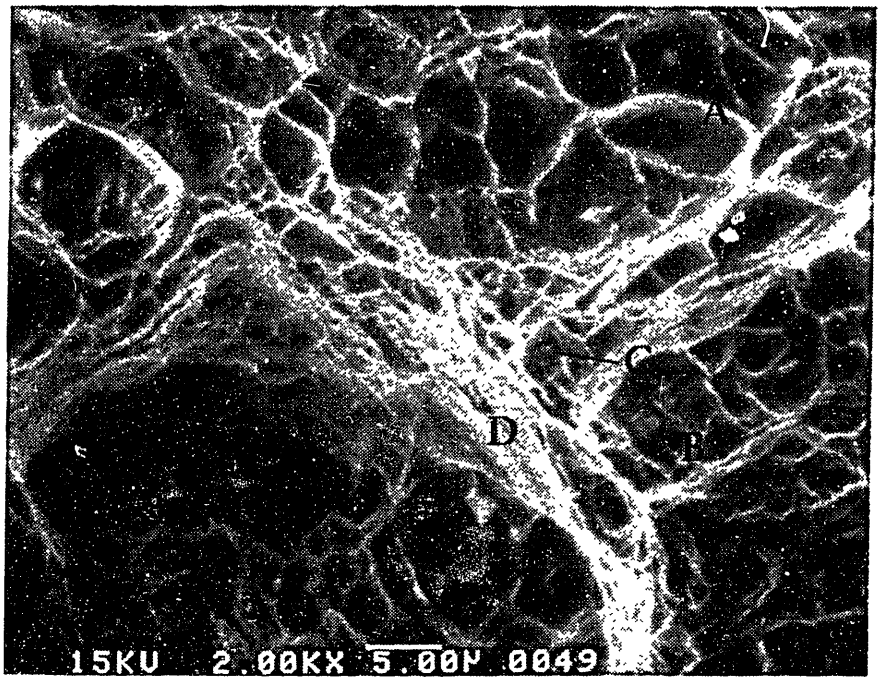

location	Fe	Ni	Cr	Nb	Al	Ti	Si
A	21.86	24.23	2.41	43.21	0.40	6.98	0.34
B	28.54	33.47	3.12	30.63	0.00	3.28	0.47
C	31.67	37.91	3.75	21.84	0.28	3.19	0.58
D	40.89	46.50	5.02	4.51	1.77	2.36	0.41

a) GTA weld with 9FA filler

Figure 66. Fracture surfaces of GTA welds with EDS analysis results of particles.

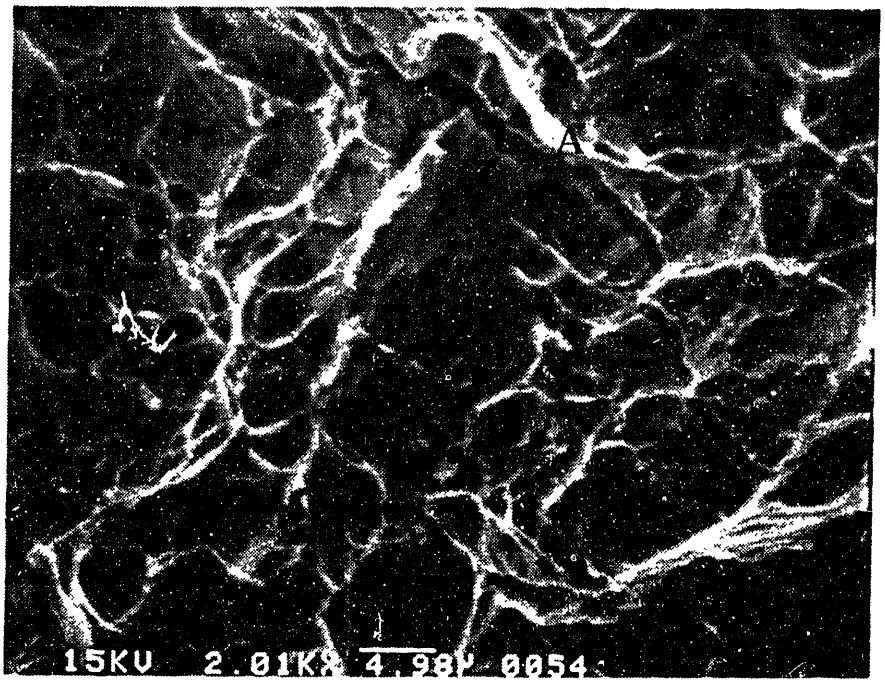

location	Fe	Ni	Cr	Nb	Al	Ti	Si
A	43.48	47.78	5.26	2.51	2.21	1.86	0.71

b) GTA weld with 9HA filler

Figure 66. Continue.

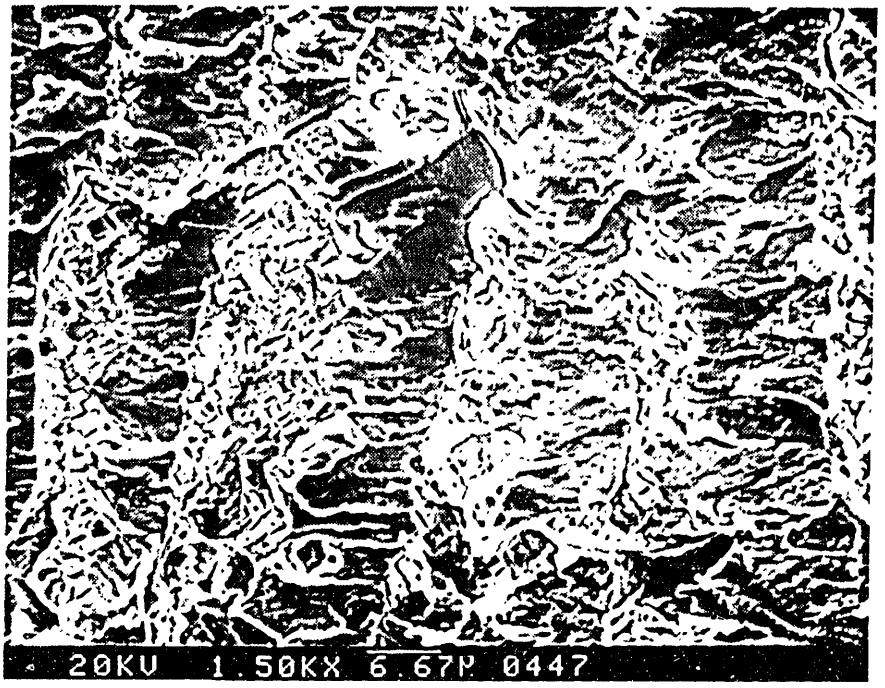

a) GTA weld with 9FA filler, 1500X

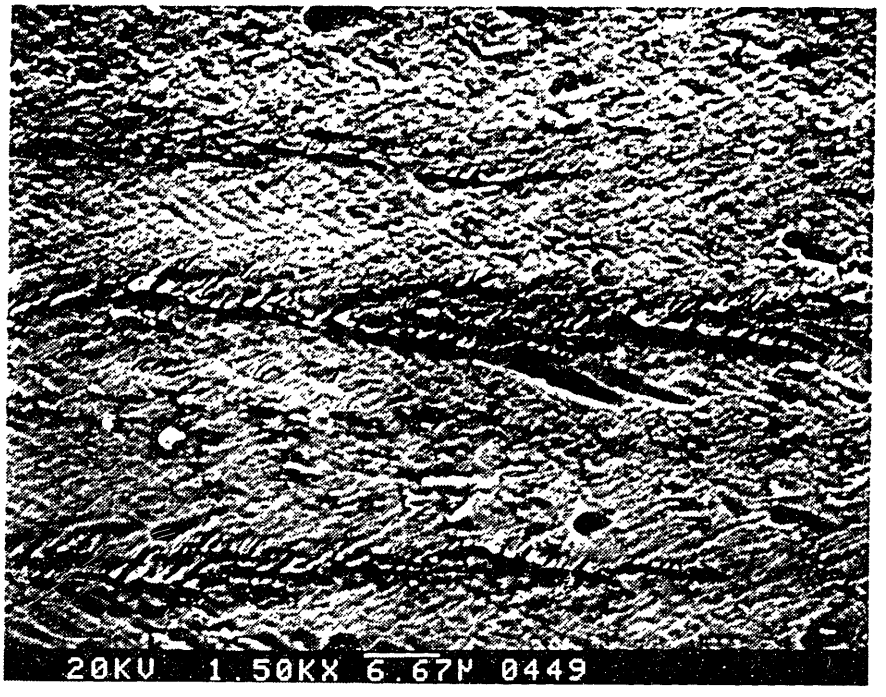

b) GTA weld with 9HA filler, 1500X

Figure 67. Fatigue surface of GTA welds..

IV.3.5 Summary and Discussion

The mechanical properties of alloy 908 GTA welds using 10 newly developed filler wires have been examined. As the Nb content in filler changes from 3 % to 0.5 %, about a 40 % increase in fracture toughness has been observed at the expense of a 7 % reduction in strength. When GTA welds with Nb contents of 1 % and 0.5 % are compared, the latter shows a 25 % higher toughness without losing strength. Further testing was done to investigate the effect of cold work and test temperature on selected GTA welds with favorable strength-toughness combinations. Cold work and low test temperature increased the strength of the GTA welds. The effect of temperature and cold work on ductility and fracture toughness showed no definitive trends with filler composition. Overall, the combined effect of cold work and decreasing test temperature is to increase strength and ductility but to decrease toughness of GTA welds.

All of the weld showed a cellular-dendritic microstructure with dendritic spacing of about 10 μm regardless of filler composition. However, precipitation within the interdendritic zone showed different characteristics as the filler composition changed. In GTA welds with filler containing more than 1.5 % Nb, the dominant precipitates are hexagonal Laves and cubic MC carbides present in the large interdendritic zone. As the Nb content decreases, the size of the interdendritic zone becomes smaller and MC carbide becomes the dominant phase.

Fracture surfaces of GTA welds showed a typical dimple rupture failure in all cases. During fracture, microvoids initiated at brittle secondary phases. In GTA welds with high Nb filler, such as 9FA and 9GA filler, segregation during weld solidification formed a large eutectic zone, high in Nb content arround precipitates. These area become brittle after aging heat treatment. Right after microvoid initiaition, these area can be easily torn apart without much resistance and, increase the size of the voids. This results in degraded fracture toughness. However, in GTA welds with 9HA filler, initial void initiation sites are relatively small MC carbides surrounded with a smaller brittle zone. In this case, more deformation is needed for crack growth, resulting in better fracture toughness.

IV.4 Simulated Production Welding

IV.4.1 Base plates selection

Mill-annealed 7-mm thick alloy 908 plates were heat treated to match the anticipated condition for the actual conduit. Based on discussion with the conduit supplier, it was determined that the conduit will be supplied with hardness of 80 or less at the Rockwell-B scale. Pieces of mill annealed plates were heat treated at 980 °C and 1050 °C for from 5 min to 1 hr. Hardness and grain size were measured for each piece. The results are shown in Table 25. At 980 °C, the hardness approached 80 after 30 minutes, but grain growth is not apparent until 60 minutes. At 1050 °C, the hardness approached 80 at 5 minutes and decreased continuously afterward. Significant grain growth does not occur until 10 minutes. Based on these results, a 1050 °C/1hr heat treatment followed by water quenching was chosen as the proper heat treatment condition to be used in simulated production welding evaluation.

For comparison purpose with previously accumulated data on manual GTA welds, which used mill-annealed base metal, one plate was welded using mill-annealed base metal.

Table 25. Hardness and grain size of base metal plate after various solution heat treatment. (Hardness shown at the Rockwell B-scale)

Temperature, °C	Time, min	Hardness	Vickers microhardness	Grain size, μm
Mill Anneal		19.3 ± 2.6 *		
980	10	86.2 ± 0.9	182.0 ± 5.7	35
	30	81.1 ± 1.5	177.8 ± 5.5	40
	60	80.5 ± 0.7	196.8 ± 13.2	70
1050	5	81.7 ± 1.1	175.5 ± 7.0	40
	10	78.9 ± 0.9	193.1 ± 5.1	70
	30	77.2 ± 1.0	176.6 ± 5.6	75
	60	73.2 ± 3.9	177.0 ± 4.0	75

* Rockwell-C scale

IV.4.2 Microstructure of Production Weld

A typical weld optical microstructure is shown in Figure 68. A cellular-dendritic structure is evident in all of the welds. At higher magnification, the existence of interdendritic precipitates are also visible. At lower magnification, shown in Figure 69, bands of primary dendrites along with thickness of weld can be seen. These bands stretched from the face of weld to near the root of the weld. SEM micrographs are also shown in Figure 71. The microstructure is similar to previously mentioned manual welds. Both Laves phase and MC carbides are present within the weld fusion zone. The results of EDS analysis on the precipitates are summarized in Table 26. The compositions of the phases are about the same as those found previously in manual gas tungsten arc weld with 908 filler. Occationally, Laves phase and MC carbides were found side-by-side, attached to each other at the same location as shown in Figure 70-b). Overall, the microstructure of production welds were the same as that of manual GTA welds with 908 filler.

Table 26. Chemical composition of precipitates found in fusion zone of production welds. (in weight percent)

	Fe	Ni	Cr	Nb	Al	Ti	Si
Laves in AAI AW	25.2	34.8	3.2	31.6	1.0	4.6	0.6
eutectic γ in AAI AW	32.7	48.1	4.2	10.8	1.2	2.6	0.4
MC in AAI AW	9.9	11.1	1.6	66.0	0.4	11.0	0

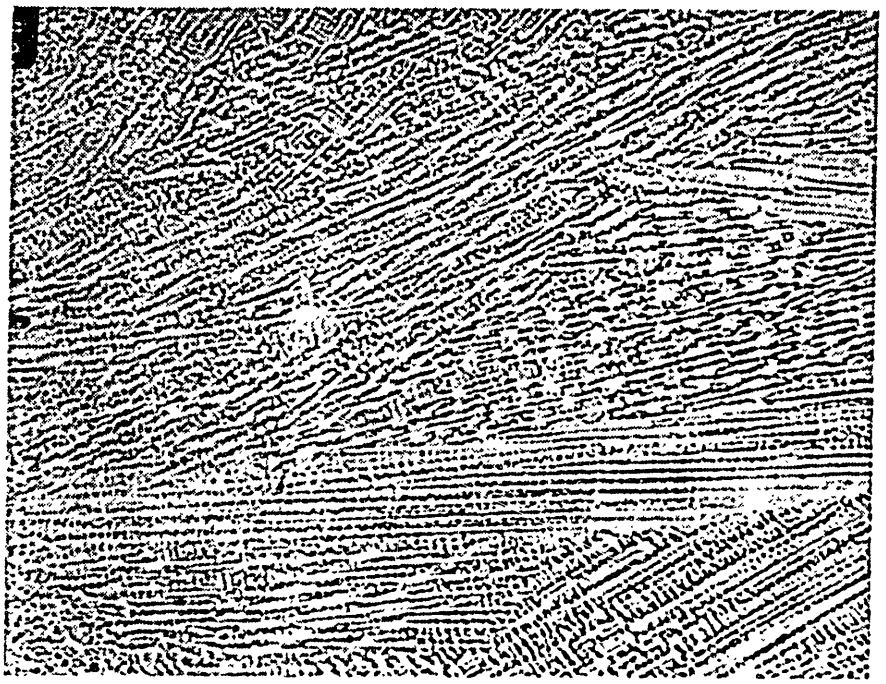

a) at 100X

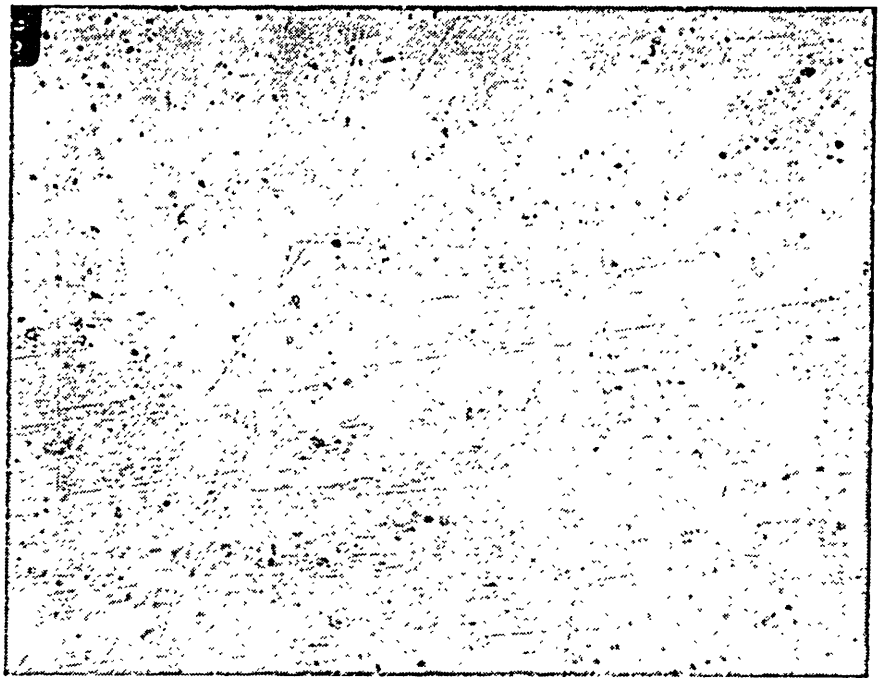

b) at 500X

Figure 68. Optical micrographs of production welds.

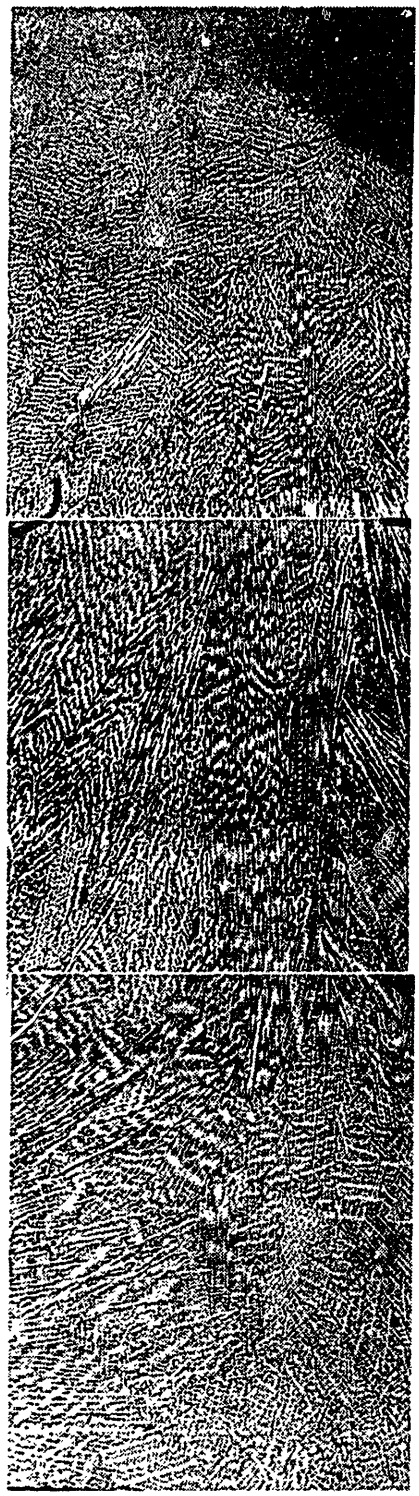

Figure 69. Fusion zone of production welds, showing the bands of primary dendrites stretching from the face to root of welds. (30X)

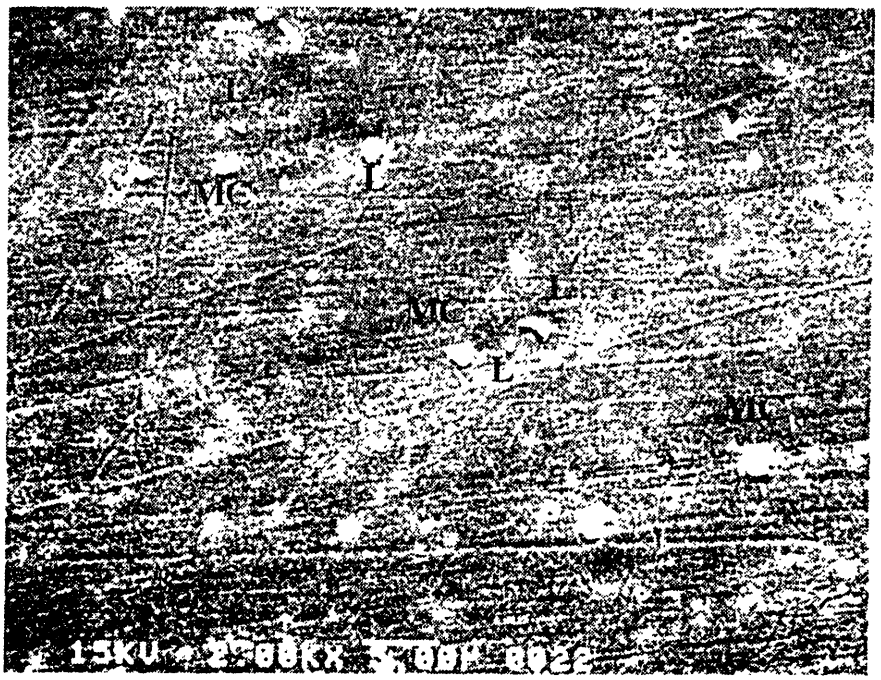

a) at 2000X

b) at 5000X

Figure 70. SEM micrographs of as welded production weld.

IV.4.3 Hardness of welds

The results of Rockwell-B hardness measurements in the as-welded condition are shown in Figure 71. For welds with homogenized base metal, the hardness decreased gradually from the center of weld toward base metal. The heat affected zone (HAZ) near fusion zone showed higher hardness compared to that of the base metal. This localized hardening can be attributed to in-situ precipitation hardening during the weld thermal cycle. For welds with mill annealed base metal, a hardness profile is reversed, showing lowest hardness at the weld. In both cases, hardness at the center of weld is 85 (Rockwell-B).

The results of micro-hardness measurements on the weld with homogenized base metal are shown in Figure 72. Near the face of weld, the hardness decreasd gradually from fusion zone to base metal. Small increase in hardness was observed at about 3 mm away from fusion line. Near the root of the weld, a much larger increase in hardness was observed at about 4 mm away from the weld fusion line. It is possible that, in these area, temperature cycle during welding caused precipitation of hardening phases. Overall, the weld area including HAZ showed considerably higher hardness (or strength) than the rest of base metal.

IV.4.4. Mechanical Properties

A. Base Metal Tensile Properties

The base metal tensile properties are summarized in Table 27. A significant difference in tensile properties was observed in the unaged condition. While yield strength and UTS for homogenization heat treated base metal (HT) are about 230 MPa and 620 MPa, those of mill annealed base metal (MA) are about 300 MPa higher. Ductility also decreased from 56 % to 38 %. The tensile properties of solution annealed base metal lie between these two extreme cases. The softening of homogenization treated base metal is caused to a great extent by the removal of residual precipitates including γ', and to a less extent by grain growth during the heat treatment.

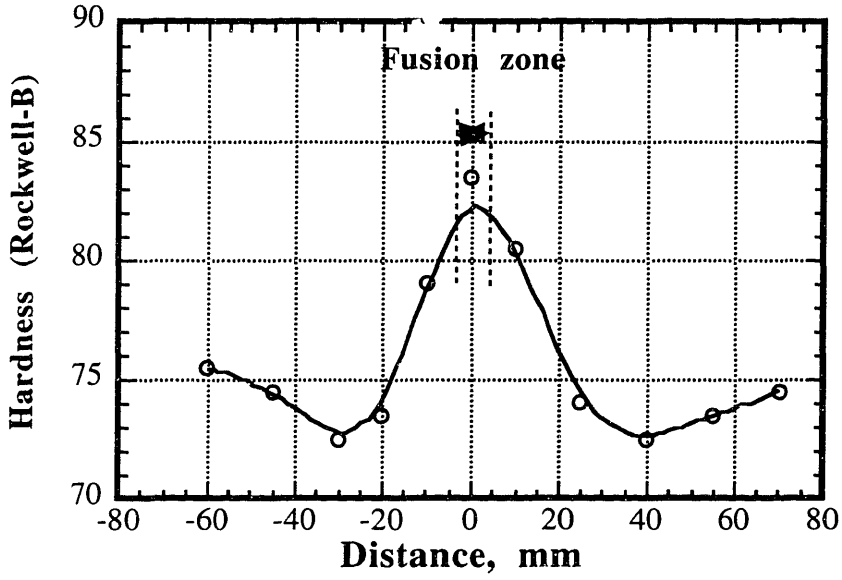

a) Production welds withhomogenized base metal

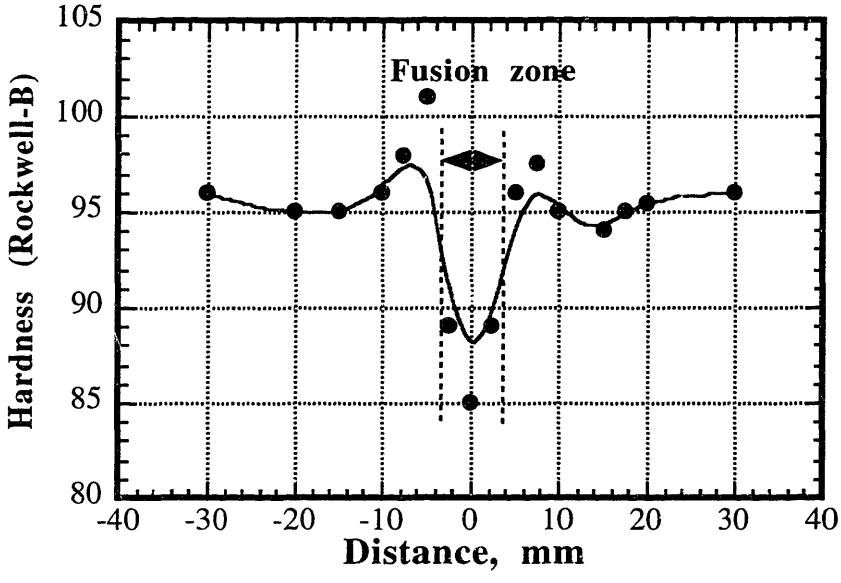

b) Production welds with mill annealed base

Figure 71. Variation of hardness around fusion zone of production welds

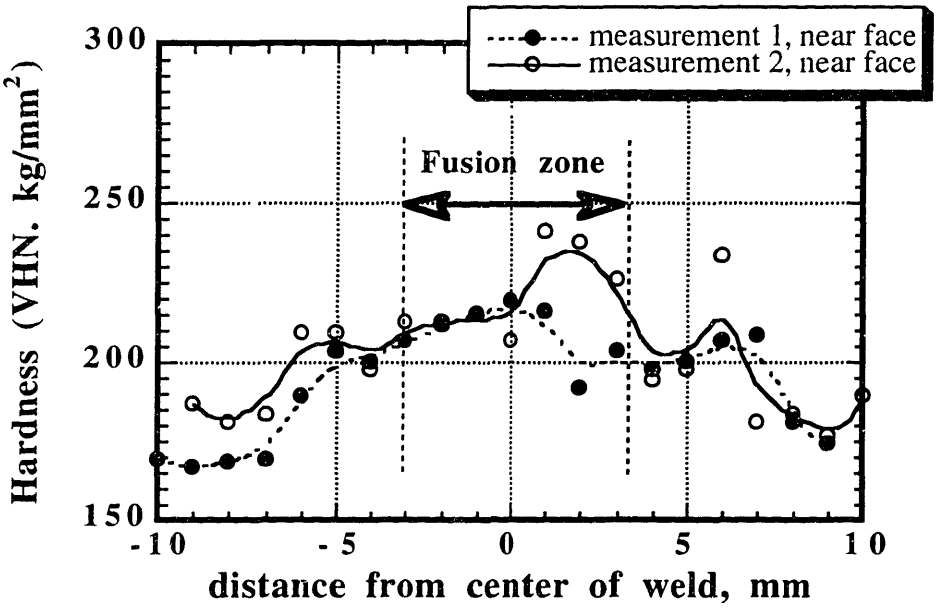

a) At 1 mm inside from the face of the welds

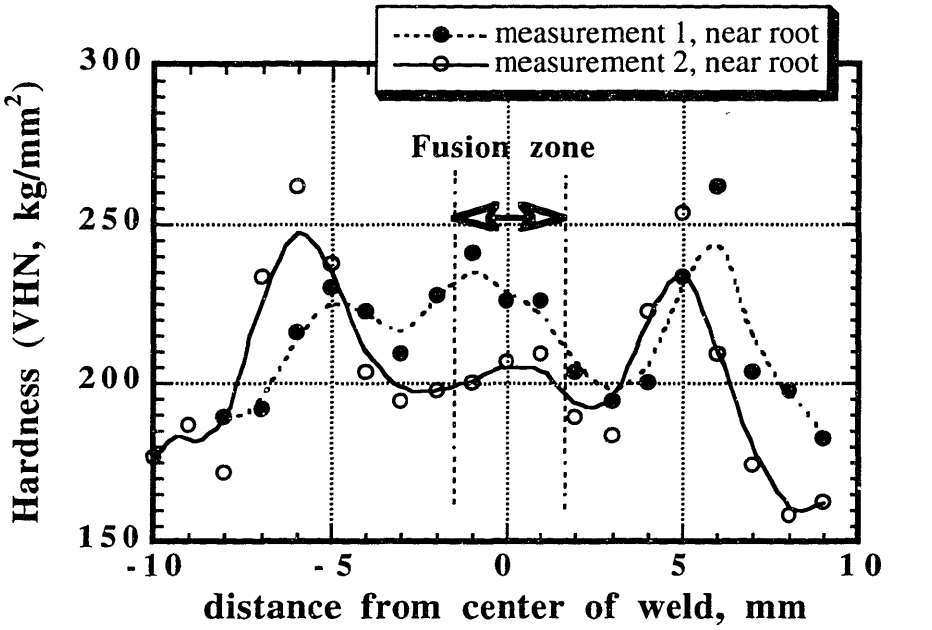

b) At 1 mm inside from the root of the welds

Figure 72. Hardness profile around fusion zone of production welds with homogenized base metal

B. Simulated Production Weld Tensile Properties

Tensile properties of the simulated production welds are shown in Table 27. In the as welded condition, welds with mill annealed base metal show slightly higher yield strength and UTS than welds with homogenized base metal. Depending on the initial condition of the base metal, two different deformation behaviors are observed. First, if the base metal is softer than the as welded fusion weld, such as the case with the homogenized base metal, yielding initiates in the base metal. Subsequent strain hardening makes the base metal stronger than the weld zone. Then weld zone is deformed too. Afterward, both base and weld deform simultaneously until the stress reaches the fracture stress of either metal. Because the length of the reduced section of tensile specimen is 0.75" (19 mm) which is about the size of in-situ hardened zone of weld where the strength would be higher than homogenized base metal, the final fracture always occurs in weld fusion zone even though the UTS of the base metal is lower than that of weld fusion zone. Thus if a larger specimen which contains non-hardened homogenized base metal within the reduced section is used, initial yielding and final fracture would occur outside weld fusion zone.

When base plates are in the mill-annealed condition, both initial yielding and final fracture occur within the weld zone. The fusion weld zone is softer, having lower yield strength and UTS than the surrounding hardened or non-hardened base metal area. Thus, the deformation is more severely constrained within the narrow band of the fusion zone. Even though some deformation is expected in adjacent base metal, the most significant deformation is limited within the weld fusion zone, resulting in substantially decreased elongation to fracture. This difference in deformation sequence explains the marked change in elongation for welds with two different base plate conditions.

In the aged condition, the strength of both weld and base metal changes. Compared to the mill annealed base metal, welds with mill annealed base metal show lower strength and lower elongation. Welds with homogenization heat treated base metal showed greatly improved elongation with about 20 MPa less strength compared to welds with mill annealed base metal.

C. Fatigue Crack Growth Rate of Production Welds

The results of fatigue crack growth rate tests of welds with homogenized plates in the as welded condition are shown in Figure 73. Using the decreasing ΔK method with fixed

K_{max}, ΔK_{th} is estimated as about 3.7 MPa$\sqrt{m}$ with Kmax = 33.33 MPa$\sqrt{m}$. This method is considered to be effective in excluding crack closure effects in measuring fatigue threshold.[65, 71] The fatigue threshold of welds is very close to that of base metal reported by Tobler.[71] Fatigue crack growth rate measurement with R = 0.1 were conducted between ΔK = 15 to 60 MPa$\sqrt{m}$ and shown in same plot. Between a ΔK of from 20 to 60 MPa$\sqrt{m}$, crack growth rate can be correlated using a Paris' law with C = 2.1 x 10^{-9} mm/cycle and m = 3.2. The data tends to deviate below a ΔK of 20 MPa$\sqrt{m}$, but there are not enough data to determine ΔK_{th} with fixed R = 0.1.

Fatigue crack growth rates in aged condition are shown in Figure 74. Welds with mill annealed base metal showed slower crack growth rates than welds with homogenization heat treated base metal. Crack growth rate can be correlated using Paris' law in the ΔK range tested, that is 17.5 to 60 MPa$\sqrt{m}$ with R = 0.1. The Paris' law constants for welds with homogenized base metal are, C = 1.45 x 10^{-10} mm/cycle and m = 4.0. Those for welds with mill annealed base metal are, C = 3.1 x 10^{-11} mm/cycle and m = 4.3.

Table 27. Room temperature tensile properties of production welds

Material	Base metal	PWHT	σ_y (MPa)	UTS (MPa)	elongation (%)	RA (%)
Base	MA	None	514±3	924±1	38.5±0.9	50.3±2.0
	SA	None	389	717	-	-
	HT	None	232±3	622±1	55.8±4.4	
	MA+Age	None[a]	1075±41	1433±0	16.5±0.8	-
Weld	MA	AW[b]	399±2	691±7	28.0±1.0	56.3±5.3
	MA	AW +Age	1024±2	1287±6	9.8±0.1	
	HT	AW	350±5	659±6	55.6	
	HT	AW + Age	1005±5	1264±10	15.1±1.2	

Note: a) data from reference [2]

b) results of manual GTA welds with mill annealed base metal.

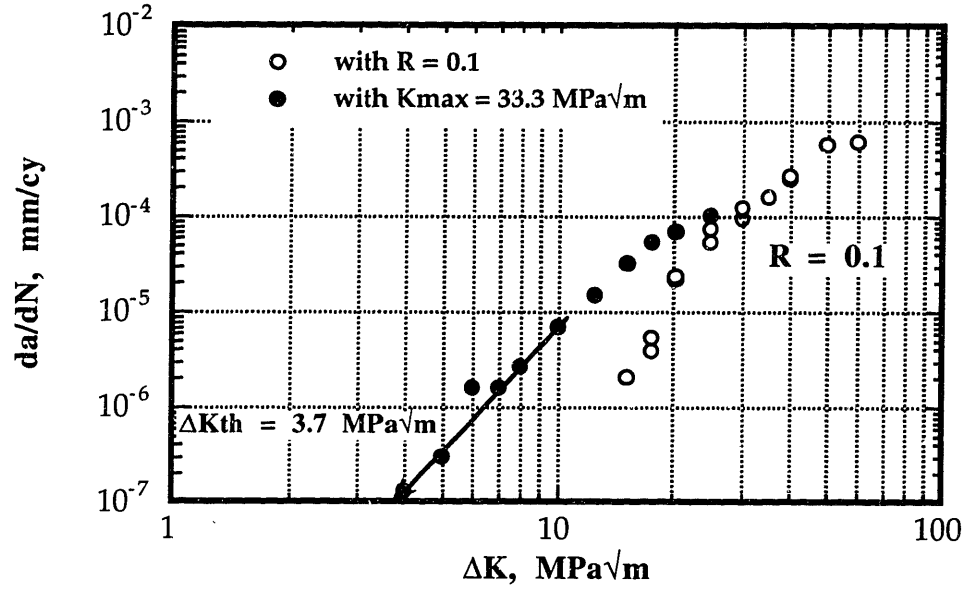

Figure 73. Fatigue crack growth rate of as-welded production welds. Also shown is the result of ΔKth test using Kmax = 33.3 MPa√m.

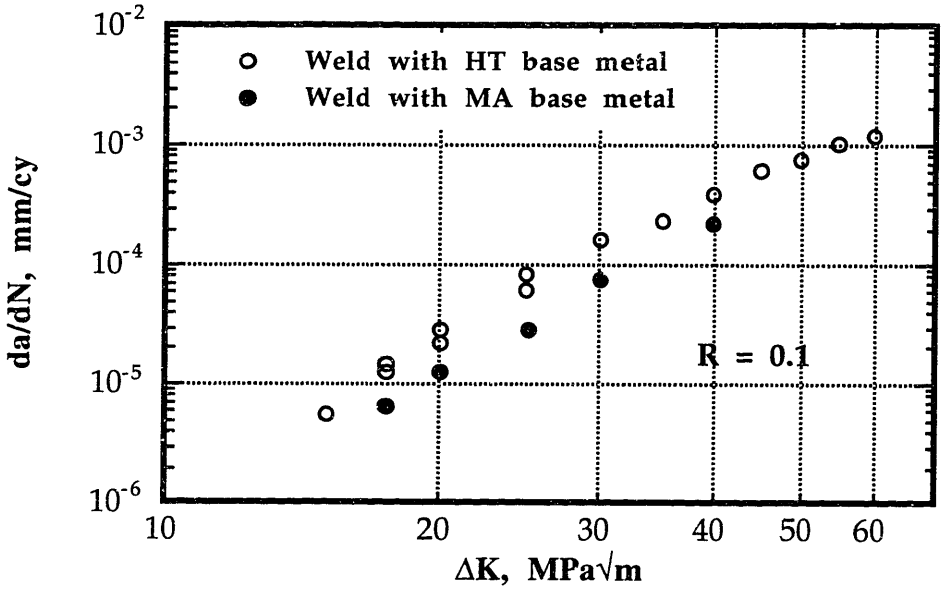

Figure 74. Fatigue crack growth rate of aged production welding

D. Fracture Toughness of Welds

Fracture toughness testing results are shown in Table 28. In the table, the minimum thickness required for valid plane strain fracture toughness tests (thickness » $25J_Q/\sigma_Y$) are shown. For unaged welds, the thickness requirement for valid J-integral test was not satisfied. (roughly 17 mm thick specimens have to be used, contrary to 6 mm thick used in this test) Fracture toughness for simulated production welding with mill nnealed base metal was 141±7 MPa$\sqrt{m}$. Fracture toughness for simulated production welding with homogenized base metal was 144±7 MPa$\sqrt{m}$. There appears to be no significant effect of the condition of base metal on the fracture toughness of welds.

Table 28. Fracture toughness of production welds at room temperature.

Base metal	Weld condition	J_Q, KJ/m^2	$25J_Q/\sigma_Y$	$K_Q(J)$, MPa$\sqrt{m}$
MA	AW +Age	99.8±9.2	~ 2.2 mm	141±7
MA+HT	AW	345±5	~ 17 mm	263±5
MA+HT	AW + Age	104.2±10.3	~ 2.3 mm	144±7

IV.4.5. Fractography Analysis of Production Welds

Fracture surfaces of production welds with homogenized base metal are shown in Figure 75. In both of the as welded and aged conditions, crack propagated as ductile dimple fracture where voids initiated in the interdendritic regions of welds. The particles in the each dimples were identified as Nb-rich phases, such as Laves phase and MC carbide. The voids are slightly larger in as welded condition than in the aged condition.

During fracture toughness testing, one of the specimens showed unusual behavior. After executing about 10 unloading compliance measurements, up to 0.4 mm crack growth, because of unknown reason further unloadings were not executed. The remaining specimen was pulled open very slowly. The photo of the specimen is shown in Figure 75. At first, the fatigue crack size at the side corresponding to face of weld is much larger than that at the root side of weld. On the fracture surface, the crack plane on the face side of root is much smoother and nearly flat. The cross sectional view of production weld is

shown in Figure 68. In the center of weld, a narrow band of primary dendrite structure is aligned in thickness direction. This band stretches from top (face of weld) to near bottom (root of weld). It can be assumed that when crack front is aligned with this band of primary dendrite, the resistance to crack growth become lower and unstable crack growth could happen. With current welding methods, in which the following weld pass is on the top of the underbead at the same x-y coordinate, it is quite possible to form a wide band of primary dendrite in the thickness direction, thus producings weak plane. So it is necessary to review current production welding procedure to eliminate such an extended dendrite band, especially in thickness direction.

IV.4.6. Summary and Discussion

The selection of the base metal condition for the welding is crucial to determine the properties of weldments in as-welded condition which is important to assess the performance of the conduit during fabrication processes of cable assembly. For the tube reduction and winding processes, enough strength and ductility is needed to prevent preferential deformation within the weld, which would result in kink and failure. When the base metal is in the mill-annealed condition, the strength of weld is the same or lower than adjacent base metal. The net effect of this is that deformation becomes more confined within the weld and ductility become smaller. As ductility will be smaller as the amount of cold work increases, it is assuring to have welds with higher strength and greater ductility than the base metal. In this respect, the base metal condition with hardness less than 80 (Rockwell-B) was selected for production weld study, based on the results of high temperature (1050°C/1hr) homogenization heat treatment. When the homogenized base metal is used, the strength of the welds is higher than surrounding base metal and the preferential deformation within the weld fusion zone can be avoided.

Fatigue crack growth rate of production welding is similar to that of other welds studied. The fatigue crack growth threshold value is about 3.7 MPa$\sqrt{m}$, similar to that of base metal. [71]

Fracture toughness of production welding is about 20 % higher than that of manual-GTAW at room temperature. The strength-toughness combination of production weld is 1005 MPa - 144 MPa$\sqrt{m}$ for weld with homogenized base metal and, 1024 MPa - 141 MPa$\sqrt{m}$ for weld with mill annealed base metal. Fracture surface analysis showed fully ductile dimple fracture, with the voids initiated in the interdendritic region.

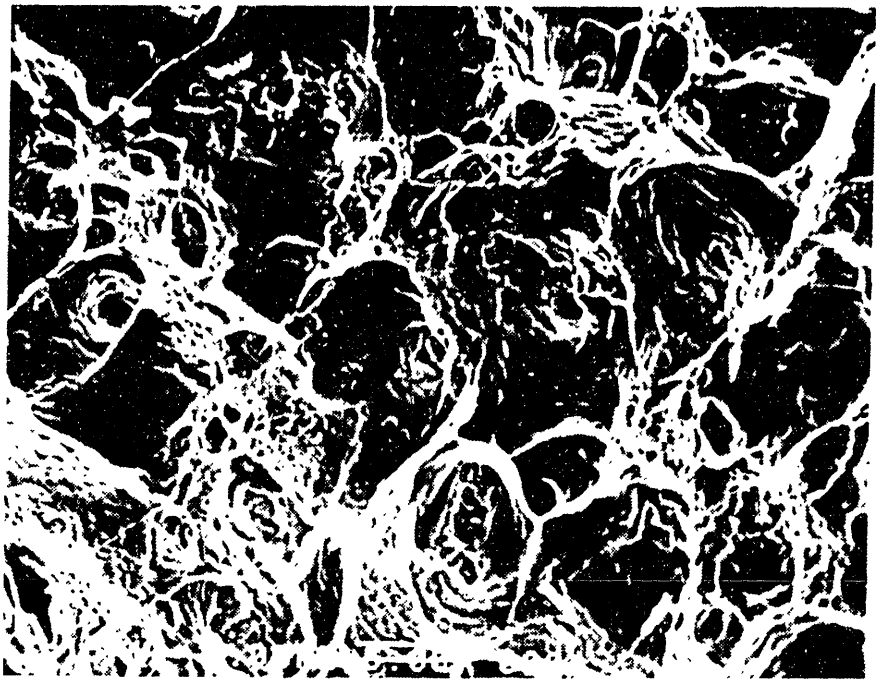

a) As welded production welds with homogenized base metal, 2000X

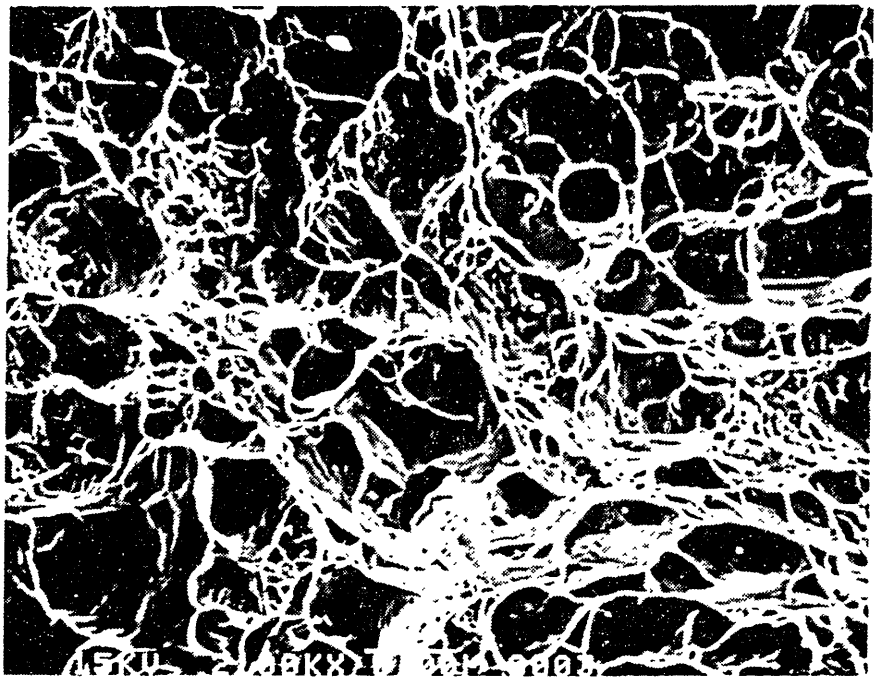

b) Aged production welds with homogenized base metal, 2000X

Figure 75. Fractographs of production welds

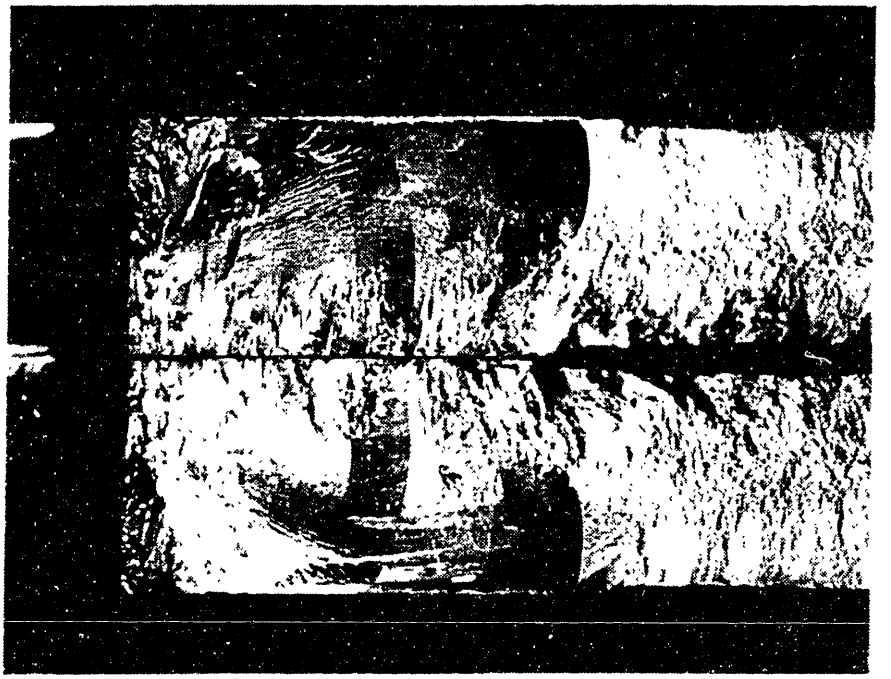

Figure 76. Surface of J-integral tested specimen, showing preferential crack growth near the face of weld.

IV.5. Evaluation of Tensile Properties for Fabrication

IV.5.1. Tensile Properties of GTA Welds with 908 Filler.

A. Weld Averaged Tensile Properties of 7 mm-thick GTA Welds with 908 Filler

The results of full-thickness tensile tests of 7 mm-thick GTA welds with 908 filler are summarized in Table 29. The relatively low UTS is explained by a loss of strain hardening ability of the weld. After 9 % cold work is applied, the yield strength increases by about 140 MPa and UTS by about 50 MPa. The strength increased further as the cold work increased but at slower rate. Ductility decreased gradually from 28 % to 12 % as cold work increases from 0 % to 13 %. Even though the ductility of welds changed considerably, reduction of area (RA) for each test condition are almost unchanged.

Table 29. Weld averaged tensile properties of 7 mm-thick GTA welds with 908 filler.

Condition	σ_y, MPa	UTS, MPa	elongation, %	RA, %
AW	399±2	691±7	28.5±0.5	56.6±5.3
AW + 9% CW	545±7	740±5	17.5±1.5	53.2±3.0
AW + 11% CW	647±2	774±3	11.8±1.6	55.3±5.2
AW + 13% CW	653±1	773±1	12.4±0.4	58.2±0.5

AW: As-welded condition

CW: Cold work

B. Tensile Properties Variation through the Thickness of 7 mm-thick GTA Welds with 908 Filler

The results of partial-thickness tensile tests of 7 mm-thick GTA welds with 908 filler are summarized in Table 30. In the as-welded condition, the root of the weld is stronger than the face of weld for all of the condition tested. Ductility decreased gradually at both the face and root of the weld as the amount of cold work increased from 0 % to 13 %. Aging increased both yield strength and ultimate tensile strength by about 600 MPa. However, ductility was decreased to about 5 % at both locations.

Table 30. Tensile properties variation through the thickness of 7 mm-thick GTA welds with 908 filler.

Condition	location	σ_y, MPa	UTS, MPa	elongation, %	RA, %
AW	**F** (face)	396±1	672±5	28.6±1.2	54.5±1.6
	R (root)	444±10	700±7	25.3±0.2	53.1±1.9
AW + 9% CW	**F**	545±29	740±28	21.3±0.1	46.4±5.3
	R	585±11	766±19	17.7±1.2	40.9±8.9
AW + 11% CW	**F**	591±6	748±4	16.4±0.8	55.3±2.0
	R	625±4	761±1	12.9±0.1	60.0±4.6
AW + 13% CW	**F**	669±12	793±1	12.9±0.6	60.7±2.5
	R	697±14	798±9	12.2±0.8	62.9±2.4
AW + 9% CW + Age	**F**	1156±2	1363±3	8.0±0.2	26.8±4.1
	R	1171±5	1345±1	8.4±0.4	31.4±0.5

Note: Description on the location where specimenes were taken is shown in Figure 26.

C. Results of Hardness Measurements of 7 mm-thick Welds with 908 Filler

The hardness profiles along the mid-plane of 7 mm-thick GTA welds with 908 filler are shown in Figure 77. In the as-welded condition, the hardness of the weld is slightly less than that of the mill annealed (MA) base metal. Increasing the amount of cold work raised hardness in both the weld and adjacent base metal. Along the mid-plane of the weld, within 2 mm of the fusion boundary, the hardnesses are almost the same in all unaged conditions. Beyond that distance, the hardness approaches nominal base metal values. As the amount of cold work increases, the hardness of fusion zone and adjacent heat affected zone becomes much lower than far-away base metal.

The hardness variation through the thickness of 7 mm-thick GTA welds with 908 filler are shown in Figure 78. Hardness is slightly higher near the root of the weld than near the face of the weld. Such profile remained unchanged with cold work. Aging reduced the hardness variation through the thickness and resulted in a uniform hardness profile.

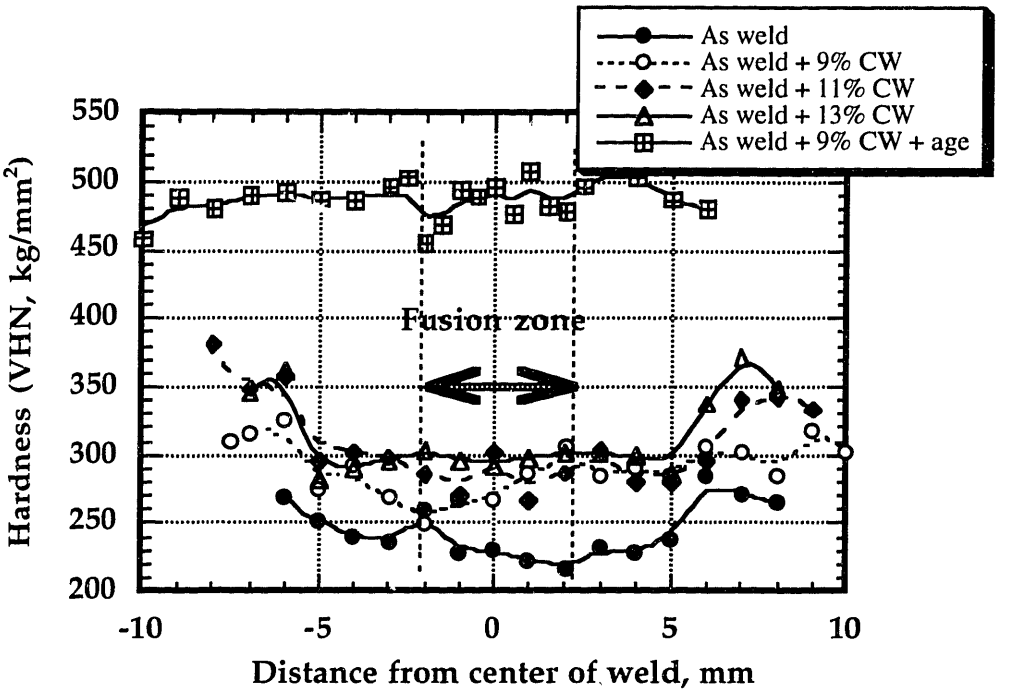

Figure 77. Microhardness profile along the mid-plane of 7 mm-thick GTA welds with 908 filler

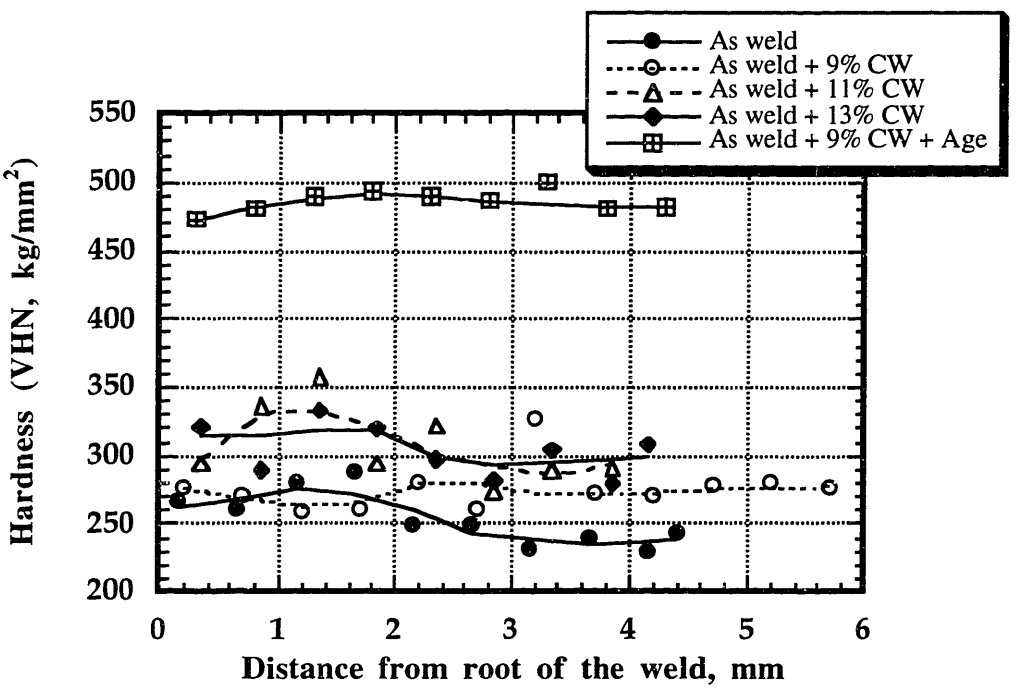

Figure 78. Microhardness variation across the thickness of the 7 mm-thick GTA welds with 908 filler.

D. Weld Averaged Tensile Properties of 13 mm-thick GTA Welds with 908 Filler

The results of full-thickness tensile tests of 13 mm-thick GTA welds with 908 filler are summarized in Table 31. As welded material showed about the same strength as 7 mm-thick GTA welds with 908 filler but with increased ductility. The increase in strength with cold work is larger than that in 7 mm-thick GTA welds with 908 filler. After 9 % cold work, ductility is about 26 %.

Table 31. Weld averaged tensile properties of 13 mm-thick GTA welds with 908 filler

Condition	σ_y, MPa	UTS, MPa	elongation, %	RA, %
AW	409	687	44.0	44.4
AW + 5% CW	522±14	735±4	29.0±2.0	40.8±0.1
AW + 9% CW	622±3	792±9	26.0±2.0	40.8±0.7

AW: As-welded condition

CW: Cold work

E. Tensile Properties Variation through the Thickness of 13 mm-thick GTA welds with 908 Filler

The results of partial-thickness tensile tests of 13 mm-thick GTA welds with 908 filler are summarized in Table 32. In the as-welded condition, the face of the weld showed lower strength than the other locations tested. Ductility showed maximum at the face of the weld while those at the other three locations showed almost identical values. At about three-quarter of the thickness from the face of the weld (location BT), the strength was lower than that of surrounding materials. This spatial variation of strength is more evident in the 9 % cold worked condition but become less significant after aging heat treatment.

Ductility also showed a similar trend of having higher ductility at the location where the strength was lower. Generally, ductility decreased to about 17 % gradually at all locations as the amount of cold work increased from 0 % to 9 %. After aging, ductility decreased substantially.

Table 32. Tensile properties variation across the thickness of 13 mm-thick GTA welds with 908 filler

Condition	location	σ_y, MPa	UTS, MPa	elongation, %	RA, %
AW	**T** (face)	344±8	614±1	41.4±1.4	
	TB	446±4	700±1	30.1±0.3	
	BT	432±8	671±21	30.5±2.1	
	B (root)	444±8	700±7	30.8±0.6	
AW + 5% CW	**T**	469±14	665±1	21.5±4.7	
	TB	551±9	727±7	23.1±1.3	
	BT	532±7	720±8	29.8±0.2	
	B	637±8	793±6	25.7±1.4	
AW + 9% CW	**T**	578±8	717±14	16.5±3.0	
	TB	684±13	844±1	17.0±1.6	
	BT	597±1	774±6	17.7±1.9	
	B	674±4	839±3	19.1±1.2	
AW + 9% CW + Age	**T**	1130	1323	6.5	26
	TB	1157±16	1343±21	7.7±0.6	20.5±3.2
	BT	1133±2	1307±1	6.2±1.5	33
	B	1162±15	1384±8	8.9±0.3	25.8±0.4

Note: Description on the location where specimenes were taken is shown in Figure 26.

F. Results of hardness measurement of 13 mm-thick GTA welds with 908 filler

The hardness profiles along the mid-plane of 13 mm-thick GTA welds with 908 filler are shown in Figure 79. In the as-welded condition, the hardness of weld is slightly higher than the adjacent base metal. As cold work were increases, the hardness profile is reversed in that the weld had slightly lower hardness after 9 % of cold work. Aging eliminated the hardness mismatch between weld and base metal.

The hardness variation through the thickness of 13 mm-thick GTA welds with 908 filler are shown in Figure 80. In all of the unaged conditions, the hardness minima occur about 3 mm away from the root of the weld. Again, aging eliminated the hardness mismatch through the thickness of the weld.

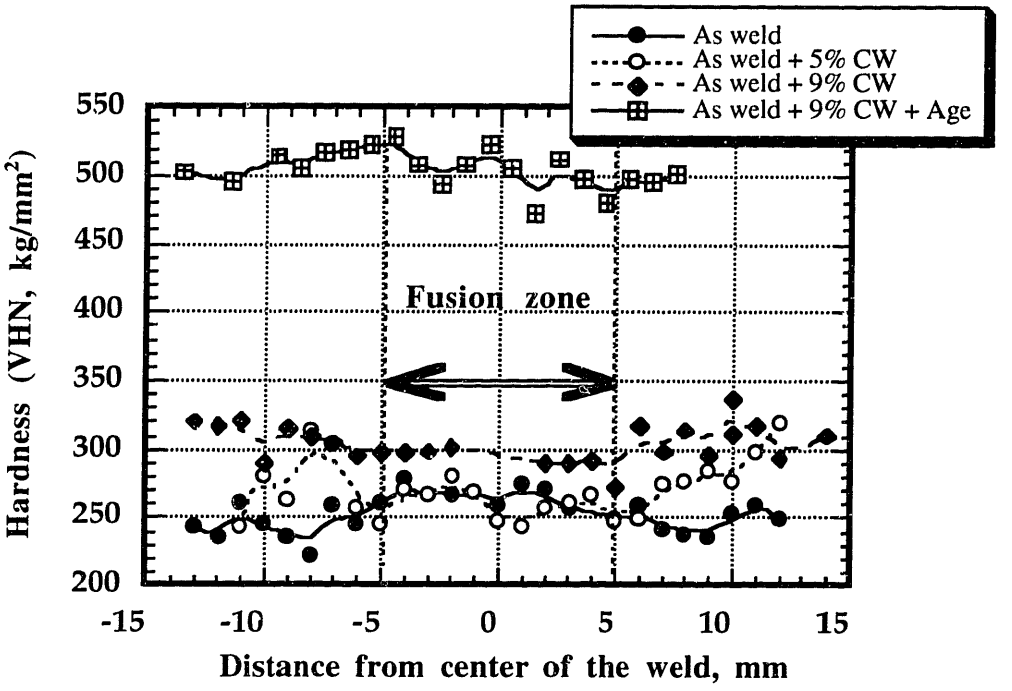

Figure 79. Microhardness profile along the mid-plane of the 13 mm-thick GTA welds with 908 filler

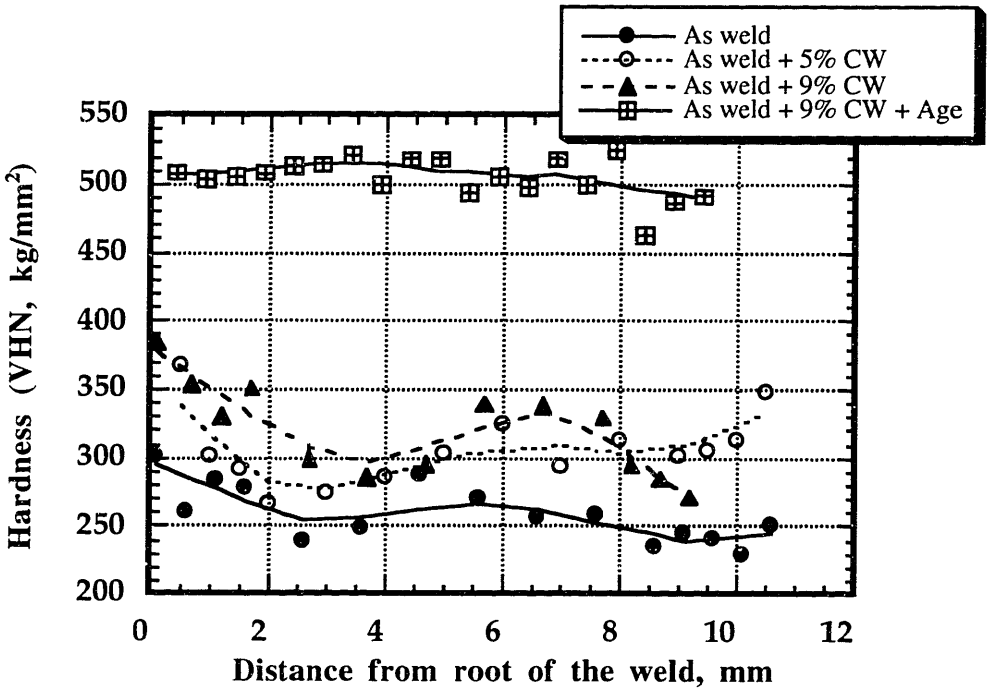

Figure 80. Microhardness variation across the thickness of the 13 mm-thick GTA welds with 908 filler

IV.5.2. Tensile Properties of GTA Weld with 9HA Filler.

A. Weld Averaged Tensile Properties of 7 mm-thick GTA Welds with 9HA filler

The results of full-thickness tensile tests of 7 mm-thick GTA welds with 9HA filler are summarized in Table 33. In the as welded condition, GTA welds with 9HA filler shows a slightly lower yield strength and ductility than those of GTA welds with 908 filler. After 9 % cold work, the yield strength of GTA welds with 9HA filler approaches that of GTA welds with 908 filler. However, ultimate tensile strength and ductility are much lower than those of the GTA welds with 908 filler at the same conditions.

Table 33. Weld averaged tensile properties of 7 mm-thick GTA welds with 9HA filler

Condition	σ_y, MPa	UTS, MPa	elongation, %	RA, %
AW	364±3	617±2	25.5±0.5	64.2±0.9
AW + 5% CW	491±7	667±3	19.8±1.2	61.9±2.7
AW + 9% CW	541±3	680±6	15.3±1.2	68.6±2.8

B. Tensile Properties Variation through Thickness of 7 mm-thick GTA Welds with 9HA Filler

The results of partial-thickness tensile tests of GTA welds with 9HA filler are summarized in Table 34. In the as-welded condition, the root of the weld is stronger than the face of weld in all test conditions. The face of weld showed larger ductility than the root of weld in all conditions tested. The difference between them decreased after aging heat treatment.

With aging, the difference of strength between the face and the root of the weld is about 70 MPa. Ductility is almost the same as that of the GTA welds with 908 filler at both location after and aging.

Table 34. Tensile properties variation across the thickness of 7 mm-thick GTA welds with 9HA filler

Condition	location	σ_y, MPa	UTS, MPa	elongation, %	ΔA, %
AW	**F** (face)	364±3	622±10	31.5±0.5	62.9±4.4
	R (root)	389±17	641±9	24.6±0.2	71.0±0.5
AW + 5% CW	**F**	416±8	610±3	23.6±0.8	69.7±1.9
	R	489±24	659±17	18.6±0.5	63.4±0.4
AW + 9% CW	**F**	524±4	671±8	20.1±1.0	60.9±1.9
	R	598±4	739±20	14.3±0.9	53.0±1.5
AW + 9% CW + Age	**F**	1029±6	1265±10	8.4±0.1	30.3±5.8
	R	1104±8	1278±8	7.5±0.1	33.5±9.4

Note: Description on the location where specimenes were taken is shown in Figure 26.

C. Results of Hardness Measurement of Welds with 9HA Filler

The hardness profiles along the mid-plane of 7 mm-thick GTA welds with 9HA filler are shown in Figure 81. In the as-welded condition, the hardness of the weld is slightly less than that of the adjacent base metal. Increasing the amount of cold work increased hardness in both weld and base metal but at different rates. For unaged conditions, within 2 mm from the fusion zone, the hardness of base metal were close to that of the weld. In the aged condition, the fusion zone has lower hardness than the base metal. Unlike the unaged condition, the hardness increases to that of the base metal right outside of the fusion zone.

The hardness variation through the thickness of 7 mm-thick GTA welds with 9HA filler are shown in Figure 82. The root of the welds showed higher hardness than the face of the welds in the as-welded and cold worked conditions. This profile remained unchaged after the aging heat treatment. In the aged condition, hardness varied from 490 at the root of the weld to about 440 at the face of the weld.

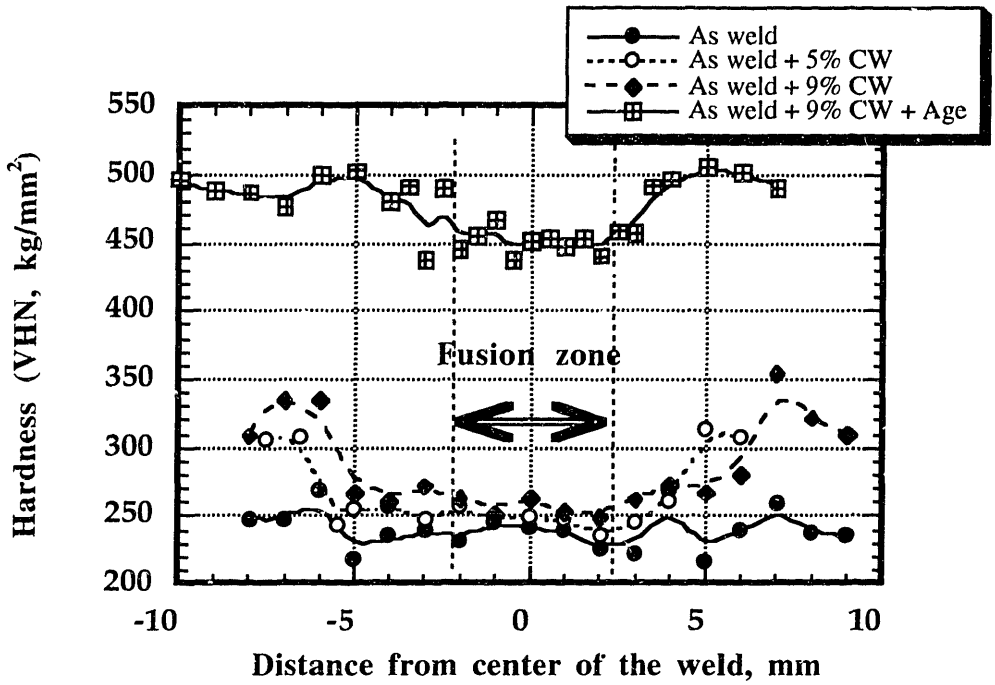

Figure 81. Microhardness profile along the mid-plane of the 7 mm-thick GTA welds with 9HA filler

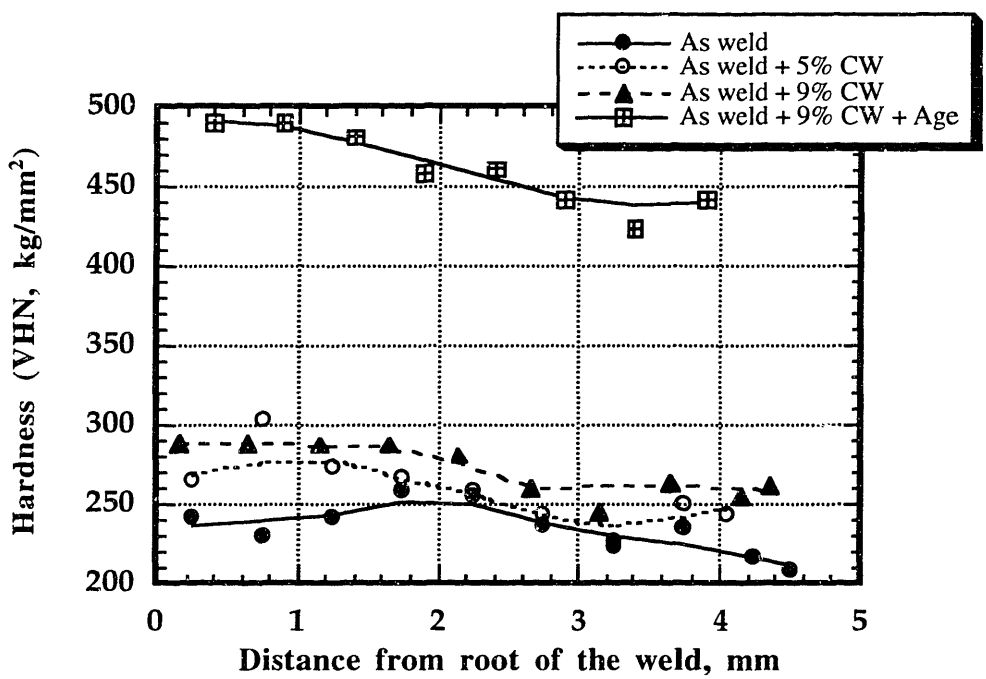

Figure 82. Microhardness variation through the thickness of the 7 mm-thick GTA welds with 9HA filler

IV.5.3. Tensile Properties of Gas Tungsten Arc Weld with 9HB Filler.

A. Weld Averaged Tensile Properties of 7 mm-thick Welds with 9HB filler

The results of full-thickness tensile tests of 7 mm-thick GTA welds with 9HB filler are summarized in Table 35. Strengths are lower than those of GTA welds with 9HA filler in all tested conditions. After 9 % cold work, yield strength is 515 MPa and ductility is about 16 %.

Table 35. Weld averaged tensile properties of 7 mm-thick GTA welds with 9HB filler

Condition	σ_y, MPa	UTS, MPa	elongation, %	RA, %
AW	328±7	556±6	25.6±1.4	72.5±0.8
AW + 5% CW	408±2	583±1	19.8±0.4	73.1±0.8
AW + 9% CW	515±4	662±3	16.6±0.4	65.8±2.8

B. Tensile Properties Variation through the Thickness of 7 mm-thick Welds with 9HB Filler

The results of partial-thickness tensile tests of 7 mm-thick GTA welds with 9HB filler are summarized in Table 36. In the as-welded condition, the root of the welds are stronger than the face of the welds for all test conditions. The faces of the welds showed larger ductility than the roots of welds except the as-welded + 9 % cold worked condition. Generally, strengths are lower than the GTA welds with 908 and 9HA fillers at both locations in all test conditions.

The differences become more evident in the aged condition. The yield strength difference between the face and the root of the weld is about 250 MPa. There is also a large difference in ultimate tensile strength at both locations. Ductiliy of the welds decreased after aging heat treatment.

Table 36. Tensile properties variation across the thickness of 7 mm-thick GTA welds with 9HB filler

Condition	location	σ_y, MPa	UTS, MPa	elongation, %	RA, %
AW	**F** (face)	313±1	531±6	26.5±1.4	72.7±5.3
	R (root)	380±2	599	22.6	72.3±10.0
AW + 5% CW	**F**	385±17	568±2	21.3±0.7	62.4±16.3
	R	483±2	635±2	17.6±0.4	74.7±3.0
AW + 9% CW	**F**	495±8	638±3	16.2±0.7	65.3±5.2
	R	561±12	751±21	18.9±0.2	52.2±1.9
AW + 9% CW + Age	**F**	843±3	1071±10	8.1±0.1	37.2±0.4
	R	1100±47	1294±40	6.5±0.5	29.3±3.9

Note: Description on the location where specimenes were taken is shown in Figure 26.

C. Results of Hardness Measurement of Welds with 9HB Filler

The hardness profile along the mid-plane of 7 mm-thick GTA welds with 9HB filler are shown in Figure 83. In the as-welded condition, hardness of GTA welds with 9HB filler is lower than that of the adjacent base metal. With cold work, the hardness profile approached the U-shape. In the aged condition, hardness within the weld, especially near the center of the weld, are much lower than that of the base metal.

The hardness variation through the thickness of 7 mm-thick GTA welds with 9HA filler is shown in Figure 84. The root of the welds are consistently stronger than the face of the welds. The hardness mismatch becomes greater after the aging heat treatment. The hardness decreases from about 480 at the root of the weld to about 320 at the face of the weld.

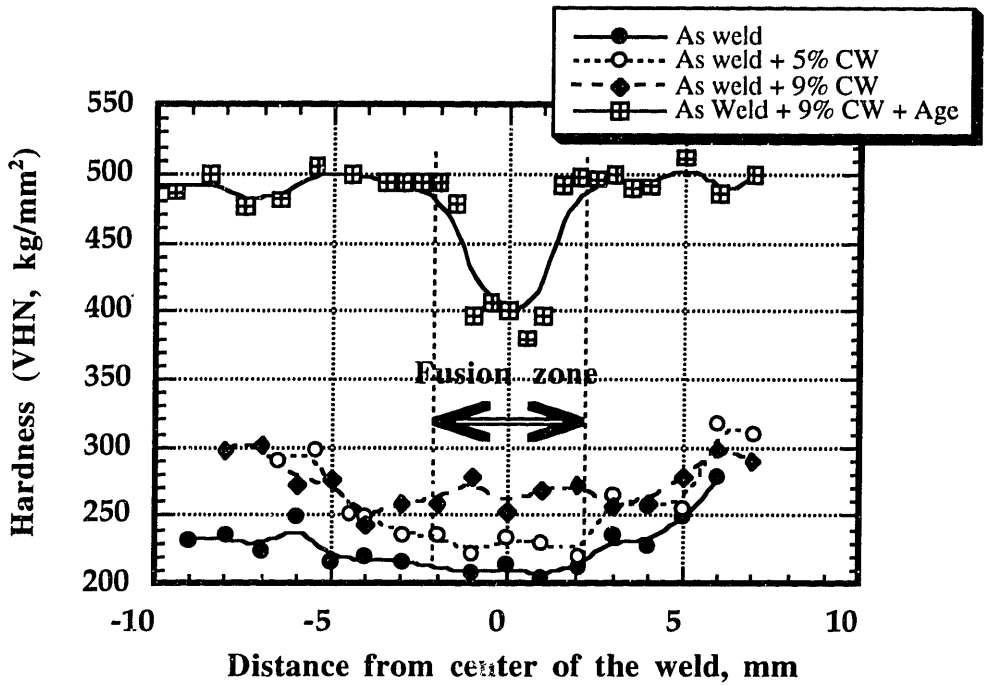

Figure 83. Microhardness profile along the mid-plane of the 7 mm-thick GTA welds with 9HB filler

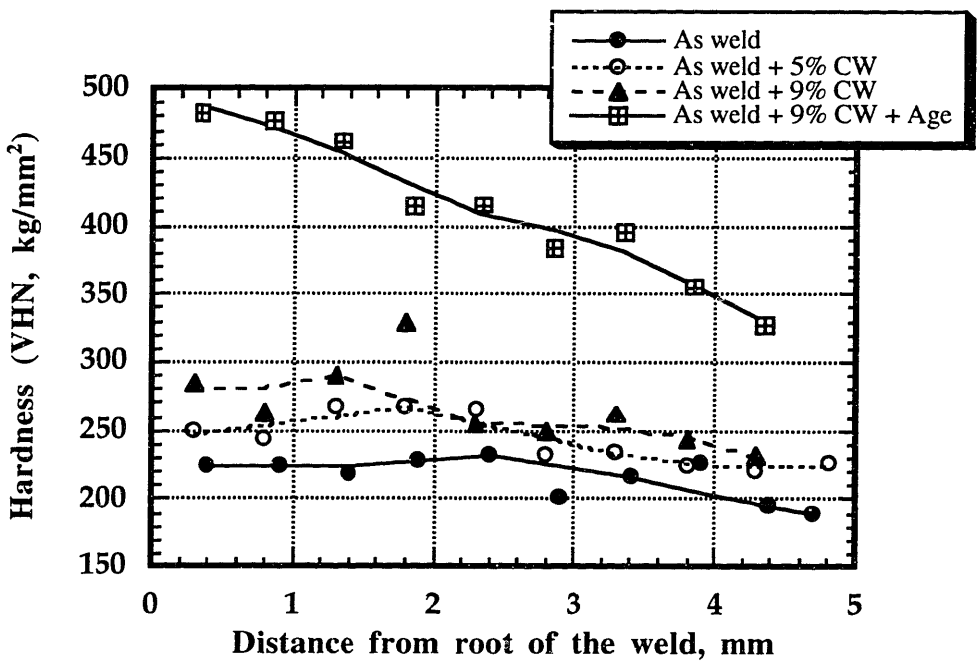

Figure 84. Microhardness variation through the thickness of the 7 mm-thick GTA welds with 9HB filler

IV.5.4. Aging responses of GTA welds

The changes of hardness of GTA welds vs. aging time at 650 °C are summarized in Figure 85. The hardness values were taken as the average of several measurements taken through the thickness of welds. Initial condition of welds is in the as-welded state. For GTA welds with 908 and 9HA filler, hardness is still increasing after 200 hours. However, hardness changes little after 100 hours.

The results for cold worked GTA welds are shown in Figure 86. For all three GTA welds, hardness reaches a plateau at about 100 hours.

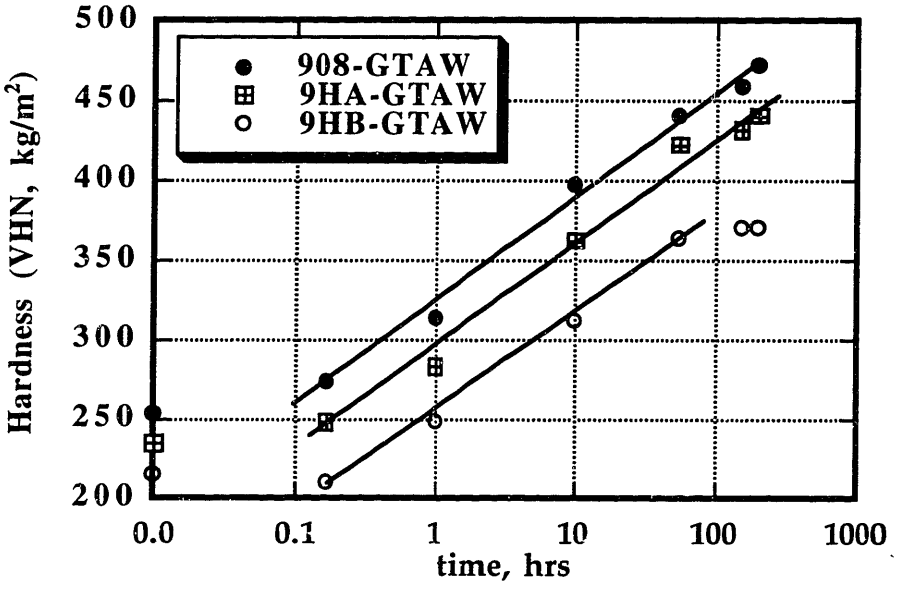

Figure 85. Aging responses of various GTA welds (initial condition: as-weld, aging temperature: 650 °C)

IV.5.5. Summary and Discussion

A. Effects of Filler Composition

The results of full-thickness tensile tests are summarized in Figure 87 including various base metal properties. Tensile properties of GTA welds vary considerably depending on the filler metal used.

In the as-welded condition, GTA welds with 908 filler show yield strength of about 400 MPa which is about the same value as that of solution annealed (SA) base metal. The removal of alloying elements (as in the case of 9HA and 9HB) resulted in a significant reduction in both yield strength and ultimate tensile strength. Some degree of solid solution hardening might have caused this strength difference even though all three alloying elements (Nb, Ti, and Al) are considered to be the precipitation hardening constituents. Aside from the possibility of limited solid solution hardening by alloying elements, in-situ aging of prior passes by subsequent welding passes would have contributed to the hardening of GTA welds, especially that of GTA welds with 908 filler.

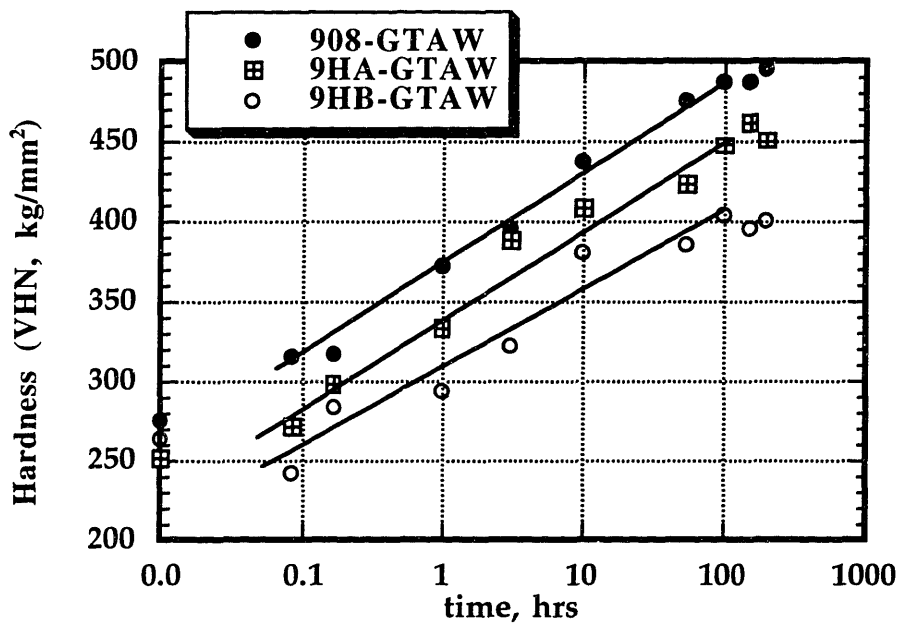

Figure 86. Aging responses of various GTA welds (initial condition: as weld + 9 % cold work, aging temperature: 650 °C)

Despite having lower strength, GTA welds with 9HA and 9HB filler showed lower ductility than GTA welds with 908 filler. This does not necessarily mean that they are less ductile than GTA welds with 908 filler. The specimen geometry used in this study is such that the gauge section contains both weld and base metal. Therefore, the ductility measured using an extensometer does not provide an accurate measure of the true ductility of the weld except for a few partial thickness specimens which had a gauge length of more than 13 mm. Rather, the ductility represent the low bound values of each test condition. In this

study, base metal plates were used as in the mill annealed condition which has a higher strength than the weld. Under loading, weld zone is deformed heavily surrounded by the stronger base metal. That combination tends to give underestimated ductility values. The flip side of that is that if the base metal can be kept softer than the weld, most of the deformation will be avoided within weld zone and be distributed in surrounding base metal. This situation would be especially important to reduce the risk of crack initiation/propagation within weld zone during the manufacturing processes.

Unlike ductility, reduction in area (RA) is more closely related to the ductility of the weld itself. Specimens failed within weld proceeded by necking without exception. The reduction of area changed inversely with strength.

With up to 9 % cold work, all three GTA welds were hardened more or less the same way. The increases in yield strength are larger than those of UTS. Ductility decreased to 50 % of that of the as-welded condition. The reduction of area did not change much with cold work.

In the as-weld + aged condition, the yield strength of GTA welds with 908 filler is slightly less than that of base metal. However, UTS is about 100 MPa less than that of base metal. Welds with 9HA and 9HB fillers showed lower strength than GTA welds with 908 filler. The difference in strength between three welds are aggravated by aging which fully utilizes the alloying elements present in filler metal. The low strength of GTA welds with 9HB filler is attributed to the very low alloying element content (total 1.5 % compared to 5.6 % in 908 filler). 9HA which has 3 % of alloying elements showed intermediate behavior with 970 MPa which is about 9 % less than GTA welds with 908 filler. Despite the diffrences in strength, ductility values are almost identical for all three GTA welds.

The effects of cold work prior to aging is to increase yield strength. The change in yield strength is the greatest in GTA welds with 9HB filler. It has been previously reported that cold work enhanced the precipitation of γ' in the 908 base metal.

The most significant effects of aging was the loss of ductility in GTA welds. A similar observation for other precipitation hardening materials had been reported earlier.[51, 72] The effects of different weld filler and/or amount of prior cold work on the ductility of GTA welds seemed minimal in the aged condition. However, it has to be mentioned that the fracture toughness of the weld is a strong function of filler metal composition.

The hardness of the weld changes gradually with increasing cold work. In the as-welded condition, the hardness of GTA welds are slightly less than the adjacent base metal in all three GTA welds. For GTA welds with 908 filler, the hardness of the weld and the base increases at about the same rate as the amount of cold work increased from 0 % to 13 %. Unlike GTA welds with 908 filler, GTA welds with 9HA and 9HB fillers showed less increases in hardness compared to base metal. The hardness of the heat affected zone is almost the same as that of weld. In all three GTA welds, the hardness profile within weld, which initially showed local fluctuation caused by different thermal cycle and residual thermal stress, approached a relatively smoother U-shape as the amount of cold work increased.

During welding, various microstructural modifications occur in both weld and base metal. The base metal within 2 mm of the fusion zone experienced thermal cycles high enough to resolutionize small amount of γ' which was formed during the mill anneal process. This zone coincides with the grain growth zone near weld.

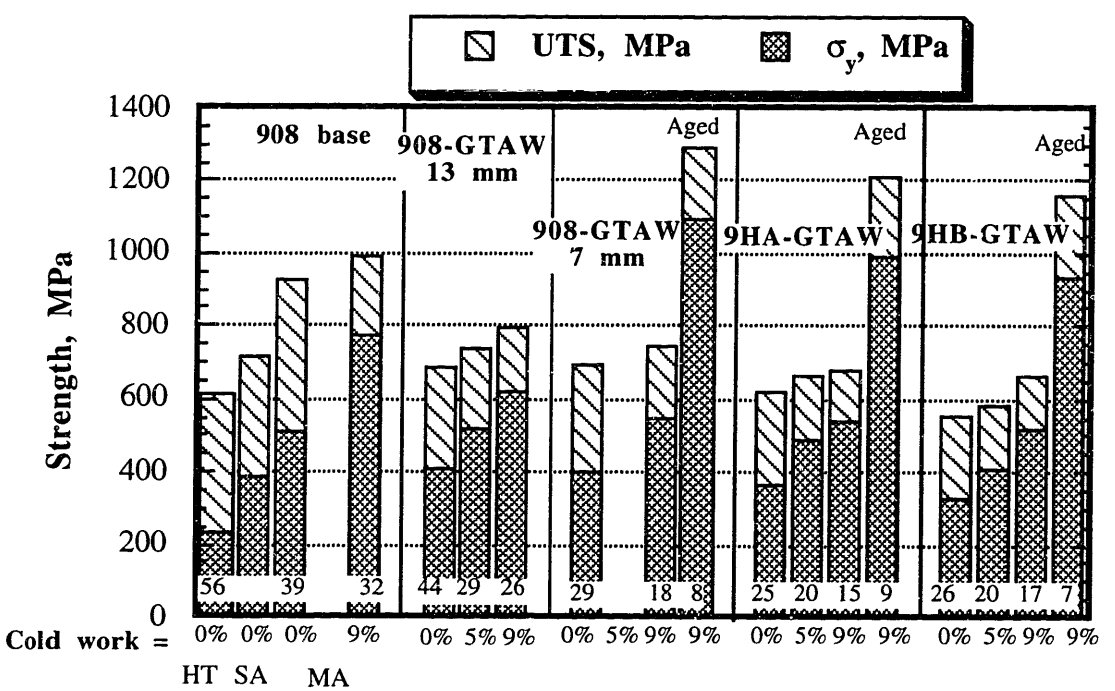

Figure 87. Whole-thickness tensile properties of 908 base and weld. Ductility of GTA welds are written at the bottom of the bar at each condition.

B. Effects of the Thickness of Weld

The effects of thickness is shown in Figure 87. In the as-welded condition, the strength of 7 mm-thick and 13 mm-thick GTA welds with 908 filler are the same even though they show a considerably different ductility and reduction of area. With 9 % cold work, 13 mm-thick welds showed higher strength and ductility than 7 mm-thick GTA welds with 908 filler. The large increase in ductility in thick section welds is due to the specimen geometry. The thick weld contains more weld metal and less of base metal within the gauge section of the tensile specimen. With such a combination, the constraint imposed on the softer weld by the stronger base become less and the ductility within the gauge length become larger.

C. Spatial Variation of Tensile Properties

In the as-welded condition, there is variation in microstructure and mechanical properties within the GTA welds. The complex thermal cycles during welding causes localized annealing, grain growth, homogenization, and precipitation of hardening phases depending on the materials being welded. In multi-pass welding, the microstructure of earlier welding passes are modified by subsequent welding passes. Also the effects of dilution become important when the chemical composition of filler is different from that of base metal.

In the as-welded condition, the material at the bottom half of the weld which contains the root of the weld showed higher strength than the one at the top half of the weld. For precipitation hardening alloys, the most dominant microstructural modification is aging of the underbead by subsequent welding passes. As shown in Figure 88, the tensile properties for material taken at location T (the first quarter near the face of the 13 mm-thick GTA welds) has the lowest strength and the largest ductility. On the other hand, the other three, TB (the second quarter of material from the face of the 13 mm-thick GTA welds), BT (the third quarter of material from the face of the 13 mm-thick GTA welds) and B (the quarter of material from the root of the 13 mm-thick GTA welds) showed nearly identical properties. The hardness measurement, shown in Figure 80, also support this argument.

During cold rolling of thick plates, the plastic deformation tends to be concentrated at the surface of the plates, resulting in relatively small effective plastic deformation at the mid-plane of the plates. In the case of weld, which has different flow characteristics depending on location, an additional factor has to be considered. When plates are rolled, the face of

weld which is softer deforms more readily than the root of weld which is stronger. This would shift the plane, where the deformation is the lowest, toward the root of weld. Thus, the lowest strength is observed below near the root of the weld. A similar spatial variation was also observed, though less extent, in 7 mm-thick GTA welds with 908 filler, as shown in Figure 89. The strength at the face of weld (F) was less than that at the root of the weld (R) in cold worked condition. This strength difference disappeared after aging heat treatment.

As shown in Figure 89, when the filler metal 9HA and 9HB were used, the strength was reduced both at the face (F) and the root of the welds (R). Unlike the GTA welds with 908 filler, this strength difference was not eliminated after aging heat treatment. In GTA welds with 9HA filler, the face of the weld has the composition of 9HA filler. However, dilution at the root of weld formed a solidified structure whose chemical composition is between that of base meatl and 9HA filler. This difference in composition causes a large difference in the strength between the face and the root of the welds. The same behavior happens in GTA welds with 9HB filler. In GTA welds with 9HB filler, the difference in the strength is far greater than that in GTA welds with 9HA filler.

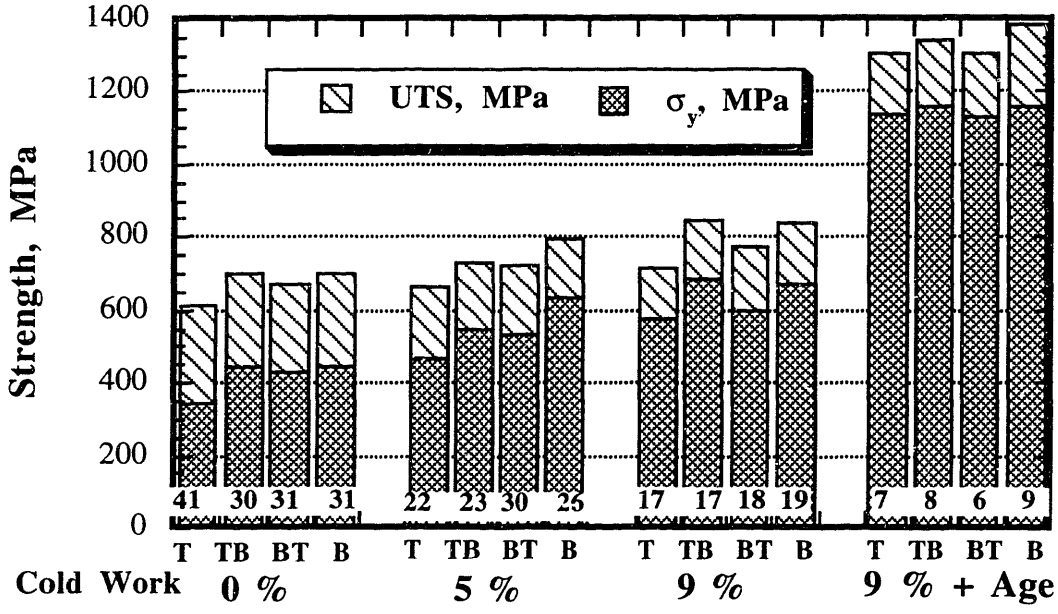

Figure 88. Partial-thickness tensile properties of 13 mm-thick GTA welds with 908 filler. Ductility values are written at the bottom of the bar at each condition. Description on the location where specimenes were taken is shown in Figure 26.

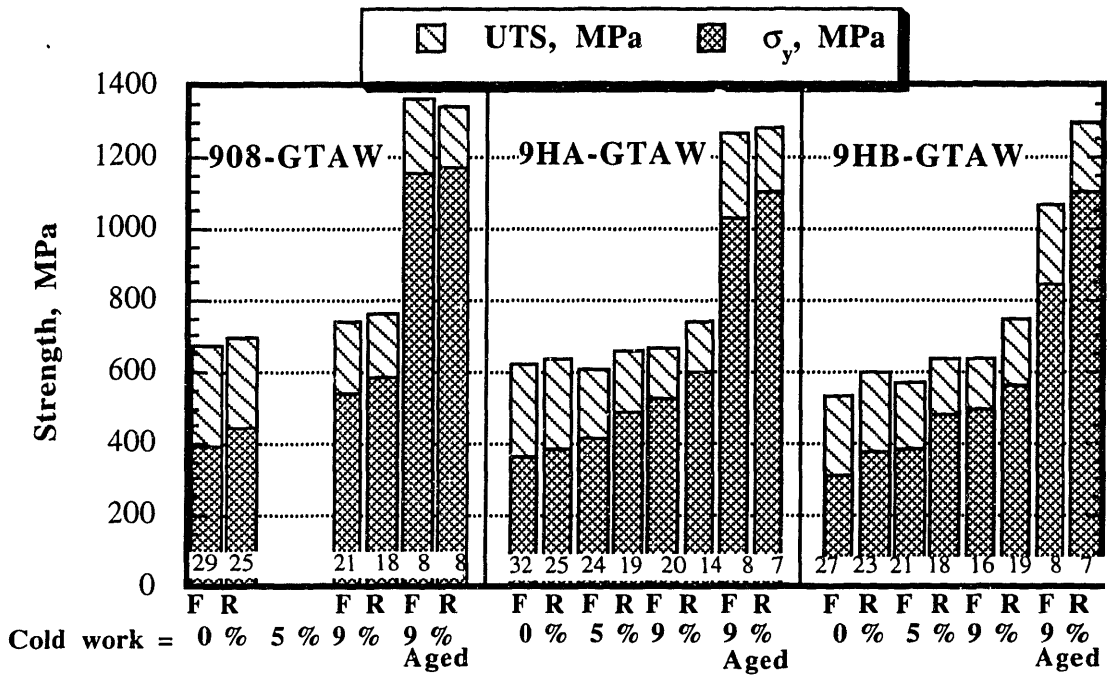

Figure 89. Partial-thickness tensile properties of 7 mm-thick GTA welds with various fillers. Ductility values are written at the bottom of the bar at each condition. Description on the location where specimenes were taken is shown in Figure 26.

D. Correlation Between Hardness and Strength of Welds

The results of the hardness measurements and tensile tests were correlated. The correlation between them was found by linear regression methods. The results are plotted in Figure 90. These equations can be used to estimate of strength based on simple microhardness test results.

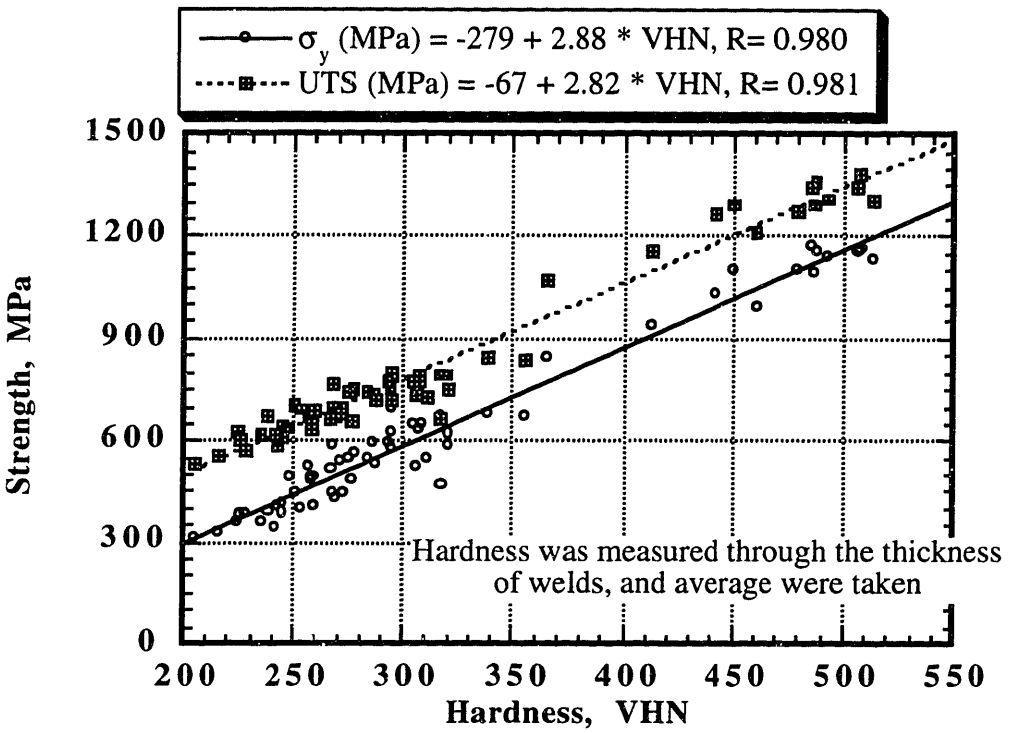

Figure 90. Correlation between strength and hardness of GTA welds.

V. Discussion

V.1 Solidification Characteristics of Alloy 908 Weld

During solidification of the weld pool, local thermodynamic equilibrium is maintained at the liquid/solid interface. The solute composition of newly forming solid is determined by solute composition of the liquid and the equilibrium partition ratio, k of the solute element. As solidification progress, elements with $k < 1$ are enriched in the liquid while those with $k > 1$ are enriched in the solid. In nickel-base or nickel-iron-base superalloys, Nb and Ti have partition ratios of less than unity and preferentially enriched in the liquid within the interdendritic zone.[34, 36, 38, 39]

Using the equlibrium temperature measured on filler metals with varying Nb content by differential thermal analysis (DTA) the low Nb side of a pseudo-phase diagram is shown in Figure 91. Unlike binary alloy systems, where the abscissa is a pure element, the liquidus and solidus temperature do not coverge at 0 % Nb. Thus the equilibrium partition ratio can not be calculated using conventional methods, such as $k = C_{Nb}^{S} / C_{Nb}^{L}$. Instead the equlibrium partition ratio for Nb was calculated by following methods. First, the solidus and liquidus lines were extrapolated. Then, the imaginary Nb content (C_{Nb}^{I}), where the liquidus and solidus temperature converge, was calculated to be - 3.14 %. The equilibrium partition ratio, k at temperature T_A can then be calculated as follow:

$$k = \frac{C_{Nb}^{S} - C_{Nb}^{I}}{C_{Nb}^{L} - C_{Nb}^{I}}$$

The resulting equilibrium partition ratio is about 0.47. The measured partition ratio in alloy 908 welds was (Nb concentration at dendrite core, 1.6 %)/(Nb concentration in 908 filler, 3.0 %) = 0.53, which is close to the above value. Similar values of k have been reported in 900-series superalloys,[38, 39] and Inconel 718.[36] Often, the equlibrium partition ratio of Nb has been treated as a constant during solidification, which is confirmed by electron microprobe analysis.[36] As shown in Figure 91, liquidus and solidus temperatures are linearly proportional to Nb content, implying that the equilibrium partition ratio of Nb in alloy 908 welds is a constant for the initial stage of solidification. The

equilibrium partition ratio at the later stage of solidification can be measured by comparing the composition of eutectic γ and lamellar eutectic constituent which contains alternating bands of eutectic γ and Laves phase.[36, 39] However, in alloy 908 welds, the final eutectic reaction takes place by precipitation of isolated secondary phase (Laves phase) and eutectic γ matrix (isolated eutectic). It is difficult to determine the composition of the eutectic constituent. For other 900-series superalloys, lamellar eutectic constituent was found in the final solidified welds, and the equilibrium partition ratio of Nb at the last stage of solidification was calculated as about 0.5 [39] which was close to the value of 0.58, reported for the initial stage of solidification.[38] Thus, approximately, the equilibrium partition ratio of Nb in alloy 908 welds can be treated as a constant over the entire solidification temperature range.

The equilibrium partition ratios of other elements were not explicitly measured. Comparing the composition of the dendrite core and bulk material, the partition ratio of other elements at the initial stage of solidification can be estimated. Titanium shows equilibrium partion ratio of about 0.67 which is close to the value reported.[36, 38, 73] At the later stage of solidification, the equlibrium partition ratio of Ti approaches unity in Inconel 718.[36] In the 900-series superalloys, Ti partitioning into Laves phase was reported.[39] In manual arc welds of alloy 908, the composition of Ti in Laves and surrounding γ matrix is about the same, suggesting the partition ratio reaches unity at the last stage of solidification. However in automatic production welds of alloy 908, the Ti content in Laves phase is higher than that in the surrounding γ matrix. It is not clear what causes this difference. Nonetheless, the segregation of Ti is less significant than that of Nb in alloy 908 welds.

Because of the low atomic weight of Al and Si, their equilibrium partition ratios were not measured in this study. A partition ratio of Al close to unity has been observed in Ni-base alloy IN100 [35,37] and in Incoloy 903.[38] Thus, it is assumed that the partition ratio of Al in alloy 908 is close to unity, also. Silicon is known to be segregated into the liquid during solidification of superalloys.[36, 39] Though the equilbrium partition ratio of Si was not measured in 900-series superalloys,[39] it was measured as 0.57 in Inconel 718.[36] Considering the similarity of solidification behavior of the alloys, it can be assumed that the equilibrium partition ratio of Si in alloy 908 is about the same. Recently, Cieslak estimated the equilibrium partition ratio if C in alloys similar to alloy 625 to be approximately 0.2 by using differential thermal analysis techniques.[74]

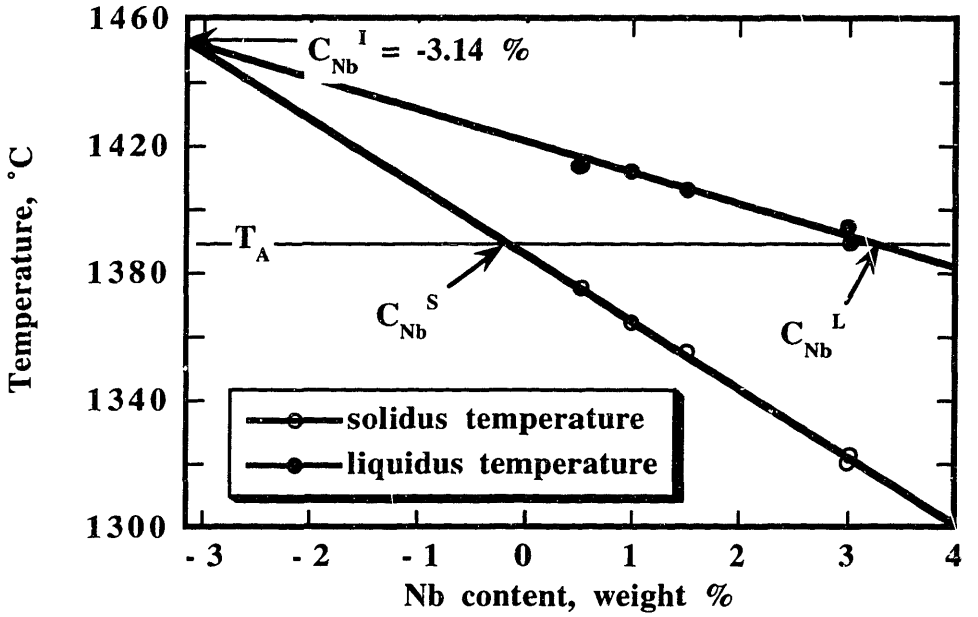

Figure 91. Extended plot of low Nb side of pseudo-binary phase diagram showing liquidus and solidus temperature.

Due to the low equilibrium partition ratio and relative abundance, segregation of Nb determines the overall microstructure of alloy 908 welds. Thus, the solidification behavior of alloy 908 welds will be discussed, focussing on the segregation of Nb, followed by the precipitation of the Nb-rich secondary phases, such as MC carbide and Laves phase. The solidification of alloy 908 welds can be explained as follows using the approach used for Inconel 718.[75] Initial dendrites of γ form and cause the liquid to be enriched in Nb and C. This enrichment continues during cooling until Nb-rich MC carbides form at around 1250 °C as confirmed by differential thermal analysis. This is close to the reaction temperature range of 1231 - 1250 °C reported for nickel base superalloys.[32, 36] Because the peak representing the MC carbide is broad, it can be assumed that MC carbides form over a range of temperatures [38, 75] rather than at a sharp invariant temperature assumed by Knorovsky et al.[36] MC carbides in alloy 908 welds precipitate as isolated particles (divorced eutectic) with morphologies varying from distinctive cubic to arbitrary shapes. A complex form of MC carbide, with lobed and arrow-headed shapes, reported in other superalloys,[31, 38] were not observed. A small amount of Ti-rich carbides are present.

As solidification progress, the simultaneous growth of γ matrix and MC carbide takes place through the epitaxial growth of existing γ and the nucleation and growth of MC carbides in the interdendritic liquid. When the liquid reaches the eutectic temperature, the terminal eutectic can be divorced with respect to carbides which can form epitaxially on existing carbides.[75] The carbon-depleted liquid then forms the γ/Laves eutectic constituents. The resulting microstructure is the precipitation of seperate Laves phase at the proximity of MC carbides in the solidified structure.[31, 43, 75] Such a microstructure is oberved in alloy 908 welds. While only one of either Laves phase and MC carbides are observed in most of the interdendritic zones in alloy 908 welds, both of the phases are observed in some of the interdendritic zones. The reaction temperature of γ/Laves eutectic was not apparent from the results of differential thermal analysis of alloy 908. The γ/Laves eutectic temperature of Inconel 718 is reported as about 1200 °C by Knorovsky et al.[36], and that of alloy 625 as about 1150 °C.[32] It can be assumed that the final eutectic reaction temperature of alloy 908 welds is close to 1200 °C.

Two kinds of MC carbides are present in the alloy 908 welds. One of them is the Nb-rich MC carbide with a composition of 86 % Nb - 13 % Ti with face centered cubic structure and lattice constant of a = 4.43 Å. The composition is similar to the MC carbides in alloy 908 base metal [20] and alloy 903 welds.[38] Also, similar lattice constants were reported in alloy 908 base metal [20], cast and wrought Inconel 718[33], Inconel 718 welds[36], and alloy 903 welds.[38] Thus, the composition and lattice constant of Nb-rich MC carbide, both in the welds and the base, of nickel-iron base superalloys can be considered the same. The peaks representing another face centered cubic crystal structure, with lattice constant of a = 4.41 Å, were detected by X-ray diffraction pattern analysis on extracted particles. Because the lattice constant of TiC is smaller than that of NbC,[76] these peaks are thought to represent Ti-rich MC carbide with about 30 % of Ti. Even though X-ray diffraction pattern analysis suggests that Ti-rich MC carbide is an equally abundant phase in alloy 908 welds, only a small number of Ti-rich MC carbide were identified by EDS analysis. It is possible that, because the Ti-rich MC carbide is smaller than the Nb-rich MC carbide, some of the Ti-rich MC carbide might have been lost when replicas were made. Also, because the replicated film was attached to conductive carbon tape, the small size of the Ti-rich MC carbide could have made it difficult to get enough signal to identify the phase by SEM/EDS analysis.

The composition of Laves phase in alloy 908 welds is 30 - 35 % Nb, 20 - 25 % Fe and 34 - 37 % Ni, determined by EDS analysis on extracted particles. Also, 1.9 % of Si is present

in Laves phase in alloy 908 welds. Silicon is known to segregate into Laves phase in other superalloys.[19, 32, 39] The amount of Nb in Laves phase in alloy 908 welds is considerably higher than those in other alloy systems,[31, 36, 38, 39] shown in Table 37. Compared to Incoloy 903 welds, Co was replaced mostly with Nb and Ni in alloy 908 welds. The crystal structure of Laves phase in alloy 908 welds is hexagonal with lattice constants of a = 4.77 Å and c = 7.76 Å, which is similar to the lattice constants of Laves phase in other 900-series superalloys.[38, 59]

The final solidified alloy 908 weld microstructure is dominated by Laves phase and MC carbides. No quatitative measurement of each phases was conducted, partly because the phases can not be distingushed by morphological difference. When, EDS analysis was conducted to identify phases, slightly more Laves phase than Nb-rich MC carbide was detected. Also, the intensity of Laves phase peaks in X-ray diffraction pattern on extracted particles was stronger than that of MC carbides. However, there are two kinds of MC carbides in alloy 908 welds, the combined peak intensity of Nb-rich MC carbide and Ti-rich MC carbide is stronger than that of Laves phase. Ernst et al.[39] observed predominantly Laves phase in the welds of 900-series superalloys. However, Nakkalil et al.[48] reported predominatly Nb-rich MC carbide in Incoloy 903 welds. Also, Thompson et al.[40] observed about 70 % increase in the volume fraction of Nb-rich carbide without change in the volume fraction of Laves phase when the C content changed from 0.02 to 0.06 % in cast Inconel 718. Thus, more research is needed to clarify the diffrences observed by the different group of researchers.

In welds with new filler metals, the dominant phase changes as the Nb-content in the filler metal changes. It should be mentioned that, though strict control of Si and C centents was specified when designing the filler metals, the composition of the filler metals was not explicitly analyzed. Considering the use of C as a deoxidizer during the vaccum induction melting process [77] and the presence of Si in the Laves phase in the welds with new filler metals, it is suspected that new filler wires have low Si and C content. Thus, the Si and C contents in the new filler metals are considered to be close to those in alloy 908 filler metal. When the Nb-content is more than 1.5 %, both Laves phase and MC carbide is present as major phases in the welds. Laves phase was not detected when the Nb-content of the filler metal was less than 1 %. Instead, MC carbide becomes the dominant phase. The composition of Nb-rich MC carbide becomes gradually richer in Ti at the expense of Nb. Cieslak [32] observed a predominantly MC carbide microstructure in high C (0.038 %) alloy 625 welds which have about 3.6 % Nb. Because the dominant phase in the welds depends on the ratio of Nb/C,[45] reducing the Nb content in alloy 908 filler has a similar

effect on the microstructure of alloy 908 welds. When the Nb content in the filler metals is small, not enough Nb is available to reach γ/Laves eutectic composition after the nucleation and growth of MC carbide. The size of the interdendritic zone, rich in Nb, surrounding the Laves and/or MC carbide, decreased as the Nb content in the filler decreased.

Table 37. Comparison of the composition of precipitates within the weld fusion zone of superalloys. (in weight percent)

Alloy	phase	Nb	Ni	Fe	Ti	Si	others	ref.
718	Laves	22.4	45.2	11.6	1.1	1.6	13 Cr, 4.9 Mo	36
		37.5	35.6	9.6	1.4	0.5	11.1 Cr, 4.2 Mo	31*
	MC	86.9	2.0	0.5	5.5	0	2.3 Cr, 2.8 Mo	31*
903	Laves	25.5	31.2	25.5	3.8	1.5	12.5 Co	39
		30.4	28.2	21.0	2.9	1.6	15.9 Co	38
	MC	85.8			14.2			38
908	Laves	35.5	37.3	21.5	2.5	1.9	1.3 Cr	Current
	MC	85.8	1.2	0.1	12.7	0.1		Current

* Originally given as atomic percents, converted into weight percent.

The kinetics of homogenization can be expressed as an Arrhenius form. The simplest model for considering solution kinetics is that of Singh and Flemings' [78] for a binary alloy containing nonequilibrium eutectic. In this model, dendritic arms are assumed plate-like and solute distribution within them are sinusoidal. In addition, eutectic is assumed isolated, and so the interdendritic region consists of plates of secondary phase with uniform composition, C_β. The amount of secondary phase is small so that motion of the α–β boundary can be neglected. Dissolution is limited by diffusion in the α-phase. The solution to the diffusion equation is given as;

$$\frac{g+a}{g_o+a} = e^{-\pi^2 (D_S t / 4 l_0^2)}$$

where $a = \frac{C_M - C_O}{C_\beta}$

where g is defined as the volume fraction of secondary phases. D_S is diffusion coefficient of solute element, l_0 is the one half of the dendrite arm spacing or the spacing between the concentration peak or precipitates to be removed. C_m is the maximum solute content in primary phase, and C_O is overall alloy composition. When heat treatment is at a temperature very close to the solvus, $C_O = C_m$, and the equation becomes:

$$\frac{g}{g_o} = e^{-\pi^2 (D_S t / 4 l_0^2)}$$

The relaxation time $t = 4l_0^2/\pi^2 D_S$, which is the time the volume fraction of secondary phases decreases to a factor of 1/e. The diffusion coefficient of elements are expressed as follows:

$$D = D_O \exp(-\frac{Q}{RT})$$

For Nb in γ Fe, $D_O = 7.5 \times 10^{-5}$ m^2/sec and $Q = 2.64 \times 10^5$ J/mole have been reported.[79] At high temperature, the above equation gives almost the same diffusion coefficient as other published results.[80] At 1050 °C, which is slightly higher than the stability limit of Laves phase in Inconel 718 [19] and Incoloy 909,[59] $D_{Nb} = 2.83 \times 10^{-15}$ m^2/sec. Corresponding relaxation times are estimated (when dendritic spacing is $2l_0 = 10$ μm) as 3580 seconds. In a spherical geometry, by which the precipitation could be more closely described, the diffusion kinetics are a lot faster than the slab geometry treated above. Approximately, the relaxation time in a spherical geometry is about 1/4 of that in slab geometry.[81] The resulting relaxation time is then about 895 sec at 1050 °C. The analytical solution for the dissolution of Laves phases are plotted in Figure 92. In one hour at 1050 °C, the volume fraction of precipitates decreases to less than 2 % in 3-dimensional geometry. In a practical sense, complete dissolution of Laves phases was achieved. The experimental result confirmed the complete dissolution of Laves phase within an hour at 1050 °C.

In addition to the dissolution of Laves phase, recrystallization of the weld microstructure occurred during the homogenization treatment. This was rather unexpected, since initially, it was thought that heat treatment at such a high temperature might produce an even larger grain size than the already elongated weld grains. Apparently, plastic deformation caused by thermal contraction and distortion during the welding could have provided nuclei for recrystallization.

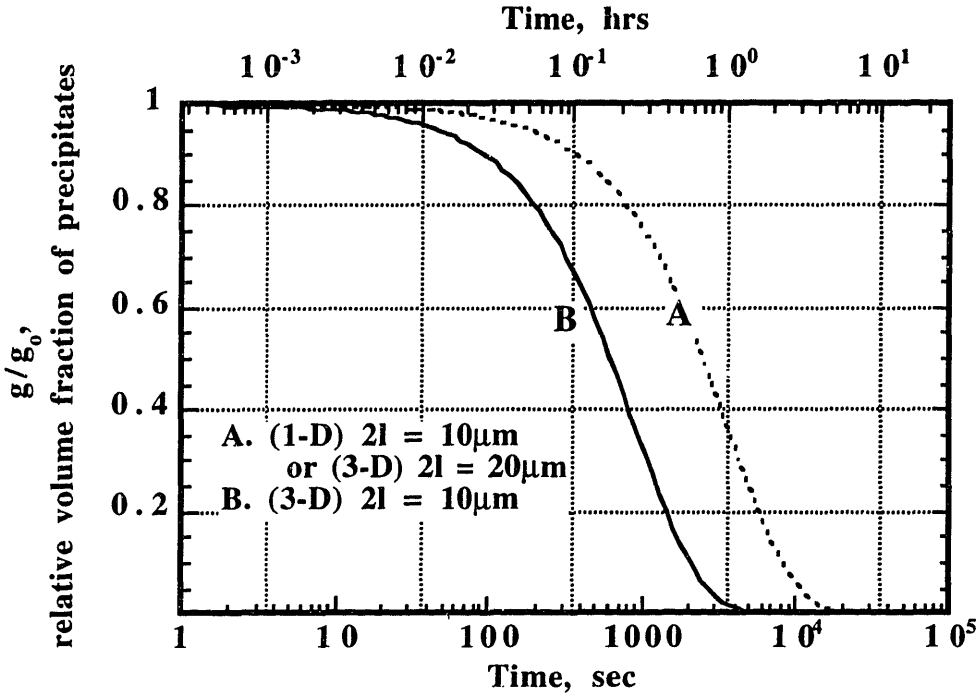

Figure 92. Analytical solution of dissolution kinetics using diffusion coefficient of Nb at 1050°C.

V.2. Mechanical Properties and Fracture Mechanics of Welds

Mechanical properties of alloy 908 welds with filler metals show a strong dependence on the Nb content of the filler metals. When the Nb content is reduced from 1 % to 0.5 %, the fracture toughness increases about 25 % without losing strength. Recently, similar results were reported on the fracture toughness of Inconel 718 weld.[82]

Cold work prior to aging increases the strength of welds. Similar behavior of alloy 908 base metal has been reported earlier.[2] However, due to a difference in the amount of cold work applied, direct comparison was not possible. The effect of lowering the test temperature was to increase the strength of the welds with filler metals both in the as weld + aged and the as-welded + cold worked + aged conditions, which is the typical response of austenitic and Invar-type alloys.[2, 83, 84, 85, 86, 87] Ductility of alloy 908 welds also increased as test temperature decreased from room temperature to 4K, showing similar behavior to the base metal [2] and other superalloy welds.[82] The combined effect of cold work and test temperature was to increase yield strength of the welds about 30 %.

The separate effect of cold work and test temperature on fracture toughness varied in each weld tested and can not be generally determined based on the results thus far. Moderate temperature dependence of fracture toughness has been reported for both the base and the welds of several superalloys.[2, 82, 86] Cold work prior to aging caused reduced fracture toughness in the base metal alloy 908 [2, 88] as well as in the welds with fillers at 4K, as shown in Figure 59. The effect of cold work on fracture toughness of welds with fillers was greater at 4K than at room temperature. Despite the mixed response to cold work and test temperature, the combined effect of cold work and test temperature can be clearly defined based on the results of this study. Fracture toughness of the welds with fillers at superconductor operating temperature is about 10 - 30 % lower than room temperature fracture toughness of directly aged welds.(see Figure 62) Overall, the mechanical properties of the as-welded + 9 % cold worked + aged welds tested at 4K showed about 30 % higher yield strength and 10 - 30 % lower fracture toughness than the as-welded + aged welds tested at room temperature.(see Figure 63)

Fatigue crack growth rate tests of the welds with filler metals were conducted only in the as-welded + aged condition at room temperature. Fatigue crack growth rates of the welds with fillers, as shown in Figure 93, were slightly lower than that of the base metal and showed little dependence on the Nb content. Similar behavior has also been reported for Inconel 706 [52]. However, the opposite behavior has been reported for precipitation hardening stainless steel (JBK-75) [89] and high Mn-austenitic steel.[90] The effect of cold work on the welds with fillers will be small as reported for base metal alloy 908.[2] The effects of temperature on fatigue crack growth rate and fatigue life of austenitic steels are well documented.[52, 85, 89, 90, 91] As temperature is reduced from room temperature to 4K, both of the fatigue crack growth rate and fatigue life improved considerably. For alloy 908 base metal similar behavior was observed.[2, 92] For alloy 908 welds with fillers, similar behavior can be expected.

In ductile dimple rupture, the correlation between fracture toughness and inclusion spacing is well known. Generally, the fracture toughness of a material increases as the inclusion spacing increases.[54, 66, 93] Unlike stainless steel welds, which showed a strong dependence of mechanical properties on welding methods,[93, 94] alloy 908 welds showed little dependence of fusion welding methods used, except production welds by automatic gas tungsten arc welding techniques, even though about a 2-fold change in precipitate spacing was observed depending on welding method. The production welds showed improved fracture toughness over the manual gas tungsten arc welds, though the dendritic structure and precipitate spacing is the same as manual gas tungsten arc welds.

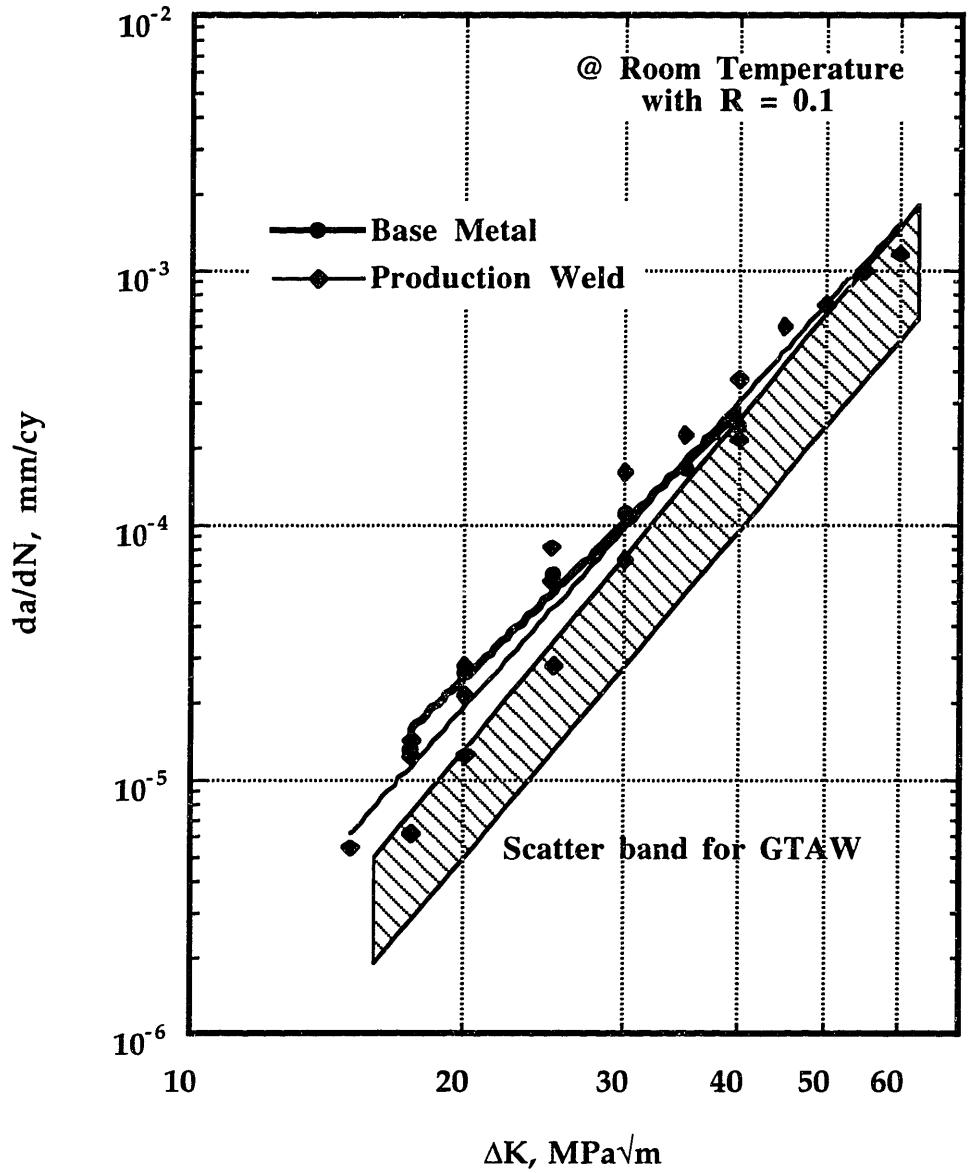

Figure 93. Comparison of fatigue crack growth rate of base metal, manual-GTAW, and production weld by pulsed-GTAW.

Fracture toughness of the welds improved dramatically when the welds were homogenized at 1050 °C/ 1hr prior to aging. This improvement in properties was achieved by reducing secondary precipitates within the welds. The benefit of high temperature heat treatment on mechanical properties of weld and base metal of superalloys have been reported by many researchers.[5, 51, 53, 58] The most significant effect of the high temperature heat treatment is to reduce or remove brittle Laves phases by dissolution, which improves fracture toughness and ductility. For Inconel 718 welds, full recovery of strength was achieved by precipitation hardening incorporating alloying elements dissolved from precipitates.[58] For alloy 908 welds, however, only fracture toughness and ductility were recovered, while the strength of the welds was lower than the base metal in the aged condition. However, when the 700 °C/100 hrs aging condition was used, homogenized welds showed much higher strength.(see Table 15) This suggests that the standard aging condition (650 °C/200 hrs) is not the optimum aging condition for the homogenized welds, at least to obtain maximum strength.

The fracture surface of alloy 908 welds shows a typical ductile rupture morphology. The mechanism of ductile dimple rupture has been well summarized by Van Stone et. al.[66] In alloy 908 welds, the void spacing on the fracture surface is about the same as the dendritic spacing in the welds with exception of laser beam welds and flash welds. Thus, it is thought that the interdendritic precipitates such as Laves phase and MC carbide provide the microvoids initiation sites during the fracture toughness test. Also, both Laves phase and Nb-rich MC carbide were identified at the base of the dimples by in-situ EDS analysis. When the Nb content in the filler metals is higher, a debris-like broken structure is visible at the base of the dimple. This debris-like broken structure is thought to be the result of the low ductility failure of the γ matrix surrounding precipitates. At the last stage of solidification, Nb-rich γ matrix is formed surrounding Laves phases, from the eutectic liquid. During aging heat treatment, this Nb-rich γ matrix is hardened by precipitation of γ', and become much less ductile than the dendrite core. Such a microstructure can explain the difference in the morphology of the dimple base between welds with 9FA filler and 9HA filler. The fracture of welds with 9FA filler can be explained as the mechanism shown in Figure 94-b). First, microvoids initiate by separation of the secondary phases, such as Laves phase and Nb-rich MC carbide. Then, the surrounding low ductility area is torn apart without much plastic deformation. This increases the void size effectively. Finally, the voids grow with plastic deformation until joined to the existing crack. On the other hand, the fracture of welds with 9HA filler can be explained as the mechanism shown Figure 94-a). In this case, the voids grow plastically, right after the microvoid formation.

Considering that most of the energy expended during dimple rupture is absorbed during void growth,[96] the combination of large secondary phases and large surrounding Nb-rich area is thought to be the cause of low fracture toughness of welds with 9FA filler metal.

The difference in fracture morphology between welds with 9FA filler and homogenized welds with 9FA filler can be explained in the same way. The removal of the Nb-rich matrix and Laves phase leaving only MC carbide resulted in dimples with extensive wavy deformation marks on the wall of dimples devoid of broken structure at its base.

Thus, it is shown that the reduction of precipitation of secondary phase and the size of Nb-rich γ matrix can be achieved by reducing Nb content (from 3 % to 0.5 %) in the filler metal. Similar results can be achieved by homogenizing the welds prior to aging. Both methods increased fracture toughness of the alloy 908 welds.

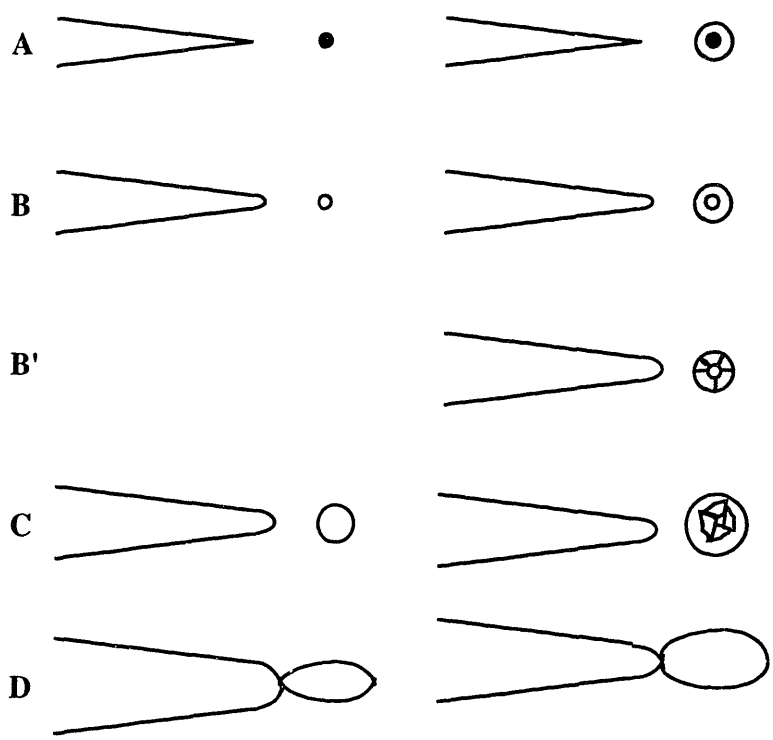

Figure 94. Schematic of void initiation, growth and coalescence. Case I: General dimple rupture, Case II: Dimple rupture in weld fusion zone, where less ductile zone is surrounding brittle phases.

V.3. Implications to Fusion Applications

The selection of base metal condition for welding is crucial to the determination of the properties of weldments in the as-welded condition. This choice will determine the performance of the conduit during fabrication of the cable assembly. For the tube reduction and winding process, where a considerable amount of plastic deformation will result, enough strength and ductility is needed to avoid preferential deformation within the weld, which will result in kinks and failure. When the base metal is in the mill-annealed condition, the strength of the initial welds will be the same or lower than the adjacent base metal. The net effect of this is that deformation will be more confined within the weld and the elongation in weldments will be reduced. On the other hand, when a softer homogenized base metal is used, the welds become stronger than the base metal and most of the deformation will occur in the base metal where ductility is greater. This case is favorable considering that, the welds area is more likely to have defects.

Currently automatic pulsed-gas tungsten arc welding with 908 filler wire has been proposed to join conduit sections. Initial mechanical testing of production welds showed improved fracture toughness over manual-gas tungsten arc welds with about the same strength. During the fracture toughness testing, one of the specimen showed unstable crack growth after small amount of crack growth. The surface of the broken specimen showed a smooth fracture surface covered with dimples. The crack path of that specimen was less tortuous than other specimens, suggesting less resistance to crack growth. The reason of such behavior is not clear. Schematics of weld fusion zone dendritic structure are shown in Figure 95. While, in most of the manual-gas tungsten arc welds, the weld bead was deposited in jig-jag pattern due to the difficulty of maintaining exact location of subsequent weld bead during welding, the position of weld beads were well maintained during automatic welding.[62] At the center of the welds, primary dendrites are aligned vertically, where the heat flow is the largest, stretching almost entire thickness of weld. Between each dendrite, brittle secondary phases are formed along with high Nb eutectic zones. When aged, these areas become high strength-less ductile zone surrounded by low strength-more ductile primary dendrite, thus providing a easier path for crack propagation without crack front adjustment which would be needed for manual-gas tungsten arc weld. When crack front is aligned with these vertical bands of dendrite, crack can propagate with little plastic deformation. Above hypothesis is too preliminary to be confirmed, but should be explored.

The tube reduction and bending processes after welding increase strength of both the welds and the base metal. Even though the strength of the welds is higher than the surrounding homogenized base metal, it is possible that the difference in strain hardening response eventually makes the base metal stronger than weld after cold work. The exact amount of cold work is not determined yet. As the elongation become smaller as the amount of cold work increases, and with the uncertainty in estimating the equivalent cold work through the fabrication process, it is better to have a weld with higher strength and greater elongation than base metal. In that respect, base plates with hardness less than 80 (Rockwell-B scale) was determined based on the results of high temperature (1050 °C/1hr) homogenization heat treatment. When the homogenized base metal is used to be joined, welds become stronger than surrounding base metal and the preferential deformation within the weld fusion zone can be avoided at certain degree.

Considering that the actual conduit will be supplied in the homogenized condition, the strength-cold work relation should be evaluated for proper fabrication processes. As a conservative approximation, the results of manual gas tungsten arc welding with mill annealed base metal can be used to estimate the properties of welds after cold work. After up to 9 % of thickness were reduced by applying cold work, welds showed at least 15 % of ductility.(see Figure 87-89)

After fabrication, the magnet assembly will be heat treated for 200 hours at 650°C. The problem of stress assisted grain boundary oxidation (SAGBO) during heat treatment has been investigated and reported earlier, but mostly on base metal alloy 908.[97] Evaluation of SAGBO resistance of the welds will be needed.

In the aged condition with prior cold work, GTA welds with 9HA and 9HB fillers showed promising mechanical properties, having over 1200 MPa - 120 MPa$\sqrt{m}$ and 1000 MPa - 160 MPa$\sqrt{m}$ strength - toughness combination at 4K.(Figure 63) Properties could be enhanced by better welding methods, if needed. Post weld homogenization heat treatment was successful in removal of brittle Laves phase and the surrounding Nb-rich zone and to recover ductility and fracture toughness of weld. Besides Laves phase dissolution, elongated weld grains were replaced with much smaller equiaxed recrystallized grains. Post weld homogenization heat treatments could be an alternative way to improve mechanical properties of welds.

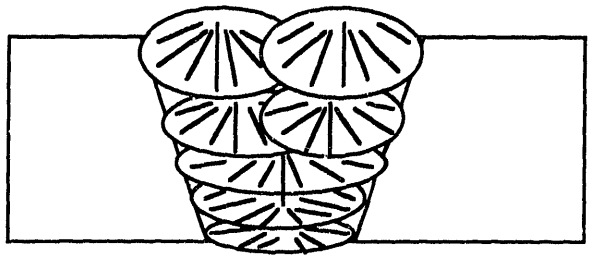

a) Manual-GTAW

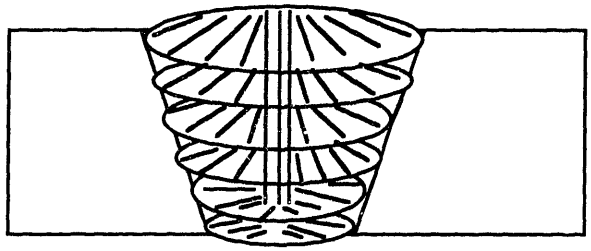

b) Automatic pulsed-GTAW

Figure 95. Schematics of dendrite orientation in weld fusion zone.

VI Conclusions

1. A fundamental understanding of the solidification behavior of Niobium-containing superalloys was developed.

A low Nb-side of Pseudo-binary solidification diagram for alloy 908 was constructed.

Hexagonal Laves phase and cubic MC carbide are the major intermetallic phases which precipitate in the interdendritic zone.

During solidification Niobium preferentially segregates to the interdendritic zone.

The equilibrium partition ratio of Niobium was determined to be approximately 0.5.

γ/MC and γ/Laves eutectic was observed to form in the interdendritic region between 1250 and 1200 °C.

The γ matrix is enriched in Niobium in the immediate area surrounding the secondary phases.

2. Based on this understanding new filler wire compositions were developed to allow welding of alloy 908.

Niobium content in the filler wire was reduced as much as possible consistent with mechanical properties criteria.

3. Filler wire compositions were optimized based on criteria which included: (1) adequate strength as measured by the yield and ultimate stress, (2) fracture toughness, and (3) fatigue crack growth behavior.

Improvement in fracture toughness was achieved as follows: (1) reducing the amount of Niobium in the filler wire. (2) homogenization of the weld prior to aging.

A homogenization heat treatment (1050 °C/1 hr) eliminated the Laves phase and homogenized the chemistry in the interdendritic region leaving only MC carbides.

Within the fusion zone, void initiation, during fracture, was dominated by the presence of Laves and/or MC carbide. Minimization of secondary phases and the surrounding Nb-rich γ matrix improved fracture toughness.

4. CICC process and fabrication variables were then accounted for in selecting the optimum , final, filler wire composition.

5. The mechanical behavior of alloy 908 welds were characterized.

Mechanical properties of alloy 908 welds were evaluated for the following conditions:

- the as-welded condition (room temperature)
- the as-welded + cold worked condition (room temperature)
- the as-welded + aged condition (room temperature, 4°K)
- the as-welded + cold worked + aged condition (room temperature, 4°K)

Fatigue crack growth rates are not a strong function of the weld filler wire composition.

Cold work after welding increased strength.

Care needs to be exercised to avoid easy paths for crack propagation which may be produced in multiple pass welds which produce a straight path between pass metal.

6. The key determining factor of welded joint performance during processing is the relationship between strength of the base and the as-welded weld metal.

A softer weld promotes localized deformation during processing.

Equal (as much as possible) strength of the base and weld metal insures safe processing.

Aging effectively eliminates differences in properties between weld and base metal.

VII. Future Work

Although production welds, using 908 and 9HA filler metals have much improved fracture toughness, unstable crack growth was observed for the specific case where long bands of primary dendrites were present normal to the tensile stress. Further work is needed to explore this case.

The actual conduit will be supplied in the homogenized condition and will be welded using automatic techniques. However, much of the work in this program made use of mill-annealed base metal and manual welding techniques. A limited number of tests were performed on automatic-welded/homogenized base metal plates to confirm that performance was consistent with mill-annealed/manual welded plates. More work is needed to fill out the data base for these conditions.

Very limited Stress Assisted Grain Boundary Oxidation (SAGBO) investigations have been conducted on 908 welds. This area is of critical importance for future work.

REFERENCES

1. Morra M.M., "Alloy 908 - A New High-Strength, Low Coefficient Thermal Expansion Alloy for Cryogenic Applications," M.S. Thesis, Massachusetts Institute of Technology, (1989)

2. Hwang I.S., R.G. Ballinger, M.M. Morra, and M.M. Steeves, "Mechanical Properties of Incoloy 908 - An Update," Adv. Cry. Eng. Mat., Vol. 38, pp. 1-10, (1992)

3. Private communication with Steeves M.M. at Plasma Fusion Center, Cambridge, Massachusetts.

4. Montgomery D.B., "Preliminary Description of ITER Magnet-Drawing Package," in Trip Report to ITER R&D Meeting at JET, July 15-16, (1992)

5. Mills M.J., "Fracture Toughness of Thermally Aged Alloy 718 Weld Metal," Welding Journal, Apr. 1987, pp. 113s-119s

6. Jang C.H., I.S. Hwang, R.G. Ballinger, and M.M. Steeves, "Development of High Toughness Weld for Incoloy Alloy 908," Adv. Cry. Eng. Mat., Vol. 40, pp. 1323-1330, (1994)

7. Bogner G., "Review of Large Superconducting Machines," Superconductor Materials Science, S. Foner and B.B. Schwartz, eds., Plenum Press, pp. 757-808, (1981)

8. Ekin, J.W., "Superconductors," Materials at Low Temperature, R.P. Reed and A.F. Clark, eds., pp. 465-513, (1983)

9. Henning C., "Magnet Design Technical Report - ITER Definition Phase," Lowrence Livermore National Laboratory, (1989)

10. Marston, P.G., "Large Scale Superconducting Magnet, Technology-Application," Handout for Course 570, MIT Independent Activities Period, Jan. 11-13, (1994)

11. Summers L.T., J.R. Miller, and J.R. Heim, "The International Thermonuclear Experimental Reactor (ITER); Design and Materials Selection," Adv. Cry. Eng. Mat., Vol. 36, pp. 769-776, (1990)

12. Suenaga M., "Metallurgy of Continuous Filamentary A15 Superconductor," Superconductor Materials Science, S. Foner and B.B. Schwartz, eds., Plenum Press, pp. 201-274, (1981)

13. Ekin J.W., "Mechanical Properties and Strain Effects in Superconductors," Superconductor Materials Science, S. Foner and B.B. Schwartz, eds., Plenum Press, pp. 455-510, (1981)

14. Ekin J.W., "Strain Effects in Superconducting Compounds," Adv. Cry. Eng. Mat., Vol. 30, pp. 823-836, (1983)

15. Steeves M.M., M.O. Heonig, and C.J. Cyders, "Effect of Incoloy 903 and Tantalum Conduits on Critical Current in Nb3Sn Cabled-in-Conduit Conductors," Adv. Cry. Eng. Mat., Vol. 30, pp. 883-890, (1984)

16. Shimamoto S., H. Nakagima, K. Yoshida, and E. Tada, "Requirements for Structural Alloys for Superconducting Magnet Cases," Adv. Cry. Eng. Mat., Vol. 32, pp. 23-32, (1985)

17. Morris, Jr. J.W., "Structural Alloys for High Field Superconducting Magnets," Adv. Cry. Eng. Mat., Vol. 32, pp. 1-21, (1985)

18. Suenaga M., K. Tsuchiya, N. Higuchi, and K. Tachikawa, "Superconducting Critical-Current Densities of Commercial Multifilamentary Nb3Sn(Ti) Wires Made by the Bronze Process," Cryogenics, Vol. 25, March, pp. 123-128, (1985)

19. Brown E.E. and D.R. Muzyka, "Nickel-Iron Alloys," Superalloys II, pp. 165-188, (1987)

20. Morra M.M., R.G. Ballinger, and I.S. Hwang, "Incoloy 908, a Low Coefficient of Expansion Alloy for High-Strength Cryogenic Application: Part I. Physical Metallurgy," Met. Trans. A, Vol. 23A, pp. 3177-3192, (1992)

21. Hwang I.S., R.G. Ballinger, and C.H. Jang, "Properties of Incoloy 908," presented at the Workshop on Structural Materials R&D for ITER, held at Boulder, CO, May 29-30, 1991

22. David S.A., and J.M. Vitek, "Correlation Between Solidification Parameters and Weld Microstructures," Int. Mat. Rev., Vol. 34, No. 5, pp. 213-245, (1989)

23. Brody H.D., "Segregation and Structure in the Weld Zone," Advances in Welding Science and Technology (TWR '86), S.A. David eds., ASM International, pp. 83-91, (1986)

24. Easterling K.E., "Solidification Microstructure of Fusion Welds," Materials Science and Engineering, Vol. 65, pp. 191-198, (1984)

25. Flemings M.C., Solidification Processing, McGraw-Hill, (1974)

26. Boettinger W.J., S.R. Coriell, and R.F. Sekerka, "Mechanisms of Microsegregation-free Solidification," Materials Science and Engineering, Vol. 65, pp. 27-36, (1984)

27. Scheil E., "Bermerkungen zur Schichtkristallbildung," Z. Metallkunde, Vol. 34, pp. 70-72, (1942)

28. Brody H.D. and M.C. Flemings, "Solute Redistribution in Dendritic Solidification ," Trans. TMS-AIME, Vol. 236, pp. 615-624, (1966)

29. Radaj D., Heat Effects of Welding, Springer-Verlag, (1992)

30. Lancaster J.F., Metallurgy of welding, 3rd ed., George Allen & Unwin, (1980)

31. Vincent R., "Precipitation Around Welds in the Nickel-Base Superalloy, Inconel 718," Acta Metallurgica, Vol. 33, No. 7, pp. 1205-1216, (1985)

32. Cieslak M.J., "The Welding and Solidification Metallurgy of Alloy 625," Welding Journal, Feb. 1991, pp. 49s-56s

33. Donachie M.J. and O.H. Kriege, "Phase Extraction and Analysis in Superalloys - Summary of Investigations by ASTM Committee E-4 Task Group 1," J. of Mat., Vol. 7, No. 3, pp. 269-278, (1972)

34. Heubner U., M. Kohler, and B. Prinz, "Determination of the Solidification Behavior of Some Selected Superalloys," Superalloys 1988, S. Reichman, D.N. Duhl, G. Maurer, S. Antolovich, and C. Lund eds., The Metallurgical Society, pp. 437-447, (1988)

35. Lecomte-Beckers J., "Study of Solidification Features of Nickel-Base Superalloys in Relation with Composition," Met. Trans., Vol. 19A, pp. 2333-2340, (1988)

36. Knorovsky G.A., M.J. Cieslak, T.J. Headley, A.D. Romig, Jr., and W.F. Hammetter, "Inconel 718: A Solidification Diagram," Met. Trans., Vol. 20A, pp. 2149-2158, (1989)

37. Zhu Y., S. Zhang, L. Xu, J. Bi, Z. Hu, and C. Shi, "Superalloys with Low Segregation," Superalloys 1988, S. Reichman, D.N. Duhl, G. Maurer, S. Antolovich, and C. Lund eds., The Metallurgical Society, pp. 703-712, (1988)

38. Nakkalil R., N.L. Richards, and M.C. Chaturvedi, "Fusion Zone Microstructure of Electron Beam Welded Incoloy 903," Scripta Met., Vol. 26, pp. 545-550, (1992)

39. Ernst S.C., W.A. Baeslack III, and J.C. Lippold, "Weldability of High-Strength, Low-Expansion Superalloys," Welding Journal, Oct. 1989, pp. 418s-430s

40. Thompson R.G., D.E. Mayo, and B. Radhakrishnan, "The Relationship between Carbon Content, Microstructure, and Intergranular Liquation Cracking in Cast Nickel Alloy 718," Met. Trans., Vol. 22A, pp. 557-567, (1991)

41. Radhakrishnan B. and R.G. Thompson, "Liquid Film Migration (LFM) in the Weld Heat Affected Zone (HAZ) of A Nickel-Base Superalloy," Scripta Met., Vol. 24, pp. 537-542, (1990)

42. Kelly T.J., "Rene' 220C - The New, Weldable, Investment Cast Superalloy," Welding Journal, Nov. 1990, pp. 422s-430s.

43. Sawai T., Y. Ueshima, and S. Mizoguchi, "Microsegregation and Precipitation Behavior during Solidification in a Nickel-Base Superalloy," ISIJ International, Vol. 30, No. 7, pp. 520-528, (1990)

44. Signes E.G., "A Simplified Method for Calculating Cooling Rates in Mild and Low Alloy Steel Weld Metals," Welding Journal, Oct. 1972, pp. 473s-484s.

45. Nakao Y., H. Ohshige, S. Koga, H. Nishihara, and J. Sugitani, "Effect of Nb/C on the Sensitivity of Liquation Cracking in 24Cr-24Ni-1.5Nb Fe-Base Heat Resisting Alloy," Japan Welding Journal. Vol. 51, No. 12, pp. 989-995, (1982)

46. Baeslack W.A., S. Ernst, and J.C. Lippold, "Heat Affected Zone Liquation Cracking in Cobalt-Free Low-Expansion Superalloy," J. of Mat. Sci. Let., Vol. 7, pp. 1204-1208, (1988)

47. Baeslack III W.A., W.P. Lata, and S.L. West, "A Study of Heat-Affected Zone and Weld Metal Liquation Cracking in Alloy 903," Welding Journal, Apr. 1988, pp. 77s-87s

48. Nakkalil R., N.L. Richards, and M.C. Chaturvedi, "Microstructural Characterization of Incoloy 903 Weldments," Met. Trans., Vol. 24A, pp. 1169-1179, (1993)

49. Jang C.H., unpublished data, (1991)

50. Inco Alloys International Technical Bulletin, Inconel Alloy 718

51. Mayor R.A., "Selected Mechanical Properties of Inconel 718 and 706 Weldments," Welding Journal, Sept. 1976, pp. 269s-275s

52. Logsdon W.A., J.M. Wells, and R. Kossowsky, "Cryogenic Fracture Toughness and Fatigue Crack-Growth Rate Properties of Inconel 706 Base Material and Gas Tungsten-Arc Weldments," Adv. Cry. Eng. Mat., Vol. 26, pp. 137-150, (1979)

53. James L.A., "Fatigue Crack Growth in Inconel 718 Weldments at Elevated Temperatures," Welding Journal, Jan. 1978, pp. 17s-23s

54. Siewert T.A. and C.N. McCowan, "The Role of Inclusion in the Fracture of Austenitic Stainless Steel Welds at 4K," Welding Metallurgy of Structural Steels, J.Y. Koo eds., The Metallurgical Society Inc., pp. 415-425, (1987)

55. Logsdon W.A., G.E. Grotke, R.E. Gold, and B. Lustman, "Cryogenic Tensile and Fracture Toughness Properties of Three Candidate Structural Materials for the Large Coil Program Superconducting Magnet Conduit Sheath," Adv. Cry. Eng. Mat., Vol. 28, pp. 771-780, (1981)

56. Wells J.M., "Evaluation of Inconel X750 Weldments for Cryogenic Applications," Adv. Cry. Eng., Vol. 22, pp. 80-90, (1975)

57. Summers L.T. and E.N.C. Dalder, "An Investigation of the Cryogenic Mechanical Properties of Low Thermal Expansion Superalloys," Adv. Cry. Eng. Mat., Vol. 32, pp. 73-80, (1985)

58. Mills W.J., "Effect of Heat Treatment on the Tensile and Fracture Toughness Behavior of Alloy 718 Weldments," Welding Journal, Aug. 1984, pp. 237s-245s

59. Heck K.A., D.F. Smith, J.S. Smith, D.A. Wells, and M.A. Holderby, "The Physical Metallurgy of Silicon-Containing Low Expansion Superalloy," Superalloys 1988, S. Reichman, D.N. Duhl, G. Maurer, S. Antolovich, and C. Lund eds., The Metallurgical Society, pp. 151-160, (1988)

60. Dawes M.G., "Contemporary Measurements of Weld Metal Fracture Toughness," Welding Journal, Dec. 1976, pp. 1052-1057

61. O'lone D.J., "Welding of High Strength Structural Materials," M.S. Thesis, Massachusetts Institute of Technology, (1992)

62. Salkin J.T., "Development of Welding Procedure for Incoloy 908 Superconductor Sheathing," Report prepared for Inco Alloys International, Inc. by Arc Applications, Inc., (1993)

63. Welding and Fabricating Data Book, Penton/IPC, Cleveland, Ohio, (1985)

64. Prager M. and C.S. Shira, "Welding of Precipitation-Hardening Nickel-Base Alloys," Welding Research Council Bulletin 128, (1968)

65. Herman W.A., R.W. Hertzberg, C.H. Newton, and R. Jaccard, "A Re-evaluation of Fatigue Threshold Test Methods," Fatigue 87, R.O. Ritchie and E.A. Starke, Jr. eds., Engineering Materials Advisory Services Ltd., pp. 819-828, (1987)

66. Van Stone R.H., T.B. Cox, J.R. Low Jr., and J.A. Psioda, "Microstructural Aspects of Fracture by Dimpled Rupture," Int. Met. Rev., Vol. 30, No. 4, pp. 157-179, (1985)

67. Nyilas A., J. Zhang, B. Obst, and A. Ulbricht, "Fatigue and Fatigue Crack Growth Properties of 316LN and Incoloy 908 Below 10K," Adv. Cry. Eng. Mat., Vol. 38, pp. 133-140, (1992)

68. Cullity B.D., Elements of X-ray Diffraction, Addison-Wesley, (1978)

69. Lippold J.C., "An Investigation of Heat Affected Zone Hot Cracking in Alloy 800," Welding Journal, Jan. 1983, pp. 1s-11s.

70. Nakkalil R., N.L. Richards, and M.C. Chaturvedi, "Precipitation of an E Phase in Incoloy 903," Scripta Metall., Vol. 25, pp. 2029-2034, (1991)

71. Tobler R.L. and I.S. Hwang, "Fatigue Crack Thresholds of a Nickel-Iron Alloy for Superconductor Sheath at 4K," Adv. Cry. Eng. Mat., Vol. 40, pp. 1315-1322, (1994)

72. Burger W. and J.G. Blauel, "Fracture Toughness of Manual Metal-Arc and Submerged-Arc Welded Joints in Normalized Carbon-Manganese Steels," Fatigue and Fracture Testing of Weldments, ASTM STP 1058, H.I. McHenry and J.M. Potter, eds., American Society for Testing and Materials, Philadelphia, pp. 272-299, (1990)

73. Cieslak M.J., T.J. Headley, and A.D. Romig. Jr., "The Welding Metallurgy of Hastelloy Alloys C-4, C-22, and C-276," Met. Trans. A, Vol. 17A, pp.2035-2047, (1986)

74. Cieslak M.J., unpublished research, Sandia National Laboratories, Albuquerque, NM, (1986): cited in [36], p. 2156.

75. Radhakrishnan B. and R.G. Thompson, "Solidification of the Nickel-Base Superalloy 718: A Phase Diagram Approach," Met. Trans. A, Vol. 20A, pp. 2866-2868, (1989)

76. Goldschmidt H.J., Interstitial Alloys, Butterworths, (1969)

77. Maurer G.E., "Primary and Secondary Melt Processing - Superalloys," Superalloys, Supercomposites and Superseramics, J.K. Tien and T. Caulfield, eds., Academic Press, Inc., pp. 49-97, (1989)

78. Sing S.N. and M.C. Flemings, "Solution Kinetics of a Cast and Wrought High Strength Aluminum Alloy," Trans. TMS-AIME, Vol. 245, pp. 1803-1809, (1969)

79. Kurokawa S., J.E. Ruzzante, A.M. Hey, and F. Dyment, "Diffusion of Nb in Fe and Fe Alloys," Metal Science, Vol. 17, pp. 433-438, (1983)

80. Nastac L. and D.M. Stefanescu, "An Analytical Model for Solute Redistribution during Solidification of Planar, Columnar, or Equiaxed Morphology," Met. Trans. A, Vol. 24A, pp. 2107-2118, (1993)

81. Geiger G.H. and D.R. Poirier, Transport Phenomena in Metallurgy, Addison-Wesley, (1973)

82. Matsumoto, K. Kohno, T. Honjo, K. Hirose, M. Okamura, K. Hattori, Y. Tsuda, and N. Suzuki, "Mechanical Properties of Large Ni-Base Superalloy Forging at Cryogenic Temperature," Adv. Cry. Eng. Mat., Vol. 40, pp. 1331-1338, (1994)

83. Tobler R.L., R.P. Reed, and D.S. Burkhalter, "Temperature Dependence of Yielding in Austenitic Stainless Steels," Materials Studies for Magnetic Fusion Energy Applications at Low Temperature - III, NBSIR 80-1627, R.P. Reed, ed., National Bureau of Standards, Boulder, Co., pp. 51-79, (1980)

84, Wang A.C., Y.Y. Li, D.F. Li, X. Zhao, C.G. Fan, and C.X. Shi, "Effect of Segregation on The Mechanical Properties of Some Precipitation-Hardened Austenitic Alloys," Adv. Cry. Eng. Mat., Vol. 40, pp. 1247-1254, (1994)

85. McHenry H.I., "Structural Alloys," Materials at Low Temperature, R.P. Reed and A.F. Clark, eds., pp. 371-411, (1983)

86. Tobler R.L., "Low Temperature Effects on the Fracture Behavior of Nickel Base Superalloy," Cryogenics, Vol. 16, pp. 669-674, (1976)

87. Grujicic M. and W.S. Owen, "A Comparison of Plastic Flow in Fe-Ni Invar and Fe-Ni-Cr Elinvar Alloys," Physical Metallurgy of Controlled Expansion Invar-Type Alloys, K.C. Russell and D.F. Smith, eds., pp. 235-249, (1990)

88. Bussiba A., R.L. Tobler, and J.R. Berger, "Superconductor Conduits: Fatigue Crack Growth Rate and Near-Threshold Behavior of Three Alloys," Adv. Cry. Eng. Mat., Vol. 38, pp. 167-174, (1992)

89. Logsdon W.A. and P.K. Liaw, "Cryogenic fatigue Crack Growth Rate Properties of JBK-75 Base and Autogenous Gas Tungsten Arc Weld Metal," Adv. Cry. Eng. Mat., Vol. 30, pp. 349-358 (1983)

90. Umezawa O., T. Ogata, T. Yuri, K. Nagai, and K. Ishikawa, "Review of High-Cycle Fatigue Properties of Structural Materials at Cryogenic Temperature," Adv. Cry. Eng. Mat., Vol. 40, pp. 1231-1238, (1992)

91. Maley V.N., S.A. Voronin, R.V. Chvartatsky, and S.V. Garrilov, "Cyclic Strength and Fatigue Life of Base Metal and Welded Joints of Candidate Steels for ITER Applications," Adv. Cry. Eng. Mat., Vol. 40, pp. 1268-1274, (1992)

92. Toma L., Incoloy Alloy 908 High Cycle Fatigue Test Report, Plasma Fusion Center, M.I.T., (1994)

93. Satoh H., T. Matsumoto, T. Funamoto, and Y. Wadayama, "Fracture Toughness of Cryogenic High Strength stainless Steel Weld Deposits," Welding International, Vol. 4, No. 9, pp. 697-702, (1990)

94. McHenry H.I. and T.A. Whipple, "Weldments for Liquid Helium Service," Materials Studies for Magnetic Fusion Energy Applications at Low Temperature - III, NBSIR 80-1627, R.P. Reed, ed., National Bureau of Standards, Boulder, Co., pp. 155-165, (1980)

95. Leslie W.C., "Inclusions and Mechanical Properties," ISS Transactions, Vol. 2, pp.1-24, (1983)

96. Shockey D.A., L. Seaman, K.C. Dao, and D.R. Curan, "A Computational Fracture Model for SA533, Grade B, Class i Steel Based upon Microfracture Process," Report NP-701-SR, Electric Power Research Institute, Palo Alto, Calif., (1978): cited in [66]

97. Morra M.M., S. Nicol, L. Toma, I.S. Hwang, M.M. Steeves, and R.G. Ballinger, "Stress Accelerated Grain Boundary Oxidation of Incoloy Alloy 908 in High Temperature Oxygenous Atmospheres," Adv. Cry. Eng. Mat., Vol. 40, pp. 1291-1298, (1994)